DISS. ETH N° 19247

Charm production in the OPERA experiment and the study of a high temperature superconducting solenoid for a liquid argon time projection chamber

ABHANDLUNG

zu Erlangung des Titels

DOKTOR DER WISSENSCHAFTEN

der

ETH ZÜRICH

vorgelegt von

Thomas Strauss

Dipl. Phys., Humboldt Universität zu Berlin

geboren am

15.03.1981

von

Berlin, Germany

Angenommen auf Antrag von

Prof. Dr. André Rubbia
Prof. Dr. Günther Dissertori

2010

Abstract

The OPERA Experiment (Oscillation Project with Emulsion tRacking Apparatus) is a long baseline neutrino oscillation experiment aiming for the first observation of ν_τ-appearance in a nearly pure ν_μ-beam (with a small ν_e-contamination). The CERN Neutrinos to Gran Sasso (CNGS) beamline has a length of 730 km and was optimized for detecting the appearance of τ-neutrinos through the reconstruction of τ-decays after a ν_τ charged current interaction. The oscillation amplitude (probability) depends on the mixing angle θ_{23} of the Pontecorvo Maki Nakagawa Sakata (PNMS) matrix elements, which is close to $45°$, i.e. the mixing is maximal. The OPERA experiment is situated in the underground hall C of the Laboratori Nazionali del Gran Sasso (LNGS) in a highway tunnel near L'Aquila (Italy). For five years of running at the nominal beam intensity, about ten reconstructed τ-decays are expected. Since at the CNGS energies the probability of a ν_μ to oscillate on its way from CERN to LNGS into a ν_τ is only a few percent, most of the interactions in the OPERA target are ν_μ charged and neutral current interactions (CC,NC). In the charged current interaction the energy of the primary interaction is high enough to allow charm production in about 4% of the events. Since the lifetime and the masses of charm and τ particles are similar, the main goal of this thesis is to demonstrate the efficient reconstruction of charm events in the OPERA detector, proving the principle for detection of short lived particles. Also the background of charm decays in the OPERA experiment was studied and is presented here.

Furthermore, the engineering and R&D studies for a magnetized liquid argon time projection chamber (LAr TPC) using high temperature superconductors (HTS) are presented in the appendix.

A poet once said, "The whole universe is in a glass of wine." We will probably never know in what sense he meant that, for poets do not write to be understood. But it is true that if we look at a glass of wine closely enough we see the entire universe.

...and you will find someday that, after all, it is not as horrible as it looks.

Richard Feynman (1918 - 1988)

Zusammenfassung

Das OPERA Experiment (Oscillation Project with Emulsion tRacking Apparatus) ist ein "long baseline" Neutrino Oscillations Experiment welches den Nachweis von ν_τ Entstehung aus einem nahezu reinen ν_μ Strahl (mit einer geringen ν_e Kontaminierung) erbringen will. Der "CERN Neutrinos to Gran Sasso" (CNGS) Strahl hat eine Länge von 730 km und wurde für die Detektierung des τ Neutrinos mittels der Rekonstruktion des τ Zerfalls nach einer Wechselwirkung des ν_τ via geladenen Strom optimiert. Die Oszillationswahrscheinlichkeit ist abhängig vom Mischwinkel θ_{23} der Pontecorvo Maki Nakagawa Sakata (PNMS) Matrix Elemente. Der Mischwinkel ist nahezu 45°, d.h. die Mischung is maximal. Das OPERA Experiment befindet sich in der Untergrundhalle C des Laboratori Nazionali del Gran Sasso (LNGS) in einem Autobahntunnel nahe L'Aquila (Italy). Nach fünf Jahren Laufzeit mit der nominellen Strahlintensität werden zehn rekonstruierte τ Zerfälle erwartet. Da bei der Energie des CNGS Strahls die Umwandlungswahrscheinlichkeit des ν_μ in ein ν_τ auf dem Weg vom CERN zum LNGS nur wenige Prozent beträgt, werden die meisten Wechselwirkungen innerhalb des OPERA Detektors aus Wechselwirkungen des ν_μ via geladenen und ungeladenen Strom bestehen. Beim geladenen Strom reicht die Energie der primären Wechselwirkung aus, um Charm Erzeugung in 4% der Wechselwirkungen zu ermöglichen. Da die Lebensdauer und Zerfallslänge von Charm und τ Teilchen ähnlich sind, war der Haupaugenmerk dieser Arbeit der Nachweis der Charm Rekonstruktion und Effizienz innerhalb des OPERA Detektors, um das Prinzip des Nachweises kurzlebiger Teilchen zu bestätigen. Auch der Untergrund der Charm Zerfälle im OPERA Experiment wurde untersucht und wird hier präsentiert.

Weiterhin wird im Appendix die Entwicklung und R&D Studie einer magnetisierten flüssig Argon Time Projection Chamber (LAr TPC) mittels Hochtemperatur Supraleitern (HTS) behandelt.

EinPoet sagte einst, "Das ganze Universum findet sich in einem Glass Wein." Wir werden nie verstehen, wie er das gemeint hatte, da Poeten nicht schreiben um verstanden zu werden. Aber es stimmt, wenn wir nur genau in Weinglas schauen, sehen wir das gesamte Universum.

...und eines Tages wirst du schlussendlich erkennen, dass es nicht so schlimm ist, wie es aussieht.

Richard Feynman (1918 - 1988)

Contents

Chapter 1

Introduction

I will explain the physics foundation of this thesis in more detail in chapter 1.1.2, now I just sketch the main motivation for this work. This thesis is dedicated to one of the most interesting fields of current particle physics, the neutrino physics. Even though the existence of neutrinos was postulated more than 80 years ago, it took about 25 years before they have been discovered in 1956. This is due to the fact, that neutrinos only make weak interactions with matter, making it difficult to detect them. Thus, it was only in the year 2000 that one finally observed the predicted third neutrino of the three known lepton families, the so-called tau neutrino ν_τ. Still, neutrinos provide new and fascinating measurements whenever they are studied. In the late 60's already one observed a missing neutrino flux in the solar neutrino flux, compared to solar nuclear fusion model calculations, leading to the hypothesis of flavor changing oscillations between the neutrino types, which was experimentally proven in the late 90's. Flavor changing implies that neutrinos have non-degenerate mass eigenstates, especially not all neutrino masses must vanish, and these mass eigenstates are different from the flavor eigenstates (neutrino mixing). The mechanism for neutrino mass generation cannot be explained with the so-called Standard Model (SM) of particle physics, this is a first hint of physics beyond the SM, and thus neutrino physics is currently one of the main interests in particle physics. Despite the fact that several experiments confirmed the oscillation phenomenon and measured some of the parameters, there are still a lot of open questions. For example one of the mixing angles is still not known, only an upper limit exits. Furthermore it is completely unclear, how the neutrino mass is generated, and which spinor can be used to described it; there exist two competing theories (Majorana or Dirac particles). And even though the two mass differences between the three neutrino flavors is known from the oscillation measurements, the mass hierarchy is unknown (see Figure 1.23). Also the absolute neutrino masses are still not known, only upper limits exist and additionally the question of the existence of sterile neutrinos is not answered yet; sterile neutrinos would not be subjected to the weak forces, thus only be observable by gravitation making them candidates for Dark Matter. There are several experiments in preparation and running to answer some of these questions, hopefully within the next years, but some problems will remain unanswered for the next decade.

One of the experiments currently running is the OPERA experiment which is expected to accomplish the final proof of tau neutrino (ν_τ) appearance from a pure ν_μ - beam from CERN. This proof is needed to complete the oscillation theory picture, as appearance in this channel has not been observed yet. The main part of this thesis will be related to work

done in the framework of this experiment, as the goal of this thesis was to understand the efficiencies and background from charm production in the OPERA target, coming from ν_μ charged current interactions.

Chapter one will cover the introduction into physics connected to this thesis, the second chapter will present the neutrino beamline, and chapter three the OPERA detector. The OPERA analysis and Monte Carlo (MC) software will be explained in chapter four and five. The efficiency and background study of charm in the OPERA experiment will be presented in chapter 5, in chapter 6 the data and Monte Carlo comparison is given. In the appendix of this thesis I will present results obtained from R&D work done in an effort to build a small magnetized liquid argon time projection chamber (LAr TPC) using high temperature superconductors (HTS). A summary of all the work will be given in chapter 7.

1.1   Physics Introduction

The main topic of this thesis is neutrino induced charm production and detection. I will start with a short illustration of the evolvement of modern particle physics, in more detail for neutrino physics, with a summary on the results of the past, and an outlook on future experiments. Afterwards I discuss the neutrino induced charm production. The historical development sketched here is based on different sources as particle physics books [1], university webpages [2, 3] and Wikipedia, and whenever possible the original publication is given.

1.1.1   Early historical development of particle physics

At the beginning of the nineteenth century, the common believe that matter consists of atoms (Greek word for the unbreakable) started to evolve, though this was a proposal already made by the Greek philosopher Demokrit living 460-371 B.C. [4]. As the experimental tools at ancient time were poor and the discussions were mainly based on philosophical arguments, this theory was not further improved and got forgotten in the middle ages. Anyway, the knowledge came back at 1800 when the understanding of chemical processes was developed by Antoine Lavoisier [5] and Joseph Louis Proust [6]. This basic knowledge helped John Dalton to develop a theory that the world was built up from atoms around 1803-10 [7]. Today we know that he was partly wrong, as he mixed up atoms and molecules in his fundamental particles, and he was corrected by Amedeo Avogadro introducing his law in 1811, stating that *"equal volumes of ideal or perfect gases, at the same temperature and pressure, contain the same number of particles, or molecules"* [8]. This was also allowing the distinction between molecules and atoms. Based on this knowledge, the kinetic gas theory was developed around 1850, finally culminating in Albert Einstein's [9] famous paper on the Brownian motion in 1905 and its experimental proof by Jean Perrin 1908 [10].

Regarding the atom itself, it was believed to be unbreakable until in 1897 J.J. Thomson observed the electron in cathode ray experiments, proving that from different atoms one common particle could be extracted [11]. As no inner structure of the atom was known, one assumed it to be filled with electrons like plums are distributed in a cake, the so-called "plum-cake" model shown in the upper part of Figure 1.1 [12]. At the same time, in 1896
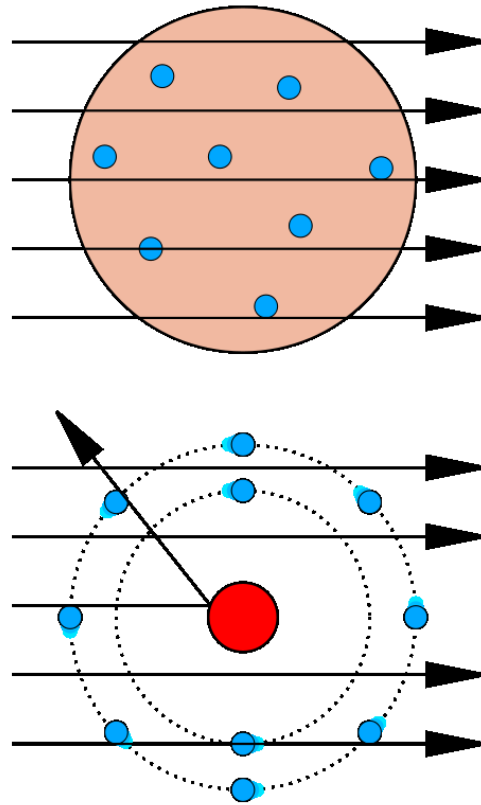
Figure 1.1: *Difference of scattering on the inner atomic structure in the plum-cake model (up) and the planetary model by Rutherford (down). Picture from the Wikipedia web site.*

Antoine Henri Becquerel discovered a new kind of radiation coming from uranium salts [13]. These rays were able to cross thin layers of paper, and in 1899 Ernest Rutherford showed that it actually were two different kinds of radiation. He called them alpha and beta radiation [14]. In 1909, when E. Rutherford, H. Geiger and E. Mardsen did their experiment of scattering alpha particles form a polonium 214 source on a thin gold foil [15, 16], the planetary model of the atom was developed. In that model a heavy positive atomic nucleus was surrounded by an outer cloud of electrons, as shown in the bottom of Figure 1.1. The main problem of this model at that time was that an electron on its orbit should emit electromagnetic radiation, thus, the resulting loss of energy would cause the electron to spiral into the nucleus.

In 1913 two big improvements in the atomic theory were accomplished, when Niels Bohr developed his theory for the atomic model [17]. He was implementing discrete energy states for the electrons, thus, they would not emit any radiation on their orbits when they are in their stationary ground states. This theory gave input to the foundation of later atomic and molecular models like the Bohr-Sommerfeld model or modern shell theories, even though it was working more or less correctly only for hydrogen atoms. The second important milestone that year was the discovery of Frederick Soddy of the existence of atomic isotopes [18] and Joseph John Thomson's work in the same area, when in the study of neon he developed the use of mass spectroscopy in physics [19].

1.1.2   Discovery of the Neutrinos

The beta decay problem

The newly found rays and particles from the experiments of Becquerel, Rutherford and Thomson were a new physics phenomenon, radioactivity. This new field was studied by many scientists, leading to three different types of radiation, alpha particles studied mainly by Rutherford, who found out in 1904 that these were actually Helium-4 nuclei. Gamma radiation was realized to be photons of "big" energy, of the order of a few MeV, emitted from the atomic nucleus. Beta radioactivity was discovered to be consisting of electrons in 1902 by the work of Pierre and Marie Curie [20, 21, 22]. The beta radiation was studied by different persons, most prominent Lise Meitner and Otto Hahn [23, 24, 25, 26, 27, 28, 29]. Still, they missed some part of the story in the beginning, assuming that in the two body decay of beta radiation, the electron was emitted having a fixed energy. The first measurements supported this idea by showing a peak in the energy. Later in 1909 when William Wilson [30] showed that the absorption of mono-energetic electrons in matter was described with a linear capturing process rather than the exponential capturing procedure one assumed before; it was implied that the spectrum of beta decay was continuous rather than a sharp peak. It was a controversial result, and it took five years till it was finally accepted, when the results were verified by James Chadwick [31]. Nevertheless, this provided a real problem for the physicists of that time, since energy and angular momentum conservation seemed to be violated.

The first historical hint solving the problem by introducing a new particle is referred to the 4th December 1930, when Wolfgang Pauli wrote a letter to his colleagues at a workshop in Tübingen, announcing the possibility of *electrically neutral particles, ...to call neutrons, which have spin 1/2.* He expected the neutron mass to be *of the same order of magnitude as the electron mass and in any event not larger than 0.01 proton masses. The continuous beta spectrum would then become understandable by the assumption that in beta decay a neutron is emitted in addition to the electron such that the sum of the energies of the neutron and the electron is constant....* In February 1932, a new heavy neutral particle of the atomic nucleus was observed by J. Chadwick [32, 33], which he called neutron. This particle was different to the type of neutron Pauli postulated to explain his theory of β-decay, as it was too heavy, but it changed the β-decay interpretation to a neutron decay $n \to pe^-\nu$. In the same year the first anti-particle, the positron, was observed by Anderson [34, 35]. This was verifying the Dirac theory, predicting the existence of particle and antiparticles [36].

In 1933 W. Pauli published his work on the "neutron" particle, emphasizing that it should only have a mass in the range of electrons or even zero [37]. In order to distinguish the neutron of W. Pauli from the one of J. Chadwick, the Italian physicist Enrico Fermi suggested to call them neutrinos, the belittled version of the Italian word for neutron, neutrone. Other theoretical work on the neutrino was done by Francis Perrin in 1933 [38], wherein he showed that the neutrino mass had to be much smaller than the electron mass. At the same time Frederic Joliot-Curie [39] observed the beta plus decay.

On the observation of this experiment and the neutrino hypothesis, E. Fermi built a theory of the beta decay as a 4 fermion point interaction including the neutrino [40] analog to the electro-magnetic interaction (see Figure 1.2), the coupling constant G_F, giving the
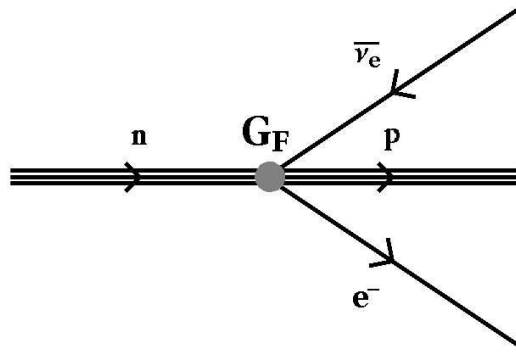
Figure 1.2: *Tree Feynman diagram of the 4 fermion point interaction in the neutron β-decay. Picture from the Wikipedia website.*

strength of the interaction as:

$$\frac{G_F}{(\hbar c)^3} = 1.16637 \times 10^{-5} \, GeV^{-2} \tag{1.1}$$

The theory was later refined from a four fermion vector current (the interaction Hamiltonian coupled two vector currents: $H_{weak} \sim j^{\mu,hadron} j_{\mu,lepton}$ with $j^\mu = V^\mu = \overline{\Psi}\gamma^\mu\Psi$) into a V-A current ($j^\mu = V^\mu - A^\mu$) when parity violation was observed. The theory was not renormalizable, but worked fine as a phenomenological description for low energies.

Shortly after Fermis theory was published, Bethe and Peierls calculated the cross section (interaction probability) between neutrinos and nucleons to be $\sigma \sim 10^{-44} \, cm^2$ at $E_\nu = 1 \, MeV$ in 1934 [41]. This cross section is several billion times smaller than the one between the electron (or positron) and matter, corresponding to a mean free flight path of neutrinos of roughly one light year in matter. In 1939 the discovery of Luis Alvarez and Robert Cornog on the radioactivity of tritium [42] provided an access to a direct probe of the neutrino mass due to its high Q-value, making it the best experimental source until today for an upper electron-neutrino mass limit, which is currently pushed further by the KATRIN experiment in Karlsruhe [43].

The first observed neutrino

The small cross section allows the observation only with large and heavy, but extremely sensitive detectors and/or very high fluxes of neutrinos. Although physicists continued their research on the beta decay, no direct observation of a neutrino was possible for a long time, until the discovery of the nuclear fission and fusion based on work done by L. Meitner [44] and Hans Bethe [45] gave the physicists an intense neutrino source. K.-C. Wang was the first to mention the possibility to detect the neutrino by an inverse β-decay experiment in 1942 [46]. Still, there was no source strong enough, until in 1946 Pontecorvo suggested an experimental approach using the resulting neutrino flux from the nuclear chain reaction to detect the neutrino [47].

Nevertheless, it took a few more years before finally in 1953 Clyde L. Cowan, Jr. and Frederick Reines proposed an experimental setup using a nuclear reactor in Hanford as antineutrino source (Hanford nuclear plant, Washington) [48]. As detector a target
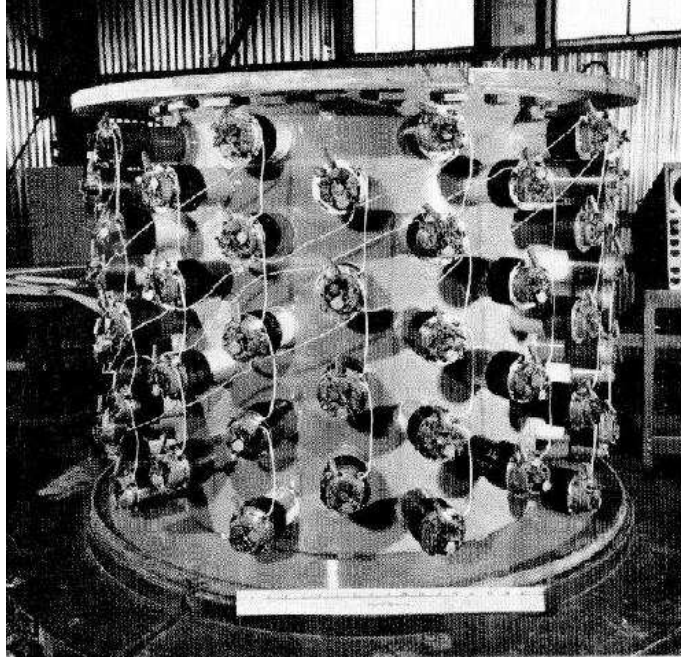
Figure 1.3: *Detector of the 1953 inverse beta decay experiment by Reines and Cowan. It held 40 kg of dissolved $CdCl_2$ in 2 tanks with a total of 200 l water. It was equipped with 110 5 inch photomultiplier tubes and had a size of only $2\,m \times 2\,m$. Picture from [2].*

made out of a mixture of 400 liters of a water and cadmium chloride was used and the measurements were finished in 1953, but no convincing results were achieved due to a large background from cosmic rays [49]. In 1956 the experiment was repeated at the Savannah River nuclear plant, South Carolina [50, 51], and due to a careful preparation (especially by reducing the background sources, which made the detection impossible before) the antineutrino was discovered with the reaction:

$$\overline{\nu}_e + p \rightarrow n + e^+ \tag{1.2}$$

The signal was a delayed coincidence between gamma's: two prompt 511 keV γ's from the e^+ e^- annihilation process followed within 5 microseconds by the γ emitted by an excited cadmium nucleus after the capture of the neutron. The calculated cross section was $6 \times 10^{-44}\,cm^2$, and they measured a cross section of $6.3 \times 10^{-44}\,cm^2$. To prove that the signal was related to the reactor activity they switched off the reactor too, and consequently observed nothing.

The ν and $\overline{\nu}$ distinction

As already mentioned, Cowan and Reines were working at the Savannah River nuclear plant. At the time of the experiment it was not clear, whether the neutrino is its own antiparticle, like the γ, Z^0 or the π^0. This question arises since the neutrino did not posses any charge-like properties like electric charge, or electric dipole moment, so this particle/antiparticle identity was possible. It was Raymond Davis jr., who was searching at the Savannah River reactor for the inverse β decay, using carbon chloride instead of cadmium chloride, with the reaction of:

$$\overline{\nu}_e + {}^{37}Cl \rightarrow e^- + {}^{37}Ar \tag{1.3}$$

He was not observing any interaction yielding an upper limit for the cross section $\sigma < 0.9 \times 10^{-45}\,\mathrm{cm^2}$, whilst the reaction:

$$\nu_e + {}^{37}Cl \rightarrow e^- + {}^{37}Ar \tag{1.4}$$

was observed with neutrinos coming from the sun's nuclear fusion process with a minimum threshold energy of $E_\nu = 0.82\,\mathrm{MeV}$ [52, 53]. Under the assumption that the ν and $\bar{\nu}$ are identical particles, the cross section for the reactions should be the same for equal energies, so Davis concluded that the neutrino and its antiparticle are different to each other.
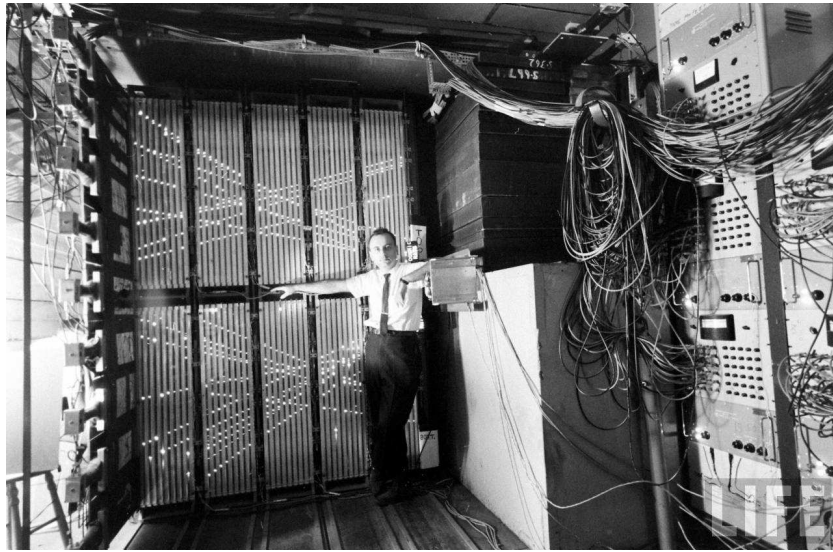
The discovery of different neutrino types

Figure 1.4: *Melvin Schwartz in front of the Brookhaven Spark Chamber. Picture taken by Fritz Goro 1962.*

Shortly after the discovery of the neutrino from β-decay the question occurred, whether one could distinguish it from the neutrino needed to explain the π^- (and μ-decays) of cosmic rays, or if it would be a different kind of particle [54]. In 1959 Schwartz proposed an experiment using an intense neutrino beam from pions, produced by a proton beam of some GeV hitting a carbon target and the subsequent decay of the pions into a muon and a neutrino [55]. The needed high intensity neutrino beams were possible by the usage of new proton-synchrotrons with high focusing capabilities, mainly CERN's PS (Proton-Synchrotron,1959) and the AGS (Alternating Gradient Synchrotron,1960) at the Brookhaven National Laboratory (BNL). The spark chamber developed by Cronin in Princeton [56] inspired the cooperation of Schwartz, Ledermann, Steinberger and Gaillard to build the detector for the experiment at the BNL [57]. The definition of the muon neutrino was:

$$\pi^- \rightarrow \mu^- + \bar{\nu}_\mu \tag{1.5}$$

$$\pi^+ \rightarrow \mu^+ + \nu_\mu \tag{1.6}$$
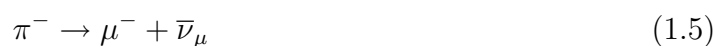
The cross section for the interaction was calculated by Lee and Yang, concluding that without the observation of

$$n + \nu_\mu \rightarrow e^- + p \tag{1.7}$$

with a neutrino from the pion decays one would need two different neutrino types to explain the previous measurements [58]. A 10 ton spark chamber filled with neon gas and shielded from muons with an iron layer was constructed in 1962 at the Brookhaven accelerator as shown in Figure 1.4. Even though several millions of neutrinos per hour were delivered by the accelerator, due to the low cross section only 40 neutrino events could be recorded. Still, for 6 events the final interaction particle was identified as an electron, while for the other events the final particle were muons. According to the calculations by Lee and Yang this was evidence for two neutrino types, since else the ratio should have been equal to one [58].

Another important work by Lee and Yang was leading to the discovery of parity violation in the weak interactions [59]. While the parity conservation was observed in electromagnetic and strong interactions, it was untested in the weak interactions. They were inspired by the τ/Θ-puzzle, where two decay modes were found for strange mesons [60]:

$$\Theta^+ \rightarrow \pi^+ + \pi^0 \tag{1.8}$$

$$\tau^+ \rightarrow \pi^+ + \pi^+ + \pi^- \tag{1.9}$$

The two final states have different parity, thus, one assumed in case of parity conservation that the original particles are different to each other. Yet, with increasing accuracy of the measurement, one observed that they had the same mass and lifetime, thus, they could be the same particle, if parity in the weak sector is violated. Thus, Lee and Yang proposed experimental tests and in 1956 Chien-Shiung Wu followed their proposal and observed parity violation in the β-decay of cobalt-60 [61]. The result was immediately verified by the group of L. Garwin, Leon Lederman, and R. Weinrich in pion decays [62]. With parity violation confirmed, the puzzle was solved (and the particle was called K$^+$ from then on). In 1957 the helicity of the neutrino was measured by Maurice Goldhaber [63] to be -1, i.e. that only left handed neutrinos exist, thus confirming the V-A theory, describing maximal parity violation in the weak interactions. Another important discovery was the strangeness by Kazuhiko Nishijima and Gell-Mann. Due to strangeness conservation, strange particles could only be produced as doublets in strong interactions, while their decay via the weak interaction was possible because strangeness was not conserved by weak interactions. This lead to the Gell-Mann-Nishijima formula describing the relation between baryon number, strangeness, isospin and charge of hadrons (Eight fold way, SU(3) symmetry of strong interaction) [64, 65, 66].

1.1.3   The development of the Standard Model

New experiments, detector technologies and particle accelerators provided a lot of new information in particle physics during the sixties and seventies. Important experiments were CHARM I & 2 (CERN-Hamburg-Amsterdam-Rome-Moscow Collaboration) [67, 68], CDHS (CERN, Dortmund, Heidelberg and Saclay) [69] and BEBC (Big European Bubble Chamber) [70] and experiments at the SLAC (Stanford Linear Acceleration Center), which will be partly described in more details later. These projects were each a series of different experiments with the same detector, giving the physics result of many new particles, the so-called "particle zoo". To explain this zoo, in 1964, Murray Gell-Mann [71] and George Zweig [72, 73] claimed that these particles could be classified according to a SU(3) flavor symmetry wherein quarks are constituents of the hadrons (nucleons) [74]. Their theory of quarks is based on the use of three quark flavors (up, down, strange). 1964 was also

the year when CP violation was observed by James Cronin and Val Fitch [75], when in the decays of long living neutral kaons, mostly decaying into three pions (CP=-1), at a 57 ft beamline (17.4 m) the decay into two pions (CP-even) was observed, which is the characteristic for the short living kaon which can not reach the end of the beam tube.
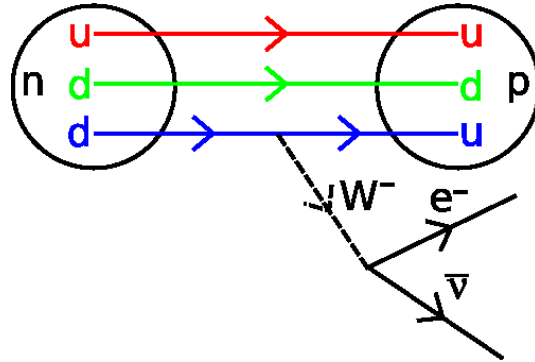

Figure 1.5: *Explanation of the β decay in the quark model. Picture from http:// commons.wikimedia.org.*

Shortly afterwards the first extension to the model of Gell-Mann and Zweig came into play, when Sheldon Lee Glashow and James Bjorken predicted the existence of a fourth quark, the charm [76], which allowed a more precise description of the weak interactions and could be used to correctly reproduce the known heavy meson masses (today known as charm particles). Around 1961-68 Abdus Salam [77], Sheldon Glashow [78] and Steven Weinberg [79] unified the two theories of weak and electromagnetic interactions into an electro-weak theory: a boson (photon) transports the electromagnetic interaction and the weak interaction is transported with either a W^+, a W^- or the Z^0-Boson. This electroweak theory, a so-called $SU_L(2) \times U_Y(1)$ gauge theory, was consisting of an $U_Y(1)$ gauge theory describing the Hypercharge, and the $SU_L(2)$ part described the isospin of lefthanded lepton doublets. To preserve gauge invariancy particles need to be massless, thus these new W- and Z-bosons were supposed to be massless. In 1964 three similar theoretical explanations were presented by Robert Brout and Francois Englert, Peter Higgs and the group of Gerald Guralnik, C. R. Hagen and Tom Kibble, giving mass to these three gauge bosons and also to all other particles, except for the photon, without destroying gauge invariance, the so-called Higgs mechanism [80, 81, 82].

The beta decay was now explained on the quark level when a d-quark of the neutron transformed into an up-quark (creating the proton) by emitting a W^-, which shortly afterwards decayed into an e^- and $\overline{\nu}_e$, as shown in Figure 1.5.

Still the existence of quarks was not widely accepted, even when in 1969 it was finally found that the proton (or neutron) consists of point-like scattering centers by deep inelastic scattering experiments at the SLAC [83, 84]. Most physicist preferred to call these new sub-particles partons, after Richard P. Feynman [85], which still remains the name for all constituent parts of hadrons, i.e. quarks, antiquarks and gluons. As a remark, the point-like scattering centers observed in the SLAC experiment were later identified as the up- and down- quarks.

In 1970 Glashow, Iliopoulos and Maiani proposed further hints towards the existence

of the fourth, the charm quark [86], the GIM mechanism, wherein the calculated ratio

$$\frac{P(K_L^0 \to \mu^+\mu^-)}{P(K_L^0 \to all)} \sim 9 \times 10^{-9} \tag{1.10}$$

was in agreement with the observation: the two Feynman graphs of Figure 1.6 almost cancel each other, yielding the very small branching ratio of equation 1.10.
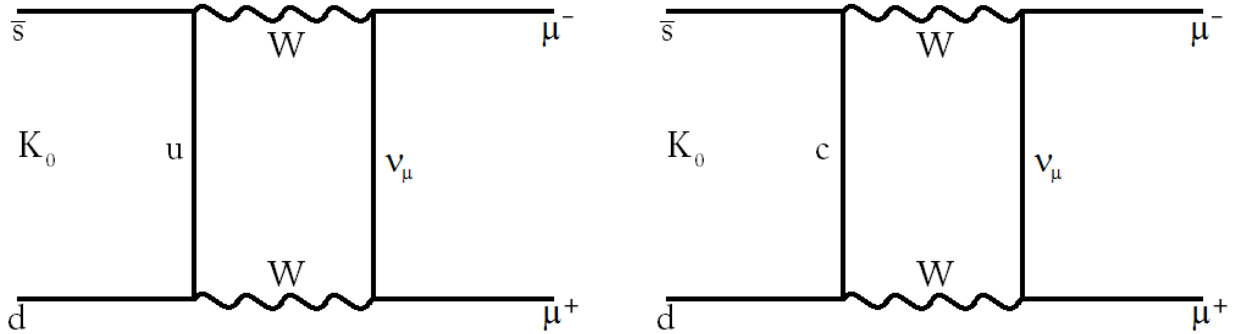

Figure 1.6: *Feynman diagrams of the K_L^0 decay in the GIM mechanism.*

The number of hypothetical flavors increased to six in 1973 when Makoto Kobayashi and Toshihide Maskawa explained the CP violation problem by introducing a third family with the two new quarks, top and bottom [87], see section 1.1.4.

The SM also predicts the so far unobserved weak neutral current interaction, mediated by the Z-boson. The neutral current was first observed in 1973 with the heavy liquid
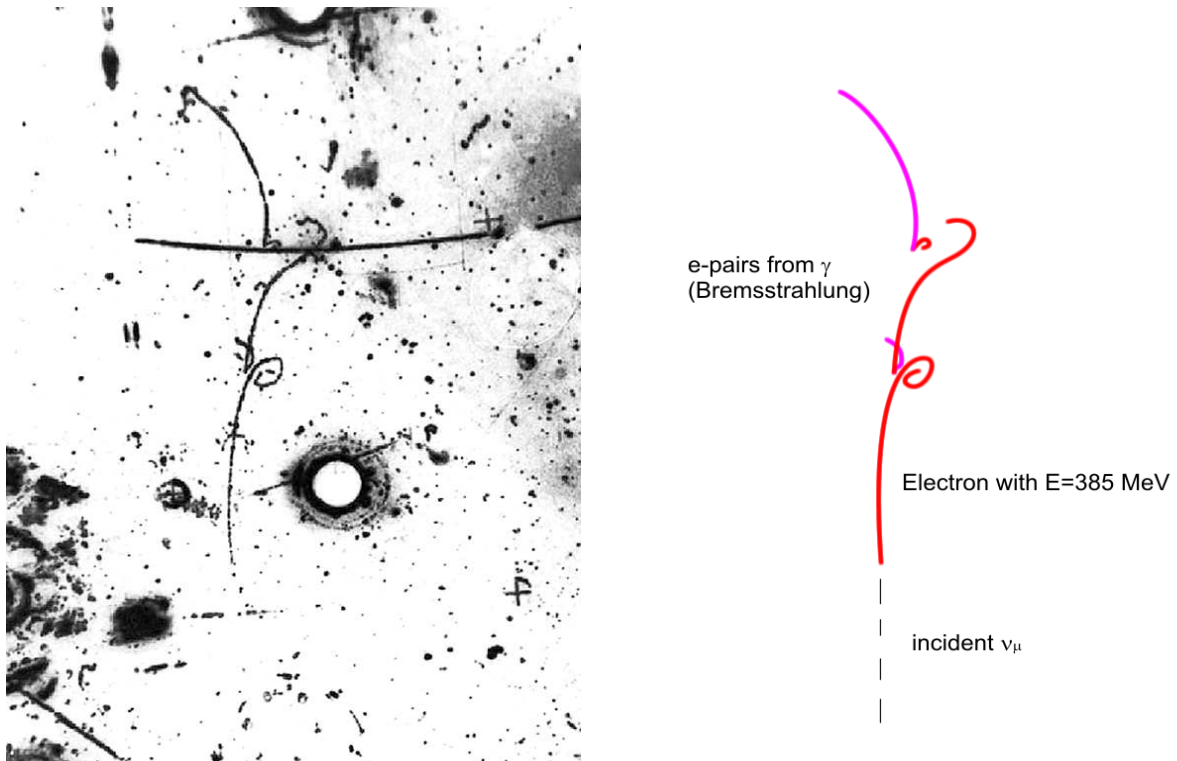

Figure 1.7: *First neutral current event observed by the Gargamelle Bubble Chamber experiment. Pictures taken from CERN teachers webpage, they can also be found at [88]*

bubble chamber experiment Gargamelle at CERN [89, 90, 88]. A bubble chamber is a detector containing a superheated transparent liquid. Crossing charged particles create ionization tracks on which the liquid vaporizes, i.e. were they produce bubbles. The density of the bubbles is proportional to the energy loss of the particle. A photograph of the bubbles is taken and analyzed to check for particle tracks. By application of a magnetic field the charge and momentum of the particle can be determined. The heavy liquid used in Gargamelle was Freon (CF_3Br, density $\rho = 1.5\,g/cm^3$), the neutrino beam was coming from CERN's PS.

Figure 1.7 shows the first leptonic neutral current interaction observed ever, the image is taken with the Gargamelle bubble chamber. In a neutral current interaction the neutrino is not transformed into an electron or muon, but exchanges a neutral interaction particle, the Z^0-boson, with the electron. The Z^0-boson transfers momentum to the electron, making it observable by its track without a parent particle in the detector. In the figure the interaction between an incoming ν_μ (going upwards, i.e. coming from the bottom) and the e^- of an atom with 385 MeV is shown. The electron is identified by the curvature of its track due to the magnetic field and the photon emitted by Bremsstrahlung (creating an electron pair (e^+, e^-)). The Z^0-boson responsible for this interaction is a virtual particle, the real particle was not yet observed. In the discussion of the background *…the probability that the single event observed in the $\overline{\nu}$ film is due to non-neutral current background is less than 3%.* For confirming the discovery *…a total of 370 000 neutrino and 360 000 antineutrino pictures were scanned twice and one single event satisfying the selection criteria was found in the antineutrino film.*

Figure 1.9 shows an example of the hadronic neutral current reaction $\nu_\mu/\overline{\nu}_\mu + N \rightarrow \nu_\mu/\overline{\nu}_\mu + hadrons$. For neutral current events the produced particles have to be hadrons,
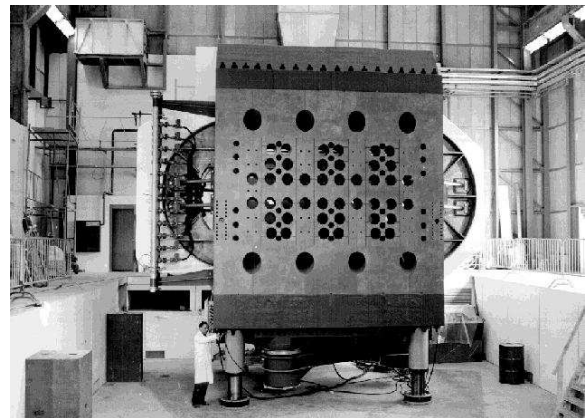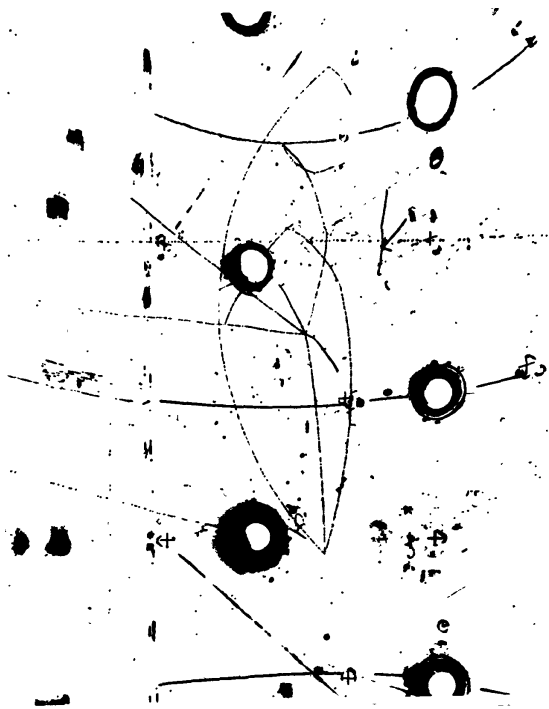

Figure 1.8: *Bubble chamber Gargamelle inside the magnetic yoke at CERN. Picture from [2].*

Figure 1.9: *Hadronic neutral current event observed in the Gargamelle Bubble Chamber in the reaction $\nu_\mu + N \rightarrow \nu_\mu + X$. Picture from [90].*

while in charged current events also leptons are observed with a ratio for CC to NC cross sections of (for the Gargamelle experiment neutrino beam energy) [90]:

$$R_\nu = \frac{\sigma(\nu_\mu N \to \nu_\mu X)}{\sigma(\nu_\mu N \to \mu^- X)} = 0.22 \pm 0.04 \tag{1.11}$$

$$R_{\overline{\nu}} = \frac{\sigma(\overline{\nu}_\mu N \to \overline{\nu}_\mu X)}{\sigma(\overline{\nu}_\mu N \to \mu^+ X)} = 0.43 \pm 0.12 \tag{1.12}$$

The charm quark was experimentally confirmed in 1974, when two experiments announced on the eleventh of November (November revolution) a new particle consisting of the charm quark and its antiquark. The group of Burton Richter from the Stanford Linear Accelerator Center named it PSI [91], after the reconstructed image it left in their detector (see Figure 4.4 in [92]), while Samuel Ting's group from MIT called it J [93]. Today, this particle is known as J/ψ and is part of the charmonium states, a collection of charm-anticharm bound states. This finally gave proof for the quark theory. With increasing energy of the accelerators in 1977 the Lederman group at the Stanford accelerator observed the Υ (Upsilon particle) interpreted as $b\overline{b}$ bound state, the first member of a third quark family was found [94]. The τ-lepton was found by Perl [95] around the same time, thus, also a third lepton family was supposed to exist.
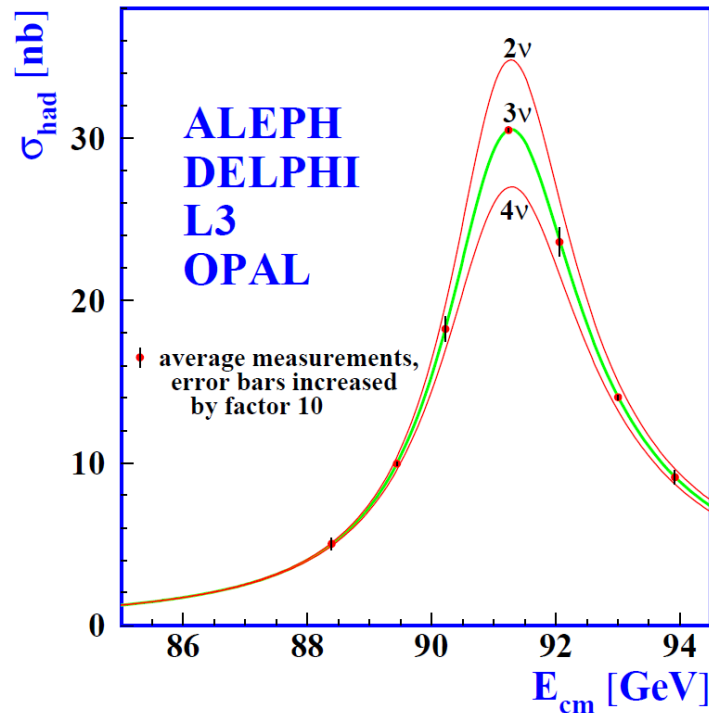

Figure 1.10: *Measurements of the hadron production cross-section around the Z resonance. The curves indicate the predicted cross-section for two, three and four neutrino species with SM couplings and negligible mass. Picture from [96].*

Still even though the existence of neutral and charged currents was known, the corresponding bosons, the W^+, the W^- and the Z^0 had not been observed directly yet. Their mass was predicted by the electroweak theory to be in the range of 80 proton masses,

i.e. around 80 GeV. On the suggestion of C. Rubbia, people at CERN developed with a tremendous effort a new accelerator complex, the Super Proton Synchrotron providing colliding beams of protons and antiprotons with an energy of 400 GeV/c each to produce these bosons in collisions. The stochastic cooling technique for using anti-protons for the collisions was developed under the leadership of Simon van der Meer [97, 98]. The newly built detectors UA1 and UA2 (UA for underground area) were collision experiments around the accelerator ring of the SPS. Shortly after the start up of the experiment, the UA1 experiment found the W-boson and Z-boson in 1983 [99, 100, 101, 102] as also the UA2 experiment[103, 104, 105].

This closed the circle and finally, nearly 90 years after the first observation of the β-decay, a consistent theory for the beta decay was confirmed. As already mentioned, the fifth quark and the third lepton had been observed, and finally, from 1989 on different experiments at the Large Electron Positron collider (LEP) made lifetime measurements of the Z-boson, showing that only three light neutrinos could exist, as shown in Figure 1.10 (see e.g. [106]). Still, neither the t-quark nor the τ-neutrino were observed yet. In fact, the experimental observation of the top-quark had to wait until 1994 [107, 108] while the ν_τ was not observed before the year 2000, when it was found at the Fermilab [109, 110].

1.1.4 Quark mixing and the CKM matrix

In 1963 Nicola Cabibbo introduced a theory to preserve the universality of the weak interaction [111]. In this theory the hadronic weak current states are a mixture of the quark mass (or flavor) eigenstates. That means the quark coupling to the up quark in the weak interaction is a superposition of the down and strange quark, the $|d'\rangle = \cos\theta_c|d\rangle + \sin\theta_c|s\rangle$. After the discovery of the charm quark, the theoretical description of Cabibbo's theory was refined to include the s' quark in weak interaction, with $|s'\rangle = -\sin\theta_c|d\rangle + \cos\theta_c|s\rangle$. Thus the mixing could be described with a unitary 2x2 matrix, the Cabibbo matrix.

$$\begin{bmatrix} |d'\rangle \\ |s'\rangle \end{bmatrix} = \begin{bmatrix} \cos\theta_c & \sin\theta_c \\ -\sin\theta_c & \cos\theta_c \end{bmatrix} \begin{bmatrix} |d\rangle \\ |s\rangle \end{bmatrix} = \begin{bmatrix} V_{ud} & V_{us} \\ V_{cd} & V_{cs} \end{bmatrix} \begin{bmatrix} |d\rangle \\ |s\rangle \end{bmatrix} \tag{1.13}$$

The Cabibbo angle determines the probability of the decay from down and strange quarks into up-quarks and is given as:

$$tan\theta_c = \frac{|V_{us}|}{|V_{ud}|} = \frac{0.2257}{0.97419} \rightarrow \theta_c = 13.04° \tag{1.14}$$

In 1973 Makoto Kobayashi and Toshihide Maskawa generalized the two quark mixing in the weak decay into a three quark mixing, taking into account the third quark family. The complex 3×3 mixing matrix, the so-called CKM matrix, also allowed to introduce a complex phase leading to CP-Violation[87]. The left part of the Equation 1.15 shows the weak interaction eigenstates d', s' and c', while the d,s and c states on the right represent the mass (or flavor) eigenstates of the quarks.

$$\begin{bmatrix} |d'\rangle \\ |s'\rangle \\ |b'\rangle \end{bmatrix} = \begin{bmatrix} V_{ud} & V_{us} & V_{ub} \\ V_{cd} & V_{cs} & V_{cb} \\ V_{td} & V_{ts} & V_{tb} \end{bmatrix} \begin{bmatrix} |d\rangle \\ |s\rangle \\ |b\rangle \end{bmatrix} \tag{1.15}$$

The CKM matrix is an unitary matrix, i.e. instead of using the d, s and b quarks for describing the eigenstates one could formulate the same matrix description using the u, c and t quarks. The 3 dimensional matrix has 3+1 free parameters, 3 quark mixing angles and one complex CP-violating phase. [To fulfill the unitarity condition, the CKM matrix needs to fulfill $\sum_k |V_{ik}|^2 = 1$, the so-called weak universality, and $\sum_k V_{ik}V_{jk}^* = 0$. This second constraint is called the unitary triangle. For a fixed value of i and j $(i \neq j)$ exist three complex numbers, forming the sides of a triangle in the complex plane. Due to combination six triangles exist in total, each having a different shape, but all triangles have the same area, as the size is related to the complex phase δ. In case of no CP-violation the area of the triangles would be zero. The values for the triangle sides, as the mixing angles are directly accessible by experiment and have been tested by several experiments. The transition from quark i to quark j is proportional to $|V_{ij}|^2$, the best values, obtained from the Particle Data Group [112], for the absolute values of the CKM matrix elements are:

$$
\begin{bmatrix}
|V_{ud}| & |V_{us}| & |V_{ub}| \\
|V_{cd}| & |V_{cs}| & |V_{cb}| \\
|V_{td}| & |V_{ts}| & |V_{tb}|
\end{bmatrix}
=
\begin{bmatrix}
0.9728 \pm 0.0030 & 0.2165 \pm 0.0027 & (3.93 \pm 0.36) \times 10^{-3} \\
0.230 \pm 0.011 & 1.04 \pm 0.06 & (41.2 \pm 1.1) \times 10^{-3} \\
(8.1 \pm 0.6) \times 10^{-3} & (38.7 \pm 2.3) \times 10^{-3} & 0.77^{+0.18}_{-0.24}
\end{bmatrix}
\tag{1.16}
$$

With the quark mixing angles θ_{ij} (Euler angles) and the CP-violating phase δ_{13} the CKM matrix can be written in the standard parametrization [113], wherein $c_{ij} = \cos\theta_{ij}$ and $s = \sin$. The angle θ_{12} is equal to the Cabibbo angle.

$$
\begin{bmatrix}
c_{12}c_{13} & s_{12}c_{13} & s_{13}e^{-i\delta_{13}} \\
-s_{12}c_{23} - c_{12}s_{23}s_{13}e^{i\delta_{13}} & c_{12}c_{23} - s_{12}s_{23}s_{13}e^{i\delta_{13}} & s_{23}c_{13} \\
s_{12}s_{23} - c_{12}c_{23}s_{13}e^{i\delta_{13}} & -c_{12}s_{23} - s_{12}c_{23}s_{13}e^{i\delta_{13}} & c_{23}c_{13}
\end{bmatrix}
\tag{1.17}
$$

Another parametrization was presented by Lincoln Wolfenstein [114], using the 4 parameters λ, A, ρ and η. They are related to the standard parametrization via $\lambda = s_{12}$, $A\lambda^2 = s_{23}$ and $A\lambda^3(\rho - i\eta) = s_{13}e^{-i\delta}$. Thus the CKM matrix can be written as follows (to the order of λ^3):

$$
\begin{bmatrix}
1 - \lambda^2/2 & \lambda & A\lambda^3(\rho - i\eta) \\
-\lambda & 1 - \lambda^2/2 & A\lambda^2 \\
A\lambda^3(1 - \rho - i\eta) & -A\lambda^2 & 1
\end{bmatrix}
+ \mathcal{O}(\lambda^4)
\tag{1.18}
$$

Giving the known values of the matrix elements one obtains $\lambda = 0.2257^{+0.0009}_{-0.0010}$, $A = 0.814^{+0.021}_{-0.022}$, $\rho = 0.135^{+0.031}_{-0.016}$ and $\eta = 0.349^{+0.015}_{-0.017}$, as shown in Figure 1.11.
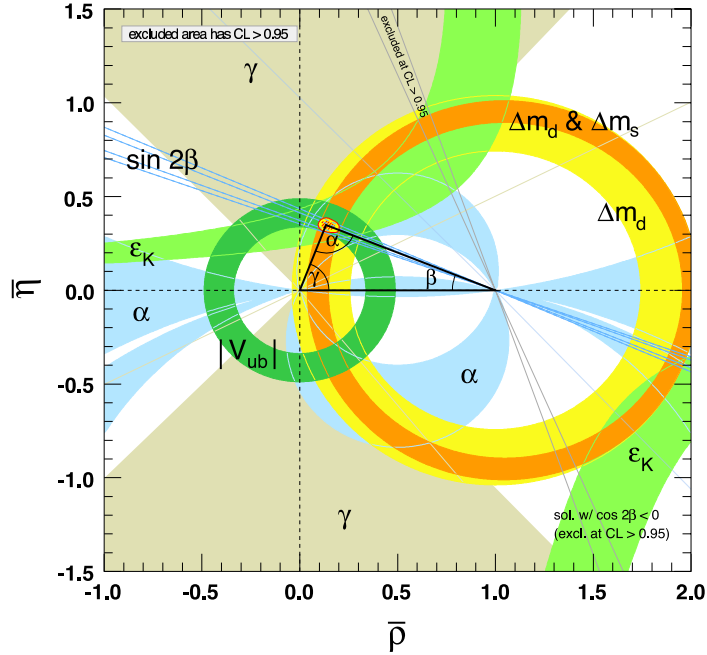
Figure 1.11: *Constraints on the ρ, η plane. The shaded areas have 95% CL. Picture taken from [112].*

1.2 The Standard Model of Particle Physics, a summary

The Standard Model of particle physics describes quarks, leptons and the three (out of four) fundamental forces between them. In theoretical terms it is a gauge theory based on the $SU(3) \times SU_L(2) \times U_Y(1)$ symmetry group, combining the gauge groups $SU(3)$ of the strong and $SU_L(2) \times U_Y(1)$ of the electroweak interaction. We already know that it cannot be the final description of the physics up to high energy scales, there are some theoretical approaches to close these gaps, but they are not proven yet. The String Theory tries to explain the unification of gravitation and the Standard Model, while Super Symmetry (SUSY) and Grand Unified Theories (GUT) try to predict physics beyond the 1 TeV scale. There are many different sub-theories among these main fields, and, especially for the SUSY and GUT theories, the Large Hadron Collider at CERN with its experiments Atlas and CMS will give data to exclude or confirm some of them [115].

Another problem of the Standard Model is its failure on cosmological scales. The visible matter and energy, described by the Standard Model, constitutes only a tiny fraction of the mass and energy in the universe ($\mathcal{O}$ 4%). The deficit is explained by so-called Dark Matter and Dark Energy and is not subject to the electromagnetic force, thus not observable with light on cosmic scales but only due to their gravitational effects. Dark Matter contributes of the order of $\mathcal{O}$ 26% to the mass of the universe, it can be briefly explained as a local effect, increasing the mass and thus the spin of a galaxy, while Dark Energy ($\mathcal{O}$ 70%) is a global affect in the sense that its density is assumed to be constant over the whole universe (cosmological constant), leading to a repulsive force accelerating the expansion of the universe, and is measured via the Hubble constant.

Force	Particle	rel. strength	mass (in GeV/c^2)	range (in m)	charge	spin
strong	8 gluons	1	< 0.02 (exp.) 0 (theory)	10^{-15}	zero e 3 colors: $c/\overline{c}$	1
weak	$W^{+/-}$ Z^0	$\mathcal{O} = 10^{-5}$	80.398 ± 0.023 91.1876 ± 0.0021	10^{-17}	$e^{+/-}$ zero e	1 1
electro-magnetic	γ	$\mathcal{O} = 7 \times 10^{-3}$	zero	infinite	zero e	1
gravitation	graviton	$\mathcal{O} = 6 \times 10^{-39}$	zero	infinite	zero e	2
none	Higgs -boson	unknown	129^{+74}_{-49}	infinite	zero e	0

Table 1.1: Boson summary table.

Even though the Standard Model cannot explain gravitation, Dark Matter or Dark Energy, it was and still is tested to a high precision describing the three fundamental forces very well in current energy limits of the experiments, and it gave excellent predictions for the W-boson mass (measured: $80.398 \pm 0.025\,\mathrm{GeV/c}$, SM prediction: $80.390 \pm 0.018\,\mathrm{GeV/c}$) or the Z boson mass (measured: $91.1876 \pm 0.0021\,\mathrm{GeV/c}$, SM prediction: $91.1874 \pm 0.0021\,\mathrm{GeV/c}$). It also predicted the existence of the top quark long before its discovery.

The carrier of the fundamental forces are bosons, summarized in Table 1.1. They are described by the Bose-Einstein statistics and have a full integer spin, thus each quantum state can be occupied by several bosons. Already observed are the gauge bosons gluon, γ and the W and Z-boson. Two more bosons are expected to exist, the graviton responsible for mediating gravitation and the Higgs-boson, generating the mass of particles. The Higgs boson, if existing, should be discovered in the experiments at LHC, if not, its existence will become highly unlikely. The Higgs boson is one possible candidate for Dark Matter.

	Name	mass (in GeV/c^2)	charge	spin
First Generation	up	2.4×10^{-3}	2/3 e	1/2
	down	4.8×10^{-3}	−1/3 e	1/2
Second Generation	charm	1.27	2/3 e	1/2
	strange	1.04×10^{-1}	−1/3 e	1/2
Third Generation	top	171.2	2/3 e	1/2
	bottom	4.2	−1/3 e	1/2

Table 1.2: Quarks, grouped in their families. Additionally to the electric charge quarks carry a color charge.

Quarks and leptons are elementary fermions. In total 12 quarks/antiquarks and 12 leptons/antileptons are known as fundamental, which are grouped into three particle families/generations with particles and their antiparticles (as proven by LEP experiments [96], see Figure 1.10). They are described with Fermi-Dirac statistics having half integer spin, and follow the Pauli exclusion principle. The quarks carry non-integer parts of the

electric charge. Since only full integers of the electric charge are observed in experiment, that means that they do not appear as "free particles", but exist in color singlets and bound states made of $q\bar{q}$ pairs (mesons, baryon number 0) or three quarks (baryons, baryon number 1,-1). Theoretical more exotic bound states are predicted, the so-called dibaryon, the pentaquark, glue-balls or hybrid states, but they have not been experimental observed yet. In Table 1.2 a summary of the quark characteristics is given.

	Name	mass (in MeV/c^2)	charge	spin
First Generation	e^-	0.511	-1 e	1/2
	ν_e	$< 2.2 \times 10^{-3}$	zero	1/2
Second Generation	μ^-	105.7	-1 e	1/2
	ν_μ	< 0.17	zero	1/2
Third Generation	τ^-	1777	-1 e	1/2
	ν_τ	< 15.5	zero	1/2

Table 1.3: Leptons, grouped in their families. The masses of the neutrinos are unknown, only upper limits exist today.

The known leptons are either only weakly interacting neutrinos or both electromagnetic and weakly interacting charged leptons. They are not under the influence of the strong force and are summarized in Table 1.3. It is possible that also sterile neutrinos exist, but the prove for their existence would be challenging, since by definition they do not interact with matter except through gravitation. Hence, also the sterile neutrino is a candidate for Dark Matter [116]. In the SM neutrinos are assumed to be massless. The generation of ν-masses beyond the SM will be discussed in section 1.3.5. For a nice phenomenological overview of particle physics, please refer too [117].

1.3   Neutrino Oscillations

1.3.1   A historical discovery
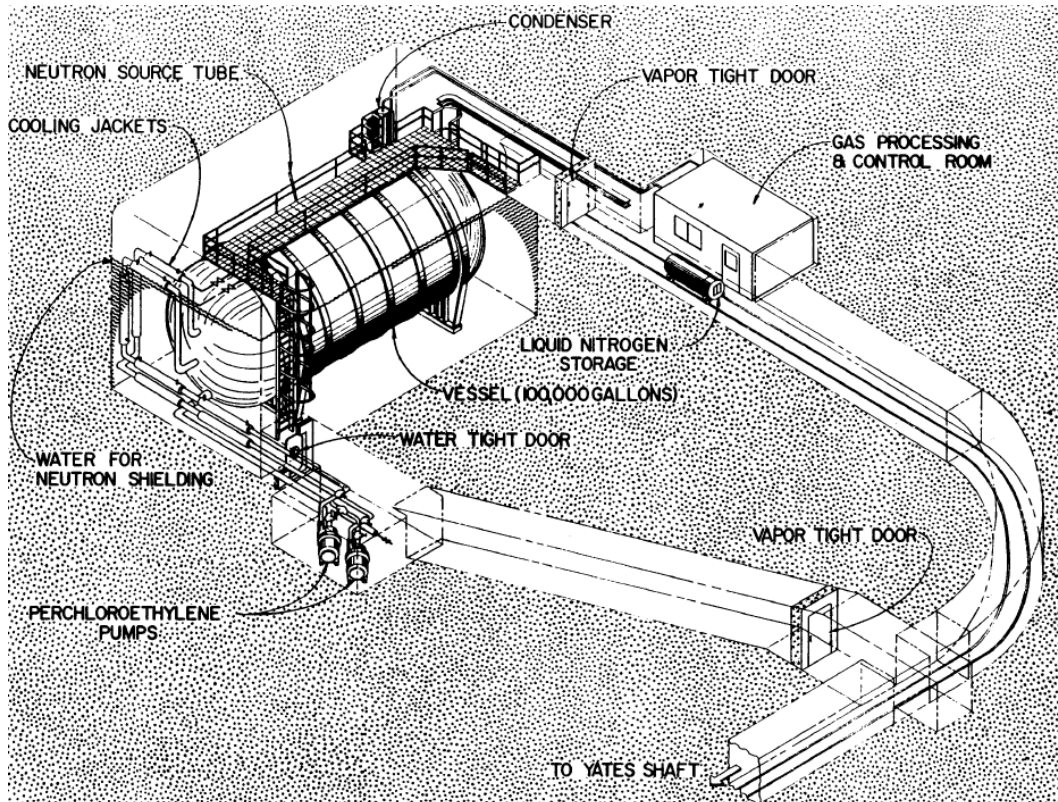
Figure 1.12: *Homestake mine detector, based on 615 t of Perchloroethylene, detects neutrinos via the inverse beta decay. Picture from [118].*

The Homestake mine detector was an experiment of Raymond Davis, jr. and John N. Bahcall (theoretical calculations) [53] and is shown in Figure 1.12. It was situated 1478 m underground and running continuously from 1970 till 1994. The detector had a mass of 615 t of Perchloroethylene, and an energy threshold of 0.814 MeV for the reaction:

$$\nu_e + {}^{37}Cl \rightarrow e^- + {}^{37}Ar \tag{1.19}$$

it was mainly sensitive to the solar neutrinos from the ^{8}B decay [45, 119]). The prove of interaction was done via the detection of the radioactive decay of the ${}^{37}Ar$, having a half-life of 35 days, thus the actual counting rate was about one ${}^{37}Ar$ decay per week. Every few months an equilibrium between the argon decay and the argon production was reached, and the argon was extracted from the tank and the decay was measured. Needless to say, that a tremendous effort on background estimation and suppression was needed. Nevertheless, the result of the experiment was a capture rate three times lower than predicted: calculated from the solar models were 1.5 ν interactions per day, when an average of $0.478 \pm 0.030\,(statistical) \pm 0.029\,(systematic)\,{}^{37}Ar/day$ was observed; the later so-called solar neutrino deficit. The measurement is shown in Figure 1.13 over the full running period of 25 years.
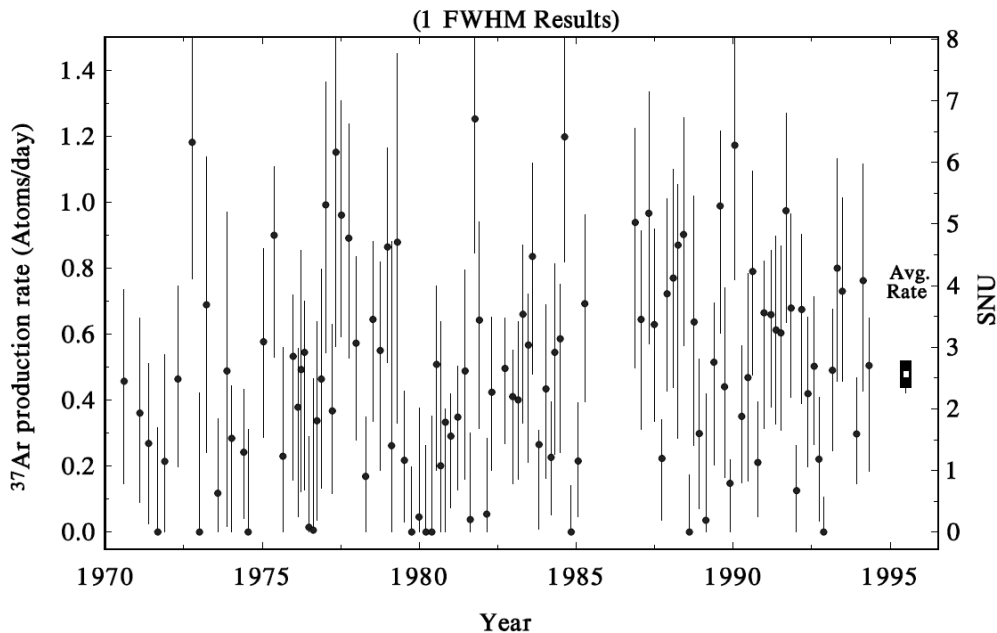
Figure 1.13: *Measured number of argon atoms produced in the Homestake mine experiment. The error bars are due to statistical uncertainties per argon extraction, the last bin gives the summed average rate with the full statistics, thus the error for this value is small. The measured rate was $0.478 \pm 0.030 \, (statistical) \pm 0.029 \, (systematic)$ produced $^{37}Ar/day$ while $1.5 \, ^{37}Ar/day$ are expected from solar fusion models. Picture from [118].*

As the experiment was only sensitive the ν_e, one plausible explanation for this deficit was that the neutrinos had oscillated on their way to the earth form one neutrino type to another, so that they could not be measured with Davis's experiment. Neutrino oscillation requests non-zero mass differences between the neutrinos, so that at least one of them had to have a mass. The theoretical foundation to describe neutrino oscillations dates from the early sixties and seventies, as described in section 1.3.2, so this result was no big obstacle to the physicists. Nevertheless, the neutrinos are supposed to be massless in the Standard Model of particle physics, hence, the neutrino oscillation is the first hint for physics beyond it. Still, at the time of the measurement the evidence for neutrino oscillation or even disappearance was not taken as proven, since the uncertainties on the calculated ^{8}B neutrino flux were high at the energy range Davis's experiment was sensitive. However theoretical physicists like Bruno Pontecorvo already expected neutrino oscillations to happen.

1.3.2 Theoretical description of ν-oscillations, the PMNS-matrix

Different neutrinos masses m_i (i=1,2,3) lead to mass eigenstates ν_i which can be a mixture of the flavor or interaction eigenstates $\nu_{e,\mu,\tau}$. Like for the CKM mixing-matrix, the flavor eigenstates can be expressed in terms of the mass eigenstates with an unitary mixing matrix U, the PMNS-matrix, named after Bruno Pontecorvo, Ziro Maki, Masami Nakagawa

and Shoichi Sakata [120, 121, 122, 123][1].

$$
\begin{pmatrix} \nu_e \\ \nu_\mu \\ \nu_\tau \end{pmatrix} = \begin{pmatrix} 1 & 0 & 0 \\ 0 & c_{23} & s_{23} \\ 0 & -s_{23} & c_{23} \end{pmatrix} \begin{pmatrix} c_{13} & 0 & s_{13}e^{i\delta} \\ 0 & 1 & 0 \\ -s_{13}e^{i\delta} & 0 & c_{13} \end{pmatrix} \begin{pmatrix} c_{12} & s_{12} & 0 \\ -s_{12} & c_{12} & 0 \\ 0 & 0 & 1 \end{pmatrix} \begin{pmatrix} \nu_1 \\ \nu_2 \\ \nu_3 \end{pmatrix}
$$
(1.20)

This matrix, where $c_{ij} \equiv \cos(\theta_{ij})$ and $s_{ij} \equiv \sin(\theta_{ij})$, contains 3 mixing angles θ_{ij} ($0 \leq \theta_{ij} \leq \pi/2$), the possibility of CP violation is expressed with the phase δ ($0 \leq \delta \leq 2\pi$); for CP conservation δ equals zero. The oscillation amplitudes depend on the mixing angles and the oscillation lengths (for a given neutrino energy) on the differences of the squared masses $\Delta m_{ij}^2 = m_i^2 - m_j^2$, details of the mathematical formalism are explained in literature [1]. There are only two independent Δm_{ij}^2, the difference of the squared masses $\Delta m_{21}^2 = m_2^2 - m_1^2$ and $\Delta m_{32}^2 = m_3^2 - m_2^2$ (the third mass difference $\Delta m_{31}^2 = m_3^2 - m_1^2$ is equal to $\Delta m_{32}^2 + \Delta m_{21}^2$).

Solar and atmospheric neutrino measurements suggest a strong mass hierarchy, i.e., $\Delta m_{21}^2 = \Delta m_{solar}^2 \ll \Delta m_{31}^2 \approx \Delta m_{32}^2 = \Delta m_{atmosphere}^2$, and the CHOOZ reactor experiment limited θ_{13} to small values.

In this case the observed neutrino oscillations can be described by the simpler two-neutrino-mixing. E.g., the solar neutrino $\nu_e \rightarrow \nu_\mu$ oscillation can approximately be written as (assuming Dirac neutrinos and $\delta = 0$, see section 1.3.5):

$$
P(\nu_e \rightarrow \nu_X) = \sin^2(2\theta_{solar}) \cdot \sin^2 \left(\frac{\Delta m_{solar}^2 L}{4 E_\nu} \right)
$$
(1.21)

where L is the flight path and θ_{solar} is the mixing angle θ_{12}.

In 1985 Mikheyev and Smirnov enhanced the Wolfenstein theory on neutrino oscillation with a resonance effect which can occur when neutrinos travel through matter, the MSW effect [124, 125]: even if in vacuum the mixing angle is small, it can become large for certain ν-energies and electron densities. Hence, the solar neutrino deficit may be affected by the oscillation of neutrinos on their path through the sun.

1.3.3 Recent ν-oscillation experiments

The MSW neutrino oscillation effect, as we know today, was first observed in the solar neutrino sector too, when the KamiokaNDE II experiment observed a deficit of 50% for solar neutrinos with an energy of more than 7.5 MeV [126] (see section 1.3.2). The KamiokaNDE II detector, a tank filled with 3000 t of pure water, recorded events via the Cerenkov light pattern of electrons from charged current neutrino interactions in the 1000 photomultiplier array. The Cerenkov light emitted by electrons has a fuzzy ring signature due to its showering, while a crossing μ from atmospheric neutrinos will create sharp rings in the PMT's.

The KamiokaNDE experiment was originally, in its first phase, intended to act as a detector for proton decays (NDE: nucleon decay experiment) and gave a good limit on the

---

[1]According to Makato Kobayashi, one of the theorists developing the CKM matrix, their solution was inspired by the MNSP theory.

lifetime of the proton. The result of Davis Homestake Mine experiment gave constantly a reduced flux of electron neutrinos since the 70's, and was discussed controversially since it relied on very complicated radiochemical methods and was not a direct observation, thus it was decided to use a water Cerenkov detector to overcome the problems of the Davis experiment, using a complementary approach and getting better results as:

- A big water volume can overcome the small cross section of neutrinos from the sun with energies between 5-15 MeV.

- The event-by-event analysis is giving the possibility to study in realtime the number of events.

- The interactions of neutrinos are mainly due to quasi-elastic scattering, thus the created electrons will mainly be directed away from the sun.

- Due to the quasi-elastic scattering, the energy of the incoming neutrinos can be studied.

- The ring shaped signature of the Cerenkov light allows a background discrimination.
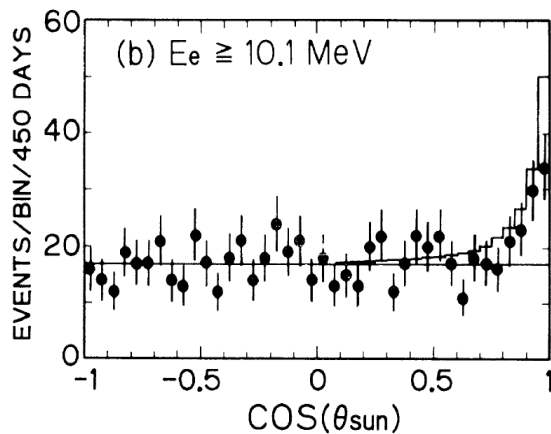
Figure 1.14: *Distribution in* $\cos\theta_{sun}$, *the cosine of the angle between the trajectory of an electron and the direction of the sun at a given time. The data are in the 680 t fiducial region with* $E_e \geq 10.1\,MeV$. *Events identified as spallation products or remaining* γ *rays have been excluded. Picture from [127].*
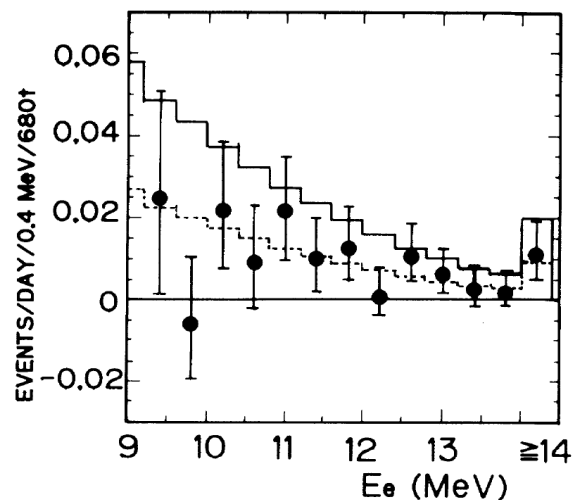
Figure 1.15: *Energy distribution of the solar neutrino signal. The solid histogram is the distribution predicted by the SSM. The highest bin corresponds to* $E_e \geq 14\,MeV$. *The dotted line shows the best fit to data (0.46 SSM). Picture from [127].*

Additional technical challenges had to be tackled before the refurbished experiment, now called KamiokaNDE II started to take physics data from 1987. It confirmed the measurement of the Davis experiment with a counting rate of $\frac{Kam-II\,data}{SSM} = 0.46\pm0.13\,(stat.)\pm 0.08\,(syst.)$ for neutrino energies greater 9.3 MeV, the result is shown in Figures 1.14 and 1.15 [127] (SSM = s̲tandard s̲olar m̲odel). Additionally, it was rewarded with the title "smoking gun signature" of solar neutrinos, directly proving the fusion reactions in the sun. The data taking went on for several years, reducing the statistical errors in the solar neutrino measurement [128]. Additionally, KamiokaNDE was able to detect the neutrino

burst of the super nova 1987A with 11 neutrino events [129, 130], and it reduced the limit on the proton lifetime too [131]. KamiokaNDE II was also the first experiment to observe the atmospheric neutrino deficit (see next paragraph), even though its mass was too small to establish this discovery [132].

Apart from the already mentioned solar neutrino experiments, there were other experiments using neutrinos coming from nuclear power plants, which gave in 1984 limits on the allowed parameter space of neutrino oscillation (Gösgen[133] and Bugey [134]). The further upgrade version of the KamiokaNDE experiment, Super-KamiokaNDE (SK), reported in 1998 a deficit of the atmospheric ν_μ when they compared the number of the neutrinos going up through the whole earth with the number of neutrinos coming straight from the earth's atmosphere [126]. Their final analysis brought the convincing proof of the atmospheric oscillation effect [135]: a variation of ν_μ disappearance with varying zenith angle (varying path length L) and neutrino energy E confirmed the typical L/E dependence of neutrino oscillations. This result was also later confirmed by the K2K experiment [136, 137]. On a statistical approach the SK experiment also reported τ-appearance as a $1.7\,\sigma$ effect on the current data sample, an appearance which is hoped to be directly observed by the OPERA experiment [138] with a significance of $3\,\sigma$.
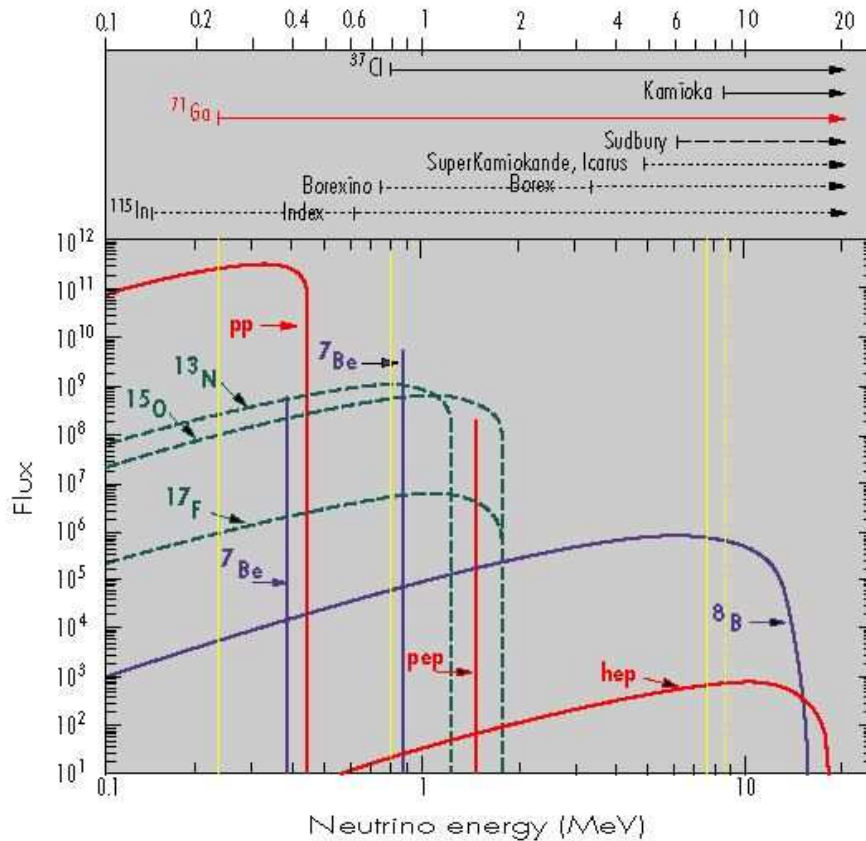
Figure 1.16: *Predicted solar neutrino flux depending on the neutrino energy, the energy domains to which different experiments are sensitive are shown above the plot. Picture from [2].*

As shown in Figure 1.16 the solar neutrino flux at energies, where the inverse β-decay of ^{37}Cl is sensitive, is 300 times less than the flux which is accessible with ^{71}Ga experiments. Thus, new experiments based on Gallium were set up to confirm the solar neutrino

deficit with a higher statistics also in the low energy sector, as the theoretical uncertainties of the ^8B flux were quite high, while the proton-proton fusion had less uncertainty. The neutrino capture rate from that time was calculated as solar neutrino unit (SNU) (for details on the SNU unit, see [1]. The experiments were called GALLEX (gallium solar neutrino experiments at the Laboratori Nazionali del Gran Sasso) [139] and $\overline{\text{SAGE}}$ (Baksan neutrino observatory Soviet-American gallium neutrino experiment) [140]. Their result over a run-period of 12 years gave a capture rate of $70.8\,^{+5.3}_{-5.2}\,(stat.)\,^{+3.7}_{-3.2}\,(syst.)$ SNU for neutrino energies above 233 keV, which corresponds to roughly half of the expected rate from standard solar models with 130 SNU [141].
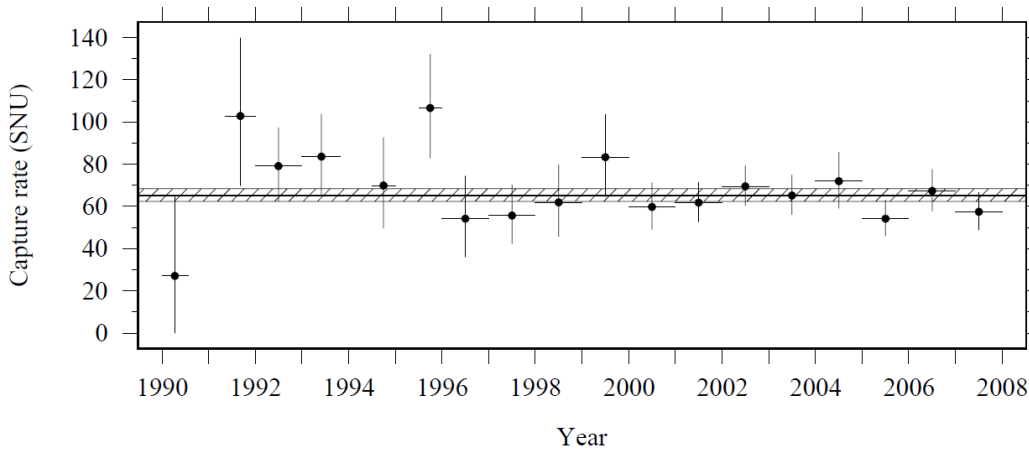
Figure 1.17: *Combined SAGE results for each year. Shaded band is the combined best fit and its uncertainty for all years. Vertical error bars are statistical with 68% confidence. Picture from [142].*

The combined analysis of the GALLEX, its successor GNO and the SAGE experiment confirmed a discrepancy between the theoretical predicted and the observed solar neutrino flux, wherein the final value of the observed neutrino flux was $66.1 \pm 3.1\,SNU$, as shown in Figure 1.17 and Figure 1.18 [142, 143].

This was a good confirmation of oscillations in the solar neutrino sector. Nevertheless, other experiments started to measure the parameters of the solar oscillation defined by equation 1.21 to a higher precision, especially remarkable was the Sudbury Neutrino Observatory (SNO) [145]. The SNO detector consisted of a 1000 t tank of heavy water (D_2O) monitored withy 9600 photomultipliers mounted with a radius of 8.5 m. It was immersed in a normal water tank, situated underground in an old mine in Canada to be shielded from cosmic ray background and was running from 1999 until 2006.

The observatory was able to detect all neutrino flavors with different neutrino interactions:

- CC interactions, wherein the neutron of the deuteron changes into a proton according to $\nu_e + n \rightarrow p + e^-$. As the energy of solar neutrinos is smaller than the threshhold for τ and μ production, only ν_e take part in CC reactions, producing electrons with an energy of about 5-15 MeV. Even though the electrons can go in every direction, statistically they point away from the sun, from where the neutrinos came from.
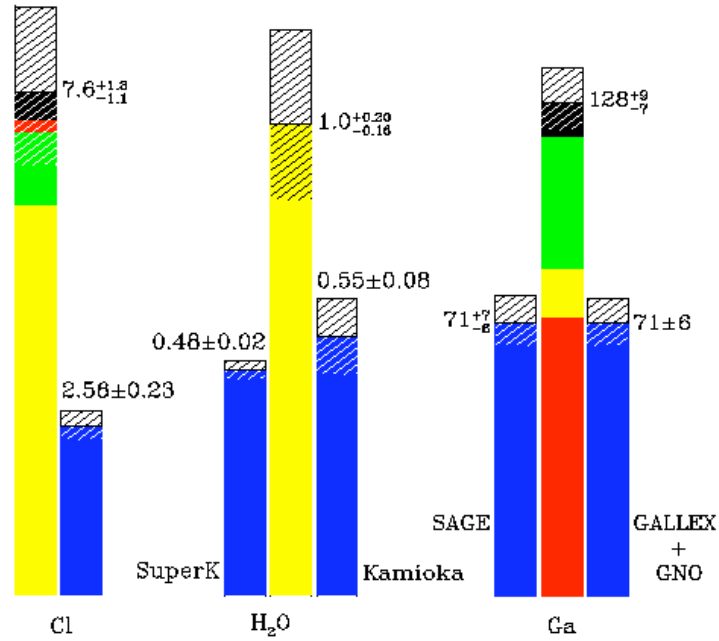
Figure 1.18: *Comparison of the total neutrino flux expected from SSM (the highest bar) and the results of various experiments. Picture from [144]*
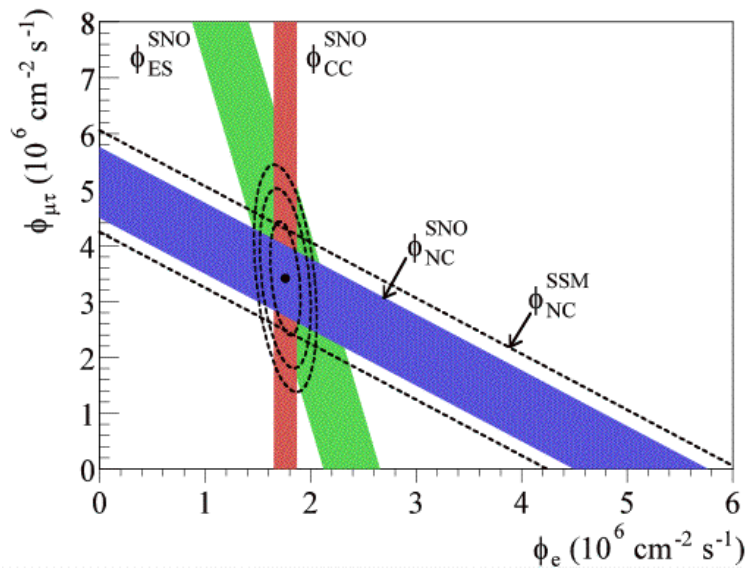
Figure 1.19: *Flux of ^8B solar neutrinos which are μ or τ flavor vs flux of electron neutrinos deduced from the three neutrino reactions in SNO. The diagonal bands show the total ^8B flux as predicted by the SSM (dashed line) and that measured with the NC reaction in SNO (solid band). The intercepts of these bands with the axes represents the $\pm 1\sigma$ errors. The bands intersect at the fit values for Φ_e and $\Phi_{\mu\tau}$, indicating that the combined flux results are consistent with neutrino flavor transformation assuming no distortion in the ^8B neutrino energy spectra. Picture from [146].*

- NC interactions, wherein the neutrino breaks the deuteron into its neutron and proton. All three neutrino flavor can partake in this interaction with equal cross section, and it is observed by neutron capturing of the deuteron, when a γ ray of 6 MeV is emitted.

- Electron scattering (ES), wherein all ν flavors can scatter on the atomic electron by Z-boson, the ν_e additionally by a W-boson exchange, generating an electron, thus dominating this channel. Due to the kinematics, the electron is pointing away from the sun.

Thus, it was the first experiment measuring the total neutrino flux from the sun with the NC reactions: the total flux was consistent with the SSM calculations, and it confirmed the deficit in the electron sector, as shown in Figure 1.19. The SNO experiment had a good sensitivity on the mixing angle θ_{solar}, while the resolution on the mass difference was quite poor. For that reason a complementary reactor experiment was set up, to give good results on the squared mass difference, KamLAND (Kamioka Liquid Scintillator Antineutrino Detector), situated in the old KamiokaNDE cavern, but using liquid scintillator instead of pure water. It was surrounded by 53 Japanese nuclear power reactors with an average baseline of 180 km.
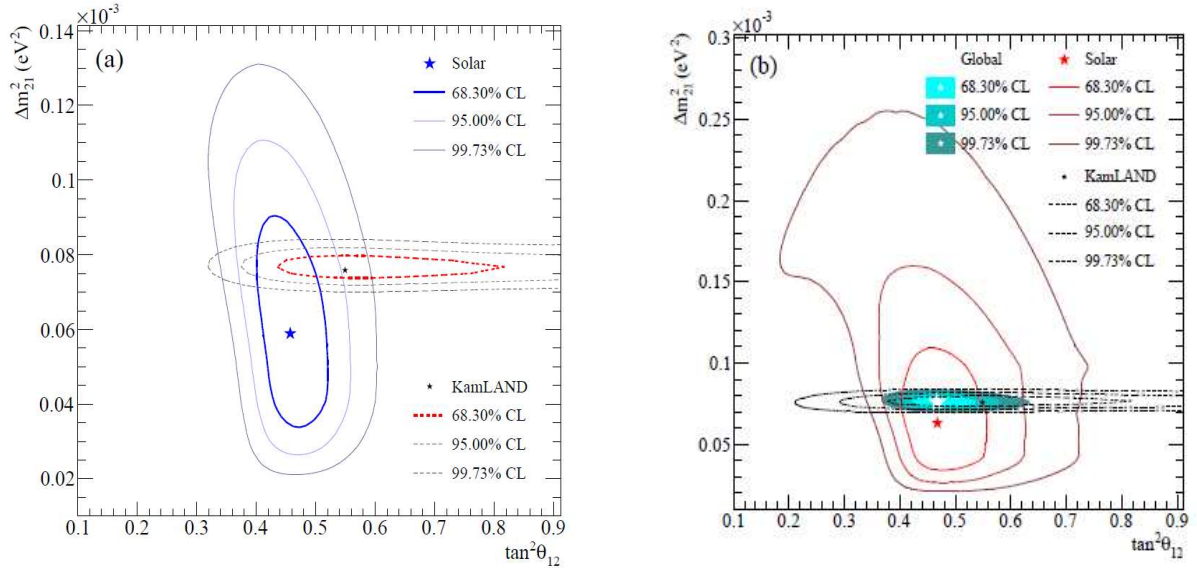
Figure 1.20: *Solar and KamLAND oscillation parameter analysis for a a) two-flavor oscillation hypothesis and b) a three-flavor hypothesis. The solar data includes SNOs LETA survival probability day/night curves, SNO Phase III integral rates, Cl, SAGE, Gallex/GNO, Borexino, SK-I zenith and SK-II day/night spectra. The χ^2 is minimized with respect to all undisplayed parameters, including $\sin^2 \theta_{13}$ and Φ_{8B}. Pictures from [147].*

The combined results of both experiments on the mixing angles, taking into account other experimental data too, is shown in Figure 1.20, wherein the SNO results are coming from [148, 149, 147] and the KamLAND results is refereed to in [150, 151, 152, 153]. KamLAND also published a first analysis on so-called geological neutrinos created in the earth crust and mantle by Thorium and Uranium decays [154].

Summary of the present status [155]

Summarizing the results from the experiments, parameters of the MNSP- and the 2 neutrino mixing scheme can be determined as follows:

2-neutrino mixing parameters:

-Solar neutrinos

For the two neutrino mixing scheme of solar neutrinos the best fit the SAGE, GALLEX, SNO, KamLAND and the SUPERKAMIOKANDE experiment is:

$$\tan^2 \theta_{12} = 0.47^{+0.08}_{-0.05}$$
$$\Delta m^2_{21} = 7.59^{+0.20}_{-0.21} \times 10^{-5} \, eV^2$$

-Atmospheric neutrinos

For the two neutrino mixing scheme of atmospheric neutrinos the best fit to the MINOS [156, 157, 158], SUPERKAMIOKANDE [135, 137], Soudan-2 [159] and MARCO [160] experiments is (see Figure 1.21):

$$\sin^2(2\theta_{23}) > 0.90 (90\% \, C.L.)$$
$$\Delta m^2_{32} = (2.43 \pm 0.13) \times 10^{-3} eV^2$$

3-neutrino mixing parameters:

For the 3-neutrino mixing parameters all data from the mentioned experiments as well as the results from Palo Verde [161] the best fit is, according to [155] and Figure A.1, summarized as:

$$\sin^2 \theta_{12} = 0.318^{+0.019}_{-0.016}$$
$$\sin^2 \theta_{23} = 0.50^{0.07}_{-0.06}$$

$$\Delta m^2_{21} = 7.59^{+0.23}_{-0.18} \times 10^{-5} \, eV^2$$
$$\Delta m^2_{31} = 2.40^{+0.12}_{-0.11} \times 10^{-3} \, eV^2$$

For the value of θ_{13} and its (3σ) value only an upper limit, mainly given by the CHOOZ experiment exists:

$$\theta_{13} \leq \begin{cases} 0.053 & (0.078) & (solar + KamLAND) \\ 0.032 & (0.058) & (CHOOZ + atmospheric + K2K + MINOS) \\ 0.034 & (0.052) & (global data) \end{cases}$$

The latest global data analysis gives a weak hint for a value different to zero, as shown in Figure 1.22.

In 1996 the Los Alamos LSND experiment observed 22 $\bar{\nu}_e$-events when only four were expected from π^+ and μ^+ decays [162]. The only reasonable explanation was an oscillation of $\bar{\nu}_\mu \to \bar{\nu}_e$, but the parameters gave a controversial result that does not fit in the picture, thus, the experiment was repeated at Fermilab, and the result of the MiniBooNE experiment disproves this experimental data [163]. In 1998, the two experiments NOMAD [164] and CHORUS [165] were searching for ν_τ neutrinos in the short baseline ν_μ beam of the CERN SPS accelerator with the result of no neutrino oscillation for $sin^2(2\theta_m) > 4.2 \cdot 10^{-3}$
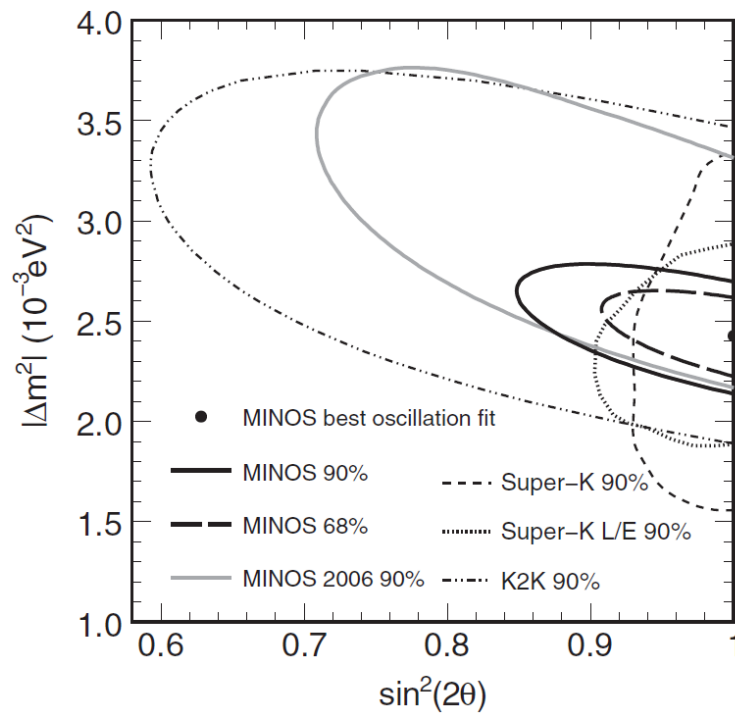
Figure 1.21: *Contours for the oscillation fit to the MINOS data, including systematic errors. Also shown are contours from previous experiments K2K and SK [135, 137] and an earlier MINOS result [156, 157]. Picture from [158].*
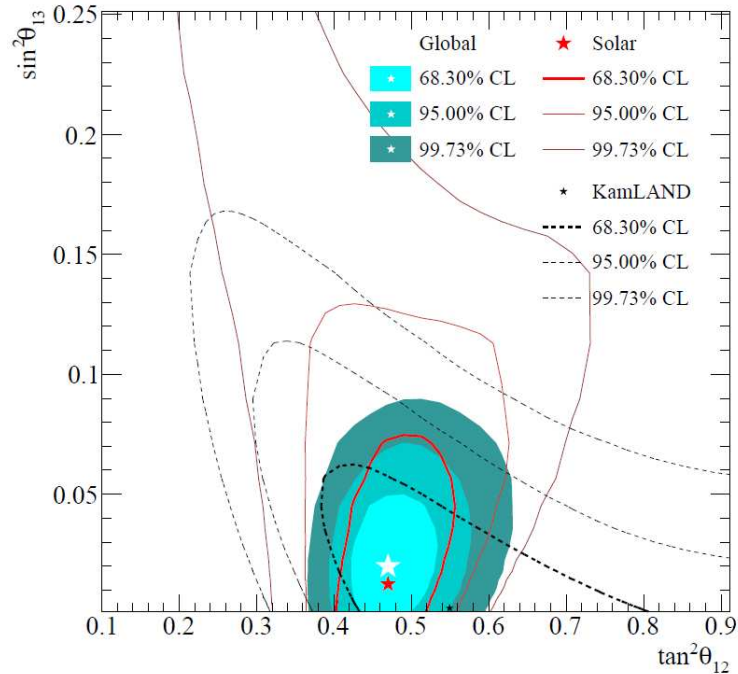
Figure 1.22: *Solar oscillation parameter analysis projected in the mixing angle space. The χ^2 is minimized with respect to all undisplayed parameters, including Δm_{21}^2 and Φ_{8_B}. Picture from [147].*

or $\Delta m^2 > 1$ eV^2. Many other experiments were looking for neutrino oscillation effects and parameters, for example the double-β decay experiments like the Heidelberg-Moscow [166], or in reactor experiments for limits on θ_{13} like the CHOOZ experiment [167] or the mass difference Δm_{23}^2 like the long-baseline MINOS experiment [156, 158], but are not mentioned in detail, as they mainly improved only already known values, see Figure 1.21. The full parameter space of neutrino oscillation and the limits given by the various experiments is summarized in Figure A.1 of the appendix.

Resulting from measurements of the tritium beta decay in Mainz the today upper mass limit for ν_e is m$_{\nu_e}$ ≤ 2.3 eV [168].

1.3.4 Current and near future experiments
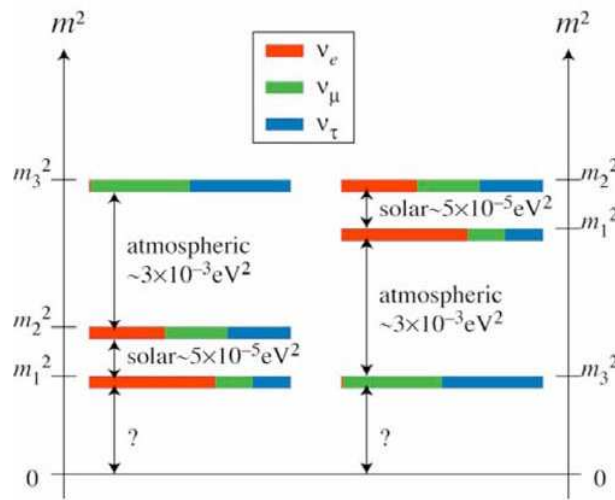
Figure 1.23: *Mass splitting in the neutrino sector. Left: normal hierarchy. Right: inverted hierarchy. Picture from [169]*

Even though neutrino oscillation is accepted as an explanation of the experiments, still many puzzling questions remain:

- Since Neutrinos have mass, can this mass be determined by flight-time measurements in long baseline experiments from $\beta = p/E$?

- As Super-KamiokaNDE observed a disappearance signal explained by $\nu_\mu \rightarrow \nu_\tau$-oscillations, can the τ-appearance be observed?

- What is the absolute mass of a neutrino?

- What are the values of the non-measured mixing angles, especially θ_{13} and is $\theta_{23} = 45°$ exactly (max. mixing)?

- Does CP violation occur in the leptonic sector?

- What is the mass hierarchy (see Figure 1.23)?

- How do neutrinos gain their mass?

- Does the neutrinoless double-β-decay exist, i.e. is the neutrino a Dirac or Majorana particle?

- Do right-handed neutrinos exist?

- Does a sterile neutrino exist?

The first question was partly answered by long baseline neutrino experiments, mainly MINOS published a result of $(v - c)/c = (5.1 \pm 2.9) \times 10^{-5}$ (at 68% C.L.) [170], the OPERA experiments aims to improve this measurement soon, as well as giving an answer to the second question. The sixth question raised will hopefully be answered by the KATRIN experiment, a tritium decay experiment [43]. The θ_{13} question on the mixing angle is currently investigated by numerous experiments; T2K, NoνA, Daya Bay, Double-CHOOZ and RENO are the experiments set up to measure this value, or to lower the limit. A good overview of these experiments can be found in [155]. A big number of theoretical models have been developed lately to give predictions for the value of θ_{13}, partly starting from the existing data and extrapolating to possible scenarios, or just by pure theoretical calculations [171, 172, 173, 174], most of these slightly *speculative* models will be excluded in the next generation of experiments.
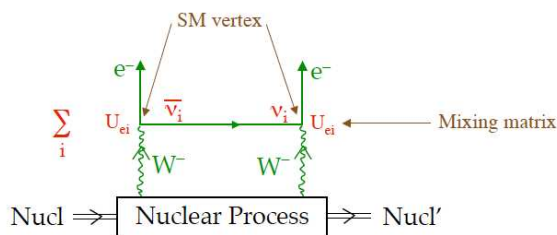
Figure 1.24: *Feynman graph of the double β decay. Picture from [169].*
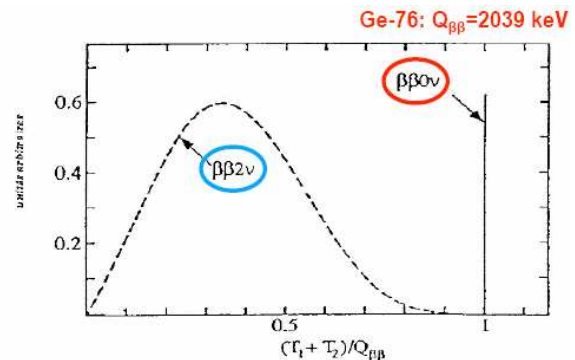
Figure 1.25: *Energy spectra of the neutrinoless double β decay. Picture from [169].*

If the angle θ_{13} will be measured by any of the above mentioned experiments, the future experimental approach in neutrino physic will be new super-beams or the so-called β-beam to detect CP violation. A β-beam is a very high intensity neutrino beam from decays of accelerated radioactive ions. In case of a really small value of θ_{13}, the future is more likely to go in the direction of a neutrino factory [175], with very large detectors, preferable magnetized (see also the second part of this thesis) [176, 177, 178, 179, 180, 181, 182, 183, 184, 185]. Also the mass hierarchy can be determined with either of the two future possibilities [186, 187].

The last questions are all related, and they depend on wether the neutrino is a Dirac or a Majorana particle. Several experiments are set up to measure the neutrinoless double-β decay, namely COBRA, CUORICINO, CUORE, EXO, GERDA, MAJORANA, NEMO-3 and SNO+. Sterile neutrinos would not undergo any weak interactions, thus only interact with gravitation and are possible WIMP (Dark Matter) candidates.

1.3.5   Mass generation for neutrinos

As already mentioned the Standard Model describes neutrinos to be massless. The experimental observed phenomenon of neutrino oscillations requires them to have a mass, and even though this mass seems to be small, the origin is still not fully understood. Extension of the Standard Model includes neutrino mass terms. There a two theoretical explanations for mass generation in the neutrino sector, the Dirac-mass or the Majorana mass term. The equations presented here are taken from [117].

Dirac mass term

If one adds a right-handed neutrino field into the Standard Model Lagrangian, one gets a mass term $L^D = -(\nu_R M^D \nu_L + \nu_L M^D \nu_R)$ where ν_R is a triplet of the right-handed neutrinos weak eigenstates (ν_L of the left-handed respectively) while M^D is a 3×3 matrix. According to the Seesaw mechanism [188, 189, 190] one assumes the ν_R to be heavy to explain the light ν_L. The physical fields which can be observed as free particles are eigenvectors of this matrix M, so one needs to diagonalize M according to $M^D = V m U^\dagger$ where V and U are unitary matrices and m is diagonal. Thus the resulting term is $L^D = -(\overline{\nu}'_R m \nu'_L + \overline{\nu}'_L m \nu'_R) = \sum m_k \overline{\nu}_k \nu_k$ with $\nu_k = \nu_{kL} + \nu_{kR}$, $\nu'_L = U^\dagger \nu_L$ and $\nu_R = V^\dagger \nu_R$. The consequence of this is that only the total lepton number is conserved, as observable neutrino mass states are mixtures of the neutrino flavor eigenstates, additionally processes like $\mu^+ \to e^+ \gamma$ are allowed and oscillations like $\nu_l \to \nu_{l'}$ should be observed, while the neutrinoless double-β decay, as shown in Figure 1.24, would be forbidden due to total lepton number conservation.

Majorana mass term

As neutrinos do not carry any electric charge, they could be a Majorana particle, thus the neutrino would be its own antiparticle. With this ansatz the Standard Model Lagrangian becomes $L^M = -\frac{1}{2}(\overline{\nu}^c_L) M \nu_L + h.c.$, where the ν_L is a triplet of the left-handed neutrinos weak eigenstates, and M is a symmetric 3×3 matrix (assuming three neutrino families). With $m = U^\dagger M U$ one gets $L^M = -\frac{1}{2} \sum m_k \overline{\chi}_k \chi_k$ wherein $\chi = U^\dagger \nu_L + (U^\dagger \nu_L)^c$, thus $\chi^c_k = \chi_k$ is a Majorana field. This means that $\nu_{lL} = \sum U_{lk} \chi_{kl}$ with $l = (e, \mu, \tau)$, i.e. the left-handed current fields are superpositions of the left-handed neutrino field components with the Majorana mass m_k, $k = (1, 2, 3)$. The introduction of Majorana masses causes violation of the lepton number, so not only the reaction $\mu^+ \to e^+ \gamma$, but also the neutrinoless double-β decay would be allowed.

1.4 Neutrino Induced Charm Production

Neutrino induced charm production is studied since several years. In the first experiments like CDHS, CCFR, CHARM1 and CHARM2 or NOMAD [191] the limit on statistics was mainly due to the fact that only the leptonic(di-muon) charm decay could be observed, with a high cut on the energy on both muons to avoid a contamination from pion and kaon secondary particles, making it difficult to exploit the energy region below 20 GeV.

The use of emulsion experiments with E531 and CHORUS [192, 193, 194, 195, 196] allowed the detection of charmed particles by their decay topology and flight length. Thus, it was possible to study also other decay channels, without presuming knowledge on the branching fractions and having a low background. The OPERA experiment observes neutrino interactions with emulsion films, interleaved with lead plates to get a total active target mass of 1.25 kt. The neutrino interactions with the target nuclei are divided into:

- Charged current interactions, wherein a flavor change occurs when a neutron of the target nucleus changes into a proton, according to $\nu_{flavor} + n \rightarrow p + l^-_{flavor}$. Even though the generated leptons can go in every direction, statistically they point away from the source, from where the incident neutrino came from.

- Neutral current interactions, wherein the neutrino interacts with the nucleons (protons and neutrons) by exchange of a Z-boson.

1.4.1 Neutrino Nucleus Scattering

Since for neutrino induced charm production the CC interactions dominate, we restrict the discussion to CC interactions. There are essentially three different processes contributing to νN-scattering, the theoretical description is taken from [197, 117, 198, 191].

- Quasi-elastic scattering: $\nu n \rightarrow \mu^- p$, where the muon is pointing away from the source.

- Resonant Scattering: $\nu N \rightarrow \mu^- \Delta$ with subsequent Δ-decay.

- Deep inelastic scattering interactions, wherein all ν scatters on one of the nucleons quarks by exchange of the W-boson (or Z-boson), as shown in Figure 1.26 for the W-boson exchange.

Deep Inelastic Scattering

Deep inelastic scattering is and was used widely as a tool to probe pertubative QCD and to obtain parton distribution functions (mainly done by the HERA accelerator, Hamburger Elektronen Ring Anlage) and its experiments ZEUS and H1. The scattering can be expressed by

$$\nu_\mu N \rightarrow \mu^- X \tag{1.22}$$

where N is the nucleon (bound in a nucleus) and X the final hadronic state(s). This CC interaction is mediated by W-boson exchange, the Lagrangian is $\mathcal{L} = -\frac{G_F}{2\sqrt{2}}(J_\mu W^\mu + J_\mu^\dagger W^{\dagger\mu}$ with J_μ as the lepton-nucleon (quark) interaction current probability density of the electroweak interaction components.
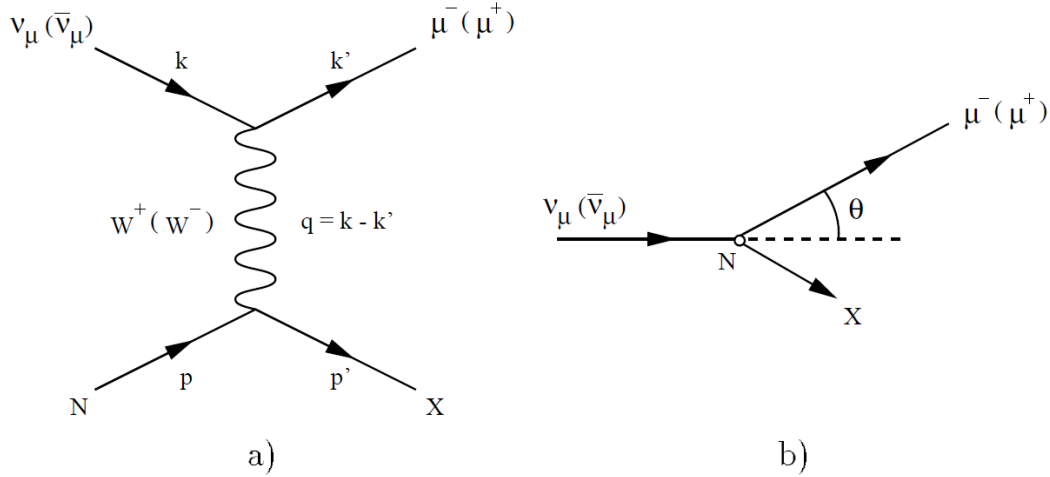
Figure 1.26: *Feynman diagram a) and laboratory frame b) of the inclusive deep inelastic CC ν_μ-nucleon interaction. Picture from [197]*

The interaction is described with the quark-parton model developed by Feynman, which was already mentioned before in Chapter 1.1.3 (in this model one assumes the nucleon to be a collection of point like partons, the three valence quarks and numerous sea quark and anti-quark pairs, in which the heavier s and c quarks are rare compared to the valence quark). The kinematical variables describing the interaction are:

- The four momentum transfer Q, given as $Q^2 = -q^2 = -(k - k')^2$

- The energy transfer in the laboratory frame is written as $\nu = \frac{p*q}{\sqrt{p*q}} = E_{\nu_l} - E_l$

- The invariant mass of the final hadronic state is $W^2 = p'^2 = M^2 - Q^2 + 2M\nu$

- The Bjorken variable $x = \frac{Q^2}{2p*q} = \frac{Q^2}{2M\nu}$

- The inelasticity $y = \frac{p*q}{p*k} = \frac{E_{hadron}}{E_\nu} - \frac{M}{E_\nu}$, where M is the nucleon mass and E_{hadron} is the energy of the hadronic final state

The Bjorken variable x is the target nucleons longitudinal momentum, carried by the interacting quark. For elastic scattering x would be equal to one, while for inelastic scattering $W^2 \geq M^2$, so $0 \geq x \geq 1$. Deep inelastic scattering usually means $\sqrt{Q^2}, \nu \gg M \sim 1\,GeV$, x fixed.

The cross section is given by:

$$\frac{d^2\sigma(\nu_\mu N \rightarrow \mu^- X)}{dx\,dy} = \frac{G_F^2 M E_\nu}{\pi} \left[xy^2 F_1 + \left(1 - y - \frac{Mxy}{2E}\right) F_2 + xy\left(1 - \frac{1}{2}y\right) F_3 \right] \quad (1.23)$$

wherein F_1, F_2 and F_3 are the quark distribution functions. If one assumes that the isospin invariance is exact and sea quarks are created in quark-antiquark pairs, according to [198] the nucleons can be described by a cloud of half integer spin point-like particles (u, d, c and s at the $E_{\nu_{OPERA}}$ for deep inelastic scattering). For a so-called iso-scalar nucleon $F_i(x) = \frac{1}{2}(F_i^p + F_i^n)$, $i = (1, 2, 3)$ the structure functions can be written as:

$$F_1 = \frac{1}{2}(u + \bar{u} + d + \bar{d} + s + \bar{s} + c + \bar{c}) \tag{1.24}$$

$$F_2 = 2xF_1(x) \tag{1.25}$$

$$F_3 = [u - \bar{u} + d - \bar{d} + c - \bar{c} + s - \bar{s} + 2(s - c)] \tag{1.26}$$

where (q = u,d,c,s) are the quark content of the nucleon. When a charm quark is produced in deep-inelastic CC scattering, the neutrino interacts with a "valence" d-quark or a "sea" s-quark and produces a c quark according to:

$$\nu_\mu N \rightarrow \mu^- c X \tag{1.27}$$

In Figure 1.27 the Feynman diagram is shown for both the CC and NC scattering processes. For NC interactions only the gluon initiated process can create c-quarks, when the gluon splits into a $c\bar{c}$ pair, which is unlikely. For the OPERA experiment only the CC induced charm production is relevant.

Thus, the parton cross sections relevant for charm hadron production are:

$$\nu_\mu d \rightarrow \mu^- c \qquad \frac{d\sigma^{\nu_\mu d \rightarrow \mu^- c}}{dy} = \frac{G_F^2 \hat{s}}{\pi}\left(1 - \frac{m_c^2}{\hat{s}}\right)|V_{cd}|^2 \tag{1.28}$$

$$\nu_\mu s \rightarrow \mu^- c \qquad \frac{d\sigma^{\nu_\mu s \rightarrow \mu^- c}}{dy} = \frac{G_F^2 \hat{s}}{\pi}\left(1 - \frac{m_c^2}{\hat{s}}\right)|V_{cs}|^2 \tag{1.29}$$

Thus, charm production is inflicted by the CKM matrix elements $|V_{cd}|$ and $|V_{cs}|$. The transition $d \rightarrow c$, thus production of charm quarks via νd scattering, is Cabibbo suppressed as $|V_{cd}| \sim \sin^2\theta_C \simeq 0.04$. The scattering process νs is not Cabibbo suppressed, as $|V_{cs}| \sim \cos^2\theta_C \simeq 0.96$, but it is suppressed due to the low number of s sea quarks.

Additionally, the phase space is suppressed by $1 - m_c^2/\hat{s}$ with

$$\frac{m_c^2}{\hat{s}} = \frac{m_c^2}{m_s^2 + 2m_s E_\nu} \simeq \frac{m_c^2}{2m_s E_\nu} \simeq 0.5 \tag{1.30}$$
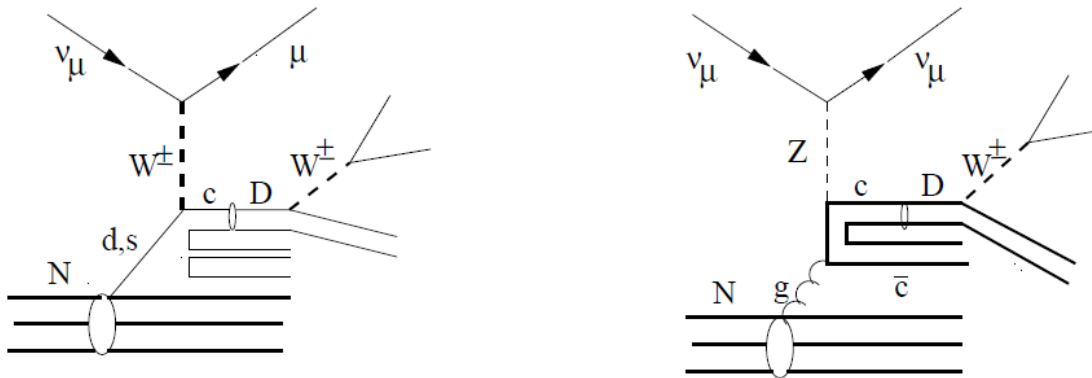
Figure 1.27: *Feynman diagram of a charm hadron production in left CC, right NC deep inelastic ν_μ-nucleon interaction. Picture from [117]*

for scattering on s quarks, with $m_s \simeq 150\,MeV$ and $m_c \simeq 1.3\,GeV$ for a neutrino energy $E_\nu = 17\,GeV$ which is the mean OPERA neutrino energy. This means that the number of charmed hadrons in deep inelastic interactions will be small.

Overall, the charmed hadrons produced in ν interactions will be 50% due to d quarks, the other 50% are caused by strange sea quarks [197]. In case of $\bar{\nu}$-DIS interactions only 10% of charm production is caused by $\bar{d}$ quarks, this is due to the fact that the d quark content of the nucleon is nine times higher than that of $\bar{d}$ (quark content proton=uud, neutron=udd, each plus sea quarks).

Taken into account the 4-momentum vector of the parton and neglecting the initial parton mass $(m_s, m_d \ll m_c)$ we get $\hat{p} = \xi p$ with $\xi = x(1 + m_c^2/Q^2)$, the slow re-scaling variable ξ probing the parton distributions, taking into account the excitation of a c quark into the mass shell [199, 200]. The differential cross section for charm production on a target T then becomes:

$$\frac{d^2\sigma^{\nu_\mu T \to \mu^- cX}}{dx\,dy} = \frac{G_F^2 s\xi}{2\pi}[u(\xi) + d(\xi) + 2s(\xi)|V_{cs}|^2]\left(1 - \frac{m_c^2}{s\xi}\right)\theta\left(\xi - \frac{m_c^2}{s}\right) \qquad (1.31)$$

As $\hat{s} = (\xi p + k)^2 \simeq \xi s$, one estimates the number of charm producing neutrino interactions by replacing $(1 - m_c^2/s\xi)$ with $(1 - m_c^2/\hat{s}) \simeq 0.5$ and setting $s(x) = \bar{s}(x)$, $c(x) = \bar{c}(x)$.

$$\frac{d^2\sigma^{\nu_\mu T \to \mu^- cX}}{d^2\sigma^{\nu_\mu T \to \mu^- X}} \simeq \frac{(U+D)|V_{cd}|^2 + 2S|V_{cs}|^2}{U + D + 2S + \frac{1}{3}(\overline{U} + \overline{D} + 2\overline{S})}\left(1 - \frac{m_c^2}{\hat{s}}\right) \qquad (1.32)$$

with $Q = \int_0^1 xq(x)dx$, $Q = U, D, S$. According to [198] we can thus calculate with $\eta_s \equiv 2S/(U+D) = 0.061 \pm 0.004$ and $\kappa \equiv 2\overline{S}/(\overline{U} + \overline{D}) = 0.40 \pm 0.05$ the ratio to be:

$$\frac{d^2\sigma^{\nu_\mu T \to \mu^- cX}}{d^2\sigma^{\nu_\mu T \to \mu^- X}} \simeq 0.5\frac{\frac{1}{\eta_s}|V_{cd}|^2 + |V_{cs}|^2}{\frac{1}{\eta_s} + 1 + \frac{1}{3}\left(\frac{1}{\kappa} + 1\right)} \simeq 0.0466 \pm 0.0066 \qquad (1.33)$$

Quasi-elastic charm production

For low Q^2 the scattering nucleon is becoming a point-like target for the virtual W-boson and the core will not break up, thus the final state is the μ^- and a charmed baryon, i.e. the Λ_c^+ as it generates the most important process via

$$\nu_\mu n \to \mu^- \Lambda_c^+ \qquad (1.34)$$

According to chapter 1.3.1. in [198], the percentage of quasielastic charm production at OPERA neutrino energy over the total charm production is to be expected in the order of $\sim 34\%$ ($< E_\nu > \sim 17\,GeV$), as shown in Figure 1.28.
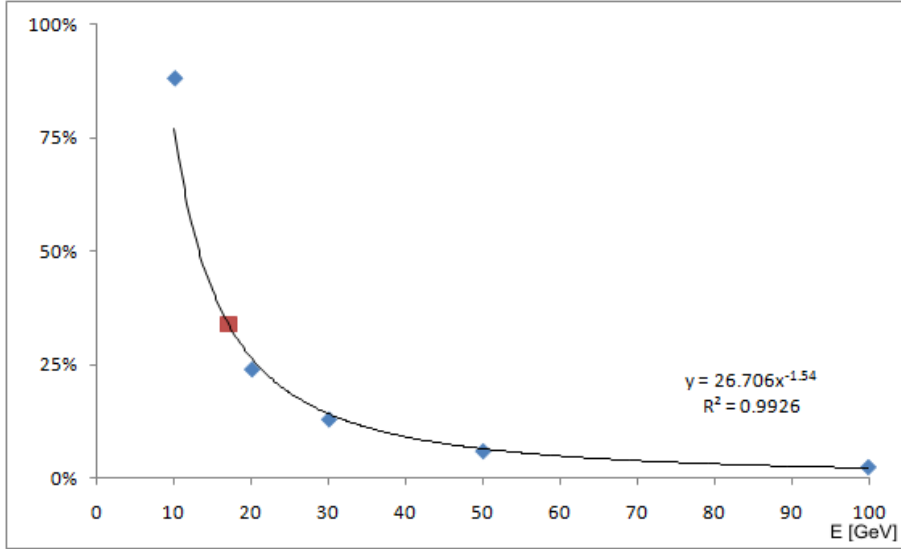
Figure 1.28: *Percentage of quasielastic charm production, according to chapter 1.3.1. in [198]. The red square corresponds to the mean neutrino energy $< E_\nu > \sim 17\,GeV$ of the CNGS beam.*

1.4.2 Charmed hadrons in OPERA

Producing the charm quark as a free particle is not possible, only color neutral hadrons can be observed. During the hadronization process the c quark combines via binding with other sea or valence quarks or antiquarks into a charmed hadron, either D^0, D^+, D_s^+ or Λ_c^+, whose characteristics are summarized in Table 1.4. The theoretical description of this fragmentation process is rather poor, and the best information still is supplied by data from the various experiments, even as a start for Monte Carlo (MC) generators. With that knowledge, one can calculate the production cross section of c quarks from the number of observed charmed hadrons, unfolding the latter number with the kinematical variables of the hadronic final states and the detector (in)efficiency. During the OPERA physics workshop in Sorrento the D^0, D^+, D_s^+ and Λ_c^+ branching fractions and topological branching ratios were presented [201]. The branching fractions with a mean neutrino energy of 17 GeV (in the OPERA neutrino beam) were extrapolated from the CHORUS experiment; the charm production in OPERA is of the order of $\mathcal{O} \sim 4\%$. The neutrino charm production in OPERA was reported as:

$$\frac{d^2\sigma^{\nu_\mu T \to \mu^- cX}}{d^2\sigma^{\nu_\mu T \to \mu^- X}} = (4.38 \pm 0.26)\% \tag{1.35}$$

The neutral charm component is $\sigma^{D^0}/\sigma^{CC} = (1.91 \pm 0.13)\%$ and the charged charm $\sigma^{C_+}/\sigma^{CC} = (2.47 \pm 0.22)\%$.

The charmed hadron production is very sensitive to the neutrino energy, since in OPERA this energy is not far above the threshold for charm production, as shown in Figure 1.29.

The topological decay branching ratios were measured by various experiments and are given in Table 1.5 [112].

Charm hadron	quark component	Mass (MeV)	τ $(10^{-15}\,s)$	$\text{BF}_{E_\nu = 17\,GeV}$ (%)
D^0	$c\overline{u}$	1864.6 ± 0.5	0.4101 ± 0.0015	43.8 ± 3.0
D^+	$c\overline{d}$	1869.3 ± 0.5	1.040 ± 0.007	21.7 ± 3.4
D_s^+	$c\overline{s}$	1968.5 ± 0.6	0.500 ± 0.007	9.2 ± 3.8
Λ_c^+	udc	2284.9 ± 0.6	0.200 ± 0.006	25.3 ± 4.9

Table 1.4: *Charmed hadron summary table including the production branching fraction (BF) at the OPERA neutrino beam with an average energy of 17 GeV [112, 201].*
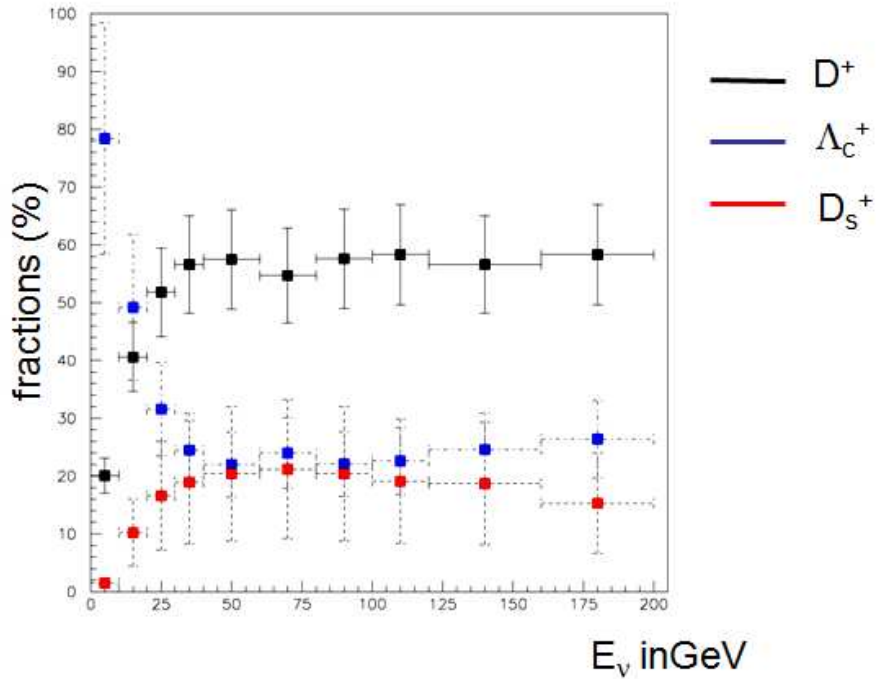
Figure 1.29: *Charged charm fraction for energies from 0-200 GeV. Picture from [201]*

Charm type	Multiplicity	BR (%)
Charged Charm	1-prong	65 ± 9
	3 prong	35 ± 6
	5 prong	0.9 ± 0.2
Neutral Charm	0-prong	15 ± 6
	2 prong	70 ± 6
	4 prong	14.5 ± 0.5
	6 prong	$(6.5 \pm 1.3) * 10^{-4}$

Table 1.5: *Charm hadron topological decay branching ratios [112].*

Chapter 2

The CNGS neutrino beam

2.1 Introduction

In this chapter I will shortly sketch the CERN accelerator facilities before concentrating on the CNGS neutrino beamline, and its optimization for τ-appearance neutrino oscillation. The information presented here is based upon the CERN website and articles, the CNGS project report [202] and CNGS status reports given by D. Autiero at various OPERA meetings [203] or E. Gschwendter [204]. To get a neutrino beam, a high energetic proton beam is directed on a target where hadrons are produced, mainly the lightest ones ($\pi^{+/-}$, $K^{+/-}$), and afterwards those decay particles are focussed in direction of the experiment by magnetic horns. After the magnetic horns, the particles travel through an evacuated decay tunnel, before the remaining hadronic component is stopped and a muon monitor is used to check the beam angle and position. In long baseline neutrino beams the muons will stop soon in the earth crust, while the neutrinos travel nearly undisturbed, until some of them are detected at the experiment.
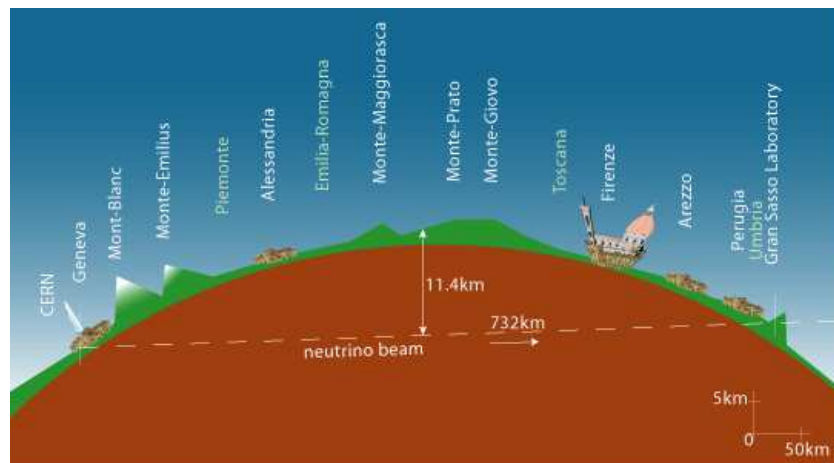
Figure 2.1: *Schematic view of the CNGS neutrino baseline. Picture from [202].*

Accelerators are used in particle physics over a century now, starting from the first electron beams with cathode ray tubes in 1897 by Karl Ferdinand Braun and Jonathan Zenneck. The proton beam used for the CNGS project is generated in the CERN accelerator complex.

2.2   The CNGS facilities

The CNGS project describes the full infrastructure at CERN needed for a long baseline neutrino beam. From CERN the beam is crossing roughly 732 km of rock before it reaches the Laboratori Nazionali del Gran Sasso (LNGS) near L'Aquila (Italy) after a flight time of about 2.5 ms. The goal of the CNGS project is to confirm the $\nu_\mu \to \nu_\tau$ oscillation. Thus, one has to make sure that the primary ν_τ component of the neutrino beam is negligibly small, i.e. the ν_τ interactions in the beamline experiments are all due to oscillation only, what will be discussed in detail later.
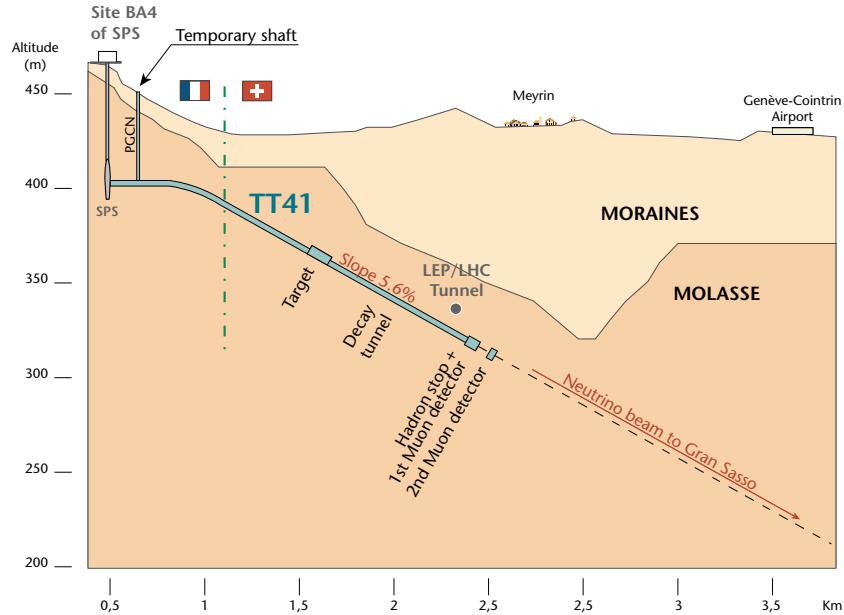
Figure 2.2: *Schematic side view of the underground structures of the CNGS project. Picture from [202].*

The intensity of the primary proton beam for a neutrino long baseline experiment has to be high to observe at least some interactions in the faraway detector. For 5 years of data taking with the nominal CNGS beam intensity, about 10 reconstructed τ-decays are expected in the the OPERA experiment. To accelerate the proton beam radio-frequency fields are used and create a pulsed beam, the timing information can be used to reduce background events in the target coming from cosmic rays. A major problem of a high proton intensity, i.e. a lot of interactions in the target, is the created radioactivity, thus, the CNGS beam was designed with special care regarding the induced radioactivity from the primary proton beam and from the collisions in the target towards its surrounding equipment and cooling liquids. Due to the high radioactivity the access of the beam target chamber is highly restricted to few minutes after a cooling period of several weeks, thus, short term interventions on the equipment are impossible. Remote handling by an overhead crane is possible, instead of repairing broken equipment, one can replace it with a spare available on site. Afterwards the broken part can stay in a storage place to "cool down" before it can be safely removed from underground. Another issue of the CNGS project was the compromise on the durability of the beam line equipment: to avoid secondary collisions after the target, as little material as possible should be placed in the beam to have a high neutrino yield, while thick materials will provide higher reliability.
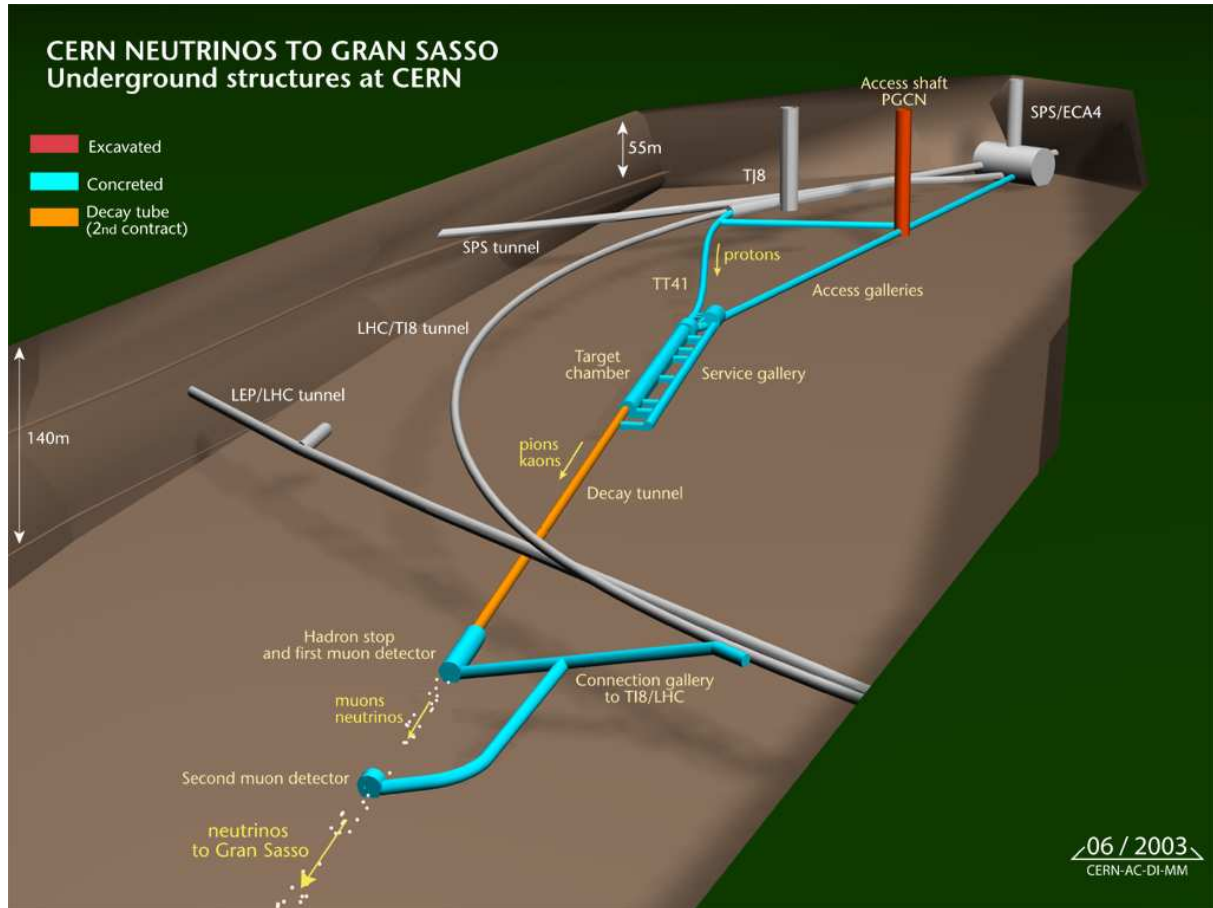
Figure 2.3: *Underground structures at CERN of the CNGS project. Picture from [202].*

The second largest accelerator at CERN, the super proton synchrotron (SPS) started to work in 1976 and has a radius of 3.5 km. It is used to accelerate the 26 GeV proton beam coming from the PS to 400 GeV and provides it to the CNGS project. Situated underground it is spanning over both French and Swiss territory. As the SPS is also used to provide protons to other experiments like LHC, a multiturn extraction of protons was designed to handle the intensities needed for CNGS [205, 206]. The primary proton beamline is tilted downwards with a slope of 58.5 mrad to direct the beam to Gran Sasso, as shown in Figure 2.2. The CNGS project is completely underground, the structures are shown in Figure 2.3.

The CNGS beamline started operation in August 2007 when a first beam test was performed. As the OPERA target was not filled at that time, the only observed interactions took place in the surrounding rock and the iron yokes of OPERA's muon detectors. A physics run started in autumn 2007, but was stopped shortly afterwards due to a failure of the CNGS ventilation system. The CNGS run 2008 and 2009 will be summarized in section 2.2.2.

2.2.1 The proton beam

The primary proton beam for CNGS is delivered by CERN's super proton synchrotron, the SPS, as already mentioned. The protons provided for CNGS have an energy of 400 GeV.

The acceleration in the SPS is obtained with electric fields with a radio-frequency of 200 MHz, while a SPS super-cycle, i.e. the repetition between one extraction scheme, takes about 40 s, as shown in Figure 2.4, depending on the number of cycles in the super-cycle. When the beam is setup in one of the flat top peaks shown in the figure, the protons are extracted with a fast-kicker system (called FE) with a septum and a kicker magnet in two proton batches of 10.5 μs each and separated by 50 ms . The radio-frequency microstructure due to the SPS is visible in the beam, as each batch will consist of short proton bunches 2-3 ns long and interspaced by 5 ns. As an SPS cycle reaches an intensity of 4.8×10^{13} protons, 2.4×10^{13} protons per FE can be delivered to the CNGS target. Taking an overall efficiency of 55% and a run time of 200 days per year for the CNGS project the total of 4.5×10^{19} protons on target (p.o.t.) per year is expected.
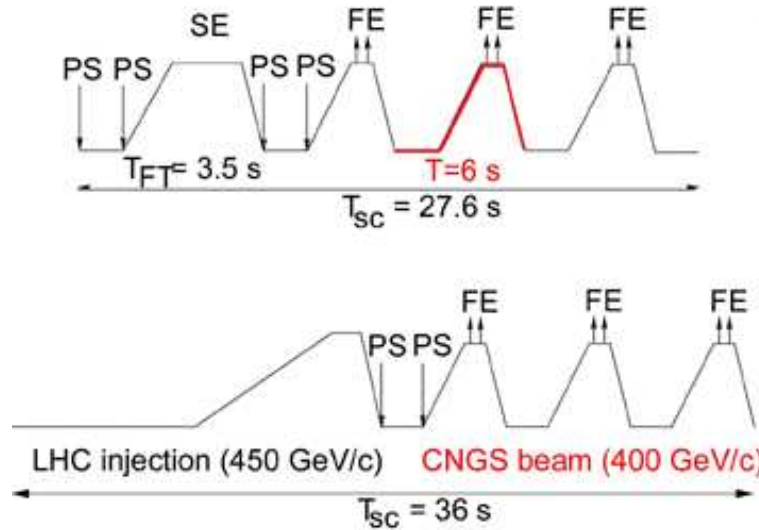
Figure 2.4: *Extraction super-cycle design of SPS. Picture from CERN webpage.*

The beamline runs 100 m from the extraction point in the LHC tunnel, together with the LHC, before it turns into a 3.1 m wide and 620 m long arc and bends towards Gran Sasso shown in Figure 2.3. It includes a 120 m long focusing section. It is constructed of 73 dipoles magnets with a field of 1.7 T and 20 quadrupole magnets with a nominal gradient 40 T/m. To control the beam, 23 beam position monitors reused from LEP, 8 beam profile monitors made of thin carbon (75 μm) or titanium (12 μm) foils, 2 beam current transformers and 18 beam loss monitors are used. The proton beam provided by the SPS has a mean energy of 400 GeV, the power of the beam is about 300-500 kW concentrated in a small beam spot of less than 1 mm diameter. Due to the short time pulse of the beam specially designed beam exit windows were needed to reduce the impact of thermo-mechanical shocks [204].

The CNGS access tunnel   To access the CNGS target chamber a separate access gallery was built, 769 m long and 3.1 m wide, visible in the upper right part of Figure 2.3.

The target chamber   The target chamber is a 6.5 m wide tunnel, 115 m long in which the CNGS target and its magnetic horn are situated. It widens to 8.5 m at the upstream end and is connected to both the proton beam and the access gallery by a 8 m long and

9 m wide junction tunnel. A parallel running service gallery of 148 m with a diameter of 3.4 m is linked to the tunnel by six 1.8 m wide crossings, allowing access for both workers and power connections. At the startup in the year 2007 two incidents happened, which requested for upgrades on the CNGS design: first the ventilation electrical control units had to be shielded against radiation, secondly the design of the water and electrical horn components needed to be replaced since the previous ones failed due to mechanical stress. Due to the improvements in shielding the radiation dose on the electronics was reduced to less than $10\mu Gr/y$, a reduction by a factor 10^6.
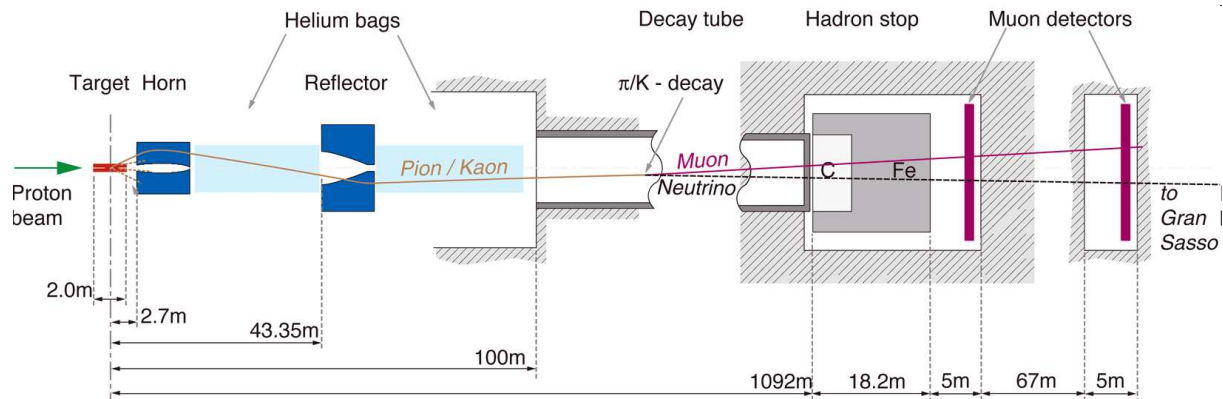
Figure 2.5: *Main components of the secondary CNGS beamline. Picture from [202].*

2.2.2 The secondary beamline

The layout of the secondary beamline is sketched in Figure 2.5. After the protons reach the target chamber, they are leaving the vacuum beam pipe through a beryllium window with $100\,\mu$m thickness, before they are hitting the CNGS graphite target. The secondary particles, mainly $\pi^{+/-}$ and $K^{+/-}$, are focussed and energy selected by a magnetic lens, made of the horn and the reflector. In the 1 km long evacuated decay tunnel they are decaying, mainly into muons and muon-neutrinos. A hadron stop made of iron and graphite at the end of the decay tube is stopping the surviving protons, pions and kaons, while further downstream a muon detector is used to monitor the beam.

The Target

The target is made out of 13 of graphite rods, as shown in Figure 2.6 and cooled by circulating helium. The first 2 rods have a diameter of 5 mm and 10 cm length, the other 11 rods have a diameter of 4 mm and 10 cm length. They are arranged with spaces between them as indicated in Figure 2.6 to a total length of 2 m, corresponding to 2.7 interaction lengths for protons with 400 GeV. Each target has a lifetime of around 1 CNGS beam year, in total 10 targets were built. They are assembled in 2 target-revolvers with 5 targets each to be easily remotely replaced, as shown in Figure 2.7. The intended duration of the CNGS beam was five years, so one of the two target-revolvers is a spare stored on-site.

Figure 2.6: *View of the CNGS graphite target. Picture from [207].*
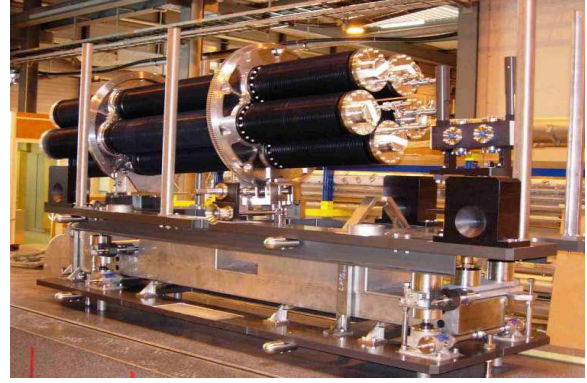
Figure 2.7: *View of one target-revolver. Picture from [204].*

The Horn and Reflector

The horn and reflector are used to focus the charged pions and kaons in the desired direction of the neutrino beam. In a wide-band neutrino beam like the CNGS they create a toroidal magnetic field between the inner and the outer conductor. They are pulsed with a high current of 150 kA for the horn and 180 kA for the reflector respectively, with a pulse-time of 7 ms, separated by 50 ms, for each fast extraction. The horn has a length of 7 m and a diaster of 70 cm. The heat generated by the current in the inner conductor is cooled by water, the conductor is only 1.8 mm thick to avoid absorption of the secondary particles.
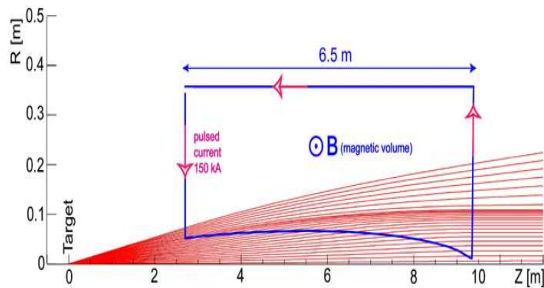
Figure 2.8: *Magnetic field and trajectories of the CNGS magnetic horn. Picture from [202].*
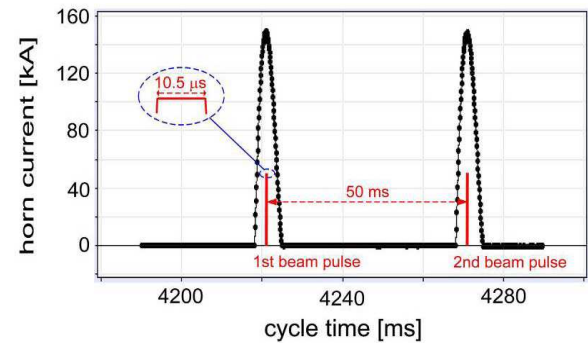
Figure 2.9: *Pulse shape of the horn and reflector current timing. The FE pulse is also shown. Picture from [202].*

The design of the magnets is made such that a parallel beam of positively charged pions and kaons is accepted to produce the ν_μ beam for the $\nu_\mu \rightarrow \nu_\tau$ oscillation study. Negative charged particles are de-focussed and most of them will not enter the decay tunnel after 100 m.

The Decay Tube

Following the magnetic system is a decay tunnel of 994 m length. It houses a 2.45 m diameter steel pipe, which is evacuated to a pressure of 1 mbar, corresponding to 0.18

interaction lengths to allow an undisturbed decay of the secondary particles into muons and neutrinos. The entrance window is made of a 3 mm thick titanium window, the exit is made of 50 mm carbon steel, which is water cooled.

The Hadron Stop

The hadron stop is situated downstream of the decay tube and is accessible from the SPS ring. The hadron stop itself consists of water cooled carbon blocks and iron, to absorb roughly 100 kW of beam power.
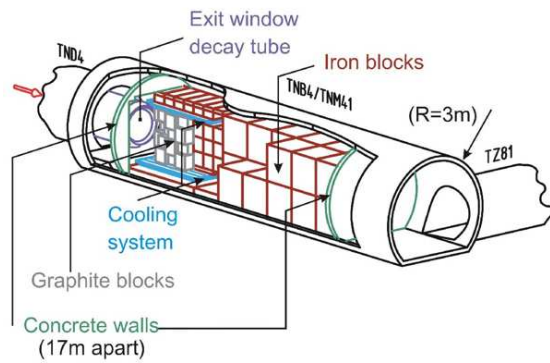
Figure 2.10: *Hadron stop of the secondary CNGS beamline. Picture from CNGS project webpage.*
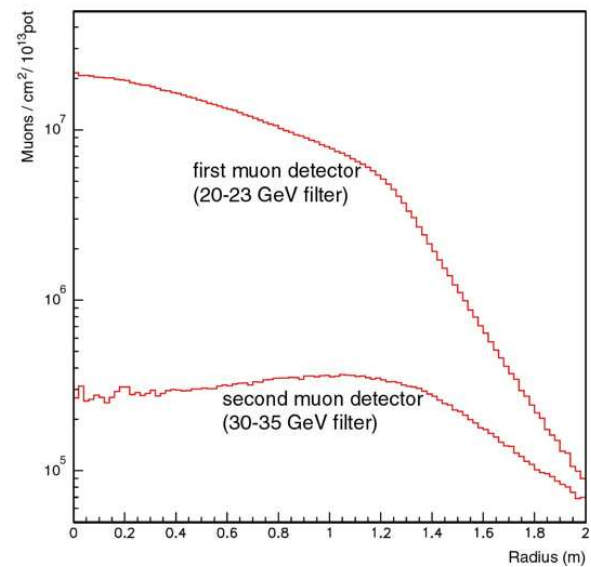
Figure 2.11: *Muon flux for the 2 muon detectors. Picture from CNGS project webpage.*

The Muon Detector

Muons will not be stopped by the hadron absorber, they are used to check the beam profile with two downstream muon detectors, separated by 67 m as shown in Figure 2.5. The muon monitors are ionization chambers, made of 60 cm long stainless steel cylinders, filled with aluminum electrodes and nitrogen, as shown in Figure 2.12. They are exposed to a muon flux of 8×10^7 /cm^2/10.5 μs. They are arranged in a cross with a length of 2.7 m, each equipped with 41 fixed monitors in 11.25 cm distance and one flexible, as seen on Figure 2.13. The muon flux is shown in Figure 2.11, with the first muon detector after the hadron stop and the second after 67 m of rock, thus, the energy cut off for the energy measurement is approximately 20-23 GeV for the first and 30-35 GeV for the second muon detector.

Figure 2.12: *View of the muon monitor without its stainless steel casing, its height is 60 cm. Picture from [204].*
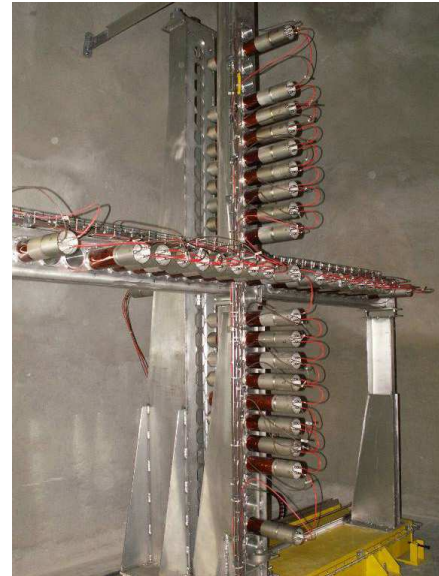
Figure 2.13: *View of the muon detector, placed in distance of 11.25 cm to cover a height/ width of 2.7 m. Picture from [204].*
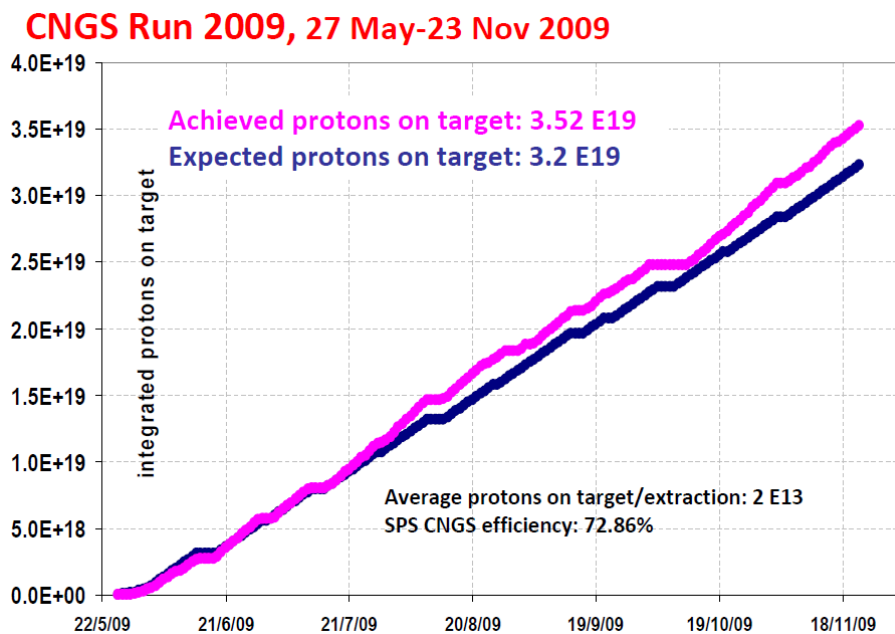
Figure 2.14: *Protons on target collected in the 2009 CNGS run. Picture from CNGS website.*

The Performance during the 2009 run

The CNGS neutrino beam started its operation in 2007 and its first real physics run took place in 2008, when 1.8×10^{19} p.o.t. were collected (40% of a nominal CNGS year). In the run of 2009 the CNGS did profit from the LHC incident, as during the day 4 CNGS cycles (with 2 FE per extraction) were included in the SPS super-cycle of 49.2 s, and

during the night the LHC extraction was excluded, thus, reducing the SPS super-cycle to 39.6 s. Additionally, a fifth extraction cycle was provided at the end of the run when the multiturn extraction scheme was tested. Thus 3.5×10^{19} p.o.t. were accumulated in 2009, as shown in figure 2.14. The design intensity of 2.4×10^{13} p.o.t. per extraction was almost reached, as shown in Figure 2.15 for the whole running time, where the upper curve shows the intensity of the first, and the lower curve the intensity of the second fast extraction. The mean number of protons per fast extraction was 1.92×10^{13} p.o.t. for the first and 2.0×10^{13} p.o.t. for the second fast extraction.
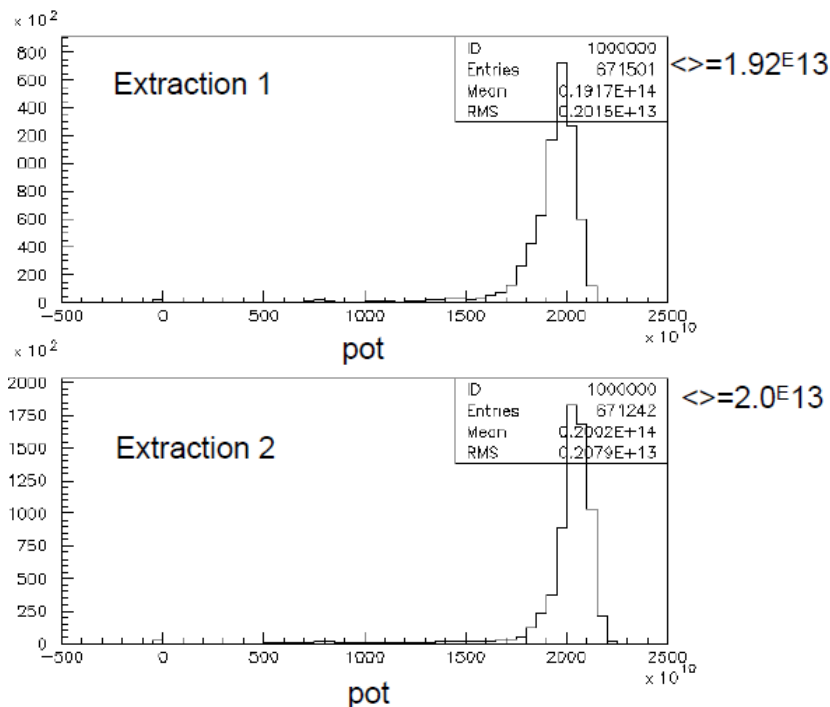
Figure 2.15: *CNGS Intensities per fast extraction summed histogram, excluding the commissioning phase . Picture from [208].*

2.2.3 Neutrino flux at LNGS

The flux of intrinsic ν_τ in the incident beam at LNGS is negligible, only due to oscillation can ν_τ-interactions occur. For the other neutrino types the flux was calculated using FLUKA MC by Paola Sala from the ICARUS collaboration [209]. Figure 2.16 shows the expected flux of the four CNGS beam components, in the upper left the $\overline{\nu}_\mu$-flux, in the upper right the expected flux of ν_μ, in the lower left the expected flux of $\overline{\nu}_e$ and in the lower right the expected flux of ν_e.

2.2.4 Optimization for τ-appearance

As already mentioned, the CNGS beam was optimized for ν_τ appearance, i.e. the following expression for the ν_τ interaction rate had to be optimized:
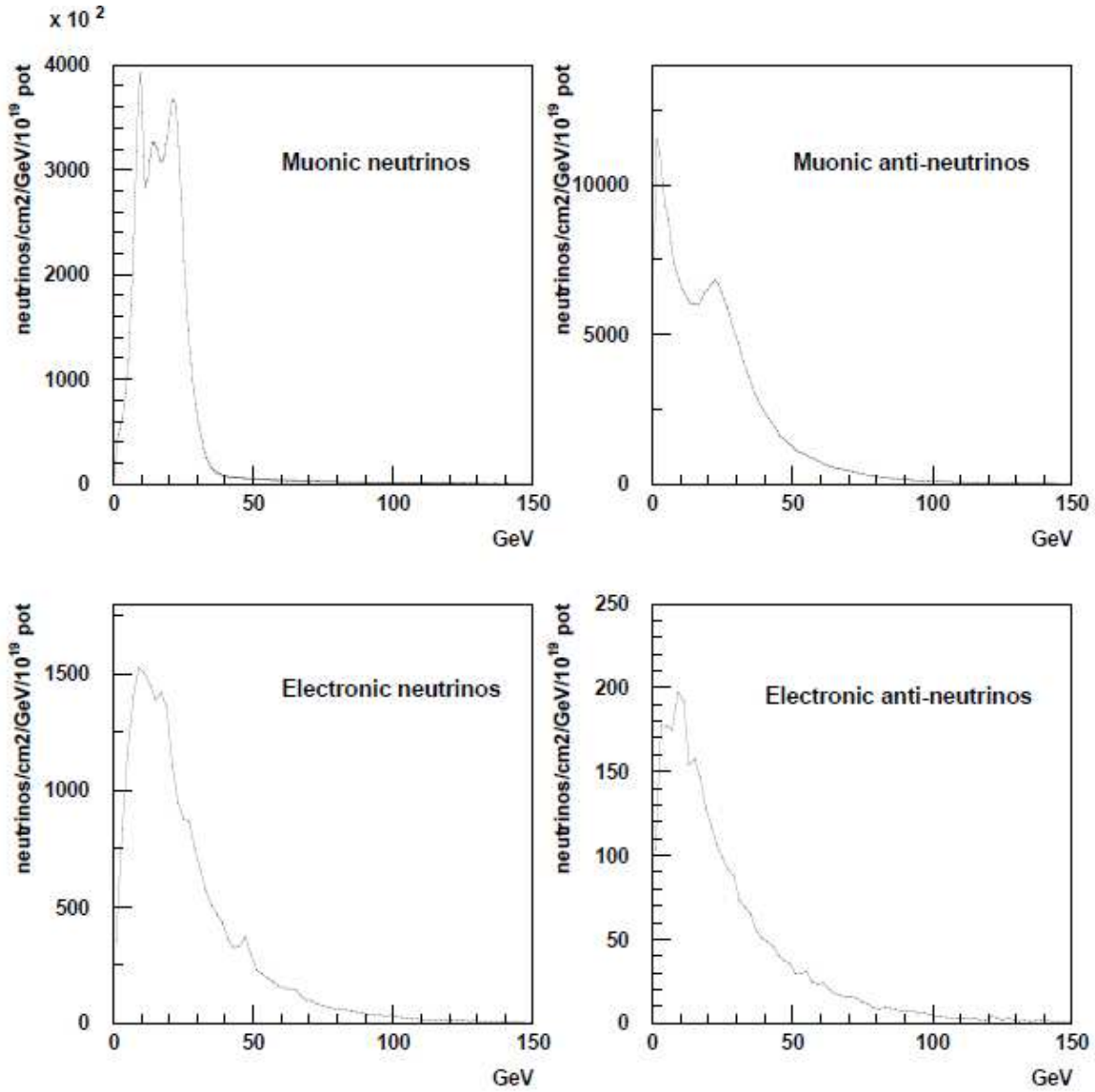
Figure 2.16: *CNGS ν-beam components; in the upper left the $\overline{\nu}_\mu$-flux, in the upper right the expected flux of ν_μ, in the lower left the expected flux of $\overline{\nu}_e$ and in the lower right the expected flux of ν_e. Picture from [210].*

$$R_\tau \sim \int dE_\tau \, P_{\nu_\mu \to \nu_\tau} \Phi(E_\tau) \frac{d\sigma}{dE}(E)\epsilon(\tau) \times M_{target} \qquad (2.1)$$

- The oscillation probability $P_{\nu_\mu \to \nu_\tau} = \sin^2 2\theta_{23} \times \sin^2(1.27\Delta m_{23}L/E)$ favors small energies.

- The production cross section $\frac{d\sigma}{dE}(E)$ requires a minimum energy for the τ production of $3.5\,\mathrm{GeV}$ (see Figure 2.17).

- The flux $\Phi(E_\tau)$ should be large.

- The efficiency for τ-detection $\epsilon(\tau)$ requests energies high enough to boost the γ-factor, so that the decay length of the τ becomes observable.

- The background should be minimized.

To address the background the horn and reflector current was set to 150 kA (180 kA) to shift the mean neutrino energy close to the maximum of the product of oscillation rate and cross section $P_{\nu_\mu \to \nu_\tau} \times \frac{d\sigma}{dE}(E)$, as shown in Figure 2.18. Additionally, it was taken care that a sharp cut-off for energies above 30 GeV was effective, to avoid undesirable background (charmed mesons) from ν_μ CC interactions.
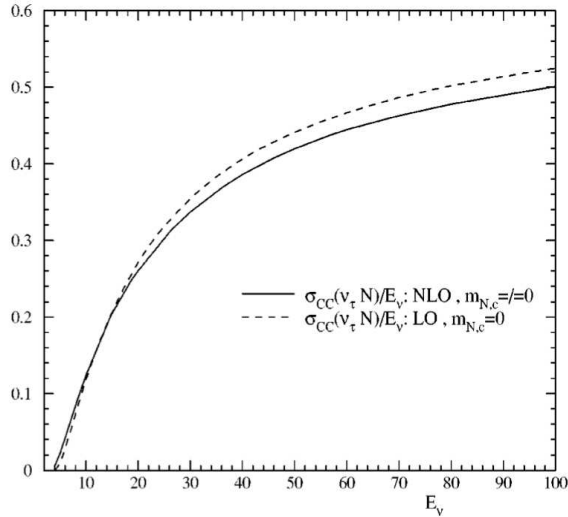
Figure 2.17: *Cross section for deep inelastic ν_τ scattering, calculated with different theories. Picture from [211].*
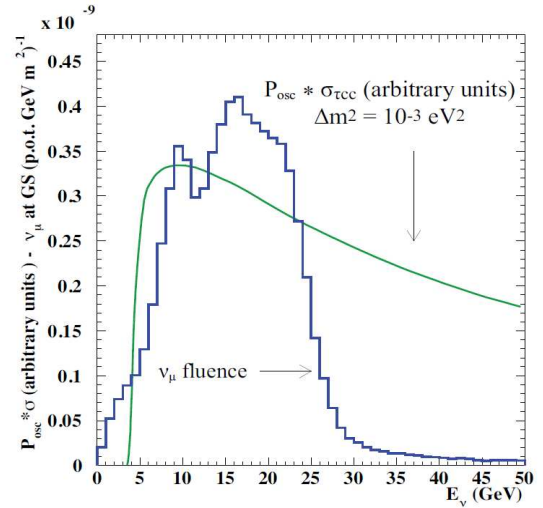
Figure 2.18: *CNGS ν-energy spectrum and oscillation probability multiplied by the ν_τ cross section. Picture [212].*

With a mean energy of 17 GeV for the neutrino beam and a distance between CERN and LNGS of 732 km this leads to an oscillation parameter of $< L/E > \approx 43$. The beam content of $\overline{\nu}_{\mu/e}$ and ν_e, shown in Figures 2.16, is expected to create a CC event contribution of 0.8% (2.0%). Given a target mass of 1.25 kt for the OPERA detector and its efficiencies for the τ-decay channels about 10 reconstructed ν_τ-events are expected to be observed after 5 years of nominal beam, or around two τ decays in the data of the years 2008 and 2009.

Chapter 3

The OPERA experiment

The OPERA experiment is a long baseline neutrino experiment, aiming at the measurement of ν_τ appearance in a nearly clean ν_μ beam, thus, giving the proof that the observed ν_μ deficit in the Superkamiokande, K2K and the MINOS experiments is indeed due to $\nu_\mu \to \nu_\tau$ oscillation, as it is assumed in ν-oscillation theory. The neutrino beam is produced with the CERN SPS accelerator in the CNGS neutrino beam project [202]. The beam is optimized in the energy for the tau-lepton production, as explained in section 2.2.4. As neutrinos are rarely interacting particles, the beam produced at CERN travels with nearly no loss underground for 730 km till it reaches the detector at the underground facilities of the LNGS (Laboratori Nazionali del Gran Sasso).
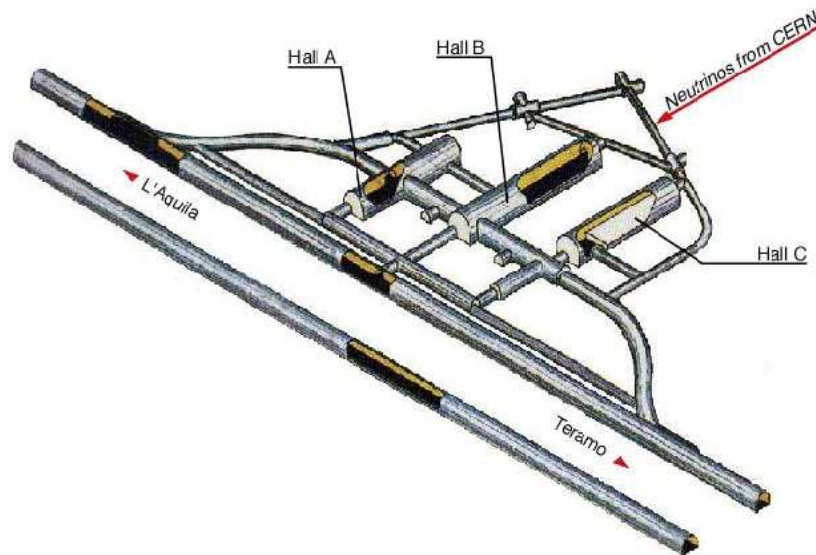
Figure 3.1: *LNGS underground laboratory. Picture from LNGS webpage.*

The underground halls of this laboratory are situated in a side cavern of a highway tunnel close to Assergi, between L'Aquila and Teramo, nearly 120 km east of Rome. Due to the 1.5 km rock shielding of the Gran Sasso massif, the rate of cosmic muons is only at a level of 1 per m^2 and hour, which makes the LNGS a perfect place for rare event experiments, used not only for neutrino physics (ν-beam, solar, astrophyiscal) but also

for astroparticle experiments, such as e.g. the search for Dark Matter. The laboratory exists since 1987 and was enlarged for neutrino experiments, needing more space, like the OPERA experiment and other experiments like:

- LVD (Large Volume Detector) which is searching for neutrinos in bursts from stellar collapses [213].

- Borexino (BORon EXperiment) which is searching for low energy (sub-MeV) Solar Neutrinos, with the specific goal of measuring the Be-7 neutrinos from the sun [214].

- ICARUS (Imaging Cosmic And Rare Underground Signal) which will be searching for atmospheric and solar neutrinos and several channels of the proton decay [215].

The new halls A, B and C are aligned with the CNGS baseline. LNGS is not only an underground laboratory, it has also an external campus, where the lecture halls, the adminstration, office space and workshop buildings are, which were extensively used by the L'Aquila university after the devastating earthquake of 2009[1]. For the OPERA experiment space was required underground not only to place the detector, but also for the brick assembling machine (BAM) and changeable sheet facility. On the outside campus a dedicated scanning laboratory and development lab for nuclear emulsions was set-up. In the following, based on [216, 210], I will present more detailed the OPERA detector in section 3.1, the OPERA brick in section 3.2, the brick handling in section 3.3 and the scanning system in section 3.4. Some OPERA electronic detector results are presented in section 4.1.4. The OPERA experiment, given a target mass of $1.25\,\mathrm{kt}$ and its efficiencies for the τ decay channels expects to detect 10.4 ν_τ-events after 5 years of nominal CNGS beam with 4.5×10^{19} protons on target per year.

Figure 3.2: *The outside campus and surroundings of the LNGS.*

---

[1]On 6th of April 2009 an earthquake with a magnitude of 5.8 (Richter-scale) destroyed most of the historic center of L'Aquila and surrounding villages, killing 308 and leaving 120'000 homeless. Several other larger earthquakes with more than a magnitude of 4 followed. The LNGS was closed for 2 weeks before the normal operation was resumed. Although the damages to the laboratory itself were marginal, many of the employees suffered losses and became homeless.

3.1 The OPERA detector
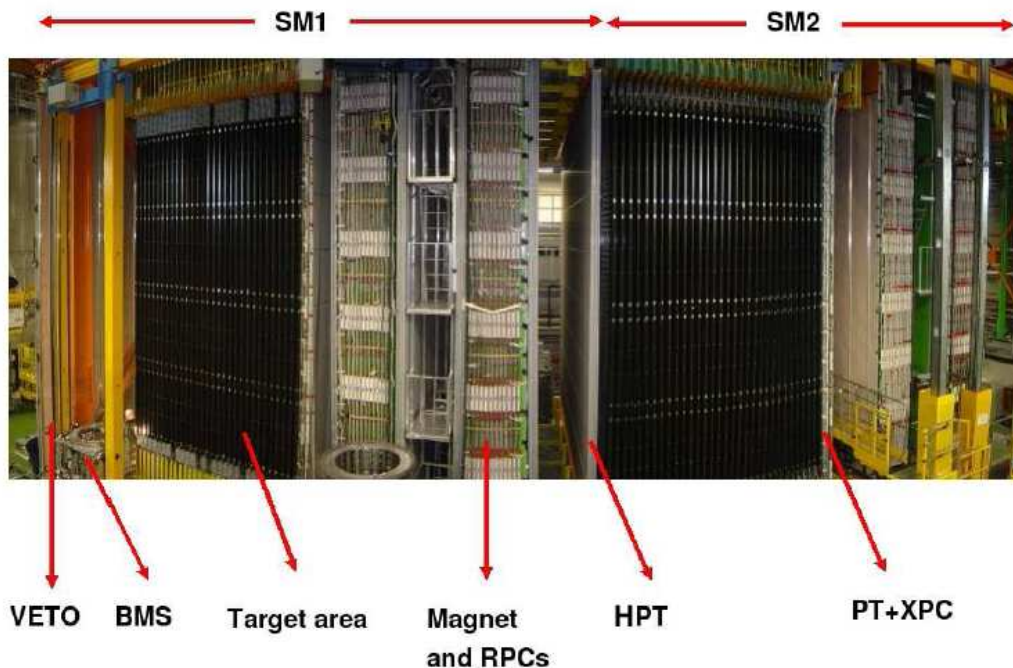
Figure 3.3: *Fish-eye side view of the OPERA detector. The upper red horizontal lines indicate the position of the two identical supermodules (SM1 and SM2). The "target area" is made of walls filled with ECC bricks interleaved with planes of plastic scintillators (TT): the black covers are the end-caps of the TT. Arrows also show the position of the VETO planes, the drift tubes of the high precision trigger (HPT) surrounded by the XPC, the magnets and the RPC installed between the magnet iron slabs. The Brick Manipulator System (BMS) is also visible. Picture from [210].*

The detector is made of two identical supermodules (SM1 and SM2, see Figure 3.3), each consisting of a target region followed by a muon spectrometer. A Veto upstream the first supermodule is used to flag muons coming from (e.g. rock) interactions upstream the first target. To observe the appearance of ν_τ one has to detect the particles from ν_τ interactions, i.e. the τ events from charged current interactions, with all observable decay modes, which are [216]:

$$\begin{aligned}
\tau^- &\to e^- \nu_\tau \overline{\nu_e} & BR &\sim 18\% \\
\tau^- &\to \mu^- \nu_\tau \overline{\nu_\mu} & BR &\sim 17\% \\
\tau^- &\to h^- \nu_\tau (n\pi^0) & BR &\sim 50\% \\
\tau^- &\to 3\pi^{+/-} \nu_\tau (n\pi^0) & BR &\sim 14\%
\end{aligned}$$

The lifetime of the τ is $(290.6 \pm 1.0) \times 10^{-15}$ s ($c\tau = 87\,\mu$m), thus, it is decaying shortly after it has been produced, i.e. the detector has to have a high granularity and a spatial resolution in the micron or sub-micron range to distinguish the decay vertex from the primary interaction. The τ specific decay properties of a short lifetime and missing transverse momentum due to the involved ν_τ are used to separate τ events from ν_μ (and other neutrino flavor) interactions and to keep the background low. At the same time one has to have a high target mass to catch enough neutrino interactions, since the
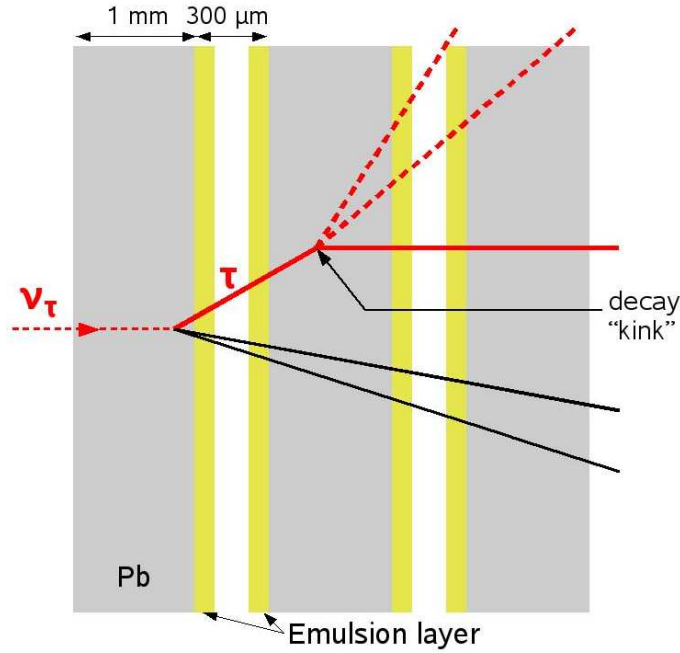
Figure 3.4: *Schematic event of a τ-neutrino interaction in the lead (grey) of an OPERA ECC. Charged particles leave a track in the emulsion layers (yellow). The interaction and the decay products of the τ have special topologies with characteristic "kinks" that can be traced, for more details see section 3.2. Picture from [219].*

cross sections of neutrino interactions are very low. These contradicting requirements were fulfilled by the hybrid detector, a part of the detector consists of active electronic detectors, used for real time measurements of the tracks escaping the detector and to determine their charge and momentum, while the fine resolution tracking is done by the passive part with the so-called ECC technique (Emulsion Cloud Chamber), already known from experiments like DONUT [217] and CHORUS [218] and illustrated in Figure 3.4.

The ECC is a packed brick made of alternating layers of lead sheets and nuclear emulsion films plus an attached CS box (changeable sheet), consisting of two emulsion plates for verification of tracks predicted by the electronic detector. With nuclear emulsions the τ decay topology of the ν_τ CC interactions can be observed by scanning the nuclear emulsions offline, thus, the technique is called passive. For a more detailed description of the ECC see subsection 3.2. To measure at least some events coming from ν_τ interactions one needs a target with a mass of $\mathcal{O} \sim 1.5\,kt$. With each ECC having a weight of about $8.5\,kg$ a total of 150'036 bricks were produced by a brick assembling machine (BAM, see section 3.3.2) to reach a target mass of $1.25\,kt$. To fill and extract the bricks from the detector a brick manipulating system (BMS) was developed, as will be explained in section 3.3.1. As bricks are extracted from the detector continuously, the maximum number of bricks inside the detector was 148'828. Over the lifetime of the experiment about 10% of the bricks will be extracted (and be replaced by so-called mechanical bricks, not containing emulsions).

The electronic detectors of the OPERA experiment have to fulfill two main tasks: The first is to find the ECC (also called brick), in which the neutrino interaction took place, the second is to measure the momentum and charge of the escaping μ and/or the energy

of the hadronic showers. Each sub-detector and its purpose will be described in more detail in the following subsections. The total detector has a length of 20 m, is 10 m high and 10 m wide. In Figure 3.3 the division of the detector in its two supermodules is seen, each SM is consisting of a target section with alternating layers of brick and scintillator Target Tracker (TT) walls and a muon spectrometer, consisting of a 1.55 T magnet in which 24 Resistive Plate Chamber walls (RPC) are built for a track reconstruction of the charged particles. Directly in front of the magnet is a tilted RPC wall mounted, the XPC. The XPC & RPC walls are used to generate the trigger for the high precision tracker walls (HPT) which are also part of the muon spectrometer. On top of the detector the read-out electronics is mounted. Additionally, an upstream veto is used to flag events from neutrino interactions in the rock before the OPERA detector.

3.1.1 The Target

Each target consists of 31 brick walls interleaved with scintillator Target Tracker (TT) walls. OPERA bricks are placed inside the target with the brick manipulating machine (BMS) from each side of the experiment (see section 3.3.1).

The Brick Walls

There are 31 target walls per supermodule, each wall has 64 rows, in which 26 ECC can be placed from the rock-side and the corridor side of the OPERA detector by the BMS, i.e. each row can be filled with 56 bricks. The final target mass of 1.25 kt corresponds to a reduction of about 25% w.r.t. the proposal, as only about 150'000 ECC cells were placed inside the detector target walls. Thus only 29 walls per supermodule were filled, with only 51 rows instead of 64. Altogether 750 t could be held by the mechanical brick wall structure per module, made out of 1 mm thick aluminium stripes welded together, as shown in Figure 3.5. This ensures a stable construction to hold the weight but keep the dead mass needed for construction as small as possible.
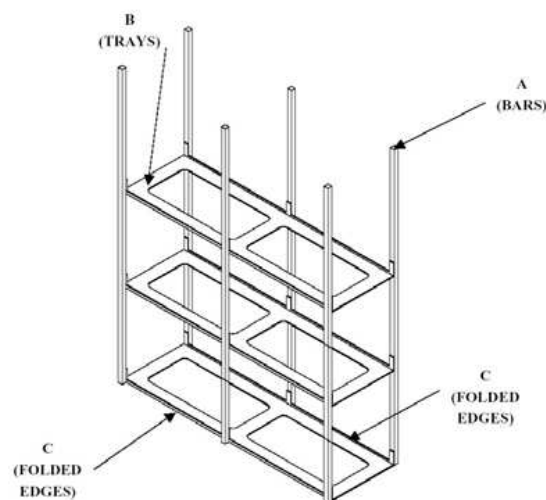
Figure 3.5: *Schematic layout of the mechanical brick wall structure. Picture from [207].*

The Target Tracker
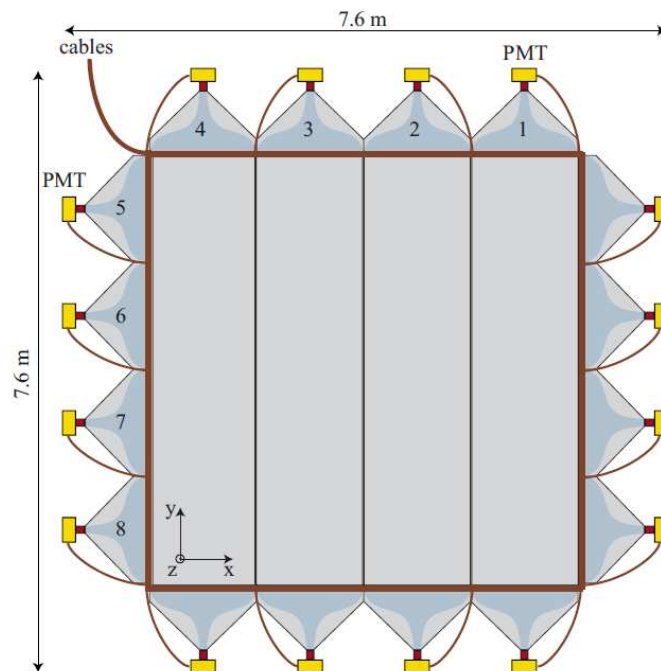
Figure 3.6: *Schematic view of the two scintillator planes of a TT wall. Picture from [220].*

The Target Tracker (TT) consist of consecutive scintillator walls after each brick wall [220]. Its main task is to indicate the emulsion cloud chamber (ECC) or brick, in which the neutrino interaction took place. This ECC will be extracted from the target and the attached changeable sheet box (CS, see section 3.2.2 for details), will be opened and the included two emulsions will be scanned, to confirm the correct choice of the ECC, before opening the whole ECC.
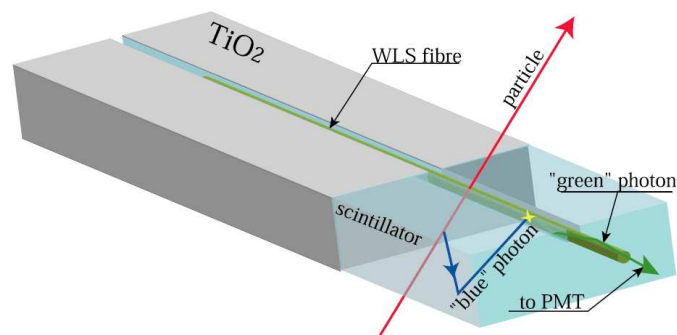
Figure 3.7: *Schematic view of a scintillator strip with the wave length shifting fiber. Picture from [221].*

Each TT wall consists of two scintillator planes with stripes oriented along the X (horizontal) and Y (vertical) axis (shown in Figure 3.6). These planes have a size of $6.7 \times 6.7\,\mathrm{m}^2$ and consist of 4 units, with altogether 256 plastic scintillator readout strips.

To allow a mass construction of the TT planes, each unit consists of 4 subunits of 16 stripes which are light-tight packed in a 0.5 mm thick aluminium case. Each stripe has a length of 6.7 m, a width of 2.7 cm and a thickness of 1 cm and is coated with reflective TiO_2 as shown in Figure 3.7. Simulations showed that a finer segmentation does not increase the resolution. Along the strip a 1.2 mm deep groove houses a wave length shifting fibre for the readout, which allows a position resolution of $\sim 1\,cm$ along the stripe. Each unit is read out with a 64-pixel Hamamatsu H7546 multi anode photo multiplier tube (m-PMT), i.e. 16 m-PMT's are used per TT wall, as shown in Figure 3.6. To instrument the whole OPERA detector with its TT planes 31'744 strips and 992 m-PMT's were used. Each m-PMT is connected with a small Linux board that can be read out via ethernet (see chapter 4.1). The TT walls cover a total area of 6000 m^2. As already mentioned, the Target Tracker is also used for a calorimetric measurement of the hadronic shower from the ν-interaction.

3.1.2 The Magnetic Muon Spectrometer
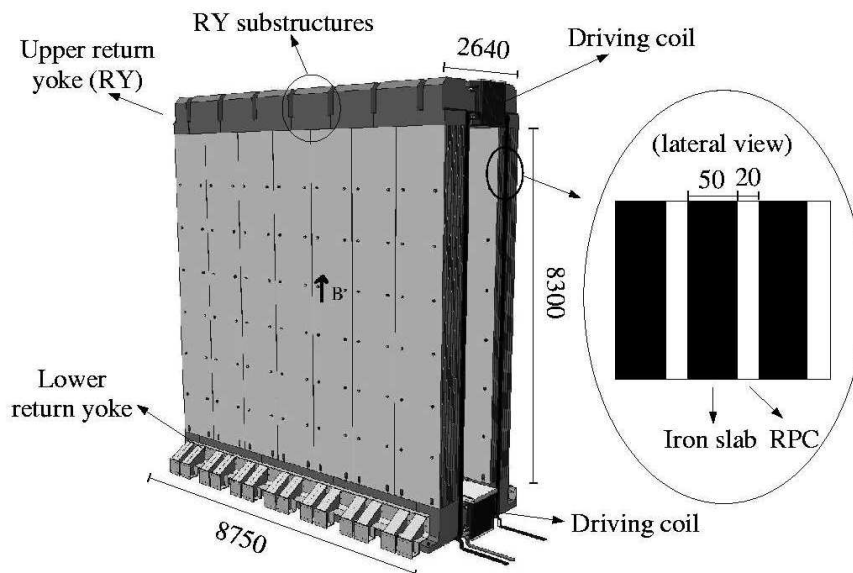
Figure 3.8: *Three dimensional view of one OPERA magnet. Units are in mm. The blow-up insert shows the dimensions of three of the twelve layers of an arm. The height of a slab is given as 8300 mm. Picture from [210].*

The muon spectrometer [210] is not only used to measure the charge and the momentum of the muons from neutrino interactions, but also for measuring the hadronic energy leaving the ECC target region. Each spectrometer consists of a dipole magnet, shown in Figure 3.8, which is instrumented with resistive plate chambers (RPC) for a coarse tracking inside the magnet iron (see Figure 3.9), a tilted RPC plane (XPC - Crossed (X) Resistive Plate Chamber) to help resolving ambiguities, and high precision tracker planes (HPT) made of drift tubes with a resolution of 0.5 mm.

The Magnet

The magnet of the muon spectrometer is a conventional dipole magnet [222, 223]. The magnet has a height of 10 m and a width of 8.75 m, while the length of the magnet is 2.64 m. The two vertical walls of the return yoke are separated by a distance of 1 m. Each wall consists of twelve 5 cm thick iron slabs, as shown in Figure 3.8.
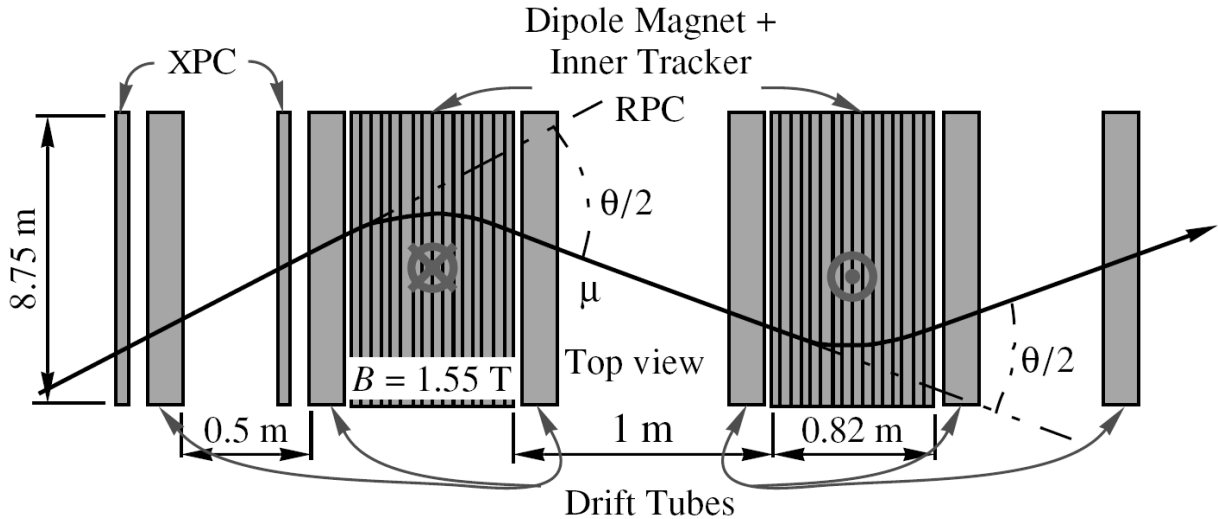
Figure 3.9: *Schematic layout (top view) of the muon spectrometer, showing the HPT and the dipole magnet planes (2×12) instrumented with RPC layers (2×11). The HPT planes (drift tubes) are aligned in 3 parts per magnet arm. The two additional RPC planes shown on the left are the XPC. Picture from [224].*

Two copper coils on the top and at the bottom are used to magnetize the iron, producing a magnetic field of 1.55 T distributed homogenously inside the magnet walls and with opposite sign for each vertical plane. The coil current is 1600 A, or 64'000 A×turns with a voltage drop of 13.4 V, i.e. the power consumption of 21 kW per magnet, which is cooled with a water circuit. The vertical magnet walls are equipped with RPC planes to allow a measurement of stopping muons and a coarse alignment for tracks between the HPT planes. The total mass of the magnet is 990 t each.

The Resistive Plate Chambers (RPC)

For each Super Module 11 + 11 RPC walls (Resistive Plate Chamber) [225, 226, 227, 228, 229] are used for the track reconstruction between the 24 iron walls of the return yoke. Each of these planes is made of 21 RPC's with a size of $2.91 \times 1.14 \, \mathrm{m}^2$, covering a total area of $70 \, \mathrm{m}^2$. The total recorded area of RPC inside each super-module is about $1500 \, \mathrm{m}^2$. Each RPC consists of two parallel, 2 mm thick bakelite plates, kept at a distance of 2 mm, as shown in Figure 3.10. Thus, the RPC has a volume resistivity of more than $5 \times 10^{11} \, \Omega/\mathrm{cm}$ at room temperature. On the opposite sides of both bakelite plates is a graphite layer.
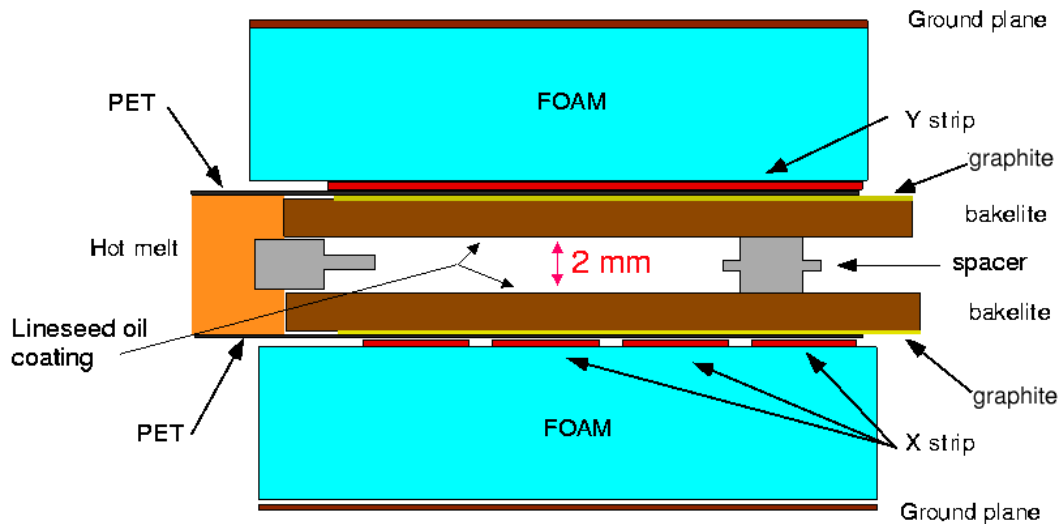
Figure 3.10: *Cross-section of a Resistive Plate Chamber with its associated strips for the readout of the induced signal. Picture from [222].*

Polyethylene terephtalate (PET) foils with a thickness of $190\,\mu$m and $250\,\mu$m are used as insulator. On top of these copper electrodes are placed to read out the planes, with a pitch of 2.6 cm in the x (horizontal) and 3.6 cm in the y (vertical) direction, put at a potential of 5.8 kV with a current of less than $100\,$nA/m^2. The area between the plates is filled with a mixture of argon gas, Tetrafluoroethylene gas, Isobutane gas and Sulfur Hexafluoride gas at the ratio of 75.4:20:4:0.6 [230]. Ionizing particles crossing the gas produce ions and electrons, which are then drifting in the electric field to the corresponding plate and induce a signal in the copper stripes. As the graphite plates have a high resistance, the spot at which the interaction took place is shortly blinded for other crossing particles for about 10 ms (dead time). As the OPERA experiment has a low event rate, this is not a problem. The read out is collected with a dedicated front end board via ethernet. Thus, the RPC allows a coarse tracking inside the magnet for muon identification and to simplify the track matching between the HPT planes. They are also used for measuring the tail of the hadronic energy from the neutrino interaction leaving the target and the range of muons stopping in the iron.

The Crossed (X) Resistive Plate Chamber (XPC)

Directly behind the OPERA target, made of TT and brick walls, is the XPC (see Figure 3.9). The XPC is a RPC plane in which the readout electrodes are rotated by $\pm42.6°$ and with a pitch of 2.6 cm in each read-out direction. Apart of that, the XPC is the same as the RPC or Veto, the used gas mixture is the same as for the RPC planes. Due to the rotation a higher resolution in the y-axis can be achieved. Another task, except for the tracking of particles, for XPC and RPC is the calorimetry measurement of hadronic showers and triggering for the HPT (High Precision Tracker), the triggering scheme is described in the section 4.1.2.

The High Precision Tracker (HPT)

The HPT (High Precision Tracker) consists of nearly 10'000 8 m long drift tubes positioned around the magnet of the muon spectrometer and is used to measure the charge and momentum of crossing muons, mainly from ν_μ-CC interactions, but also helping to identify the $\tau \rightarrow \mu$ decays and to decrease the background event rate [231, 232]. In each drift tube a gas mixture with 80% argon and 20% CO_2 is used with argon as drift gas and CO_2 as quench gas with a total volume of 80'000 l. Ionizing particles crossing the drift tube will produce electrons (and ions) which will drift to the anode (cathode respectively) with a drift velocity of a few cm/μs for electrons, thus, a radial measurement of the distance from the crossing particle to the wire is possible. To get the explicit position of the crossing particle, 4 drift tube hits are needed to track the particles with a resolution of a few hundred μm, thus, the drift tubes are arranged in four staggered layers to HPT walls and placed around the two magnets, optimized by Monte-Carlo simulation. Each wall consists of several modules, usually 17 modules build up one wall, except for three layers close to the target, where the outer modules can not be placed to allow the BMS a smooth operation, i.e. these walls consist of only 15 modules. The walls cover an area of $7.9 \times 8.5 \, \text{m}^2$, respectively $7.9 \times 7.5 \, \text{m}^2$. Each module consists of 48 aluminium tubes, each 8 m long, arranged in 4 alternating layers with 12 tubes. The layout, shown in Figure 3.11 was optimized with a Monte-Carlo simulation to allow an explicit track reconstruction for which 4 hits in different drift tubes are needed; the distance of 4 mm between the tubes
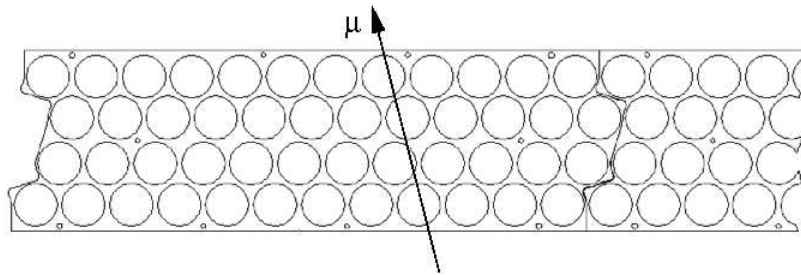
Figure 3.11: *Sketch of the mechanical reinforcement plate used for one HPT module, showing how the drift tubes are arranged inside each module. Picture from [232].*
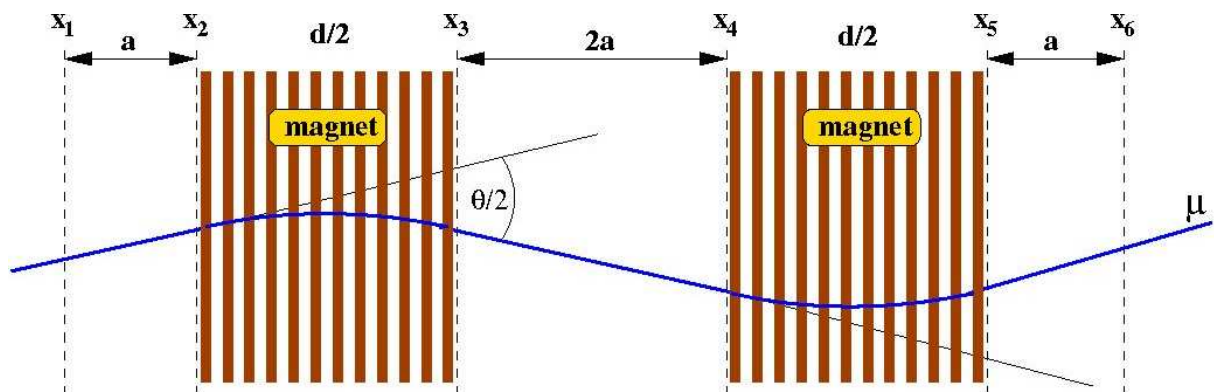
Figure 3.12: *Sketch view of the muon spectrometer. The dashed lines symbolize the HPT walls, the angle can be measured, and thus the momentum can be reconstructed. Picture from [232].*

does not impose a loss in tracking resolution. Each drift tube has a diameter of 38 mm and a wall thickness of 0.85 mm. Each module has a closing plate used for mechanical stabilization and to ensure a tight sealing of the tubes, as electronegative impurities like oxygen and water would reduce the tracking resolution and thus, have to be avoided. Each module has a single connection to the gas system for all drift tubes inside. In the middle of each tube a 45 μm diameter, gold-plated tungsten wire is used as the anode wire with a voltage of 2350 V. To avoid deformation due to electrical fields the wires are tensioned with 186 g, which is below the elastic deformation limit even in the case of temperature fluctuations. A dedicated read-out electronics is situated on top of the walls. The HPT is able to measure the μ-momentum up to an energy of 20 GeV with a resolution better than $\frac{\Delta p}{p} \leq 0.20$. Each μ crossing the spectrometer will be deflected two times by the angle $\frac{\theta}{2}$, given as $\theta = \frac{eBd}{p}$, with the magnetic field B=1.55 T and iron thickness d=1.2 m (see Figure 3.12). Taking into account multiple scattering the maximal track reconstruction error ϵ is ∼640 μm, including the error from the drift time measurement, wire position and module displacement. The probability η of tracking a single hit in a single drift tube, i.e. the ratio signal to no signal per hit, is about 98%.

The Gas System

To supply the RPC and XPC with the gas mixture a dedicated distribution system was setup, as for the HPT, needing argon and carbon-dioxide. The station was optimized to run automatically, the only human check needed is for the filling status of the storage bottles. The gas station is situated in the connection tunnel between Hall B and C.

3.1.3 The Veto

Figure 3.13: *Picture of the OPERA detector. The beam is entering from the left. The Veto is the white plane behind the staircase.*

The main task of the Veto is to reduce the false trigger rate due to so-called "rock-muon" events, neutrino interactions upstream of the OPERA detector, i.e. either inside the rock before the experiment or in the BOREXINO experiment. Figure 3.13 shows the Veto plane at the most upstream part of the OPERA detector. It consists of two $9.6 \times 9.2\,\mathrm{m}^2$ planes at a distance of $10\,\mathrm{cm}$. The planes are divided by a matrix of 64 glass-RPC.

3.2   The OPERA Brick/ECC

To detect particle decays within $\leq 1\,\mathrm{mm}$ from the production vertex, the Emulsion Cloud Chamber (ECC) showed its potential in the CHORUS [192] and DONUT [109] experiments. The idea behind the ECC is to observe the charged particle tracks with emulsion films, interleaved with a heavy material to gain a large target mass. Charged particles with a short lifetime and their decay vertex can be distinguished from the primary neutrino interaction vertex due to the spatial resolution of the emulsion in the sub-micron range.
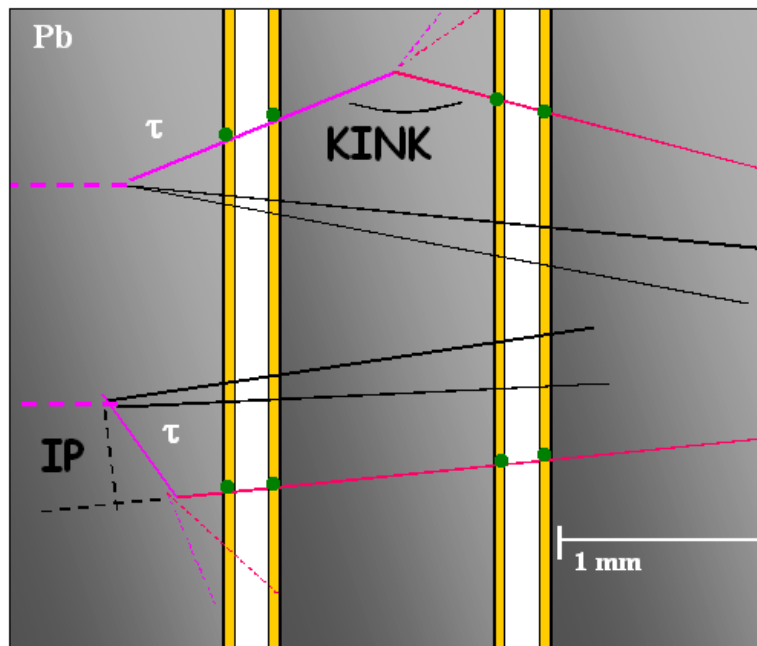
Figure 3.14: *Schematic picture of the τ detection technique in the ECC cell for long (top) and short (bottom) decays. Picture from [233].*

In the OPERA experiment, the golden channel for the detection of τ-appearance is the $\nu_\tau \to \tau^- + X$ with the subsequent decay channel $\tau^- \to \mu^- \nu_\tau \overline{\nu}_\mu$, wherein the muon is detected by the spectrometer. To detect the τ decay, one searches for a kink in the path of the track from the primary vertex, a so called long decay event, as described in Figure 3.14 (top). Due to the short lifetime of the τ, most τ particles will decay inside the same lead plate in which it was produced, the so-called short decays (see Figure 3.14, bottom) identified through their impact parameter (IP) to the primary vertex. To detect the decay of short living particles, the emulsion plates around the primary neutrino vertex

will be scanned, as explained in section 4.2.3 and analyzed according to the decay search procedure, explained in appendix D.

3.2.1 The OPERA brick

The Emulsion Cloud Chamber is the basic element of the OPERA detector. Each emulsion cloud chamber consists of 57 emulsion films and 56 lead plates, stapled in a plastic box and pressed together with an aluminium spider and wrapped in aluminium to ensure light tightness. Two additional emulsion films, packed in aluminium foil inside a plastic box, the so-called CS, are added to provide an easy way to confirm that the ECC is containing an event, as predicted by the electronic detector (see section 4.1.3 and 4.2.3). In the OPERA language, the ECC is also referred to as 'OPERA Brick' or 'Brick' shortly, having a size of $12.8 \times 10.2 \times 7.9\,\text{cm}^3$ and a weight of about $8.3\,\text{kg}$ (see Figures 3.15 - 3.18).

The thickness of $7.5\,\text{cm}$ assures ten radiation lengths (X_0), a length which was chosen because:

- The brick has to be removed from the detector for analysis, thus, its mass should represent only a small fraction of the total target mass.

- In the transverse and in the beam direction the ECC has to be much larger than the uncertainties of the interaction vertex Z-position, predicted by the electronic detector to reduce the number of wrongly extracted bricks.

- To allow electron and γ identification, their shower behavior will be checked by a neural network, which requires about 3-4 X_0 to distinguish the particles.

- Multiple scattering over a length of more than $5\,X_0$ allows a momentum measurement of the particle for momenta $\leq 6\,\text{GeV}$.

For the OPERA experiment 150'036 bricks were produced by a dedicated fabrication line, the brick assembling machine (BAM) which is described in 3.3.2. The insertion and extraction of the bricks to the OPERA target is handled with the Brick Manipulating System (BMS), described in 3.3.1. Each emulsion has a size of $10 \times 12.5\,\text{cm}^2$, the total emulsion surface in OPERA is about 112'500 m^2. To scan this area a dedicated scanning system had to be developed, and is described in 3.4.
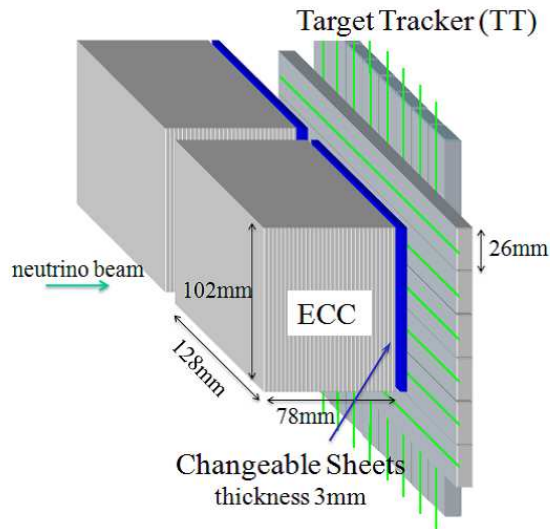
Figure 3.15:   *Schematic view of the OPERA ECC cell inside the detector. Picture from [207].*
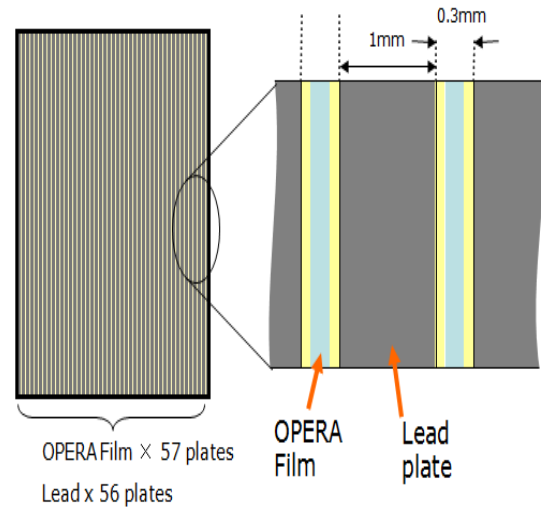
Figure 3.16:   *Cross section view of the OPERA ECC cell.   Picture taken from [207].*

Figure 3.17:   *The OPERA Brick with CS-box.   To identify the brick a matrix code is printed on it.   The dimensions are $12.8 \times 10.2 \times 7.9\,cm^3$*

Figure 3.18: *Opened plastic CS box of the OPERA ECC cell, with the two emulsion layers packed in an envelope. Picture from [207].*

The Emulsion Film
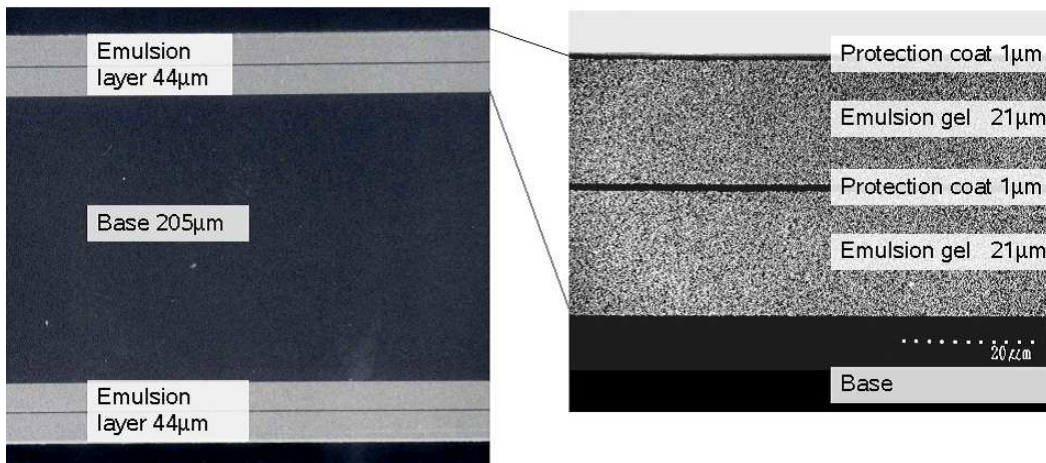
Figure 3.19: *Schematic picture of the OPERA film. Picture from [207].*

Each emulsion film consists of a transparent plastic (triacetate) base with a thickness of $205\,\mu$m coated on both sides with an emulsion layer of $44\,\mu$m thickness. To allow the direct contact with the lead and to reduce black patterns from the development, they are protected by a thin gelatine layer ($1\,\mu$m), as shown in Figure 3.19. The emulsion films were produced by Fuji Film Company in a R&D collaboration with the Nagoya University [233].
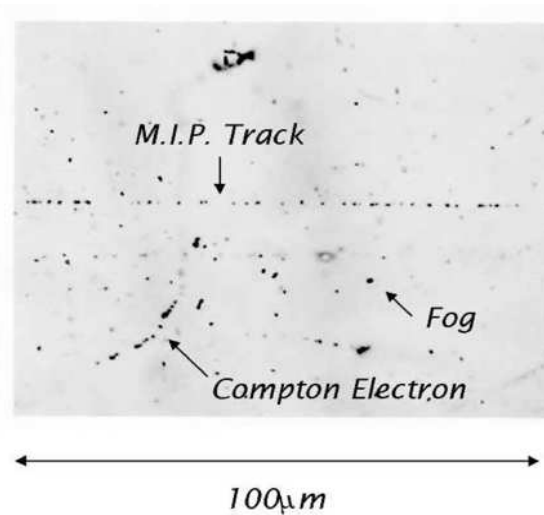
Figure 3.20: *Photograph of minimum ionizing particles recorded in emulsion. Picture from [234].*

The emulsion itself has following physical properties: a density of $\rho = 2.4\,\mathrm{g/cm^3}$ with an average atomic number of $<$A$>= 18.2$ and average atomic charge of $<$Z$>= 8.9$. The radiation length of the emulsion is $X_0 = 5.5\,\mathrm{cm}$, where the energy deposit of a minimum ionizing particle (mip) is $(dE/dx)_{mip} = 1.55\,\mathrm{MeV/g/cm^2}$ or $37\,\mathrm{keV}/100\,\mu$m. The nuclear collision length is $\lambda_T = 33\,\mathrm{cm}$ and the nuclear interaction length is $\lambda_I = 51\,\mathrm{cm}$.

This is achieved by the use of embedded silver halide crystals (AgBr) with a diameter of around $0.2\,\mu$m, which are ionized by charged particles. This is similar to regular photographic emulsions, but in the OPERA emulsion the silver halides are uniformly in size and sensitivity and in much higher densities and the layer itself has a higher thickness than ordinary films.
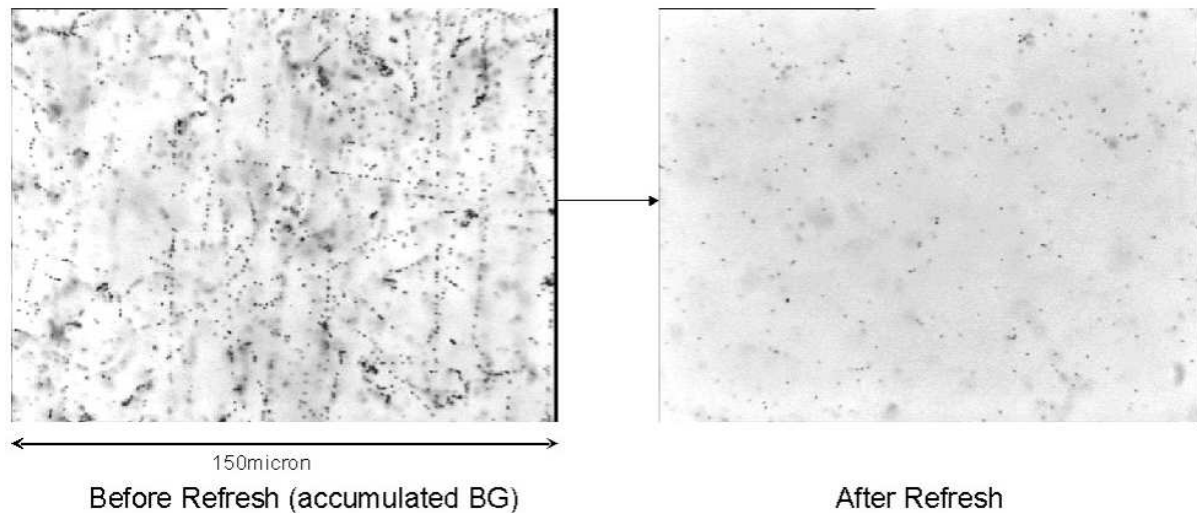
Figure 3.21: *Effect of the refreshing procedure on developed OPERA emulsion films. Picture from [207].*

From the time of fabrication and the transport to the LNGS the emulsions were exposed to cosmic rays, so a refreshing took place to clean the emulsion before using it in the brick fabrication. This refreshing process is depending on external air conditions like temperature, humidity and pressure. For high temperature and humidity the sensitivity decreases and the latent image (see appendix B) is less stable, thus fading away. As the emulsion is sensitive to radiation and charged particles directly after production, it is accumulating many minimum ionizing cosmic rays during transport and storage, which could create background, thus, the fading is introduced artificially to erase images of unwanted minimum ionizing tracks as shown in Figure 3.21.

Initial sensitivity before refreshing	36 grains/100 μm
Surviving grain density of recorded tracks after refreshing	13 grains/100 μmm
Sensitivity after refreshing	33 grains/100 μm
Fog density before refreshing	2.5 grains/1000 μm^3
Fog density after refreshing	3.5 grains/1000 μm^3

Table 3.1: *Sensitivity for minimum ionizing particles and fog grain density in the OPERA emulsions, as measured before and after the refreshing procedure. Table from [233].*

It is possible to refresh emulsions without spoiling their sensitivity, this so-called "refreshing" procedure was done in Tono-mine in Japan for the OPERA emulsions by exposing the emulsions three days at a temperature of 30° C and 98% relative humidity, before they were transported to the LNGS. The features of the emulsion after the refreshing are

reported in Table 3.1, as one can see in Figure 3.21, the emulsion does not deteriorate in its properties too much, but allows a significant reduction of background tracks. After the refreshing procedure the emulsion films were packed vacuum-tight in "brick"-like piles of 57 emulsion layers and sent to Gran Sasso laboratory to await the brick assembling in a temperature and humidity controlled environment, see also 3.3.2.

The sensitivity of the emulsion (i.e. the grain density) has to be calibrated and is about 30-35 grains/100 μm for a minimum ionizing particle (mip) in case of the OPERA experiment, measured with high energy π-beams (see [234, 233]). The fog is randomly distributed grains with ≤ 10 grains/1000 μm^3. To obtain a sub-micron tracking precision one needs a stability of the relative grain position during and after the development. Two main deformation effects occur for emulsions, the shrinkage and distortion [233]:

Shrinkage Inside the emulsion, the silver halide crystals occupy a certain volume of the emulsion, but only a small fraction is contributing to the latent image. The rest of the crystals are removed during the development, leading to a substantial reduction in the emulsion thickness. This shrinkage factor is defined as the emulsion thickness at the exposure time divided by the thickness after the development. Typical values of shrinkage factors for nuclear emulsions in past experiments were ~ 2. The shrinkage is taken into account by the tracking algorithm, as the measured track slopes must be corrected by this factor to obtain the real value (see Figure 3.22). For the OPERA experiment this volume reduction is less crucial, as a lower halide/gelatine ratio has been chosen. Additionally, a glycerine treatment of the emulsions after the development was defined, restoring the original volume by emulsion swelling.
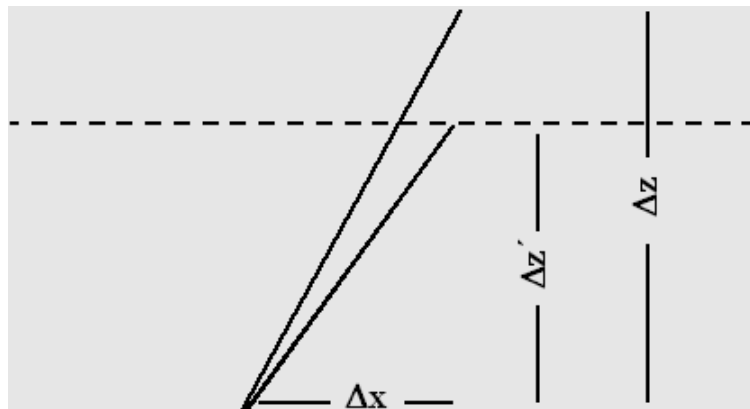
Figure 3.22: *The shrinkage effect: the measured track slope $\Delta z'/\Delta x$ does not coincide with the real slope $\Delta z/\Delta x$. The shrinkage correction is obtained by multiplying the measured slope by the shrinkage factor $\Delta z/\Delta z'$. Picture from [233].*

Distortions Even though emulsions are mechanically strong materials, they are soft and pliable. The tension applied in the production is released during the development, thus the emulsion is swollen. This increases the mobility of chemical agents but causes tensions to relax, which build up at the time of pouring. Due to the automatized processing in the OPERA experiment one generates lower distortion effects. This local effect is shown in a typical distortion map measured for an OPERA emulsion in Figure 3.23 [233]. The
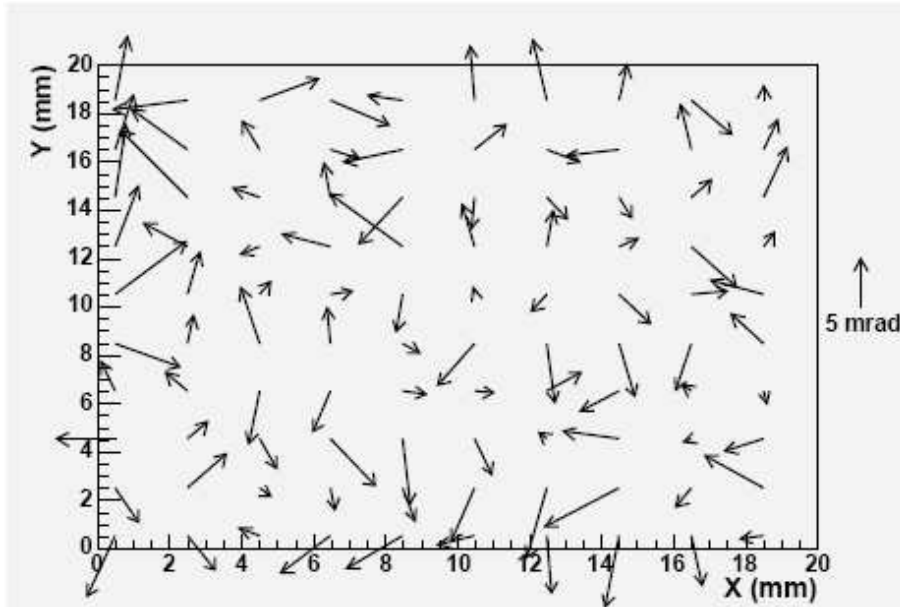
Figure 3.23: *A typical distortion map of an OPERA nuclear emulsion. Picture from [233].*

arrows are indicating the direction, their length gives the value of the distortion. An average measured distortion angle of ~ 5 mrad inside the emulsion is measured. As in OPERA double-sided emulsions coated on a plastic support plate are used, the angular resolution is improved to $\lesssim 2$ mrad, as the track direction is defined from the two points close to the support plate, being practically free of distortion.

The Lead

As passive material for the OPERA ECC lead was chosen [235], as it has a shorter radiation length and higher density compared to the emulsion. Thus the ν-interaction rate is increased. The lead allows a momentum measurement by multiple scattering and electron identification. As a drawback, lead has some radioactive isotopes creating background tracks. Due to the use of low radioactivity lead these rates are estimated to be about $\sim 10\,\alpha$ and $\sim 50\,\beta$ tracks per day and cm^2 leading to a mismatch of low energy segments of $\sim 1/$mm^2 without taking into account track fading. The thickness of the plates varies within less than $15\,\mu$m$/102$ mm or 0.15 mrad [236]. During the production of the OPERA bricks about 30'000 to 45'000 lead plates were produced per day at JL Goslar[2] and shipped in three weekly deliveries to the BAM at Gran Sasso.

3.2.2   The Changeable Sheet (CS)

Each ECC has an attached Changeable Sheet box [237], in which two emulsion films are packed, as shown in Figures 3.17 and 3.18. After the brick finding algorithm identified an ECC, it is extracted from the detector and the CS is developed and scanned. The scanning procedure for the CS is the so-called general scanning (large area), described in section 4.2.3. This step was introduced to get a fast feedback if the brick was correctly found by

---

[2]JL Goslar GmbH, Im Schleeke 108, D-38640, Goslar

the brick finding algorithm, described in 4.1.3. The CS acts also as a veto for tracks found in the ECC, as the ECC will be exposed to cosmic rays for alignment reasons, while the CS is not, as shown in Figure 3.24. The electronic detector has a vertex prediction of $1\,\mathrm{cm}$ accuracy for charged current (CC) events, but for neutral current (NC) events the hadron track accuracy does not allow a position prediction inside the brick, thus about $50\,\mathrm{cm}^2$ are scanned on average per CS box. For muons the angle can be reconstructed within some mrad accuracy by the electronic detector, this is used to constrain the number of track events in the CS. The scanning is performed at the CS Scanning station, located at the Gran Sasso laboratory, and in the Nagoya scanning laboratory (see 4.2.3).
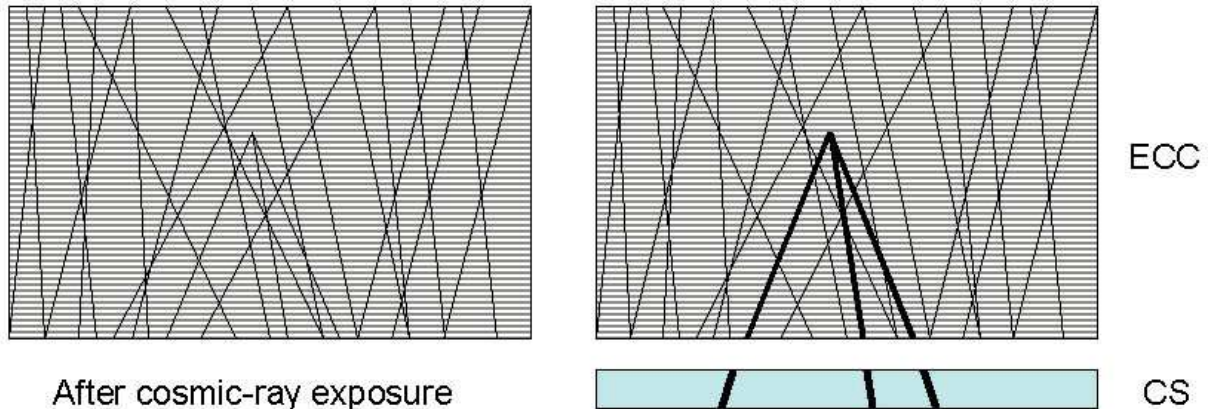
Figure 3.24: *Usage of the CS to reject cosmic ray tracks needed for alignment of the emulsion films. Picture from [207].*

3.3   Brick Handling

As already mentioned, the OPERA detector is situated underground at the LNGS. As an emulsion experiment built of many ECC cells, it has a demanding infrastructure: the Brick Handling Machine (BMS) to insert and extract the ECC from the detector, the Brick Assembling Machine (BAM) which was needed to produce the more than 150'000 ECC, one underground development laboratory for the changeable sheets (CS) to avoid their contamination with cosmic ray tracks, another development laboratory on surface for the bricks. The brick will be exposed to cosmic rays for about twelve hours to allow the submicron alignment of the emulsion films, before the development.

3.3.1   The BMS

To handle the $\sim 150'000$ ECC/bricks needed to reach a target mass of $1.25\,\mathrm{kton}$ a dedicated robot was developed to automatize the insertion and extraction of bricks from the detector; the Brick Manipulating System (BMS) [210]. On each side of the detector, called the *corridor side* and the *rock side*, one BMS robot takes care of the insertion and extraction in both supermodules. It consists of the carousel part and the loading station. To keep control of the various activities of the insertion during the target filling,
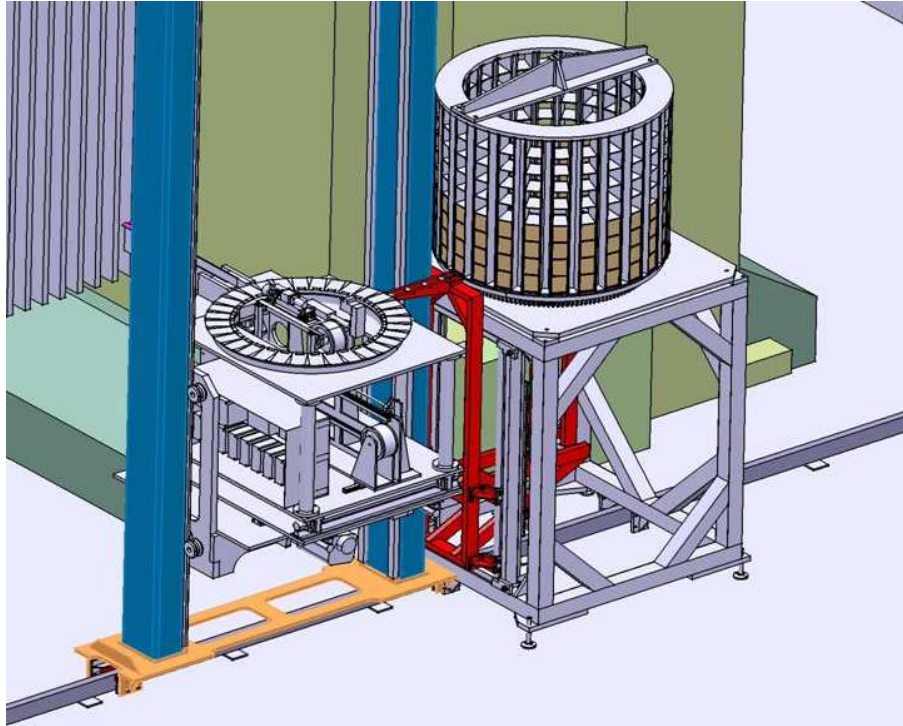
Figure 3.25: *Overview over the BMS. In the left the Carousel robot is shown, on the right the loading station with a half filled drum.*

and the later extraction and reinsertion during the run of the experiment, a database is maintained to keep track of every brick and its history from the assembly until it was disassembled and scanned.

Loading Station and brick drum

For each side of the detector exists one loading station, shown in Figure 3.25. On this station a brick drum can be placed, hosting up to 243 bricks in nine rows. The brick drum can be quickly replaced to allow a continuous operation during the target filling and extraction of bricks with a possible ν-interaction. On the one hand the drum was needed to transport the bricks from the BAM in the neighboring underground hall B to the detector in hall C, on the other hand it reduces the mechanical stress on the brick, so that submicron resolution can be achieved. The drums are placed downstream the last HPT plane, so that the BMS carousel can access the full side (both SM's) of the detector.

The Carousel

This part of the BMS is the actual robot inserting and extracting the bricks. It has an intermediate storage for 26 bricks, corresponding to the amount of bricks needed to fill one half-row of the OPERA target. As shown in Figure 3.26 it pushes the bricks inside the detector, to extract them a small "sucker"-vehicle can drive inside the target rows to catch the bricks.
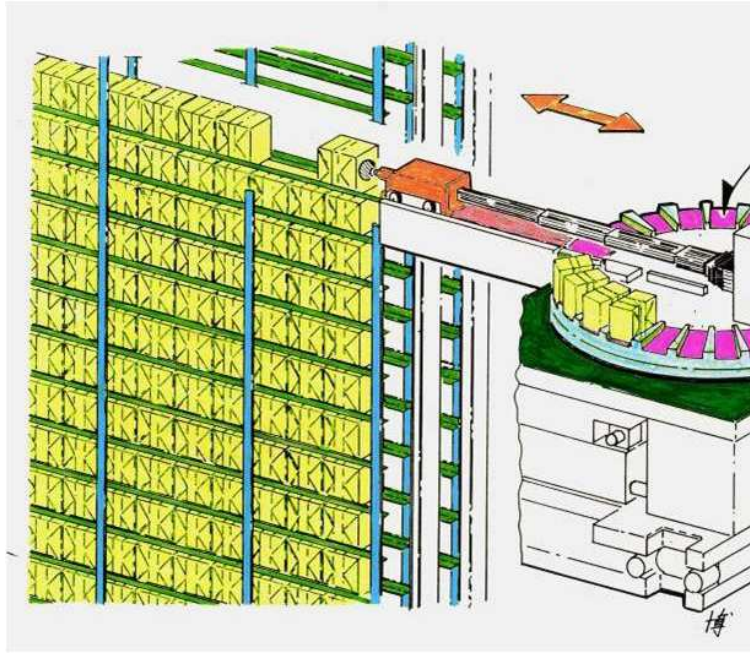
Figure 3.26: *Schematic view of the BMS carousel. Picture from [207]*

X-ray marking

The X-Ray marking of the ECC is needed to align the CS to the first emulsion of the brick, and also used to define the order of the emulsion films and to give a first reference frame for the scanning. The X-ray machine is tuned to print four calibration marks in the corner of the CS and the first emulsion plate, before the X-rays are absorbed by the first lead plate, as indicated in Figure 3.27. This alignment, summarized in [238, 237] allows already a resolution of a few microns between the CS and the ECC plates, see Figure 3.28 for a view of the X-ray spot. Other optical and X-ray marks are printed on the brick to allow an ordering of the emulsion films, and a first coarse alignment of a about five microns from ECC plate to ECC plate in case when the cosmic ray exposure of the ECC is not done, e.g. for so-called black CS cases, where due to failure of CS development or a too high fog level the CS cannot be analyzed.
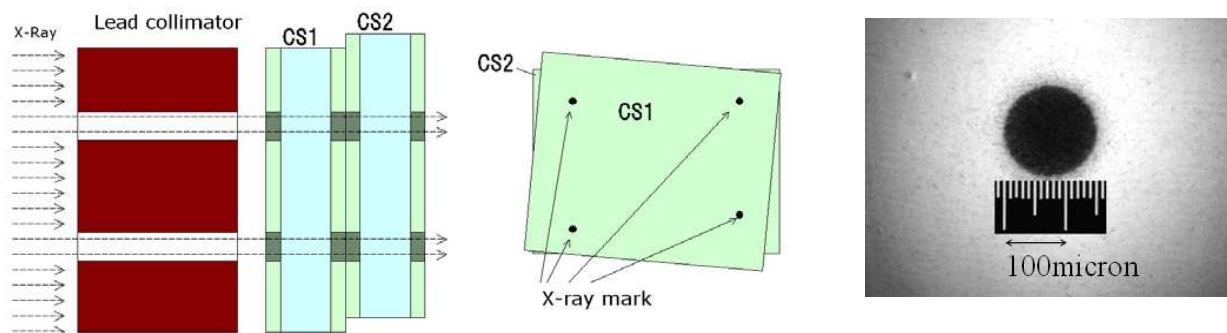
Figure 3.27: *X-ray marking of the OPERA ECC and layout of the four X-ray spots. Picture from [207].*

Figure 3.28: *Photograph of one X-ray spot. Picture from [207].*

3.3.2   The Brick Assembling Machine (BAM) and CS facility
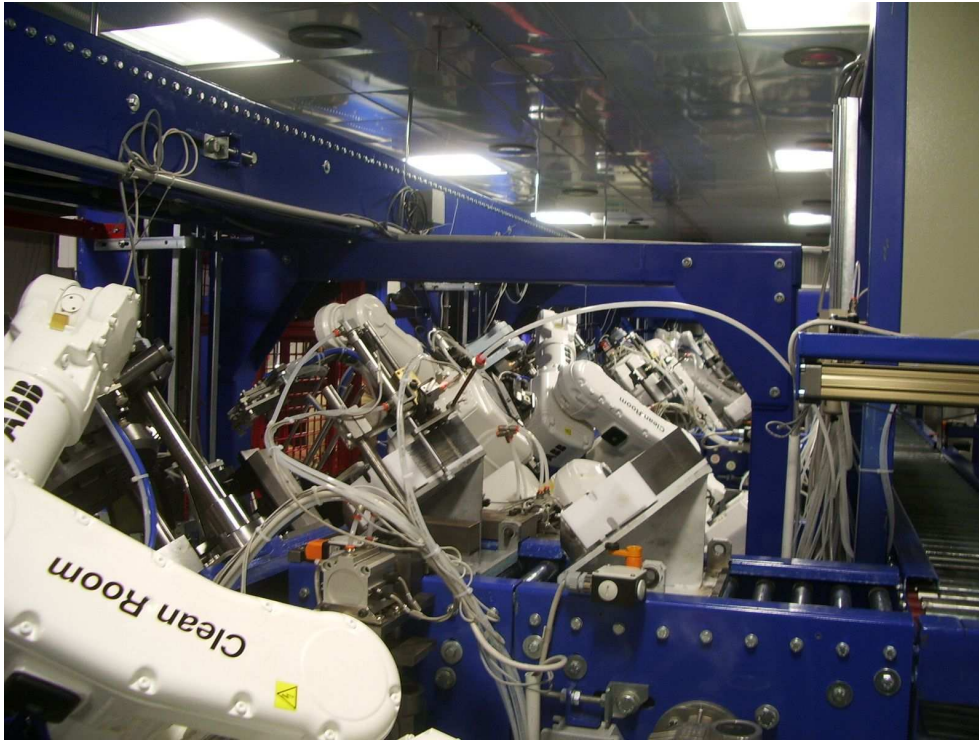
Figure 3.29: *The BAM assembling line.*

The assembling of the more than 150'000 OPERA bricks was done with a dedicated assembly line in the Gran Sasso underground laboratory. The Brick Assembling Machine (BAM) was situated in a connection tunnel between underground hall A and B. It was setup to be a clean room environment with humidity and temperature control. Running over a period of nearly two years, it had a production rate of up to 1000 ECC per day. Additionally to the BAM also a CS facility barrack was set up (see Figure 3.30); it was needed to refresh the emulsion needed for the CS and their packaging and is now used as CS development laboratory.

The Brick Assembling Machine (BAM)

The Brick Assembling Machine (BAM) was the production line for the OPERA ECC, developed by Techno Cut[3]. It was consisting of five piling stations, shown in Figure 3.29 and one wrapping station and was situated underground. The design speed of a piling station was 250 bricks per day, while the wrapping station could handle more than 1200 bricks per day. The lead used for the piling of the bricks was sent on time from the JL Goslar company in Germany, and stored intermediately in the hall B. The lead is transferred from outside of the dark room area by small plastic pallets, on which 56 lead plates for one ECC are stored. Two ABB robots[4] were serving a piling station, one for the lead plates and one for the emulsion films. After the piling the ECC was closed with

---

[3]Tecno-Cut Srl, via L. Ariosto 116, 20099, Sesto San Giovanni (Milano), Italy

[4]ABB Sadelmi S.p.A., P.le Lodi 3, Milan, Italy

an aluminum clamp at a pressure of 3 bar, to hold the brick together. While the piling station robots were only able to move in two axes, the robot of the wrapping station was able to move in three dimensions. In the wrapping station the piled brick was sealed light-tight with aluminum foils, and sent outside the dark room, where the CS box was attached. Afterwards the bricks dimension were measured and if they were within the fabrication tolerance it was loaded into a brick drum and sent to the BMS loading station.

The CS facility

The CS facility consists of a two story barrack, in the upper part a dark room was built to refresh and pack emulsion films for the CS. As indicated in Figure 3.30, two refreshing cabinets and a packing table are located inside the dark room area, while in the light area the final packing step was done, when the envelope containing two emulsion sheets was put in the white plastic cover, that later can be attached to the brick by the BAM. Further references to the CS facility can be found in [238, 207]. About 300'000 emulsion films were refreshed and produced in the CS facility, additionally 60'000 were needed to replace CS which had a high fog level (black CS), found after the first year of running; the high fog was due to the previous evacuation of the CS envelopes at the startup of the packing operations.
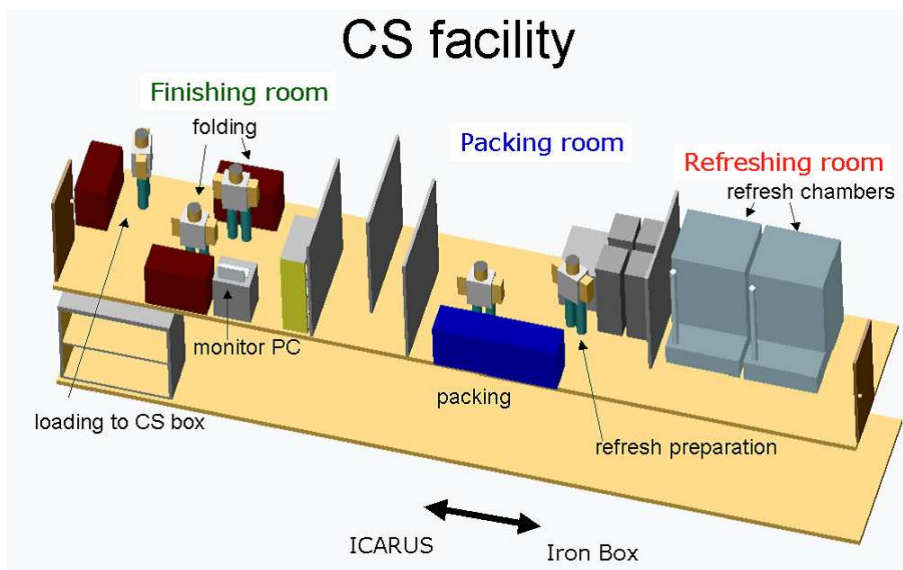
Figure 3.30: *The CS facility barrack. Picture from [207]*

3.3.3   Development Laboratories

In the OPERA run about 20 ν-interactions are recorded each day. An agreement between Europe and Japan regulates the sharing of the emulsions, half of the events are analyzed in Japan, the other half in Europe. The run goes on for the full 7-day week during 7 months per year, but, except for the supervision of the detector, the development of emulsion films is done only during the usual working weekdays, thus the requirement for the CS and ECC emulsion development was to process about 3'900 emulsion films per day, with

a development process that takes about three hours to follow the many step procedure summarized in table 3.2. The development of the OPERA ECC emulsion requires not only a system which can process high numbers, it needs also good development quality and stability, which is described in section 3.3.3 [239]. The external brick processing consists not only of the development of the emulsion, but also a cosmic ray exposure and the dismantling of the ECC, which is done in the OPERA building on surface. This building was built specially for the OPERA experiment and provides a cosmic ray pit, in which the cosmic ray exposure takes place, a large dark room area for the emulsion development facility and office rooms. About 20-25 people are working continuously for the OPERA experiment over the year on site, either in handling the BMS or the work at the development or the CS scanning station. During the CNGS beam period only one additional shifter and the run coordinator is required to monitor the electronic detector.

CS development laboratory

The underground area is situated above a drinking water reservoir, so that the amount of dangerous liquids brought underground has to be minimized as much as possible. Since an exposure to cosmic rays is needed for the brick scanning, only the development of the CS emulsions is done underground in the CS barrack, where about 65 CS films can be treated per day for development. The CS development is placed in the lower level of the CS barrack in hall B, as shown in Figure 3.30.

Figure 3.31: *The brick development laboratory.*

The ECC development laboratory

In the OPERA building on the outside area of the LNGS a large development laboratory was set up to handle the high number of bricks that needed to be developed. With a

rate of about 20-30 events located per day during the runtime, it was designed to process more than 25 ECC bricks per day. After the bricks are exposed to cosmic rays, they are disassembled in darkness and processed in one of the six development chains, shown in Figure 3.31, at a constant temperature of $20°$ C [239]. The latent image left by charged particles in the emulsion is fixed by a chemical development, reducing the ionized silver atoms to metallic Ag. The full procedure is shown in Table 3.2. After washing out the undeveloped crystals and fixing the developed image, the path of the ionized particle is visible as a sequence of black grains in the emulsion (as seen in Figure 3.20). After half a day of drying, the emulsions are available for scanning and shipped to the scanning laboratories.

Step/ Bath	Time	**Chemical** Composition
Presoak	10'	Na Sulphate (70 g/l)
Development	25'	Developer + starter (by Fuji-Film Co.)
Stop	10'	Al Sulphate - n H_2O (8.5 g/l)
		Acetic Acid (5 ml/l)
Fixation	35'	Na Hyposulphite (300 g/l)
		Na Sulphite (12 g/l)
		Acetic Acid (9 ml/l)
		Al-K Sulphate (5 g/l)
Washing	4×20'	demineralized Water
Alcohol	20'	Ethyl Alcohol (600 ml/l)
		Glycerine (200 ml/l)
Dry well	1"	*Drywell* (5 ml/l) by Fuji-Film Co.

Table 3.2: *The full development procedure for the OPERA emulsion sheets. Table from [233].*

The Cosmic Ray Pit

In the basement of the OPERA building on the outside LNGS campus is the Cosmic Ray Pit. The bricks are stored here for about 8 to 12 hours to accumulate high energetic (straight) cosmic ray tracks, which is needed for the emulsion plate to plate alignment with a precision of a few μm. Above the cellar room a shaft with a 40 cm thick iron shielding was put to filter low energetic cosmic ray electrons, to shield the ECC from ambient radioactivity they are stored in lead containers.

3.4 The scanning systems

The emulsion scanning in the OPERA experiment is shared equally between Europe and Japan. As the scan area required to locate the ν-interaction in the OPERA experiment is large with respect to previous experiments, as shown in Figure 3.32, new scanning systems for high speed automatization were developed, both in Japan and in Europe.

To increase the image acquisition rate, two different design ideas were followed, in Japan the speed of the existing system was increased (S-UTS) [240, 241, 207], while in

Europe a large number of high-speed microscopes with standard components (ESS) was preferred. Here only the hardware of the European scanning system is described, for details on the image processing see section 4.2, the Japanese scanning system is described in appendix C.

125mm x 100mm OPERA CS scan for events without Muon

50mm x 50mm OPERA CS scan for events with Muon

5mm x 5mm Donut General Scan

1mm x 1mm CHORUS Point Scan
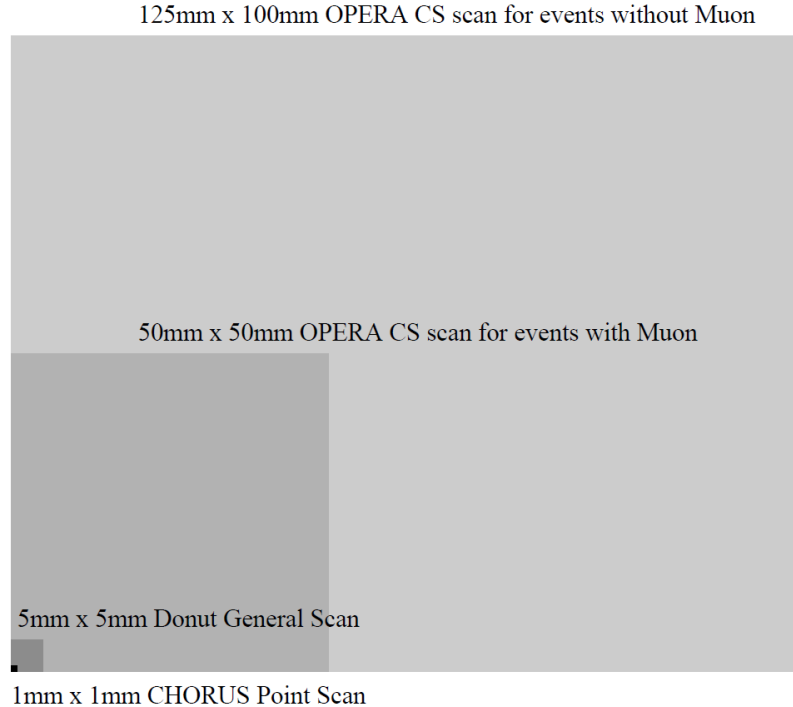
Figure 3.32: *Scan area required in OPERA CS for muon and muon-less events with respect to the previous CHORUS and DONUT experiments. Picture from [207].*

To confirm the result of the brick finding of the electronic detector, the CS is detached from the predicted brick and developed underground and scanned, the ECC is taken outside the underground area only in case of a CS confirmation. With the CS scanning the μ-angle of a CC interaction can be reconstructed with an error of a few tens of mrad, constraining the track candidate predictions from the CS for the Scanback procedure of the ECC [238]. The European CS Scanning is performed at LNGS in a dedicated scanning laboratory, shown in Figure 3.34, while the Japanese bricks are scanned in Nagoya.

3.4.1 The European Scanning System (ESS)

The design goal of the European laboratories was to develop an automatic microscope stage with a scanning speed of $20 \, \text{cm}^2/\text{hour}$, shown in Figure 3.33, and described in detail in [233, 242, 243, 244]. To achieve the scanning speed required by the OPERA experiment, multiple microscopes are used. The main design idea is the software-based approach for data processing. Thus, new algorithms can be easily tested and by the integration of commercially available components to build the microscope, upgrades due to technological improvements are possible.

The ESS microscope is shown in Figure 3.33, it consists of a mechanical stage from the
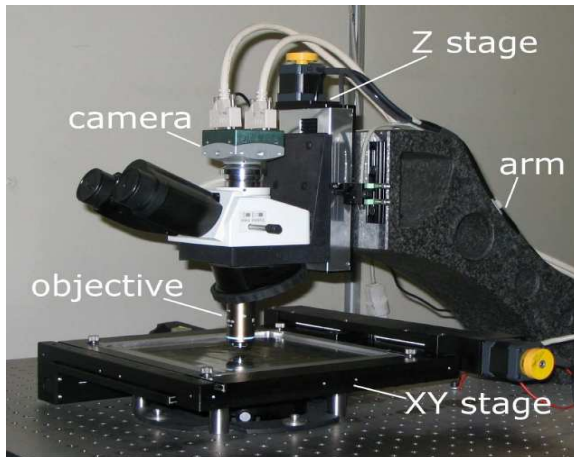
Figure 3.33: *ESS Microscope setup. Picture from [244].*

Figure 3.34: *CS scanning laboratory at Gran Sasso.*

MICOS company[5], equipped with nano-step motors VEXTA[6] (5-phase). Optical encoders with a resolution of $0.1\,\mu$m allow the positioning of the stage by a National Instruments[7] motor-controller (PCI-7344) via the PCI bus. The stage has a working range of $20\,$cm for the X- and Y-axis and $5\,$cm on the vertical Z-axis. The XY movement is about $125\,$ms per $300\,\mu$m-step, needed to go from one view to the next, including the relaxation time of the stage. The position reproducibility is $0.3\,\mu$m.
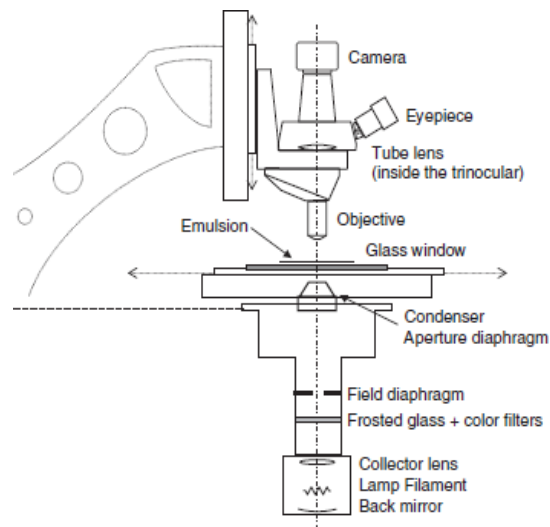
Figure 3.35: *Schematic layout of the ESS microscope optical system. Picture from [243].*

The optical system, shown in Figure 3.35, consists of standard microscope components from NIKON-Italia[8]. The illumination is done with a lamp and the condenser (WD 4.2 mm, NA 0.85), mounted from below the microscope table, the rest of the optical system is mounted via a granite arm and moveable in the Z-axis. Mounted to the Z-stage are a

---

[5]http://www.micos.ws/
[6]http://www.orientalmotor.it/
[7]http://www.ni.com/
[8]http://www.nikon.it/

trinocular tube and the $50\times$ NIKON CFI Plan achromat oil immersion objective (WD 0.4 mm, NA 0.9), producing achromatic planar images through the whole thickness of the emulsion. In case of the Berne dry-scanning the $50\times$ NIKON CFI Plan Apo (WD 0,14 mm, NA 0.95) is used [245]. The images are taken in 18 views along the Z axis of each emulsion layer, with a continuous movement along Z and a high shutter speed. The depth of field in one view is approx. 3μm. The first and last image are not taken into account further, thus, 16 images are used for reconstruction. These "tomographic" images are captured with a CMOS camera, the Mikrotron MC1310[9] with a maximum frame-rate of 376 frames per second. The resolution of the camera is 1280×1024 pixels, and the ixel size is such, that one view covers an area of $390 \times 310 \,\mu m^2$.

Everyday about 30 single CS emulsion sheets are scanned at the Gran Sasso Scanning laboratory, equipped with 12 microscopes, shown in Figure 3.34. About five to ten neutrino interactions are located per week in the Berne scanning laboratory with five microscopes. While in the Gran Sasso scanning station only 2 emulsion films per brick are scanned, in the various scanning laboratories around Europe up to 57 emulsion films per brick have to be scanned. To automatize the changing of emulsion plates, two plate-changing robots were developed, one dry scanning robot in Bern [219], shown in Figure 3.36 and an oil scanning robot in Italy, shown in Figure 3.37.

Figure 3.36: *Berne dry plate changer. Picture from LHEP Bern.*

Figure 3.37: *Oil emulsion plate changer, here the prototype at LNGS.*

---

[9]http://www.mikrotron.de/

Chapter 4

OPERA Data Acquisition and Analysis Framework

In this chapter I will present the analysis and data acquisition software of the OPERA experiment, as well as the Monte Carlo framework. The data taking is done in two steps, the first step is the online data acquisition with the electronic detector at the time of the neutrino interaction (see section 4.1), the other step is the scanning of the emulsion films in the various scanning laboratories some months later (see section 4.2). The OPERA experiment uses a hybrid detector, combining the electronic detector with its Linux DAQ environment and the scanning software, based on Windows XP for the European Scanning System (ESS) and MS-DOS for the Japanese S-UTS. Additionally, the software in the OPERA experiment varies not only in the operating system, but also on the requirements for additional software versions and system architecture. The first Monte Carlo (MC) software parts of the OPERA experiment (see section 4.3) were written more than 10 years ago, using the CERN ROOT[1] version 4.00 and the "gcc" compiler in version 3.2 (see section 4.3.3) on a 32bit architecture, while the newest analysis software OpRelease is using CERN ROOT 5.21 and is installed on a 64bit cluster at the Lyon computing center (see section 4.3.2). So far the analysis of the electronic detector and the emulsion bricks is done separately, and the results are combined afterwards, but in the future a combined MC simulation and analysis framework for both detector parts will become available (see section 4.3.4).

4.1 Data acquisition with the electronic detector

The key part of the on-line data taking in the OPERA experiment is the electronic detector. Without this, the high target mass required by OPERA for an observation of $\nu_\mu \rightarrow \nu_\tau$ oscillation would not be possible. The detector is described in chapter 3.1, here the focus is on the data acquisition, the idea of the data-readout via the ethernet using the timing from a global network clock, and how the trigger for an event is issued. Afterwards I will explain the brick finding inside the detector.

---

[1]http://root.cern.ch/root

4.1.1   Ethernet based DAQ

Most of the tracks occurring in the OPERA detector are related to cosmic muons, only when protons of the CNGS beamline are hitting the target, neutrinos are produced and sent to Gran Sasso, as described in Chapter 2. To sample these events, a time stamping of the events with a synchronization of 10 ns between the detector components is required [210, 246]. In total only about 20'000 ν-interactions are expected inside the OPERA target after five years of running, thus, most events triggered are either cosmic muons or background events, mainly due to electronic noise and the photo-multipliers dark current with a trigger rate of 10 Hz. Due to the low rate an Ethernet read-out of the frontend detector electronics was installed. The neutrino interactions are well localized in time in correlation with the CNGS beam spill. This time-stamp is created by using the common time reference with respect to the Universal Time Coordinated (UTC). A Global Positioning System (GPS), both at CERN and at LNGS is used to allow the creation of this time-stamp and to establish the correlation. Thus, one assures that the detector is sensitive during the spill time, when the DAQ system runs continuously in a triggerless mode. Shown in Figure 4.1 is the time structure of the OPERA events (see also Chapter 2).
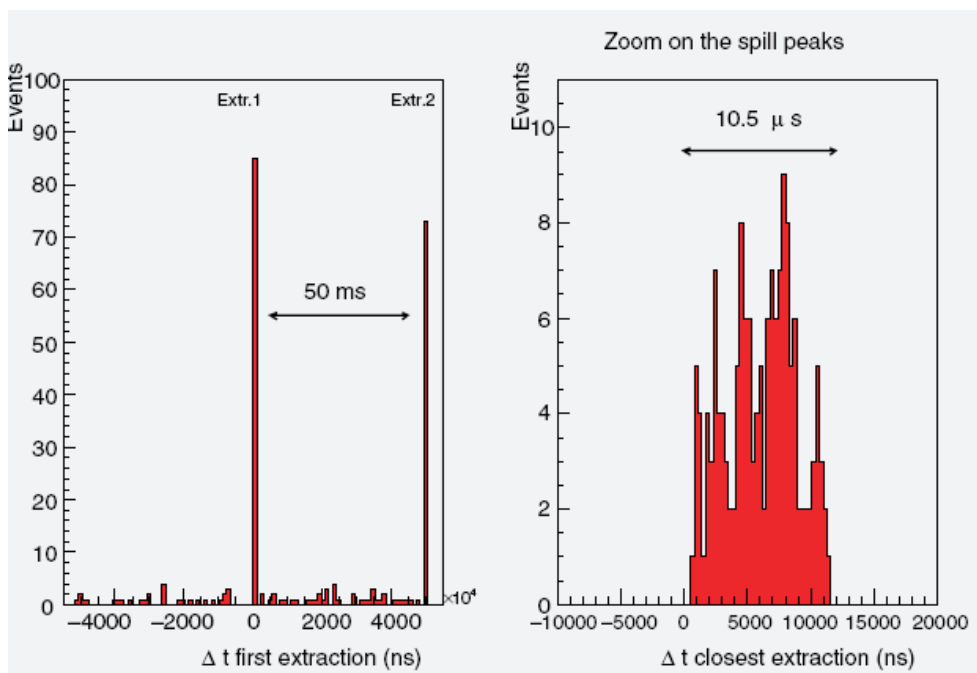
Figure 4.1: *CNGS beam time structure seen in OPERA. Picture from [247].*

The global DAQ is built like a standard Ethernet network, shown in Figure 4.2. The client nodes are the Ethernet Controller Mezzanines (ECM) plugged on Controller Boards (CB), each operating autonomously and possessing its own Internet Protocol (IP) address [247]. This CB is designed to interface and control each sub-detectors specific frontend electronics, and to sort the data to the "Event-Building-Work-Station" (EBWS), consisting of commercial PC's. Additionally, the CB boards are handling and monitoring the slow control, managed by the "Global-Manager".
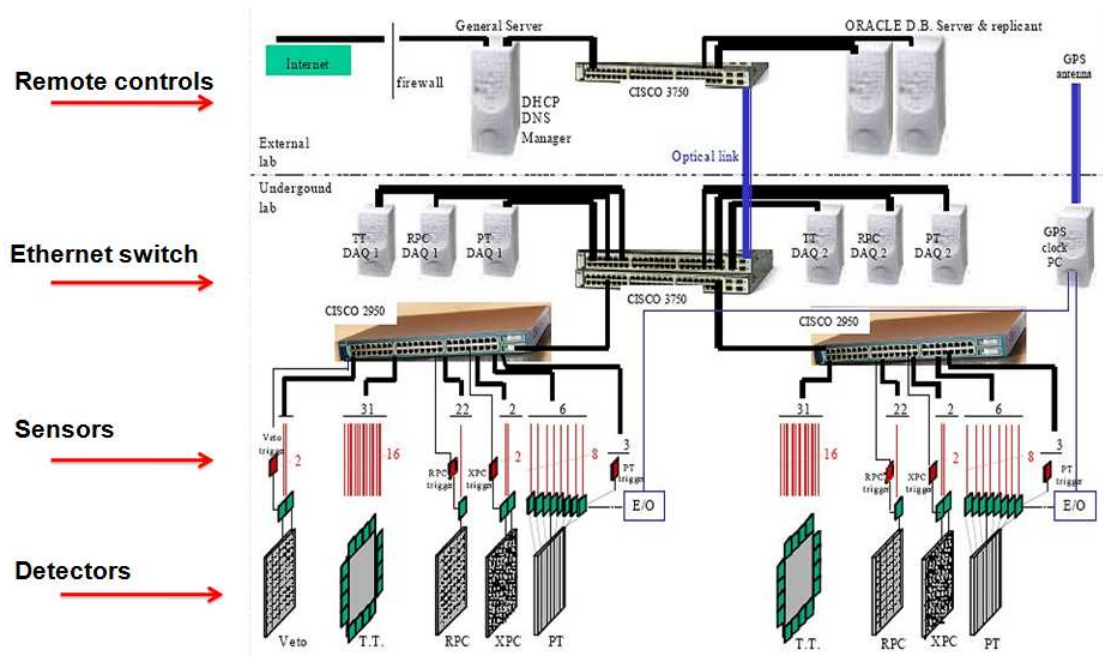
Figure 4.2: *Scheme of the OPERA data acquisition system. Picture from [248].*

The Target Tracker frontend readout of the data, acquired by the Hamamatsu m-PMT's is done via multi-channel chips, where analog signals are digitized and pre-processed on a custom motherboard developed at Lyon. The self-triggering chips allow the compensation of the pixel-to-pixel gain spread of the multi-anode PMT. The readout frontend of the muon spectrometer 3.1.2 is located on the top of the experiment. It consists of VME-like boards collected in VME crates and power supply stations. The distributed client/server software is based on the CORBA (Common Object Request Broker Architecture), offering a global framework linking the applications running on the sensors, on the EBWS and on the Manager. The data storage is performed by a database cluster (Oracle 11.1 RAC) on two dedicated servers. The global DAQ network is divided into two parts; the Ethernet network from the EBWS to each Ethernet Controller used for data transfer and sub-detector configuration, monitoring & slow control, and the clock distribution system from the Central Clock Unit, synchronizing the GPS signal with each sensor.

An Oracle Database is used in the OPERA experiment to store all information of the experiment, not only the full brick history from manufacturing till disassembling, but also the run conditions and the results of the emulsion scanning. The size of the database will be incrementally increased over the years to cope with the increasing data, reaching about 100 TB finally. The physical storage of the database is at the computing center in Lyon (OpFra), a backup mirror is placed at the LNGS (OpIta). In the various scanning labs in Europe, small database clients store the data of each scanning labs emulsions, thus the risk of data losses are minimized.

4.1.2 The Trigger

The triggering in the OPERA experiment consists of two main parts, the TT and the muon spectrometer trigger. While in the periods of no CNGS beam only the TT will be

used to record cosmic ray events, during the run cosmic tracks will be recorded with the full electronic detector, i.e. the TT and the spectrometer. The trigger for data taking depends on the run-condition: during the CNGS beam spill the detector runs in a so-called triggerless mode, i.e. all sensor data are taken without stop until the CNGS spill finished, i.e. no detector dead time due to electronic read-out occurs.

The TT trigger

The TT is controlled by small frontend electronics boards, housing a 64 channel Hamamatsu PMT. The PMT counting rate is defined by the intrinsic noise of the PMT (photocathode thermo-emission), typically at a rate of 15 Hz (discriminator level 1/10 photo-electrons) [248]. A common threshold, set on the frontend chip, takes the OR of the 32 channels per TT wall (X and Y coordinate) to provide a trigger output signal whenever at least one channel is over threshold. To reduce the noise (PMT, radioactivity, electronic noise, external electronic noise induced by the brick extracting system) a X-Y correlation of the TT plane is done, and the readout of the TT includes every X-Y correlation found in any wall. The time correlation window of the coincidence has to be large enough to take into account the 30 m cable length (150 ns) and the delay added by the transit time in the frontend buffers (50 ns).
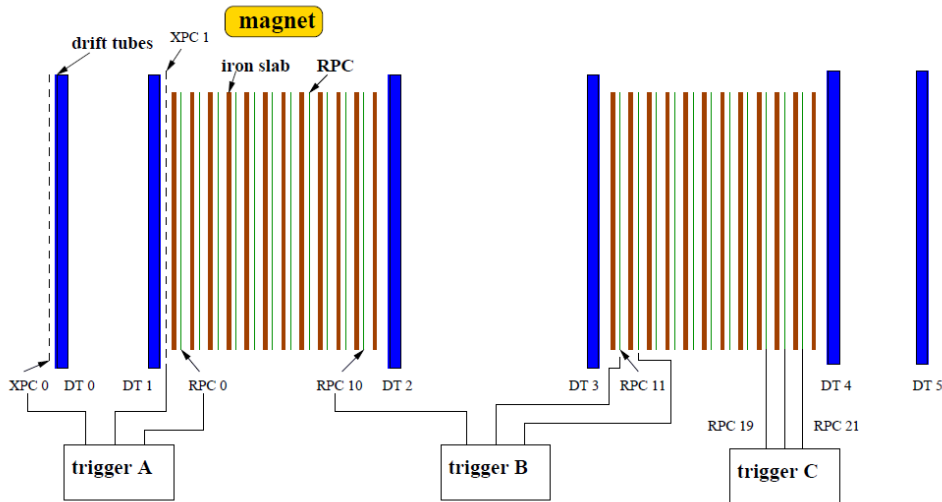
Figure 4.3: *The spectrometer trigger scheme for one supermodule. Picture from [210].*

The Muon spectrometer trigger

The frontend electronics of each RPC plane is divided into nine boards, readout serially by one Controller Board, receiving the TT trigger signals (defined by the fast OR of 32 channels). The HPT is readout by a TDC board, the trigger signal is generated by the RPC-/XPC layers via 3 trigger stations, consisting of three planes each (see Figure 4.3). A trigger to readout the data is given when two out of three stations observed a signal. The trigger rate is about 1.2 Hz, reducing the dead-time of the tubes practically to zero. The trigger scheme of the spectrometer is shown in Figure 4.3, and is described in further detail in [249].

4.1.3 The Brick Finding

The Brick Finding is a combination between the electronic detector and the ECC. Only, when the neutrino interaction left enough visible energy in the electronic detector, the event can be reconstructed; Charged Current (CC) events, classified by a muon in the spectrometer, will be correctly reconstructed when the μ-energy is at least about $1\,\mathrm{GeV}$, (range $>660\,\mathrm{g/cm^2}$). Lower energy muons will not be identified as CC, but as neutral current (NC) events [250].
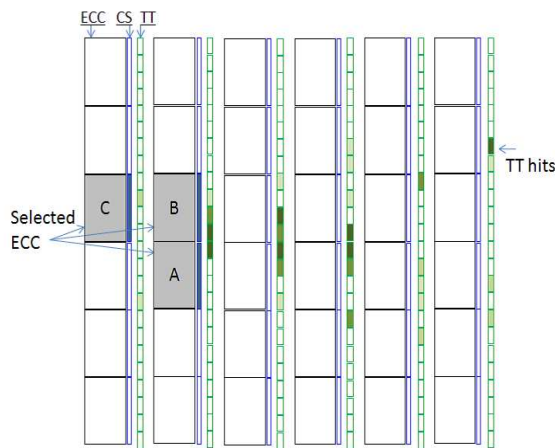
Figure 4.4: *Event Display for a simulated MC event in the detector. The bricks A,B and C are selected candidates from the Brick Finding, wherein brick C is less likely (backscattering). Picture from [207].*
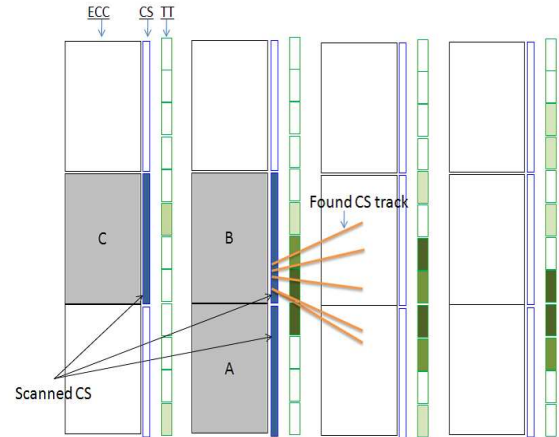
Figure 4.5: *After the bricks are extracted, the CS scanning result is superimposed to a zoom of the TT display. Clearly brick B is the brick containing the event and thus developed. Picture from [207].*

The ECC finding procedure is based on the track reconstruction of the electronic detector; the track is fitted by a linear and by a Kalman filter to detect the most probable brick. The hits inside the target tracker are filtered, to increase the efficiency and to avoid cross talk of the PMT's channels, spoiling the resolution. This reduces in CC interactions the mismatch of the track reconstruction due to the hadronic shower or backscattering, as indicated in Figure 4.4. The most probable bricks are extracted with the BMS and their CS is sent to the CS scanning. Then, the CS tracks are superimposed with the electronic detector reconstruction and checked with the database of cosmic events to confirm, if the result is positively identifying the ECC of the ν-interaction, as shown in Figure 4.5.

4.1.4 OPERA electronic detector results

The OPERA experiment is running since 2007 [251], and since 2008 with a filled target [252, 253, 254]. Apart from the neutrino interactions observed inside the ECC during the scanning of the emulsion films, it produced already other results: a measurement of the cosmic muon charge ratio [255] and several performance tests of the electronic detector. [256, 257, 238, 258].

Muon charge ratio of the CNGS ν interactions

The first comparison of electronic detector muon data of the year 2008/09 with MC simulations was presented in [250] and is shown in Figure 4.6. The result on the muon range in the detector showed a good agreement between the MC simulation and the electronic detector data.
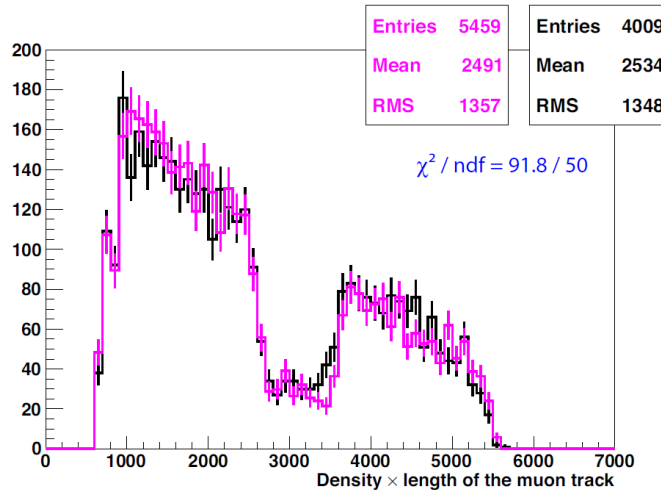
Figure 4.6: *Length times density for 3D muon tracks in $g \times cm^2$ for MC (pink) and data (black) normalized to the number of real events. Picture from [250].*
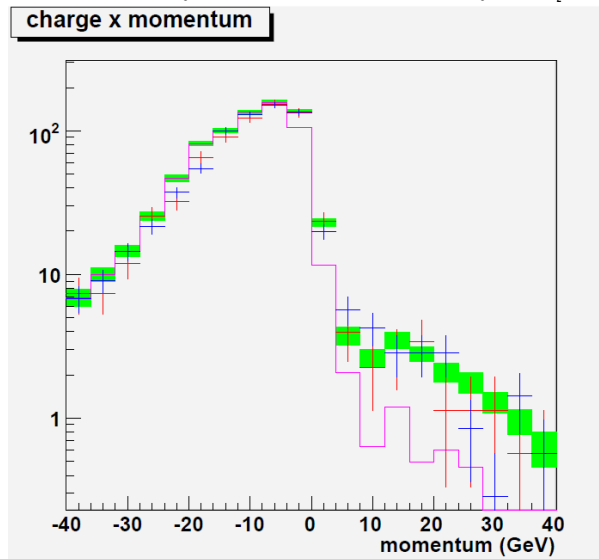
Figure 4.7: *Signed momentum distribution of the three dimensional tracks identified as muons recorded in 2008 and 2009, red and blue crosses, respectively. The statistical uncertainty is shown by the vertical error bars and the number of events has been scaled to 10^{19} p.o.t. The green boxes show the corresponding MC prediction which includes both ν_μ and $\overline{\nu}_\mu$ CC interactions. The CC ν_μ component alone is shown by the pink histogram. Picture from [258].*

The muon charge ratio from the CC-interactions for the data of 2008 and 2009 was studied in [258], shown in Figure 4.7 and calculated to be in agreement with the expec-

tations (in the ranges [8,40] and [-40,-8] GeV, respectively):

$$\mu^+/\mu^- (run - 08) = 3.6 \pm 1.0 (stat.)\% \tag{4.1}$$

$$\mu^+/\mu^- (run - 09) = 4.2 \pm 1.1 (stat.)\% \tag{4.2}$$

Cosmic muon map
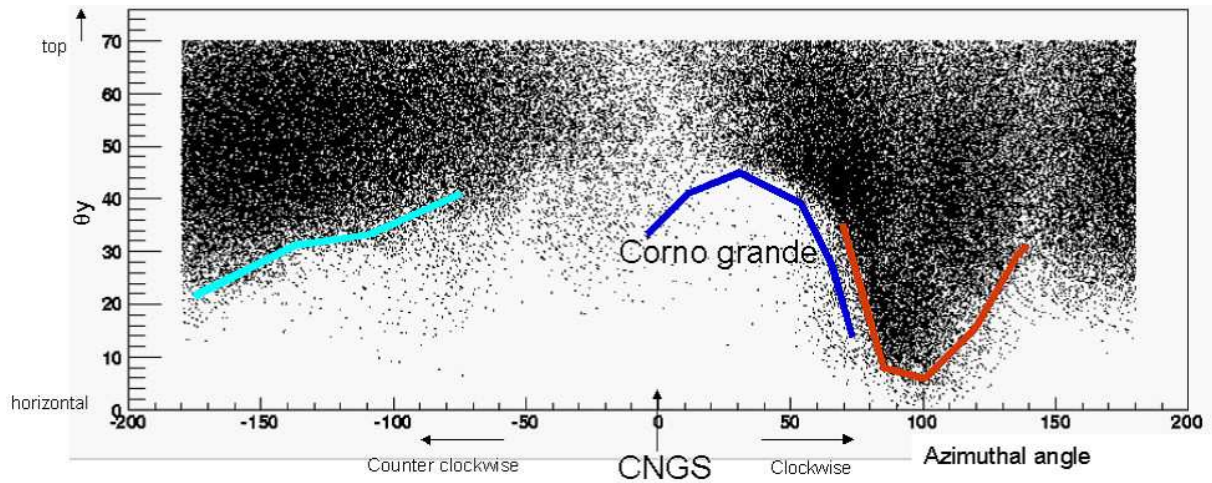
Figure 4.8: *Angular distribution of cosmic muons in the OPERA detector. Picture from [207].*

Figure 4.9: *Interpretation of the cosmic angular distribution with respect to the rock surrounding the detector. Picture from [207].*

Apart from the neutrino interactions, the OPERA spectrometer was able to measure cosmic muons, their angular distribution is shown in Figure 4.8. Using the geological

shapes of the Gran Sasso massif, one is able to reproduce the mountain shapes from the angular distribution, as shown in Figure 4.9.

Cosmic muon charge ratio

The Bologna group produced an analysis of charged cosmic muon tracks observed in the OPERA detector during a four month run period in 2008 [255]. Their result, shown in Figures 4.10, agrees with previous measurements and is given as:

$$R_\mu^{unf}(n_\nu = 1) = 1.377 \pm 0.014(stat.)^{+0.017}_{-0.015}(syst.) \tag{4.3}$$
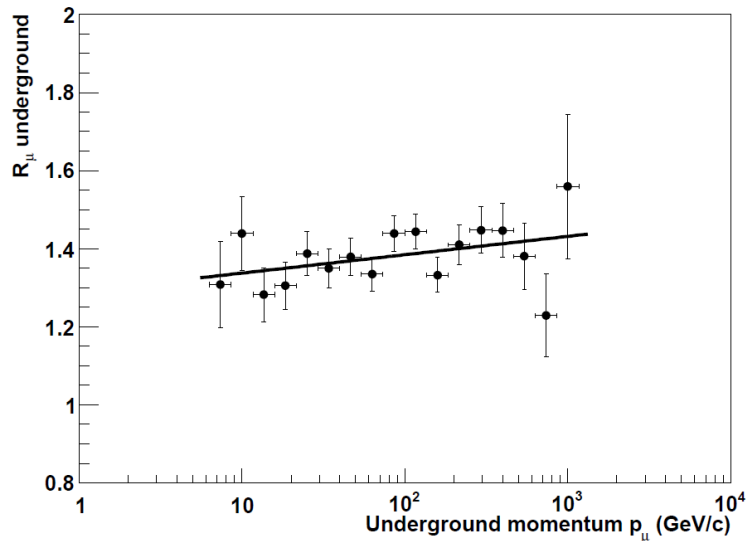
Figure 4.10: *Measured charge ratio of underground muons as a function of the reconstructed muon momentum. Picture from [255].*

4.2   Processing of tomographic emulsion images

The data acquisition of the emulsion is divided into many steps, the first is the online processing of tomographic images acquired from the emulsion films into grains and clusters. Afterwards the grains and clusters, left by charged particles in the emulsion, are converted into reconstructed tracks, microtracks for each emulsion layer and basetracks connecting two microtracks, in an nearly online computation. The two images processing software packages are:

- The Japanese Scanning System S-UTS (MS-DOS, see appendix C)
- The European Scanning System SySal [259] (Windows XP, see section 4.2.1)

After the reconstruction of the microtracks and basetrack, other software packages are used to do an offline reconstruction, first to align the emulsion plates, and then to reconstruct the tracks and vertices. The software for these steps will be explained later in section 4.2.2. In section 4.2.3 the various scanning procedures are described, first results of the scanning are presented in section 4.2.4.

4.2.1 ESS image processing

The European ESS acquires the emulsion images with a CMOS camera at a rate of about 370 frames per second, corresponding to 470 MB/s. The images are grabbed and processed using the Matrox[2] Odyssey frame grabber/vision processor running on a double-core Windows XP PC. The scanning software used to reconstruct microtracks and basetracks from the acquired images is called SySal (Systema di Salerno) [242]. The software is programmed to asynchronous data taking, i.e. the parallel processing of several threads, that are synchronized at the end of each cycle:

- Thread A: Movement of the optical system along the Z-axis during the image acquisition; at the end resetting of the Z-axis position and moving the X-Y stage to the coordinates of the next field of view ($390 \times 310 \, \mu m^2$).

- Thread B: Acquiring of the tomographic images via the frame grabber.

- Thread C: Digitizing the acquired images, data storage in a temporary memory buffer.

- Thread D: Loading of the processed images of the previous field of view, reconstruction of clusters and track recognition.

The thread A is running the motor controllers, thread B and C are processed on the Matrox Odyssey board, while the thread D runs on the PC CPU, and can be split into

---

[2]http://www.matrox.com/
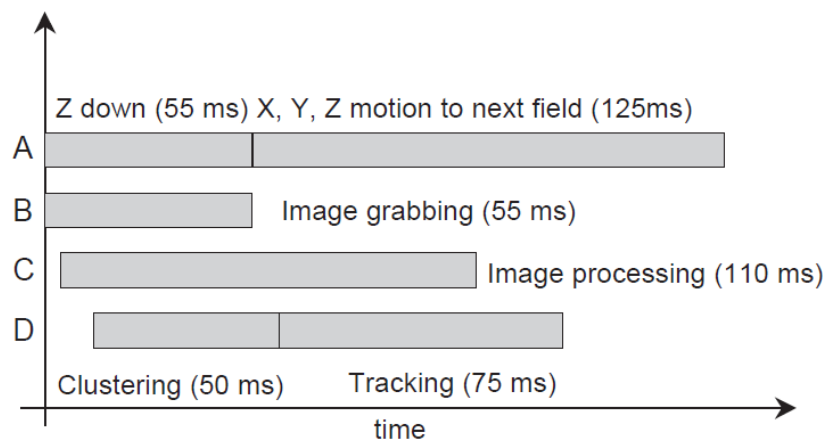
Figure 4.11: *Time diagram of a typical scanning data-taking cycle. The letters on the left indicate the threads that perform the various operations (see text). Images are processed as soon as they are taken, but image processing is slower than acquisition. Therefore, the cluster recognition and tracking of the images (thread D) that takes place is belonging to the acquisition of the previous field of view. The time actually needed for these two operations depends on the number of grains in the image, thus average values are shown. The time for X, Y, Z motion includes X-Y oscillation damping and Z-axis acceleration for constant speed motion during the image grabbing. Picture from [242].*

sub-threads to exploit the processing power of multi-processors. As only thread A and B are responsible for the image taking, they are the only ones to be synchronous (camera & stage), nevertheless, if C and D would be slower than the cycle, the data rate of 470 MB/s would saturate the memory quickly. Thus, the software can provide a feedback from the number of clusters as function of depth to adjust the Z-position during data taking within each of the $44\,\mu$m of emulsion layers. The time structure of the SySal cycle is shown in Figure 4.11, each cycle lasts about 180 ms, including the time needed to wait for the damping of the X-Y oscillation from the X-Y stage movement before the Z movement (in contrary to the S-UTS, where the Z-axis movement is synchronized with the stage).
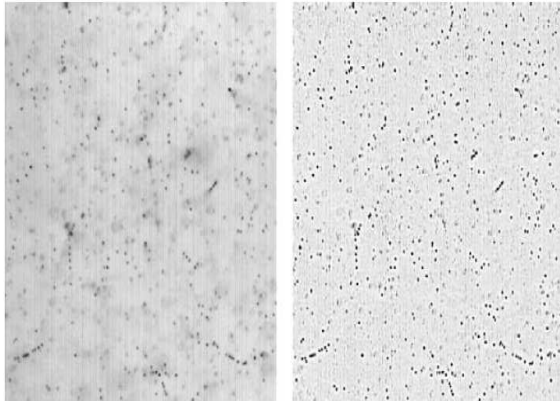
Figure 4.12: *A typical emulsion image (left) and effect of the FIR filter on it (right). For the sake of clarity, the image shown is a 512×512 excerpt from a field of view of 1280×1024 pixels. Picture from [242].*
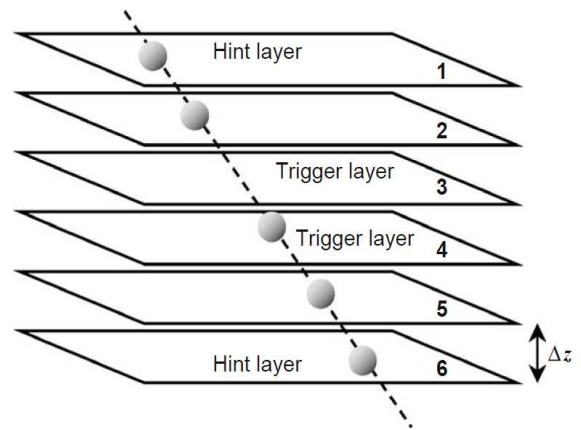
Figure 4.13: *A track hint consisting of two grains in levels 1 and 6 is shown; if the hint is confirmed in at least one of the internal trigger levels, the tracking procedure is applied to all levels. Picture from [242].*

As already mentioned, the tracking and reconstruction thread D can be parallelized for multiple processing machines. Thus, as the SySal framework is used for emulsion and track reconstruction at the CS scanning station for very large scanning areas at LNGS, the processing is done on several servers, the so-called ScanGrid. A "flat-field" image inside the plastic emulsion base is taken once and subtracted from each tomographic view, to equalize local pixel-defects of the camera and to account for the different AD conversion per CMOS pixel. To enlarge the dark grains on the otherwise "white" emulsion a Finite Impulse Response (FIR) filter is used [242], the effect is shown in Figure 4.12. Afterwards, the images are binaries and transferred from the Odyssey board into the PC memory, were an algorithm is executed to find the clusters. About 1000-2000 clusters are found per view, mostly due to random background. Via quality cuts on the shape and size their number can be reduced by 60%, before using them for the tracking.

A microtrack consists of a straight line, along which the clusters are placed in the different tomographic views. In the 100 ms used for the tracking, about 20'000 grains have to be checked. To avoid that every combination is used, thus increasing the time required tremendously, two checks are used for filtering good hints for a microtrack:

- Only physically interesting track slopes are accepted, with an angular acceptance of $\tan\theta < 1$ (with $\tan\theta_{x,y} = \frac{dx,dy}{dz} = TX, TY$; dx,dy - distance in X (Y) between top
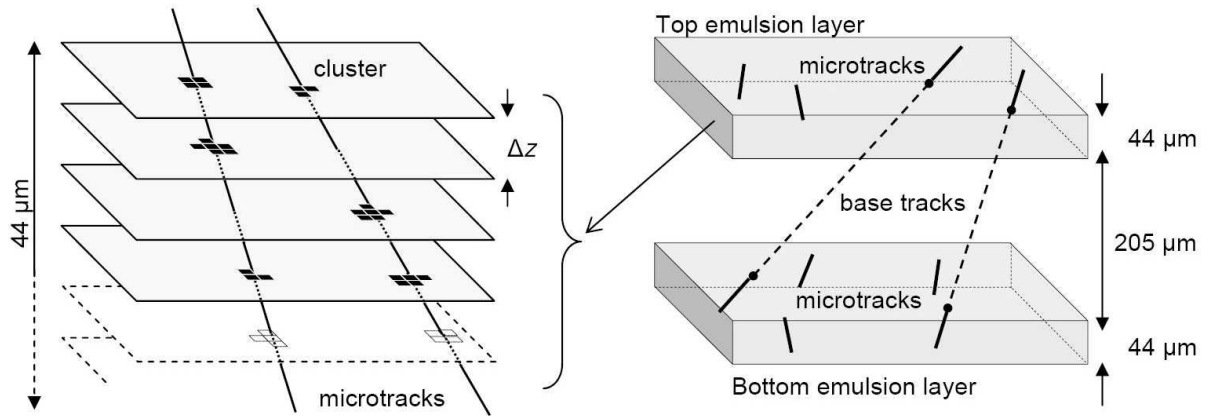
Figure 4.14: *(left) Microtrack reconstruction in one emulsion layer by combining clusters belonging to images at different levels; (right) Microtrack connections across the plastic base to form base tracks. Picture from [244, 243].*

and bottom X (Y) position of the MT in the emulsion layer, dz - thickness of the emulsion layer).

- The emulsion sensitivity for minimum ionizing particles (m.i.p.) is 31 grains/100 μm, thus the average number of grains per emulsion is 13. For each grain-pair internal trigger layers are defined, only when another grain is found in one of these layers, the microtrack search for this combination continues. The minimum number of grains for a microtrack is 6 (see Figure 4.13).

If after the microtrack search a grain belongs to more than one microtrack, only the one with the higher number of grains is kept. As shown in Figure 4.14 the final tracking step is the combination of microtracks to basetracks, where each microtrack's stopping Z
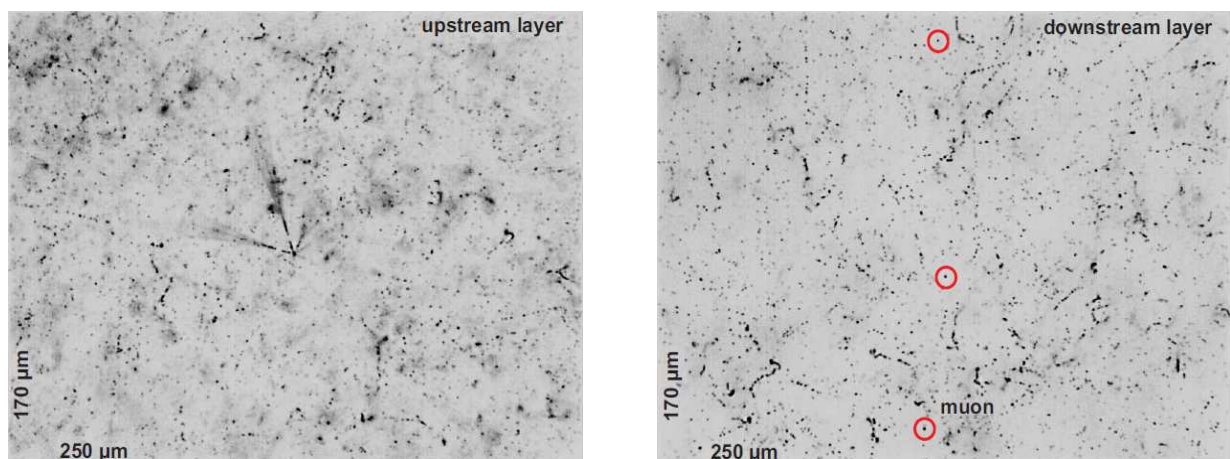
Figure 4.15: *Left: Picture of the ν-interaction vertex in the bottom emulsion, as seen by the microscope CMOS camera. The nuclear fragments produced in the interaction are visible. Right: Picture taken about 200 μm far from the interaction vertex in the opposite top emulsion layer. The minimum ionizing particles produced in the interaction are indicated by a circle. The muon track is also indicated. Picture from [253].*

position is extrapolated towards the corresponding Z level of the plastic support, and if two microtracks agree within certain position and slope tolerances, they are considered as correlated, i.e. a basetrack.

In Figure 4.15 shown is a ν_μ-interaction vertex, which occurred in the bottom layer of an emulsion, shown in the left panel. The spreading out of the three tracks is visible in the top emulsion layer in the right panel of the figure. The connections between the primary vertex and the segments in the top layer are the basetracks. Both microtracks and basetracks will be saved in the database later on, the grains and clusters, i.e. the raw data will not be stored, reducing the data storage need.

4.2.2   Emulsion Reconstruction Software - FEDRA

To reconstruct the particle tracks in the scanned emulsion films, first an alignment between the plates has to be done. Afterwards the tracks are reconstructed and a vertex finding algorithm is executed. Two analysis frameworks for these steps are used in Europe, the framework AlphaOmega, running under Windows XP and developed in Salerno and the framework FEDRA, running under Linux and developed in Naples. The *F*ramework for *E*mulsion *D*ata *R*econstruction and *A*nalysis (FEDRA) [260] is able to remotely execute and control the SySal environment, i.e. the ESS, thus the track reconstruction and alignment of emulsion plates can be done on an external powerful server, while the microscope can continue with the scanning without handing over processing power to the further reconstruction task. In this thesis only the FEDRA reconstruction framework was used. FEDRA is a package written in C++ with use of ROOT, it handles emulsion data reconstruction starting from the microtrack and/or basetrack level up to the vertices and event analysis. It includes many sub-libraries as the shower library developed in Neuchatel/Berne to identify electron or γ showers and reconstruct their energy (electron-pion separation), the multiple Coulomb scattering method for momentum reconstruction from the Annecy group, a graphical reconstruction interface for scanning laboratories called "Eda-Display" from Bern and was used as reconstruction interface of the Monte Carlo framework ORFEOv7.9 (see section 4.3.4).

4.2.3   Emulsion Scanning

Different scanning steps can be defined for the OPERA experiment, four automatic steps and the eye-check, two of them are illustrated in Figure 4.16:

- Changeable Sheet scanning: The first scanning step of the two CS emulsion layers attached to the brick, done in Nagoya or at Gran Sasso. A large area of several cm^2 is scanned to check for the predictions from the electronic detector.

- Scanback (SB) track scanning: To follow the tracks predicted in the CS upstream inside the ECC to find the neutrino vertex (done in the various scanning laboratories in Europe or in Japan). The Scanning area is small for the Point Scan, or prediction scan, when the X-Ray grid is used for alignment. For higher precision an area of about 1 cm^2 has to be scanned to allow an alignment with cosmic tracks.

- Total volume scanning: After the confirmation of the stopping point of the SB track, an area of $1\,cm^2$ of emulsion film is scanned for five plates up-, and ten plates downstream the stopping point.

- ScanForth track scanning: After the vertex was found, the tracks are followed downstream to search for possible hadronic re-interactions or decays and to measure the momentum with the multiple Coulomb scattering (MCS) method [261].

- Manual Check: Human eye inspection of the tracks, including stopping point confirmation and electron-pair checks.
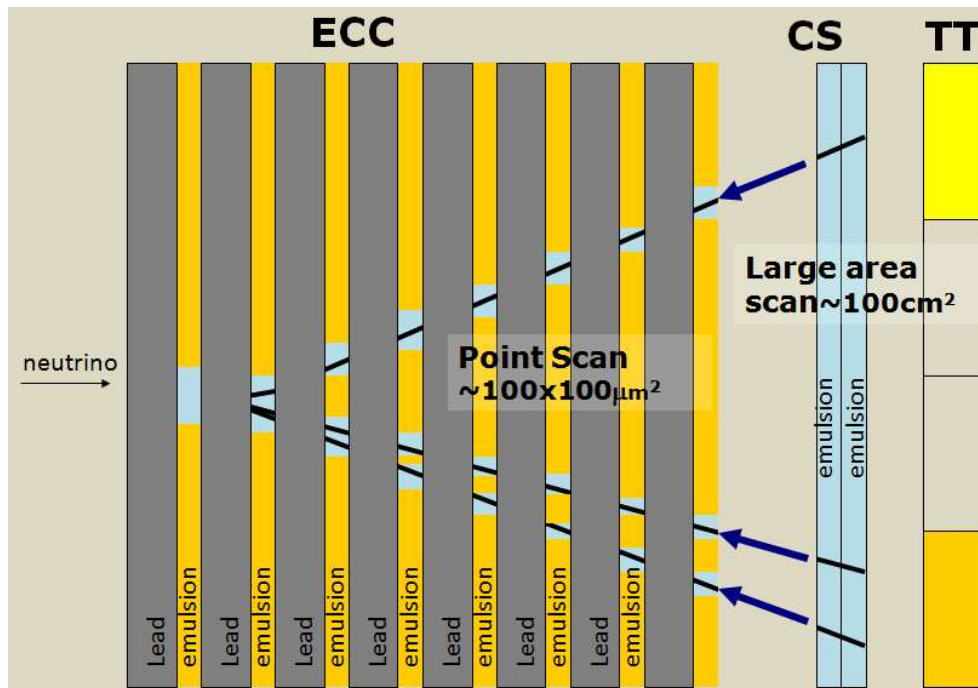
Figure 4.16: *Scanning Procedures overview in the OPERA experiment. Picture from [207].*

Even though the automatization of the emulsion scanning was developed, by introducing plate changing robots and new read-out and data acquisition systems, the human factor in emulsion scanning is undeniable important, i.e. the human eye checks. From eye-inspection the BT finding efficiency and background rejection due to fake microtracks is up to >99%.

Changeable Sheet Scanning

When a possible neutrino interaction is localized by the brick finding algorithm in one ECC, the brick is extracted and the X-ray marking is done. Afterwards the CS is detached and developed to be scanned, while the ECC will remain underground to await the CS scanning result. In the CS scanning, an area of $4 \times 6\,cm^2$ per emulsion is scanned around the muon prediction in case of CC interactions, for NC events a larger area is scanned, this scanning is the so-called general scan. Inside the scanning area of $24\,cm^2$ only a few tracks related to the event are expected, and will be confirmed bye eye-check afterwards.
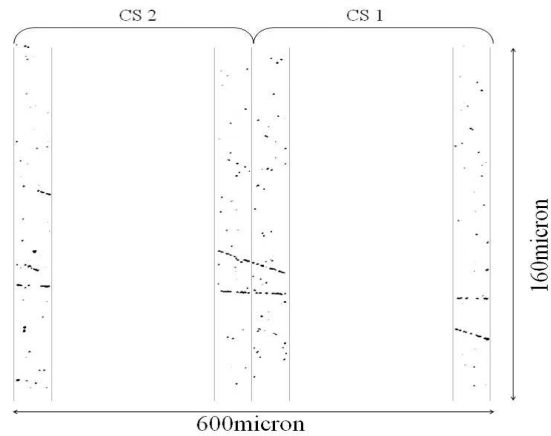
Figure 4.17: *Sketch of tracks and fog distributed in the CS. Picture from [207].*

Shown in Figure 4.17 is a pair of CS tracks inside the emulsion; only tracks with 4 visually confirmed microtracks are selected as CS tracks.

To match the two CS sheets, the position marks of the X-ray grid are used, an even better matching can be achieved by the alignment of the Compton-electron tracks found in both CS (see Figure 4.18). This second alignment will be done if no CS track candidate was found after the first scanning, and since it is only a computational task, no additional general scanning of the CS is needed. Afterwards a "3-out-of-4" search can be performed i.e. the eye-check for a fourth microtrack in case a probable CS track with only three automatically found microtracks exists. If after the Compton-alignment and the "3-out-of-4" procedure no CS track candidate was found, the CS will be re-scanned at least once, or even more with an improved prediction of the electronic detector. If the scanning result stays negative, the next probable brick is extracted and its CS scanned, and the original extracted brick is attached with a new CS and re-inserted in the OPERA target.
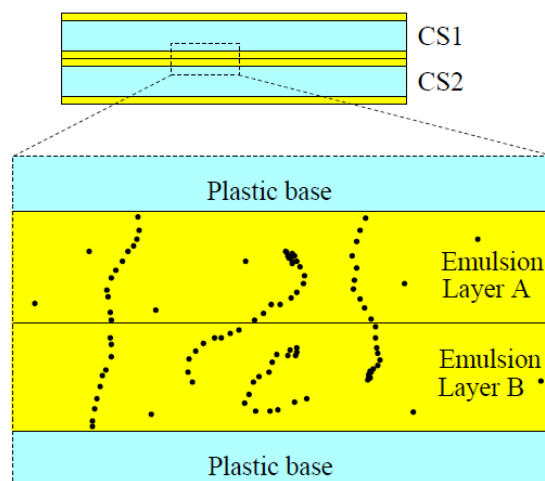
Figure 4.18: *The alignment between the two layers is done by matching the Compton-electron tracks. Picture from [207].*

If during the Brick Finding two or more bricks have the same or similar probability

to be the interaction brick, as indicated in Figure 4.5, both bricks will be extracted and scanned simultaneously to speed up the procedure.

Scanback scan

After the CS scanning gave a positive result, the ECC is disassembled and the emulsions are developed and sent to one of the various scanning laboratories around the world. During the Scanback procedure the extrapolations of the CS tracks back into the brick are followed upstream, until the tracks can not be found anymore. To find the CS track prediction in the first emulsion plate, an area of $3 \times 3\,mm^2$ is scanned, as the mechanical alignment between brick and CS is about $1\,mm$. During the Scanback procedure two scans are done: an inter-calibration area scan to align the emulsion plates with cosmic ray tracks, typical of the size of 0.25 up to $1\,cm^2$, and the prediction scan with an area of one view $(390 \times 310\,\mu m^2)$, in which the prediction from the previous plate is used to define this area. The extrapolation from the previous plate has an accuracy of 10-20 microns, due to the inter-calibration. The disappearance of the prediction marks the stopping point, and is confirmed bye eye-check of the predicted position in the four consecutive planes upstream. If more than one CS prediction exists, as shown in Figure 4.19, they can already build a vertex. The ν-interactions are randomly distributed inside the brick, so on average about 30 plates per event have to be scanned for the localization of the ν-interaction.
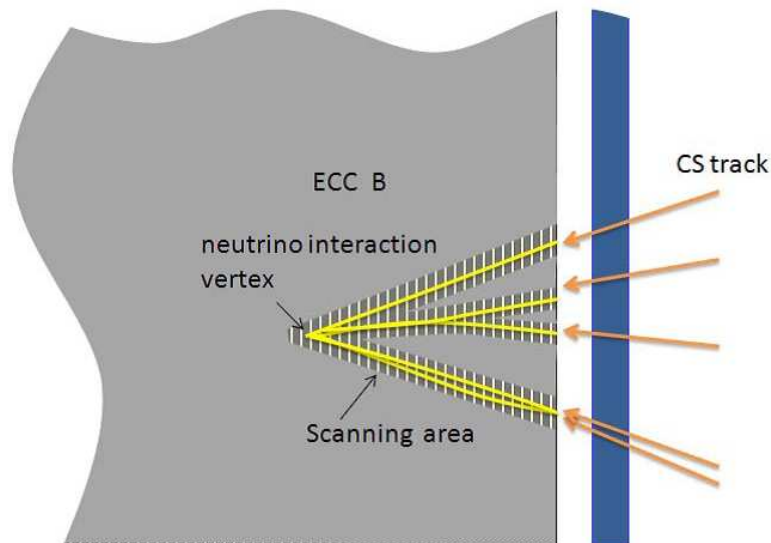
Figure 4.19: *If a CS track was found in the CS, the prediction is followed upstream in the brick until a stopping point or vertex is found. The following up inside the brick is done by point-like scanning. Picture from [207].*

Total scan

After the CS tracks was confirmed as a stopping point, the total scan is performed. The scan volume consists of 15 consecutive plates, 10 downstream of the stopping point, 5

upstream, each scanned with an area of $1\,cm^2$. If the inter-calibration volume, scanned during the Scanback, was large enough, it can be used as the Totalscan volume. Inside this volume the Decay Search Procedure (DSP, see appendix D) is performed to reconstruct the ν-interaction, either as a vertex or a single track. To find possible interesting events, as τ or charm-decays and/or ν_e-interactions, a topological search of decay daughters or parent tracks is done, including a electron/gamma separation search for showers. The topological analysis of the event is finalized with the momentum measurement of the found tracks, thus a reconstruction of the neutrino interaction, the event energy and the type of the ν-interaction can be done.

ScanForth scanning

During the ScanForth scanning, tracks that were found at the vertex and do not match the CS track predictions, are followed downstream the brick to find their stopping point or a possible re-interaction, thus, the ScanForth methods allows to distinguish muons (isolated stop) from hadronic tracks (re-interaction). The ScanForth data is used to estimate the momentum of the tracks by the multiple Coulomb scattering (MCS) method.

4.2.4   Results of the CS scanning

After the run in 2008 a first analysis of the CS scanning and matching with the electronic detector and the bricks was done [210]. For CC events, where the muon was reconstructed with the electronic detector, the predicted slope and position of the muon in the CS with respect to the CS results is shown in the a) and b) plot of Figure 4.20. The position and slope residuals between the two CS emulsion films is shown in c) and d), this precision is achieved due to the alignment with X-ray marks and Compton electrons. Plot e) and f) show the matching between the tracks found in the CS doublet and the first emulsion plate of the ECC and plot g) and h) show the matching between the tracks inside the ECC. While with lateral marks a position resolution in the order of $5\,\mu$m is achieved, the cosmic ray alignment yields a mean value between the prediction and the measurement of $0.5\,\mu$m.
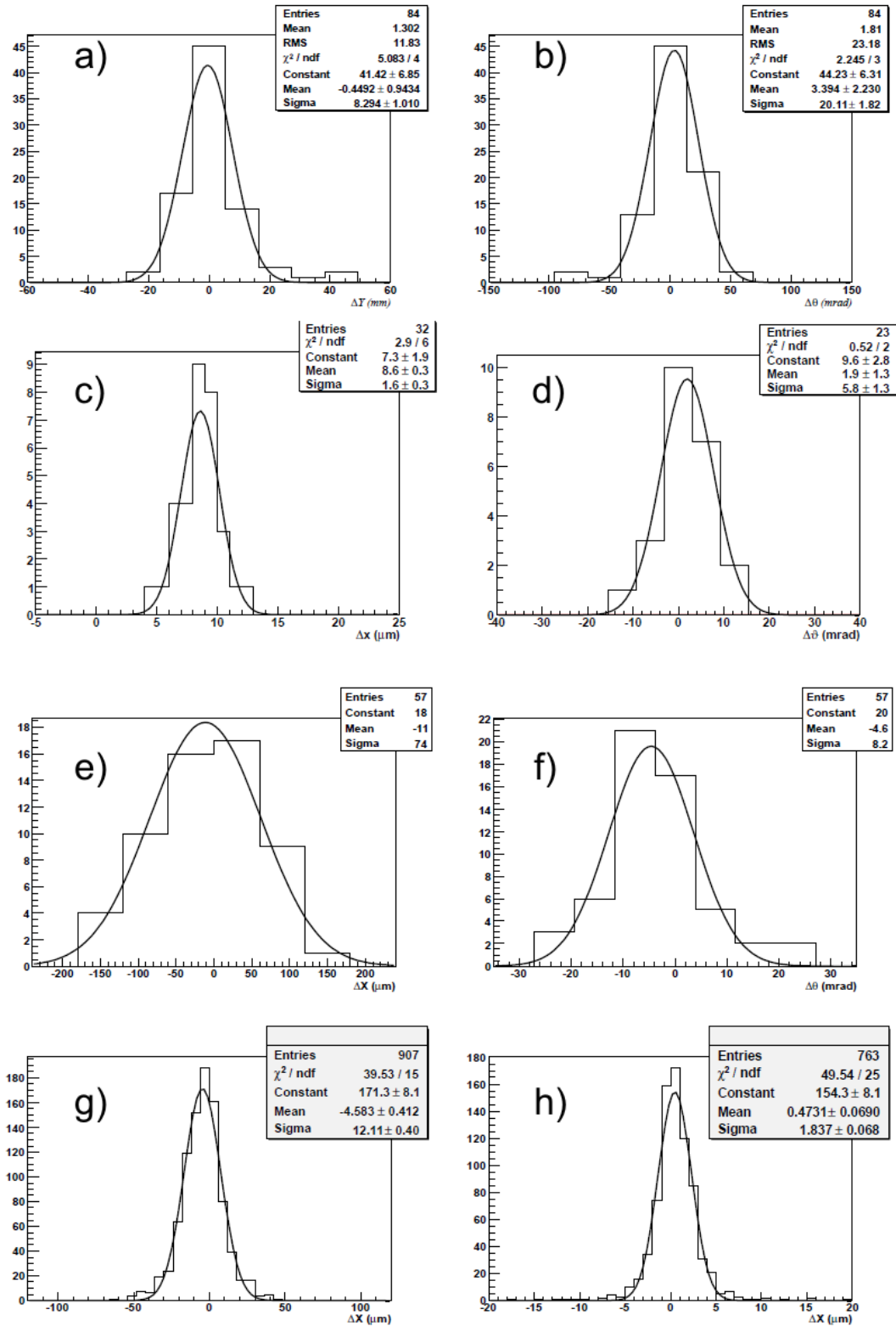
Figure 4.20: *Distribution of: The position (a) and angular (b) residuals between the muon prediction from the TT and the track measured in the CS films. The position (c) and angular (d) residuals between the base-tracks measured in two CS films. The position (e) and angular (f) residuals between the track measured in the CS doublet and the one found in the most downstream film of the brick. The position residuals obtained in the track follow-up with the film-to-film alignment performed with lateral X-ray marks (g) and cosmic rays (h). Picture from [210].*

4.3   Monte Carlo simulations

To test the data analysis software, and to crosscheck theoretical input with experimental data Monte Carlo (MC) simulations are used in particle physics. For the OPERA experiment, there are several MC steps, the neutrino event generation by NEGN (see section 4.3.1). The particle track propagation inside the experiment is done either with the electronic detector simulation OpRelease (see section 4.3.2) with or without the ECC, or with the simulation of the ECC only with one of the two packages FEDRA-VMC (see section 4.3.3) or OpROOT (see section 4.3.3). To analyze the Monte Carlo Data, either OpRelease OpEmuRec (see section 4.3.4) for the full detector or ORFEOv7.9 (see section 4.3.4) are used.

4.3.1   MC Event Generation - NEGN

The neutrino event generation in the OPERA experiment is the first step of MC studies, in the OPERA experiment it was done using the NEGN neutrino generator, described in [262, 261]. The NEGN generator is derived from the NOMAD experiment and is needed to generate a large sample of neutrino interactions. It profits from the experience of NOMAD, where a large sample of ν-interactions with their final states was accumulated, so that for the NEGN generator the simulation of the hadronic system could be tuned, based on the fragmentation parameters and nuclear re-scattering effects. The adaptions needed for the OPERA experiment included the description of the beamline, the neutrino energy, the CNGS target and the output format. As described in [262], the deep inelastic ν-interactions are based on a modified version of the LEPTO 6.1 generator, while the fragmentation process is described with a modified version of JETSET 7.4. Occurring nuclear re-interactions from hadrons produced in the fragmentation process are described with the Formation Zone Intra-nuclear Cascade (FZIC) code (extracted from the DP-MJET II.4 generator) and reinserted in the JETSET simulation. The quasi-elastic and resonant scattering ν-interactions as well as the Fermi momenta generation of the target nucleons is described in more details in [261].

Several thousand neutrino events were created, grouped in so-called beamfiles with pure CC or NC ν-interactions. For the τ and charm analysis dedicated beamfiles with pure τ or charm events were produced. To combine the results from the different beamfiles into a common result for the OPERA physics, one has to take the correct branching ratios and fractions of all subfiles into account.

4.3.2   MC Event simulation - Full detector: OpRelease

The software framework OpRelease is the main software of the OPERA experiment [263], used as well for data analysis as for Monte Carlo simulations (MC). It is designed with special care to allow different Monte Carlo programs as Geant3[3], Geant4[4] and Fluka[5] for particle propagation. Shown in Figure 4.21 is the OpRelease framework overview of relevant Monte Carlo packages, as one can see the framework is built of several sub-packages like the OpGeom package, a set of C++ classes describing the detector geometry.

---

[3]http://wwwinfo.cern.ch/asd/geant/index.html
[4]http://geant4.web.cern.ch/
[5]http://www.fluka.org/fluka.php
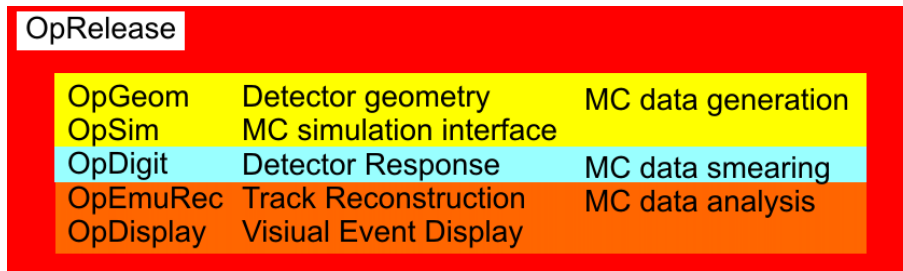
Figure 4.21: *Overview of the OpRelease Monte Carlo Framework and its sub-packages.*
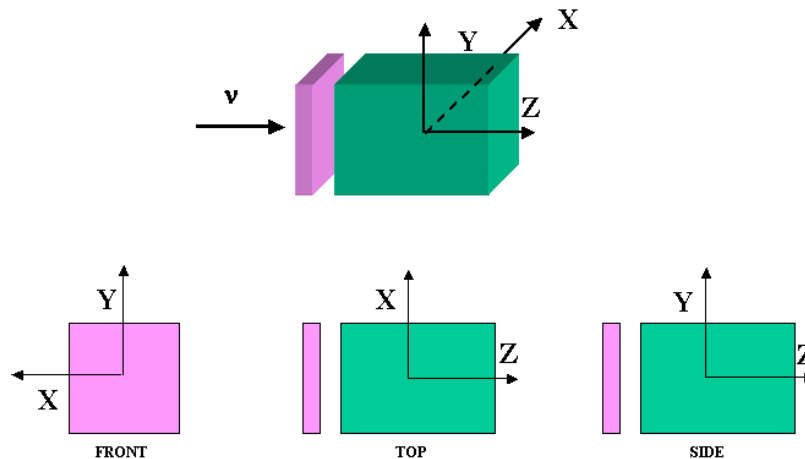
Figure 4.22: *Software reference coordinate system. Picture from [263].*

The OpGeom package is one of the most important packages, as the geometry of the OPERA target is changing over the time of the experiment due to the insertion and extraction of the ECC's. The OpGeom package is a single shared library libOpGeom.so, thus, it can be dynamically loaded by software. As for all OpRelease packages it is managed by the Concurrent Version System (CVS) and stored on the OPERA CVS repository at a 64-bit cluster in Lyon. This allows to keep track of changes in the software in a coherent way. The internal organization and the external interaction with other OpRelease packages is performed through the Configuration Management Tool (CMT). The coordinate system used for the experiment is defined in Figure 4.22.

The full detector MC simulation in the OPERA experiment is based on the OpSim package of the OpRelease framework. The geometry used for the simulation includes the full layout of the hall B and surrounding rock to simulate also so-called "rock muons" coming from upstream interactions unrelated to the detector and are registered with the OPERA detector. OpSim is based on the ROOT VMC package[6]. By defining the geometry in accordance with ROOT classes, the VMC allows a free choice of the transport engine to propagate the particles. The output of OpSim is further handled with OpDigit to convert it into the data format by applying the detector response, before it can be analyzed, one can choose to either ignore the ECC hits and use the electronic detector only, or to propagate the tracks in a 3×3 cube of bricks around the neutrino interaction, to simulate the full processing chain of brick finding, CS scanning and vertex localization.

---

[6]http://root.cern.ch/root/vmc/VirtualMC.html

4.3.3   MC Event simulation - ECC level

On the level of the ECC several packages exist to simulate stand-alone ν-interactions on the brick level. With an age of ten years, the oldest of them, OpROOT (see below), was enhanced (by Luca Scotto) to be compatible with the ORFEO package (see section 4.3.4) which is based on Geant3 and Fluka only. The FEDRA VMC (see below) was developed to use the output from OpSim and regard it only on the brick level, i.e. without the rest of the detector. A dedicated OpBrick [219] framework was developed in Berne to handle only interactions in the brick with Geant4 for their electron/γ studies, but will not be discussed here.

OpROOT

OpROOT is one of the oldest OpRelease packages, derived from the Alice experiment software. It is still used for MC event raw data generation at the microtrack level, e.g. the MC studies presented in this thesis. Due to the age of the software used for stand-alone brick MC, one has to use very old machines on the state of 2002 to avoid conflicts due to changes in programming of kit software needed, as the gcc compiler or CERN ROOT. By using Geant3 and (old) Fluka for particle propagation, the OpROOT environment takes the beamfile output of the neutrino generator NEGN and simulates the particles crossing the ECC by returning the microtracks of the flight paths of charged tracks. One can either assume a fixed starting position for all vertices, or a randomly chosen position inside the brick, as long as the primary vertex is inside a lead plate.

FEDRA-VMC

FEDRA-VMC stands for FEDRA Virtual Monte Carlo. The output of OpSim is used to simulate the ν-interactions in the OPERA bricks alone. The tool was developed to allow the tuning of ECC reconstruction algorithm depending only on the ECC scanning and the effects related to the misalignment effects for the single ECC. The FEDRA VMC is linked to FEDRA, which is described in more detail in section 4.3.4 and indicated in Figure 4.23. Thus, the package can handle the full chain of simulation, reconstruction and analysis. It also allows the simulation of neutrino interactions in an array of bricks, to include simulated cosmic muon background and to apply misalignment of emulsion layers in the OPERA brick.

4.3.4   MC Analysis frameworks

To analyze the OPERA data generated during the scanning (either in the scanning laboratory or in MC simulation), several systems are used. On the level of the brick scanning in Europe the SySal.NET and FEDRA software can handle the track reconstruction in emulsions. For the later analysis a combined global OPERA data set will be used, thus, a dedicated analysis framework, OpEmuRec, was developed to include the electronic and emulsion data from all scanning laboratories. For the stand-alone brick MC simulation, the ORFEO framework can be used to convert the OpROOT MC raw data into a format that can be accessed with FEDRA reconstruction routines, while the FEDRA-VMC is already in a correct format for the FEDRA routines. The development of the OpEmuRec
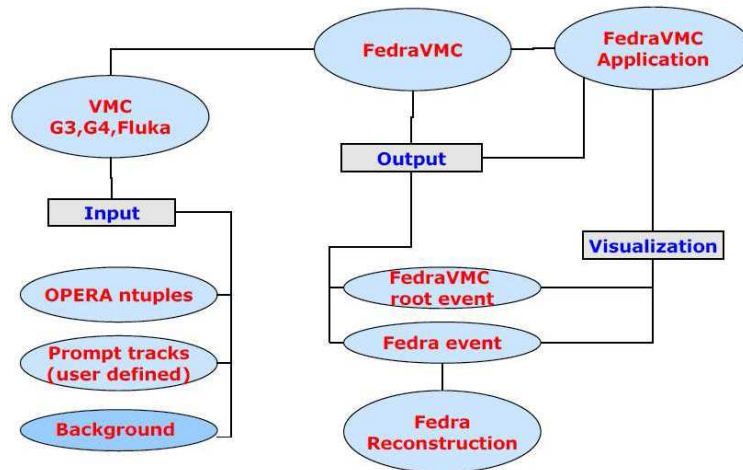
Figure 4.23: *Organization of FEDRA-VMC packages. Picture from [264].*

software was not finished at the time of this thesis, instead the ORFEO framework was used.

OpEmuRec

The scanned data in the OPERA experiment will finally be stored in a central database, from which the reconstruction of events takes place. The handling of events extracted from the database for analysis purposes is done in OpRelease with the OpEmuRec package. After the insertion of scanned data on the microtrack level, different reconstruction steps as basetrack linking, plate alignment, track linking and vertexing for the analysis can be handled with different reconstruction algorithm by that package, either coming from the European SySal or the FEDRA, or the Japanese S-UTS environment.

ORFEOv7.9 and FEDRA

The ORFEO package was developed to handle the OpROOT MC output files. With this package, one can apply several effects like smearing, misalignment and scanning efficiencies on the MC tracks propagated in OpROOT, as shown in Figure 4.24. Additionally, the ORFEOv7.9 framework gives the possibility to loop over the MC events and apply reconstruction algorithms, such as track linking and vertexing with routines of the FEDRA software. To check the reconstruction, user developed code can be used, while the ORFEO routines allow the access of the MC truth of the particles/tracks. The ORFEOv7.9 package was developed in Napoli and Bari, the version 7.9 mainly by Luca Scotto. Its features are:

- Smearing: i.e. to apply a random Gaussian distribution on the true X, Y, Z position and the TX and TY angle (TX=$\tan\theta_{x,y} = \frac{dx,dy}{dz} = TX, TY$, dx (dy) distance in X (Y) of the two MT at the top and bottom of the emulsion layer, dz = thickness of the emulsion) of microtracks generated in the OpROOT MC simulation.

- Efficiency: i.e. a randomly chosen pulse height (number of grains) value between 1 and 16 for the microtrack (MT) is generated. If the pulse height is larger than 12, the MT is accepted, otherwise rejected for further analysis.

- Linking: i.e. the reconstruction of basetracks (BT) with the raw data format from the OpROOT MC.

Contrary to the real scanning, where a track can be re-checked bye eye and a manual position and angle measurement is possible, the MT is lost in the ORFEOv7.9 framework when an inefficiency is applied. This leads to a loss of track information around the vertex point, where the eye-check is crucial in real data taking. Thus, the track efficiency I applied on the MC data was left at 100%. With this change, the number of short segmented tracks(less than 3 segments) in the final dataset will be enlarged, but as tracks below $\sim 1\,$GeV are rejected for the charm analysis, this will not imply a large bias; tracks with higher energy will have at least 10 basetracks (BT); with an efficiency of $\sim 95\%$ for a BT from scanning, the chance to miss one of these tracks is negligible.
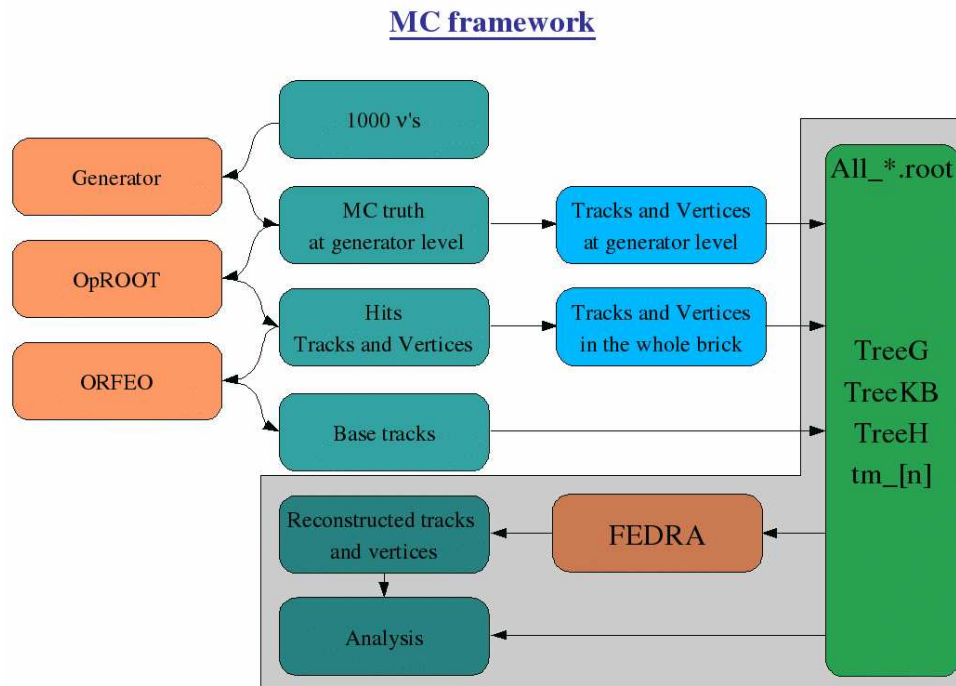
Figure 4.24: *Organization of ORFEO MC packages. Picture from L. Scotto.*

Chapter 5

Monte Carlo study of charm detection in OPERA

5.1 Introduction

As already mentioned in the previous chapters this thesis is dedicated to study the ν-induced charm production in OPERA. As explained in section 1.4.2, the production for charm is $4.38 \pm 0.26\%$ of the ν_μ-CC interactions in the OPERA experiment:

$$\frac{\sigma^{\nu_\mu T \to \mu^- cX}}{\sigma^{\nu_\mu T \to \mu^- X}} = (4.38 \pm 0.26)\% \tag{5.1}$$

Wherein the neutral charm component is $\sigma^{D^0}/\sigma^{CC} = (1.91 \pm 0.13)\%$ and the charged charm component is $\sigma^{C^+}/\sigma^{CC} = (2.47 \pm 0.22)\%$. In the Tables 5.1 and 5.2 the produced charm mesons and their decay topologies are repeated [112, 201].

Charm hadron	quark component	Mass (MeV)	τ $(10^{-15} s)$	BF$_{<E_\nu>=17\,GeV}$ (%)
D^0	$c\bar{u}$	1864.6 ± 0.5	0.4101 ± 0.0015	43.8 ± 3.0
D^+	$c\bar{d}$	1869.3 ± 0.5	1.040 ± 0.007	21.7 ± 3.4
D_s^+	$c\bar{s}$	1968.5 ± 0.6	0.500 ± 0.007	9.2 ± 3.8
Λ_c^+	udc	2284.9 ± 0.6	0.200 ± 0.006	25.3 ± 4.9

Table 5.1: *Charmed hadron summary table including the production branching fraction (BF) at the OPERA neutrino beam with an average energy of 17 GeV [112, 201].*

Charm type	Multiplicity	BR (%)
Charged Charm	1-prong	65 ± 9
	3 prong	35 ± 6
	5 prong	0.9 ± 0.2
Neutral Charm	0-prong	15 ± 6
	2 prong	70 ± 6
	4 prong	14.5 ± 0.5
	6 prong	$(6.5 \pm 1.3) * 10^{-4}$

Table 5.2: *Charm hadron topological decay branching ratios [112].*

To analyze the events in the ECC's the automatic FEDRA reconstruction was used on a MC sample of pure charm-CC and ν_μ-CC interactions, provided by the NEGN and ORFEOv7.9 framework (see sections 4.3.1 and 4.3.4 for details). Each sample contained 9000 events, and for the charm-CC sample 7362 events were reconstructed, in the ν_μ-CC sample 7511. The reduction of the initial 9000 events is due to the requirement of a muon track with more than $1\,\mathrm{GeV}$ leaving the ECC in plate 57, to be able to reconstruct a CC event in the electronic detector (see section 5.2 for details). With the last two numbers the background and efficiency was calculated, assuming that they correspond to the number of located events in the ECC data sample. The weight between both MC results is given by the charm production rate, i.e. the full charm-CC sample contributes 4.38% to the total number of CC-events. For a comparison with real data the expected background and the expected number of observed charm decays were scaled to 901 located ν_μ-CC events from the 2008 and part of the 2009 data.

Event topology	primary interaction	secondary interaction	class name
short	single muon	secondary track	short_pt_st
	single muon	secondary vertex	short_pt_sv
	primary vertex	secondary track	short_pv_st
	primary vertex	secondary vertex	short_pv_sv
longn	single muon	secondary track	longn_pt_st
	single muon	secondary vertex	longn_pt_sv
	primary vertex	secondary track	longn_pv_st
	primary vertex	secondary vertex	longn_pv_sv
longc	primary vertex	secondary track	longc_pv_st
	primary vertex	secondary vertex	longc_pv_sv

Table 5.3: Used event topology categories.

The events are divided into categories according to their topology: short, long neutral and long charged (see Table 5.3). The *Short* category contains all events with a decay in the same lead plate where the primary ν-interaction took place (see e.g. Figure 6.14). *Long neutral (longn)* means, that the found daughter track(s) is (are) at least one emulsion film (also called plate) downstream of the primary vertex, and that no parent track (i.e. charged particle) was (were) found, while the category *long charged (longc)* tags events where the parent track and its decay can be observed. Furthermore we distinguish the topology according to the found multiplicity, reconstructed quasi-elastic-like events are tagged as *single muon*, i.e. only an isolated muon can be found to reconstruct the primary interaction, while *primary vertex* means that at least two tracks are found that form a vertex for the primary interaction. The secondary vertex is similarly classified, if only a single daughter track can be found, we call the topology *secondary track*, if a vertex with at least two tracks can be reconstructed, the topology is called *secondary vertex*. In Table 5.3 the different topologies are summarized.

5.2   The decay Search Procedure (DSP)

After a ν-interaction is localized in a scanning laboratory, the so-called Decay Search Procedure (DSP, see appendix D) has to be performed to find possible decays downstream

of the primary vertex, as explained in section 4.2.3. The DSP was implemented in the FEDRA framework and was hence applied to the Monte Carlo generated events. If an interesting decay candidate is found by the automatic part of the procedure, the DSP prescribes some eye-checks to be performed on the primary vertex plate and within up to 10 plates downstream. Especially one has to check the vertex plate and confirm by eye possible found electron-positron pairs (e-pairs). Additionally, the effect of a manual vertex reconstruction and inspection was implemented, these human interventions are explained in further detail in section 5.4.4. With studies done in Bern and by myself, the need of a common procedure for event analysis was shown and the DSP was optimized using these results, especially taking into account a higher number of emulsion films to be scanned to recover efficiency losses of reconstructed tracks due to bad emulsion quality.

5.3 Event reconstruction with the ORFEOv7.9 software

As already mentioned in section 4.3.4, the ORFEOv7.9 framework was used for the MC analysis. The framework provides the handling of the MC truth and the reconstructed basetracks. As the decay search procedure is starting from the Totalscan data, only a 15 emulsion plates volume of $1\,\text{cm}^2$ around the primary vertex is checked. Thus, the first step was to select a volume of interest via the Scanback track stopping point. To select a Scanback track in CC interaction MC studies, the ORFEOv7.9 framework takes the position and slopes of the muon from the MC truth, and gives back the stopping point by a simulated Scanback procedure, if the muon is visible in the last emulsion film of the ECC, its slopes in $\tan\theta_x = \frac{dx}{dz} = TX$ and $\tan\theta_y = \frac{dy}{dz} = TY$ are smaller than $0.6\,\text{rad}$ (with $dx = X_{MT(top)} - X_{MT(bottom)}$, $dy = Y_{MT(top)} - Y_{MT(bottom)}$ and $dz = 200\,\mu m$) and if its energy is higher than $1\,\text{GeV}$. The requirement of the Scanback track to be found in the last plate is natural, without it no CS prediction of the muon track can be found. The slope cuts are due to the limitation of the emulsion scanning efficiency, in general scan mode only slopes up to 0.6 rad will be found automatically, above the efficiency is too low. The energy cut of $1\,\text{GeV}$ for the muon is motivated by the requirement that the muon has to reach the spectrometer, so that the event can be identified as 1-μ event, otherwise the CC interaction can only be classified as 0-μ event. Studies done by the electronic detector group showed that the electronic detector can identify muons with a track that crosses $660\,\text{g·cm}^2$. This range corresponds to a kinematical muon energy of $970\,\text{MeV}$, thus the cut on $1\,\text{GeV}$ [250].

After the stopping point is selected, a total scan volume is opened and the basetracks are loaded into the FEDRA class object EdbPVRec() called gAli. The gAli object is the starting point of the FEDRA algorithm, thus, it is the interface between MC and scanning data and the analysis software. This means that any software, starting from the gAli object, can be applied to both MC and real data. The format loaded into the object can be compared to the so-called CP-files in the scanning labs, each storing the basetrack information of one plate (files with found couples of microtracks, i.e. basetracks). The next step is the plate aligning and afterwards the basetracks, loaded into the gAli object, are linked between emulsions into tracks. Afterwards the ORFEOv7.9 framework checks again, if the muon was reconstructed as a track inside the volume, before any vertex reconstruction can start.

5.4   Software developed for the charm analysis

The software developed for the charm search started from the basetracks (stored in the gAli object) after the track linking procedure. First of all I applied the automatic FEDRA vertexing routine. A vertex marks the point between tracks, where each track has a minimal distance to this point [260]. The vertexing routine is based on a pair based approach, i.e. first all two track combinations are searched with a minimal distance approach, and afterwards a check is performed to find higher multiplicity vertices, using a covariance matrix of the tracks (x, y, tx, ty, p) and a Kalman Filtering technique [265]. If a higher multiplicity vertex is found, the tracks are combined, and the previous two prong vertex is flagged as unused (but kept). The vertexing is copying the gAli object into the EdbVertexRec object, called gEVR. The gEVR object is enhanced in comparison to the gAli object by a list of all reconstructed vertices. Due to the pair based approach, the ordering of tracks attached to a vertex is having an influence on the final X, Y and Z position of the vertex, and the impact parameter (IP) of the tracks w.r.t. the vertex point. In cases where no vertex was reconstructed, a flag was set to avoid problems when accessing this empty, but initialized list.

As a position and slope smearing was applied to the reconstructed basetracks, the next step of the software was to search for the reconstructed muon (Scanback track). Due to the smearing, the slope and position between the muon in the MC truth, defining the Scanback track, and the muon reconstructed inside the volume is different. Thus, the list of vertices was checked, if one vertex had a track with an agreement of 0.020 rad in the slopes w.r.t. to the muon (MC truth), and was found within a $600 \times 600 \times 1300 \, \mu m^3$ cube around the MC truth X and Y position of the muon in the stopping plate, this vertex was labeled as primary vertex, and the track as muon. If no vertex can be found to which the muon is attached, the list of tracks is checked with the same acceptances to find a muon track and a found track is labeled as isolated (or single) muon. If no reconstructed muon can be found, the event is discarded from further analysis, which happens for about 1.2% of all MC events. If only the single muon track is found, a second (improved) vertexing is done, as explained in section 5.4.4. The muon selection was crosschecked with MC truth, and only in 32 of 7362 events in the charm-CC and also 32 of 7511 events in the ν_μ-CC sample the track selected was not the muon. The source of this misidentification was checked, and was found to be due to additional primary vertex tracks with a slope similar to the muon, in case of charm also partly from secondary vertex tracks. As one can not distinguish these two tracks in real data either, the events were further processed.

5.4.1   Improved primary vertex reconstruction (after applying the DSP)

The next implemented routines were closely related to the Decay Search Procedure, explained in appendix D. In case of a primary vertex, first all tracks with a missing basetrack in the vertex plate are detached, second the remaining tracks are checked by eye to eliminate electron pairs (see section 5.4.3). Afterwards tracks with low momentum ($\leq 500 \, \mathrm{MeV}$) or a low number of segments (< 3 basetracks) are detached, the tracks with an IP of more than $10 \, \mu m$ w.r.t. the primary vertex are detached, as they are likely daughter track candidates of charm and τ short decays (see Appendix D). After applying the DSP and the eye checks, an improved vertex position was calculated with the remaining tracks.
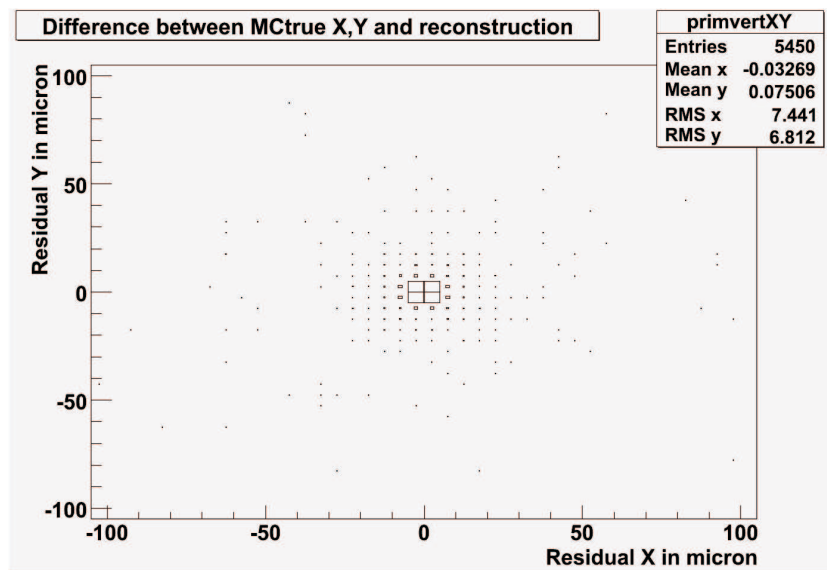
Figure 5.1: *Reconstructed position in X, Y of the primary vertex w.r.t. the MC truth position of the ν-interaction in the charm-CC MC sample with the automatic FEDRA procedure.*

Figure 5.2: *Reconstructed position in X, Y of the primary vertex w.r.t. the MC truth position of the ν-interaction in the charm-CC MC sample after the decay search procedure and eye-checks were applied.*
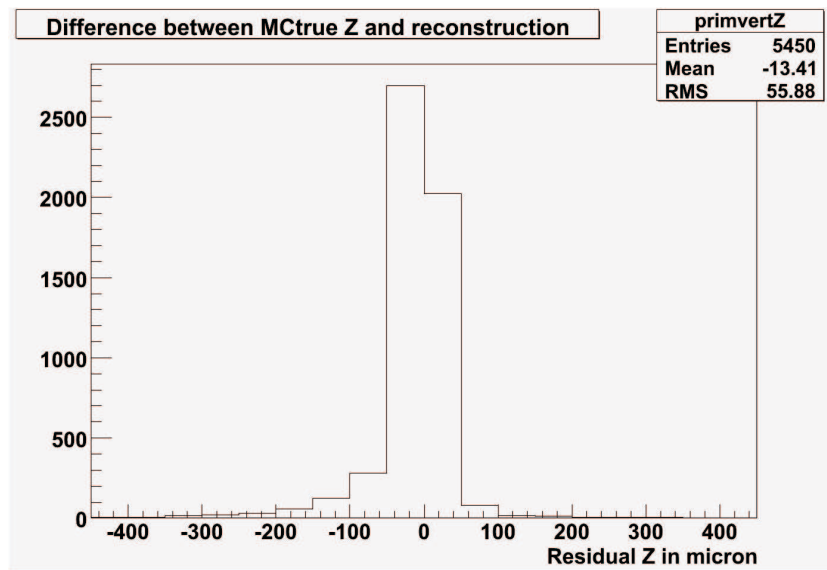
Figure 5.3: *Reconstructed position in Z of the primary vertex w.r.t. the MC truth position of the ν-interaction in the charm-CC MC sample with the automatic FEDRA procedure.*
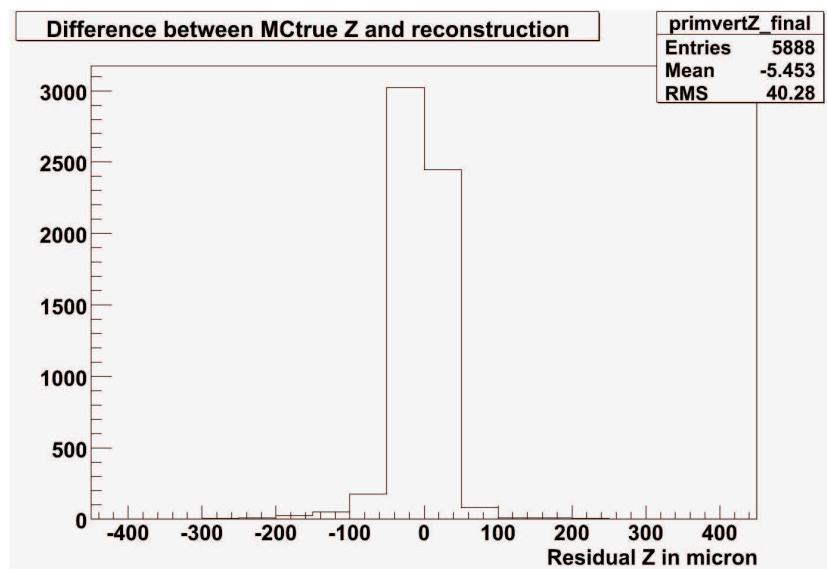
Figure 5.4: *Reconstructed position in Z of the primary vertex w.r.t. the MC truth position of the ν-interaction in the charm-CC MC sample after the decay search procedure and eye-checks were applied.*

Shown in Figures 5.1 and 5.2 are the residuals between the MC truth and the X and Y position of the reconstructed vertex in the charm-CC sample before and after the DSP and the recalculated vertex reconstruction was applied. Due to the improvement in the vertex reconstruction, the residual mean square (RMS) is reduced by a factor 1.5. Shown in Figures 5.3 and 5.4 are the residuals of the Z position, also here the RMS is reduced. Additionally, the number of reconstructed vertices is increased due to the recovering of single basetrack charm events, which were not reconstructed before due to the requirement of at least two basetrack to create a track.

5.4.2 Track search around the ν-vertex

After the vertex redefinition, the decay search foresees the daughter track candidate search to check for short lived particle decays of τ and charm. Depending on the reconstruction of the primary interaction as vertex or isolated muon two different acceptance sets for daughter tracks exists, as defined in appendix D. In the ORFEOv7.9 MC simulation package the microtrack level is not included in the reconstruction, thus, the minimum request on the number of microtracks to accept a track as daughter candidate is slightly increased to 6 w.r.t. to the DSP, where at least 5 microtracks are requested. To check for parent tracks, a single basetrack search was implemented, to locate decays where the parent is found in one plate only and was thus previously not found. A parent is identified when the IP of the parent basetrack w.r.t. the primary vertex, or minimum distance to the single muon was smaller than $20\,\mu$m, and the minimum distance between the parent and its daughter smaller than $10\,\mu$m. Because only the matching of one basetrack with a daughter is required, a large number of low momentum tracks, mainly protons with $\leq 1.5\,$GeV, are found in this step too, most missing the first segment due to a large scattering angle due to multiple Coulomb scattering. Other tracks found in this step are originating from rare particle decays as Λ and K_s^0 or the scattering of higher energetic hadrons. These background tracks request that certain cuts on the minimum momentum and transverse momentum are applied on the daughter track candidates selected, to clean the selection and identify possible charm or τ-daughter tracks (see section 5.5.2).

After the event reconstruction several checks were implemented to adapt the selection of tracks with the work done in the scanning lab. First of all, low momentum tracks, scattering with large angles, are reconstructed by FEDRA as a series of different tracks and basetracks. To avoid that a track was found more than once, a cleaning procedure was implemented. Low momentum tracks can be found in subparts, thus several times. To avoid a double counting, the track selection was checked if on track could be built between long-long and short-long track combinations. If a combination was found, the segments of the more downstream track were attached to the upstream track, and the $\Delta\theta_{i,T,L}$ (see Appendix D for details) was re-calculated, to sort out low momentum tracks. Furthermore a check was implemented to crosscheck if one of the selected tracks was wrongly detached by the IP cut of 10 microns because it was wrongly detected as a low momentum track, or if a good vertex with a Z-position further upstream could be built (see section 5.4.4).

After these steps a secondary vertex reconstruction with the selected daughter track candidates selected by the DSP track search was done. The secondary vertex was then further analyzed to check if it was truly coming from a charm decay. The secondary vertices were found in three categories: *short decays* in the same plate as the primary
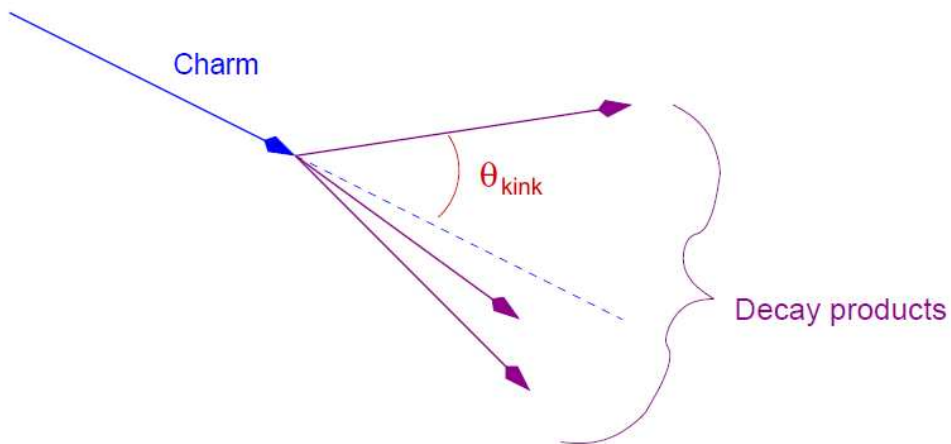
Figure 5.5: *Definition of the kink-angle between the charm parent and daughter track. Picture from [198].*
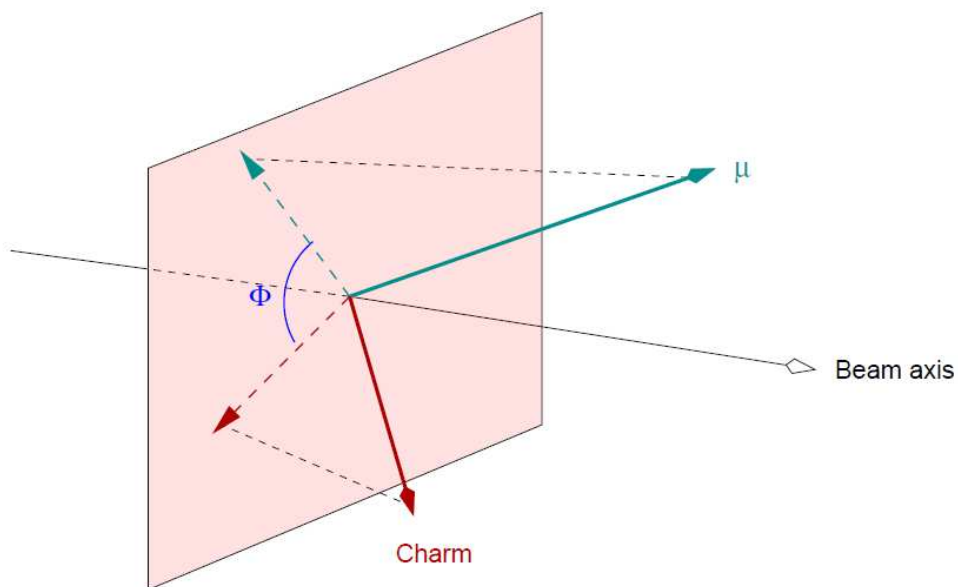
Figure 5.6: *Definition of the Φ-angle between the charm and muon track. The angle is calculated in the plane perpendicular to the incident neutrino beam direction. Picture from [198].*

interaction, *long charged decays* where a basetrack or track was connecting both vertices and *long neutral decays*, and according to Table 5.3 divided in sub-categories, to find possible cuts. Naturally, the situation of a reconstructed vertex for both the primary and secondary interaction is the best, as it allows a precise reconstruction of the charm flight length and the slopes TX and TY of the parent. Between **each** charm (or τ) daughter and its parent (neutral or not), a kinkangle exists, the definition of the kinkangle between charm and daughter can be seen in Figure 5.5.
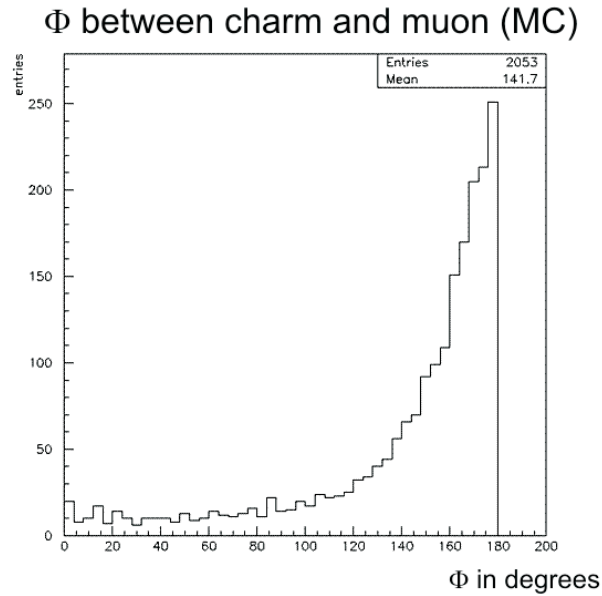
Figure 5.7: *Calculated Φ-angle distribution between charged charm and muon tracks in the charm-CC MC sample (MC truth).*

This kinkangle is further used to calculate the transverse momentum of the daughter ($P_t = \sin(kinkangle) \times P$). If only one daughter is found with a charged parent, this event is called "kink" topology (which can be mimicked by hadronic scattering). Additionally another angle can be determined, the Φ angle between charm and muon in the plane perpendicular to the ν-beam direction (see Figure 5.6). The possible background is evenly distributed, the charm (or τ) prefers to be opposite to the muon (primary hadrons), as shown in Figure 5.7 for the MC truth of charm events.
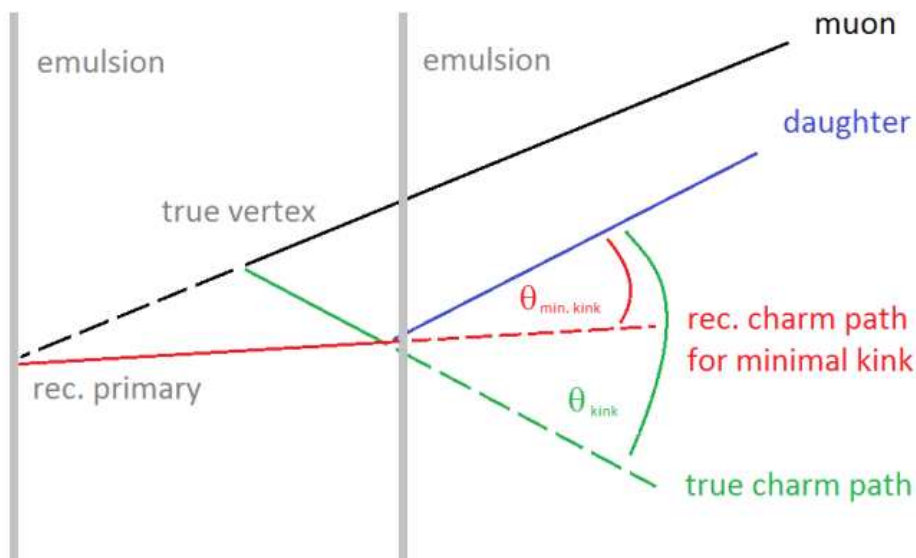
Figure 5.8: *Definition of the minimal kink-angle between the charm parent and daughter track when one (or both) vertices are found as single tracks only.*

Nevertheless, also cases, where one of the found vertices (stopping points) is built by a single, isolated track have to be taken into account. For the single muon and the single decay daughters, the exact location inside the lead plate can not be determined. For these cases the muon position was extrapolated $1000\,\mu$m upstream, i.e. to the end of the previous emulsion plate, while the secondary daughter track was assumed to start at the beginning of the emulsion plate, i.e. it was unchanged. Thus, a minimum kink-angle of a charm decay could be calculated as shown in Figure 5.8, and thus a minimum transverse momentum of the daughter track, as well as a minimum Φ angle.

5.4.3   Electron pair search

In real emulsions, the beginning of a track (stopping point) will be checked by eye for two reasons: first of all to confirm the stopping point, i.e. if the last found basetrack really is a beginning track and not a fake basetrack/microtrack, or a missing basetrack/microtrack while the track continues further upstream. In the MC simulation, this effect can be neglected, as the track is given by the efficiency smearing, which was 1 for this MC study, as explained before.
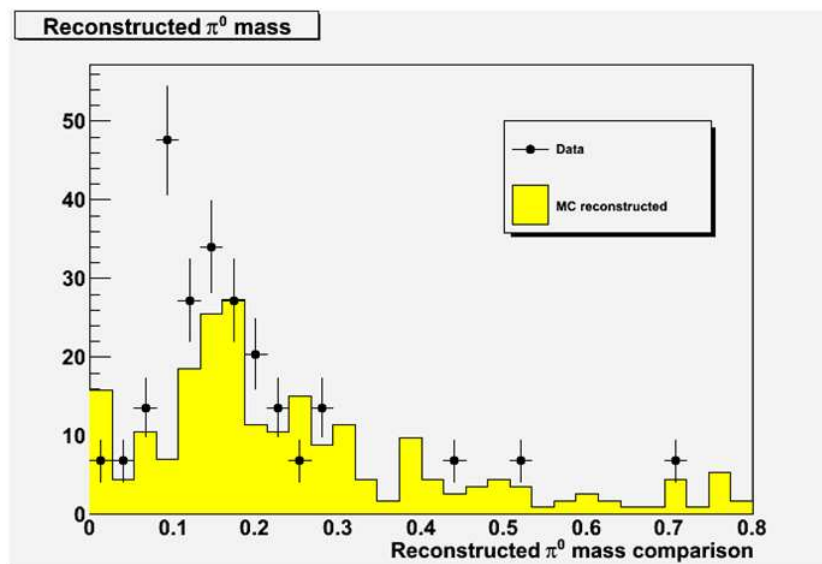
Figure 5.9: *Reconstructed π^0 mass of γ showers in OPERA bricks scanned in Bern. Picture from F. Juget (LHEP Bern).*

Secondly, electron pairs will be produced by decay γ's, thus, two basetracks, which are close in position and have nearly parallel slopes are a hint for a γ-conversion. In reconstructed data, the pair check is only partly possible, as the first microtracks are usually very close, so it can happen that in the scanned data only one basetrack is found due to a failure in the basetrack linking. Here, the human eye-check allows to detect these electron pairs and recover the beginning of the γ shower, which then will be analyzed with the Bern shower algorithm. In MC events, this eye-check is not possible, as only reconstructed data is available, i.e. the microtrack level is missing, additionally the number of MC events to check is too large (several thousand). Thus, I implemented a routine, that looks around the basetrack, if a second basetrack can be found within $30\,$microns

distance, with an opening angle of less than $50\,$mrad between them. In that case, the track is regarded as electron-pair. Studies by Frank Meisel from LHEP showed, that with the applied selection more than 95% of all γ conversions will be selected. Most of the other missing γ showers have a large separation, thus, they can not be observed in one view with an eye-check.

Electron pair (or γ) search is important for the reconstruction of π^0 decays, shown in Figure 5.9 are the reconstructed data and MC comparison from F. Juget (LHEP Bern). The identification of electron pairs, and subsequently π^0 reconstruction, allows to differentiate hadronic scattering/re-interaction vertices from charm and τ-decays, which is helpful in the so-called kink channel, when only one daughter track of the charm is found, since one can loosen the transverse momentum cut.
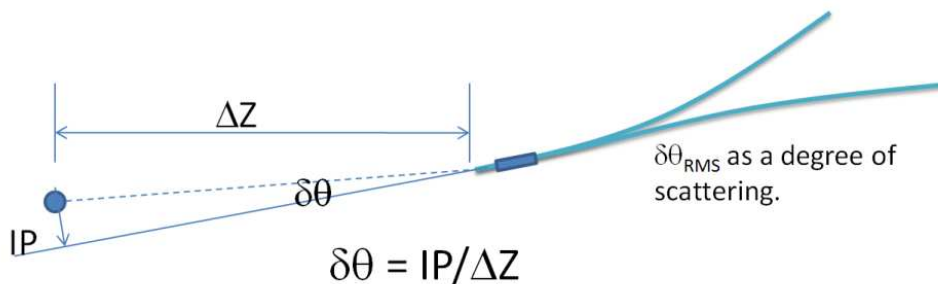
Figure 5.10: *Definition of the angular accuracy of γ showers w.r.t. the vertex. Picture from A. Ariga (LHEP Bern).*

Not all found electron pairs will be useful as discriminator; with increasing distance between the γ conversion point (e-pair) and the vertex, the uncertainty on the origin of the γ becomes larger, as indicated in Figure 5.10 and the γ can not unambiguously be attached to one of the vertices: Even though the IP w.r.t. to one vertex might be smaller than the other, both IP will be compatible for attaching the γ, thus, it remains unclear whether it belongs to the primary or the secondary vertex. Nevertheless, the eye-check was simulated with results similar to the results of the scanning laboratory work and thus the number of fake track candidates due to electron pairs from γ conversion is minimized.

5.4.4 Corrections of FEDRA vertex reconstruction

As already mentioned previously, the automatic FEDRA reconstruction was used as starting point for this MC study. The reconstruction works very well for ν_μ-CC interaction vertices with no short lived particles decaying close to the primary vertex. In case of charm (or τ) decays, I encountered some errors, for which a dedicated recovery was implemented, as in the real scanning laboratory these mistakes would have been observed due to the human intervention during the vertex confirmation. First of all, due to the smearing applied to the Monte Carlo truth, an effect of missing primary vertices was observed, as explained in the next paragraph. Another effect observed was the "badly" reconstructed vertices, where two tracks are combined even though they are physically not from the same vertex, but close in space, the so-called low probability vertices (see second paragraph of this section). Last, the secondary vertex had to be corrected when the reconstructed primary vertex was made by a primary track and a secondary track,

where additional tracks on both, primary and secondary interactions, could be found (see last paragraph of this section).

Primary Vertex Recovery

If during the check of the Scanback track, i.e. the muon, only a single muon is found, an additional step was implemented to reproduce the work done in the scanning lab. During the FEDRA vertexing it can happen, due to the position smearing, that only in one direction, i.e. X-view or Y-view of the interaction, the tracks merge to form a vertex. In these rare cases, the result will be that no vertex is found automatically, while in the scanning lab these tracks can be merged to form a vertex by hand, as usually their impact parameter is well below few microns. To simulate this manual intervention and to recover the vertices, a loop over all tracks in the track list was implemented with the following criteria:

- If a track is in the same plate as the muon (and is no electron pair), calculate the minimum distance (Dmin) between the this track and the muon.

- If the minimum distance (Dmin) between muon and the track is smaller than three microns, build a vertex out of these two and check, if the reconstructed vertex has a vertex probability ≤ 0.9.

If a vertex satisfying these criteria can be found, this vertex becomes the primary vertex, else the event is classified as a single muon event.

Low probability charm vertices

All reconstructed vertices will be checked in the scanning laboratories by eye before they are accepted. In the automatic reconstruction however this is not possible due to the large number of events that are processed, thus, in the automatic reconstruction a vertex probability is calculated, taking into account the covariance matrix of all vertex parameters, for details see [260]. In the upper plots of Figures 5.12 and 5.13 the vertex probability distribution from FEDRA for the reconstructed primary vertices in the ν_μ-CC and charm-CC MC sample after the automatic FEDRA reconstruction are shown, starting from the
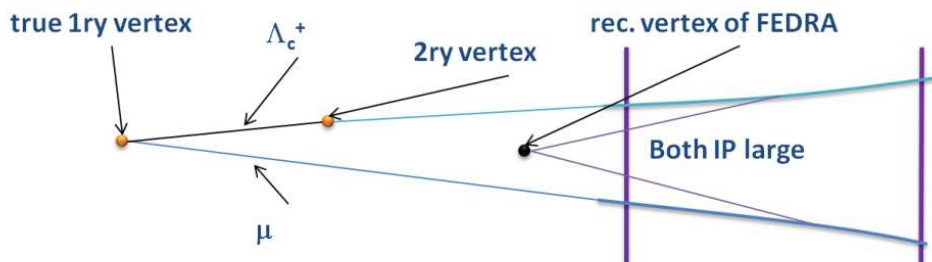
Figure 5.11: *Automatic reconstructed FEDRA vertex with a low probability due to a wrong vertex finding.*
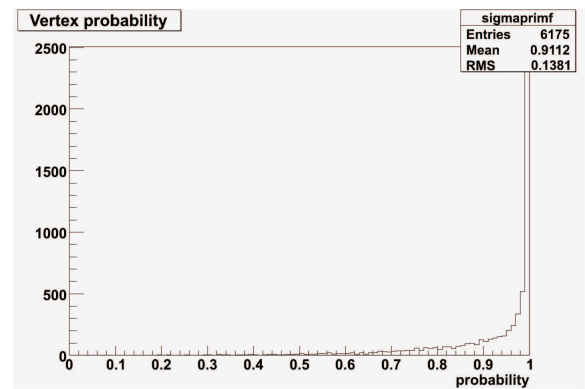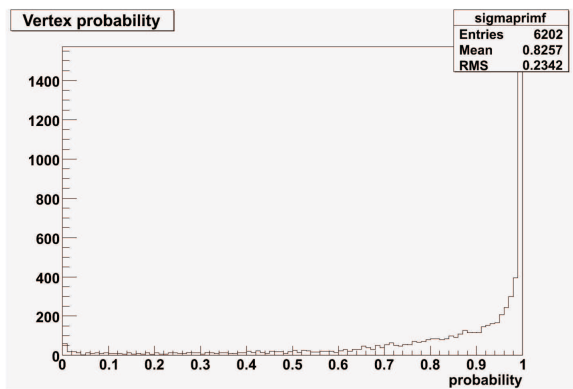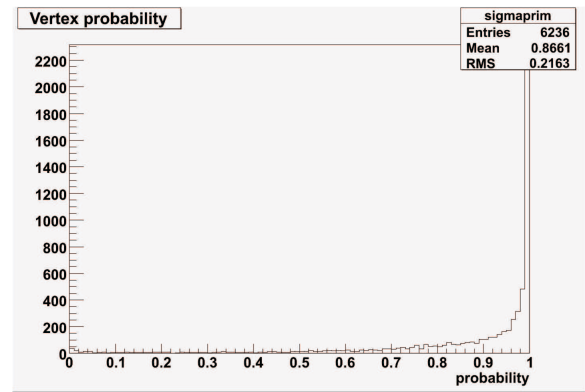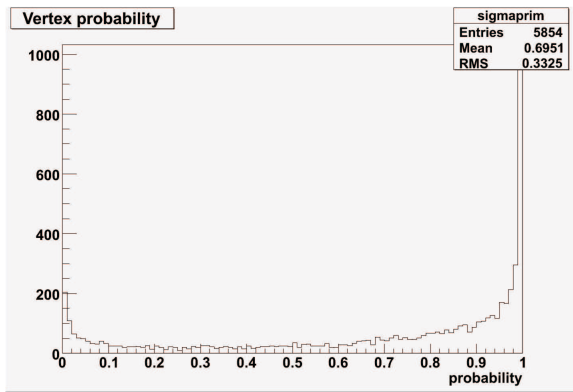
Figure 5.12: *Vertex probability-distribution in the charm-CC sample before (top) and after (bottom) the decay search procedure was applied.*

Figure 5.13: *Vertex probability-distribution in the ν_μ-CC sample before (top) and after (bottom) the decay search procedure was applied.*
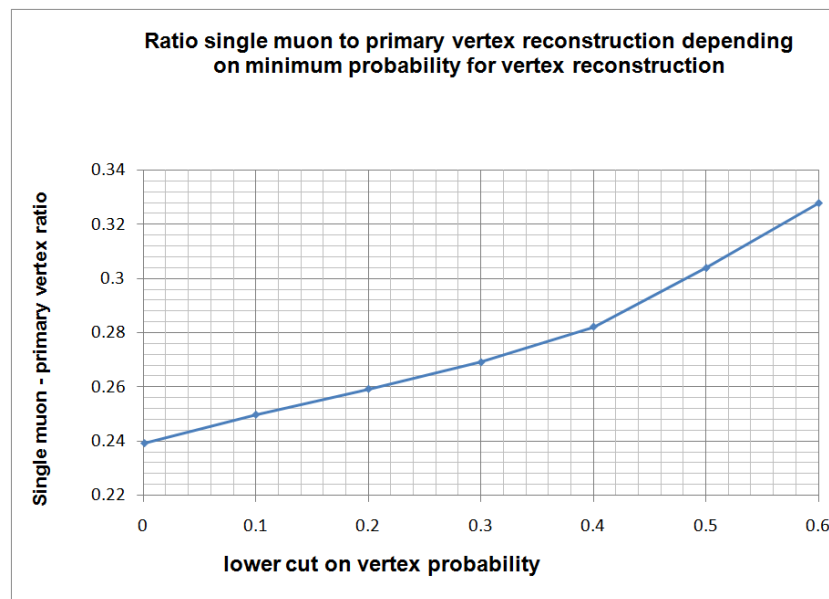
Figure 5.14: *Ratio of single muon events to events where a primary vertex was reconstructed in the charm-CC MC sample, depending on the minimum vertex probability cut during the FEDRA vertexing.*

initial lower cut on the vertex probability of 0.001. Even though both curves look similar for probabilities close to 1, it is obvious that in the charm sample a large number of vertices with a vertex probability smaller than 0.1 is reconstructed. By checking a sub-sample of these reconstructed MC events by eye, I observed that the low probability vertices presence were due to short particle decays close to the original primary vertex, as shown in Figure 5.11. Using the reconstruction display, the found vertices would not considered as vertex, but as two distinct single tracks, as their IP w.r.t. each other is larger than 10 microns.

After applying the decay search procedure, due to the improved reconstruction, the vertex probability-distribution in the final vertex sample has a higher mean and a smaller RMS, i.e. the reconstructed vertices are of higher quality and many of the low probability vertices are recovered as two single tracks. Nevertheless, a sub-sample of these events are still present, as shwon in the lower plots of Figures 5.12 and 5.13. The only way to avoid these remnants was to increase the cut on the lower vertex probability, thus, a study of the influence on the best minimum vertex probability for a the total charm efficiency was performed and will be discussed in further detail in section 5.5.1 and 5.5.3. Not surprisingly, the rate of single muon events is depending on the cut on the minimum vertex probability set as parameter in the FEDRA vertexing routine, as shown for the charm-CC sample in Figure 5.14.

Secondary vertex confirmation

The reconstruction of vertices in the ν_μ-CC sample works quite well, in the charm-CC sample a problem occurred. Several times, the reconstructed primary vertex was not built with the primary tracks, but also with charm daughter tracks that had a low minimum distance w.r.t. the muon, thus, in the automatic FEDRA vertexing the two-track association had a high vertex probability. While for high multiplicity vertices this did not imply a big problem, as due to the high multiplicity the correct primary interaction is found, in the so-called 2-Vee topology there is a non-negligible chance for finding a wrong primary vertex, as indicated in Figure 5.15. Here, the muon track is associated with a charm daughter to build a fake primary vertex. The decay search procedure will find both remaining tracks, but the charm reconstruction will fail and provide no useful vertex. In real emulsion scanning an eye-check of the event can identify this problem, when the decay length is at least about $100\,\mu$m. The automatic processing needed a small modification: vertex associations between all short daughter candidates and the μ-track
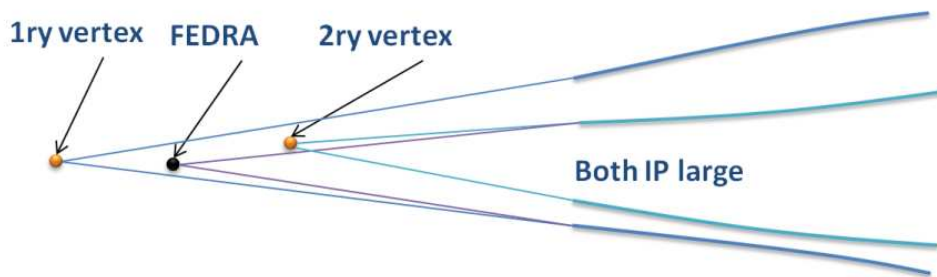
Figure 5.15: *Reconstruction failure of the primary vertex for short decays in FEDRA.*

were implemented. If a vertex can be built more upstream and with a higher vertex probability than the original one, the primary vertex will be changed to the new association, and the previously attached tracks will become short daughter candidates.

5.5 Charm efficiencies

5.5.1 Efficiencies after applying the DSP

To estimate the efficiency of charm detection with the OPERA detector, the Decay Search Procedure, as described in appendix D was implemented into the ORFEO/FEDRA framework, see section 5.2. The feedback of the procedure was a list of tracks for each short, long neutral and long charged topology events. To crosscheck the charm efficiency, the selected tracks MC-ID was compared to the MC truth of the charm daughters. If at least one of the tracks was truly a charm, and found in the correct category, i.e. short for short events, the event was classified as found. Otherwise, the event was a background event. Tracks that did not belong to the charm interaction were also accounted as wrong hints, thus a discrimination between background and charm data became possible, and will be described in the section 5.5.2. As already mentioned, the content of the charm-CC sample had to be corrected for the branching ratio and the charm decay topologies. Additionally, the ratio between short and long decays was taken into account. Furthermore each ECC was divided into two zones, plate 1-47 and plate 48-57, i.e. two regions where either 10 plates downstream of the primary vertex or less were available for the decay search, as indicated in Figure 5.16.
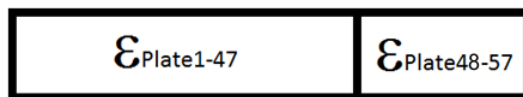
Figure 5.16: *The two zones in the ECC, one from plate 1-47, the other from plate 48-57 to account for the shorter reconstruction volume in the last plates.*

In the region starting with plate 53 the request on the minimum number of basetracks for a daughter track was reduced to two, to take into account the small number of plates available. From the efficiencies of all considered event categories summarized in Table 5.4, the results are combined before mean efficiency values are calculated to finally obtain an overall charm efficiency for the OPERA experiment: In the following the steps of combination are explained and the results of the individual steps are presented (the production branching fraction of charm particles were summarized in Table 5.1 and in Table 5.2 the topological decay ratios, the defined sub-categories for decay search in Table 5.3). For the 0 prong topology of all charmed particles the reconstruction efficiency was set to zero, even though, especially for D^0 decays, γ showers might point to the vertex.

In the first step the located events for event categories with a reconstructed primary vertex/track in the emulsions 1-47 and 48-57 are combined. The results of step 1 are summarized in Table 5.5. In the second step the located events for short and long charm decay topologies are combined. The results of the second step are summarized in Table 5.6. In the third step the long and short charm decay topology located events are combined

charm-type	primary vertex/track	1 prong		3 prong	
		entries	found	entries	found
D$^+$	prim. vertex (plate 48-57)	20	8	52	44
	prim. vertex (plate 1-47)	176	87	223	190
SHORT	prim. track (plate 48-57)	13	7	32	28
	prim. track (plate 1-47)	143	68	133	128
D$^+$	prim. vertex (plate 48-57)	66	20	92	64
	prim. vertex (plate 1-47)	306	165	419	345
LONG	prim. track (plate 48-57)	4	0	0	–
	prim. track (plate 1-47)	18	0	1	1

charm-type	primary vertex/track	2 prong		4 prong	
		entries	found	entries	found
D^0	prim. vertex (plate 48-57)	211	141	60	48
	prim. vertex (plate 1-47)	1142	805	261	221
SHORT	prim. track (plate 48-57)	35	25	10	10
	prim. track (plate 1-47)	224	193	25	25
D^0	prim. vertex (plate 48-57)	186	154	43	38
	prim. vertex (plate 1-47)	938	878	188	172
LONG	prim. track (plate 48-57)	20	120	4	4
	prim. track (plate 1-47)	147	143	26	25

charm-type	primary vertex/track	1 prong		3 prong	
		entries	found	entries	found
D$_s^+$	prim. vertex (plate 48-57)	5	2	11	6
	prim. vertex (plate 1-47)	49	26	91	75
SHORT	prim. track (plate 48-57)	12	8	8	7
	prim. track (plate 1-47)	45	38	39	38
D$_s^+$	prim. vertex (plate 48-57)	6	5	12	7
	prim. vertex (plate 1-47)	44	34	64	58
LONG	prim. track (plate 48-57)	0	–	0	–
	prim. track (plate 1-47)	0	–	0	–

charm-type	primary vertex/track	1 prong		3 prong	
		entries	found	entries	found
Λ_c^+	prim. vertex (plate 48-57)	35	7	90	48
	prim. vertex (plate 1-47)	222	36	432	225
SHORT	prim. track (plate 48-57)	55	17	35	33
	prim. track (plate 1-47)	302	107	229	197
Λ_c^+	prim. vertex (plate 48-57)	1	1	3	2
	prim. vertex (plate 1-47)	12	10	20	19
LONG	prim. track (plate 48-57)	0	–	0	–
	prim. track (plate 1-47)	0	–	0	–

Table 5.4: Located charm event tables for D$^+$, D^0, D$_s^+$ and Λ_c^+ decays for the two brick zones containing the primary vertex. The entries are the number of generated (analyzed) MC events.

charm-type	primary vertex/track	1 prong entries	found	3 prong entries	found
D$^+$ SHORT	prim. vertex	196	95	275	234
	prim. track	156	75	165	156
D$^+$ LONG	prim. vertex	372	185	511	409
	prim. track	22	0	1	1

charm-type	primary vertex/track	2 prong entries	found	4 prong entries	found
D^0 SHORT	prim. vertex	1353	946	321	269
	prim. track	259	218	35	35
D^0 LONG	prim. vertex	1124	1032	231	210
	prim. track	167	163	30	29

charm-type	primary vertex/track	1 prong entries	found	3 prong entries	found
D$_s^+$ SHORT	prim. vertex	54	28	102	81
	prim. track	57	46	47	45
D$_s^+$ LONG	prim. vertex	50	39	76	65
	prim. track	0	–	0	–

charm-type	primary vertex/track	1 prong entries	found	3 prong entries	found
Λ_c^+ SHORT	prim. vertex	257	43	522	273
	prim. track	358	124	264	230
Λ_c^+ LONG	prim. vertex	13	11	23	21
	prim. track	0	–	0	–

Table 5.5: Located charm event table for D$^+$, D^0, D$_s^+$ and Λ_c^+ decays for events with a reconstructed primary vertex or only a primary track. The entries are the number of generated (analyzed) MC events.

charm-type	1 prong entries	found	2 prong entries	found	3 prong entries	found	4 prong entries	found
D$^+$ SHORT	352	170			440	390		
D$^+$ LONG	394	185			512	410		
D^0 SHORT			1612	1164			356	304
D^0 LONG			1291	1195			261	239
D$_s^+$ SHORT	111	74			149	126		
D$_s^+$ LONG	50	39			76	65		
Λ_c^+ SHORT	615	167			786	503		
Λ_c^+ LONG	13	11			23	21		

Table 5.6: Located charm event table for all short and long decays.

and the efficiency is calculated:

$$\epsilon_{Charm_{X\,prong}} = \frac{found\,entries_{Charm_{short\,(X\,prong)}} + found\,entries_{Charm_{long\,(X\,prong)}}}{total\,entries_{Charm_{X\,prong}}} \tag{5.2}$$

The results are given in Table 5.7.

charm-type	ϵ_{0prong}	ϵ_{1prong}	ϵ_{2prong}	ϵ_{3prong}	ϵ_{4prong}
BF charged (PDG)	–	0.65±0.09	–	0.35±0.06	–
BF neutral (PDG)	0.15±0.06	–	0.70±0.06	–	0.145±0.005
D^+	–	0.476±0.018	–	0.840±0.012	–
D^0	0.	–	0.813±0.007	–	0.880±0.013
D_s^+	–	0.702±0.036	–	0.849±0.024	–
Λ_c^+	–	0.283±0.018	–	0.648±0.017	–

Table 5.7: Efficiency table for all branching topologies, for all charm types. The errors for the efficiency are statistical, and computed using Equation 5.6. The BF for the decay topologies are taken from Table 5.2.

In the fourth step the decay topology efficiencies for the four charm particles are averaged to obtain the total efficiency for the individual particles (BF - branching fraction, taken from the PDG [112], and shown in Table 5.2):

$$\epsilon_{D^+} = BF_{1\,prong} * \epsilon_{D^+_{1\,prong}} + BF_{3\,prong} * \epsilon_{D^+_{3\,prong}} \tag{5.3}$$

for the D^+ as example for charged charm (D^+, D_s^+ and Λ_c^+) and for neutral charm D^0 as:

$$\epsilon_{D^0} = BF_{2\,prong} * \epsilon_{D^+_{2\,prong}} + BF_{4\,prong} * \epsilon_{D^+_{4\,prong}} \tag{5.4}$$

The results of the fourth step are summarized in Table 5.8. The systematic error is due to the uncertainties of the topological branching fraction, as given in Table 5.2.

Finally, an overall charm efficiency is obtained by weighting the individual charm efficiencies with their production branching ratio (BR, see Table 5.1):

$$\epsilon_{charm} = BR_{D^+} * \epsilon_{D^+} + BR_{D^0} * \epsilon_{D^0} + BR_{D_s^+} * \epsilon_{D_s^+} + BR_{\Lambda_c^+} * \epsilon_{\Lambda_c^+} \tag{5.5}$$

The result is also given in Table 5.8.

charm-type	BR	efficiency
D^+	$21.7 \pm 3.4\%$	0.603±0.013 (stat.)±0.066 (syst.)
D^0	$43.8 \pm 3.0\%$	0.696±0.005 (stat.)±0.049 (syst.)
D_s^+	$9.2 \pm 3.8\%$	0.753±0.025 (stat.)±0.081 (syst.)
Λ_c^+	$25.3 \pm 4.9\%$	0.411±0.013 (stat.)±0.046 (syst.)
TOTAL	$\frac{\sigma_{charm}}{\sigma_{CC}} = 4.38\pm0.26\%$	**0.609±0.005 (stat.)±0.054 (syst.)**

Table 5.8: Efficiency table for all charm type and total efficiency.

The error calculation of the statistical error in the Table 5.7 was calculated using the formula

$$\Delta\epsilon_{stat} = \pm\frac{1}{n}\sqrt{\frac{x(n-x)}{n}} \tag{5.6}$$

with x - number of charm events found per channel and n - total number of charm events per channel. The larger systematic error in Table 5.8 is due to the uncertainty in both branching ratio and branching fraction of the charmed particles and are only affecting the combined efficiencies in Table 5.8. To summarize, the overall charm efficiency of the DSP is 60% before any cuts are applied. However, without applying any cuts there is an expectation of background events due to low momentum tracks (0.6-1 GeV), detached from the primary vertex in ν_μ-CC events, scattering and re-interaction of hadronic tracks, strange particle decays (K_s^0, Λ), electrons with a long range before showering, etc. As the scanning laboratories made a pre-selection on the events, based on their experience, different from laboratory to laboratory, the background was not calculated for this efficiency before applying cuts.

Crosscheck with Napoli/Bari study

To crosscheck the result of this work, an independent study from the Napoli/Bari groups was performed, starting from another charm-CC beamfile. Their results, as given in Tables 5.9 and 5.10 are in good agreement with the results given in Tables 5.7 and 5.8. No statistical error is given here, as the starting numbers of the sample are similar, it should have the same order of magnitude.

charm-type	ϵ_{0prong}	ϵ_{1prong}	ϵ_{2prong}	ϵ_{3prong}	ϵ_{4prong}
BF charged	–	0.65	–	0.35	–
BF neutral	0.15	–	0.70	–	0.145
D^+	–	0.45	–	0.82	–
D^0	0.	–	0.78	–	0.85
D_s^+	–	0.63	–	0.82	–
Λ_c^+	–	0.28	–	0.57	–

Table 5.9: Efficiency table for all branching topologies (Naples/Bari study).

charm-type	BR	efficiency
D^+	0.217	0.58±0.06 (syst.)
D^0	0.438	0.67±0.07 (syst.)
D_s^+	0.092	0.70±0.08 (syst.)
Λ_c^+	0.253	0.38±0.04 (syst.)
TOTAL	–	**0.58±0.06 (syst.)**

Table 5.10: Efficiency table for all charm type and total efficiency (Naples/Bari study).

Dependence off the efficiency on the lower vertex probability cut

As already mentioned, the influence of the lower cut on the minimal vertex probability parameter of FEDRA was studied. The results, presented in Figure 5.17 show that with a higher cut value the total charm efficiency increases.
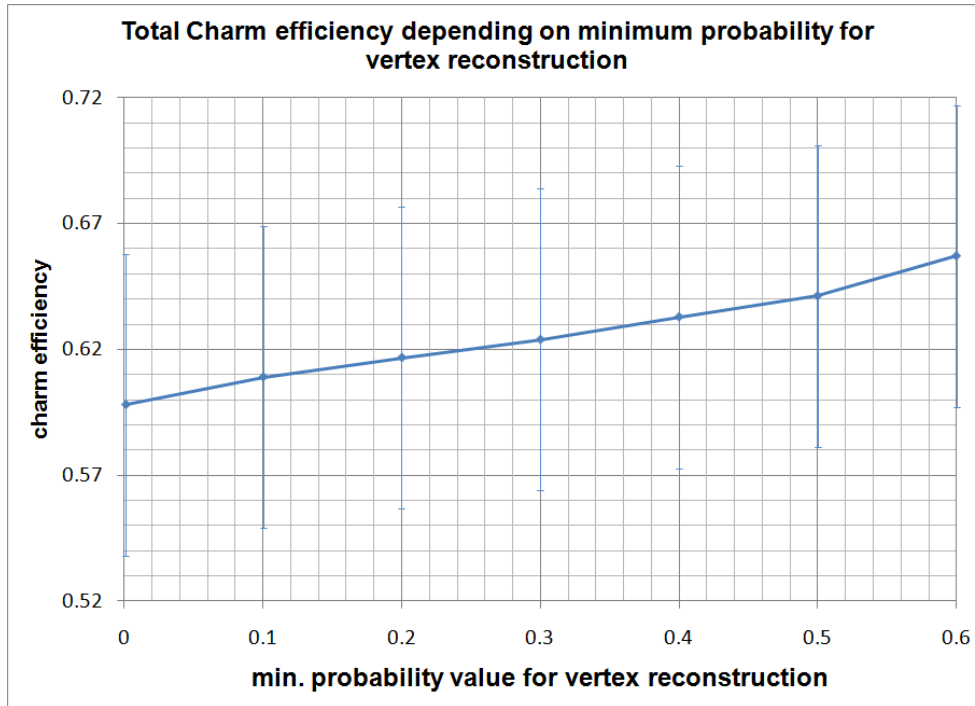
Figure 5.17: *Total charm efficiency depending on the lower vertex probability cut during the FEDRA vertexing. A lower cut of 0.1 was used to calculate the efficiencies given in Tables 5.4 - 5.8.*

This increase is related to the fact, that Λ_c^+ daughters previously attached to a primary vertex with a low vertex probability, are no longer attached to this vertex and become decay daughter candidates. Thus, the single prong efficiency increases from about 28% (see Table 5.7) to about 65%. The drawback of a higher initial cut is that the expected background increases when large cuts on the probability are reached, since also true primary track candidates, previously attached are no longer used to build a vertex (see Figure 5.14). Since the background for the probability cut of 0.001 and 0.1 are the same, and the efficiency is higher in the latter case, the charm efficiencies reported in section 5.5.1 are calculated with this probability cut.

5.5.2   Cuts and remaining background for a high purity charm sample

The efficiency calculated in the previous section is the maximal possible charm finding rate without cuts applied to suppress the background. Nevertheless, it will be influenced by fake events found. Mainly the following event categories contain fake (background) events:

- Short: Large IP tracks at the primary vertex due to smearing effects of the MC (in real data its due to the minimal resolution, emulsion shrinkage and distortion). Decays of other short lived particles, like K_s^0

- Long Charged: Multiple Coulomb scattering (MCS), or low momentum daughters at the vertex for kink; π/K-re-interactions.

- Long Neutral: K_s^0 decays into pions (rare) or scattering tracks with a missing base-track.
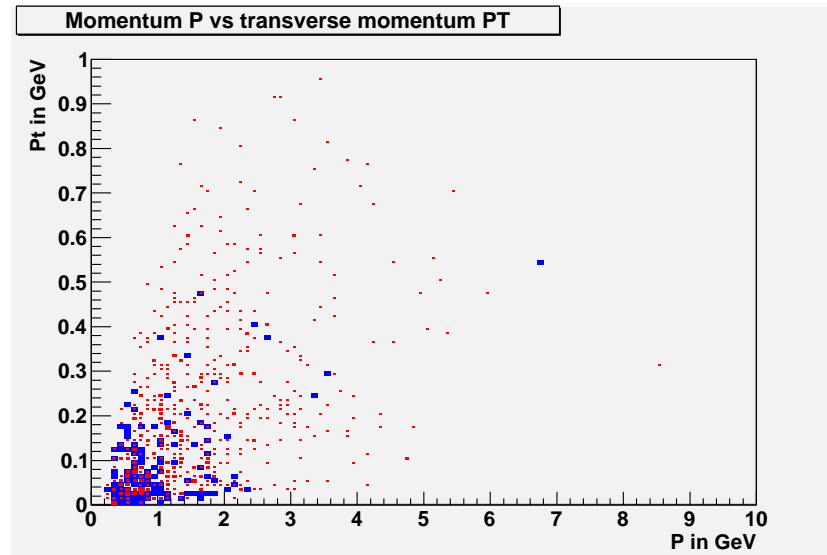
Figure 5.18: *Momentum P versus transverse momentum P_t (relative to parent track) for daughter tracks of the single muon, secondary track short decay topology. In red the number of true charm candidates are shown, in blue the background due to non-charm daughters.*

Additionally, all channels are influenced by low momentum tracks, belonging to the primary vertex, especially the short and long charged channels. To reduce the number of fake tracks in the selection of the decay search procedure list, cuts had to be defined for decay daughter candidates, based on the momentum data from MC truth. Starting from the distribution of the momentum P versus the transverse momentum P_t (transverse momentum to the parent track), shown in e.g. Figure 5.18 for the primary muon, secondary track short decay class as defined in Table 5.3, the optimal cut on the momentum P and transverse momentum P_t was calculated according to the "figure-of-merit" :

$$\epsilon_{charm} * (1 - \epsilon_{background}) * \frac{signal}{background} \tag{5.7}$$

To calculate the best cut in regions where only signal exists, the ratio of the signal to background was set to one. As already mentioned in Table 5.3, ten different track classes for tracks selected in the decay search procedure exist, additionally, the cut on the lower vertex probability was varied, thus, for each cut on the lower vertex probability and its 10 classes the optimal cut values for the momentum P and transverse momentum P_t was calculated for two different cut shapes: the cut was performed either on momentum and
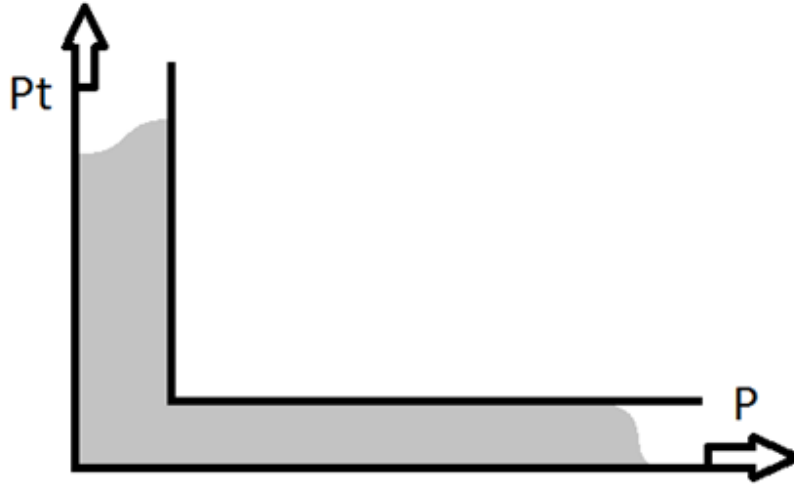
Figure 5.19: *Area selected by the "P&&P_t" cut on momentum an transverse momentum, the excluded area is indicated in grey. The P_t cut has to selected in such way, that $P_t \leq P$.*

transverse momentum (P&&P_t), or on momentum or transverse momentum (P||P_t), as shown in Figures 5.19 and 5.20. Not shown in the Figures is the upper limit of the cut defined by $P_t \leq P$, as $P_t = \sin(kinkangle) \times P \approx \sqrt{(\Delta TX)^2 + (\Delta TY)^2}P$ with $\Delta TX/TY$ as the difference in the TX/TY slope between parent and daughter. As shown in Figure 5.18, the scale of the Y-axis is a factor 10 smaller than the X-axis, thus this implicit cut is not needed to be plotted in the Figures as it is represented by a nearly vertical line close to the Y-axis, i.e. it is already included.

Figure 5.20: *Area selected by the "P||P_t" cut on momentum an transverse momentum, the excluded area is indicated in grey. The P_t cut has to selected in such way, that $P_t \leq P$.*
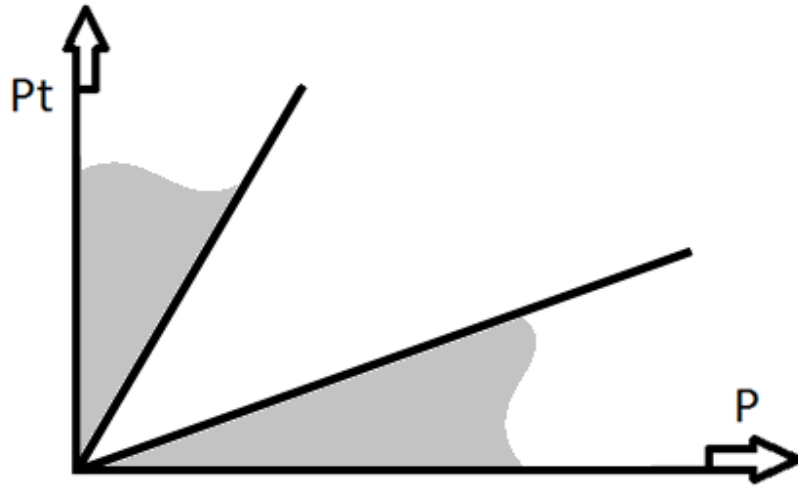
Figure 5.21: *Area selected by a third possible cut on momentum an transverse momentum, the excluded area is indicated in grey. The P_t cut has to selected in such way, that $P_t \leq P$.*

The third possibility investigated was the cut selecting an area in the P-P_t-plane as shown in Figure 5.21. Since the background is mostly concentrated at low P and/or P_t values, as one can see from the P versus P_t plot in Figure 5.18 (and the others in the Appendix E), the third cut probability was less effective than a rectangular cut due to the centering of the background at low P and P_t values and thus, was not further regarded.

Due to the momentum resolution of the MCS method of 20%, the step-size of the calculated cut was 0.5 GeV for the momentum P and 0.05 GeV for the transverse momentum P_t. Here I will present only the selection for the cut on the lower vertex probability of 0.5 (the plots of the "figure-of-merit" and the efficiency for all other cuts on the lower vertex probability are available, they are similar, only for larger cuts on the lower vertex probability an increase on the momentum cut, and thus a decrease of the efficiency is observed, as also good primary tracks will not be used to form the primary vertex and hence enlarge the number of decay daughter candidates). Shown in Figures 5.22 and 5.23 are the calculated values for single muon, secondary track short event class, as defined in Table 5.3, the plots for the other classes can be found in the Appendix F, Figures F.1 - F.18. Each class has the plots for the "P&&P_t" cut in the left column, in the right column the "P||P_t" cut plots are shown. The upper two plots show the "figure-of-merit" in 3-d and in 2-d, while in the lower two plots the charm efficiency is shown in 3-d and 2-d. The charm efficiency plots are needed in case that two equivalent cuts for the "figure-of-merit" exist, in that case the cut with the higher charm efficiency was chosen. For each plot, the bottom left corner of each bin marks the selected cut value for P and/or P_t.

From the scales of the top plots in Figure 5.22 and 5.23 one can see that the P||P_t-cut has a higher value for the "figure-of-merit", thus this cut shape was selected for this class. The peak in the distribution is reached for the bin which has the left bottom corner values 2.0 GeV for P and 0.25 GeV for P_t, thus selecting the cut. The other cuts are selected in an identical way and summarized in Table 5.11.
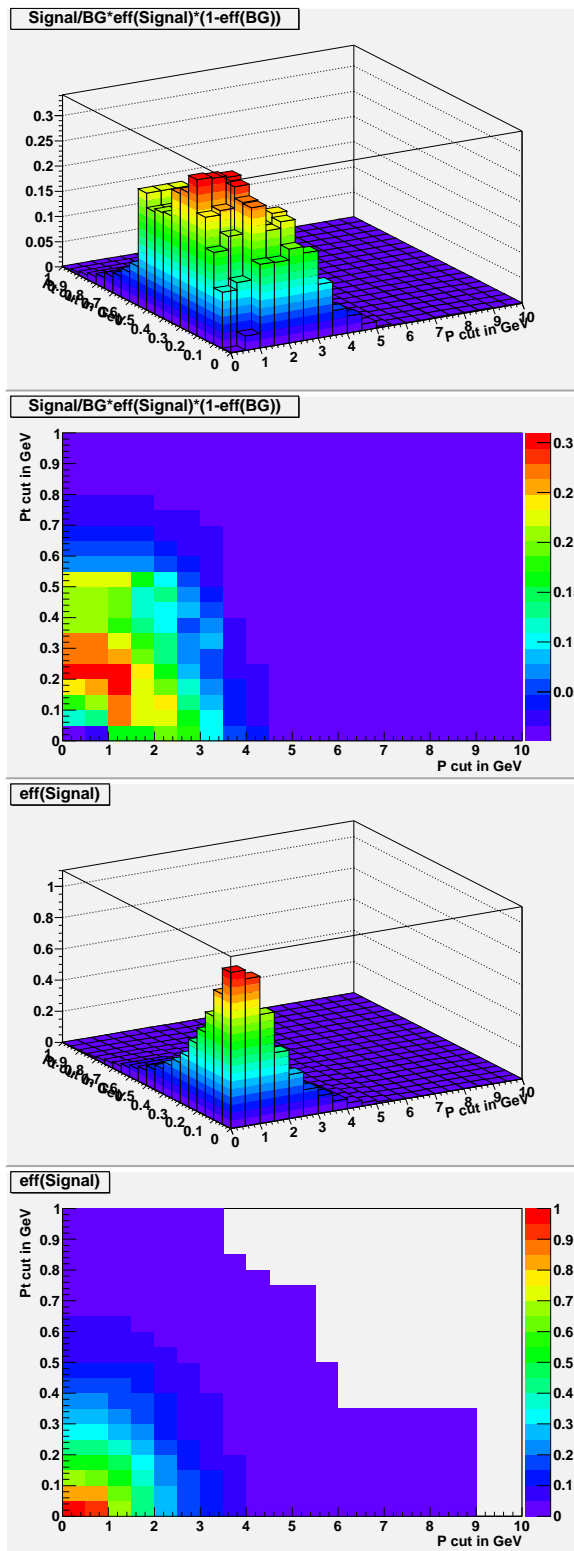
Figure 5.22:   "$P\&\&P_t$" cut for the class short_pt_st: (top) 3-d view of the "figure-of-merit" calculation for the cut, 2-d view below. (bottom) 3-d view of the charm efficiency for the cut, 2-d view below.
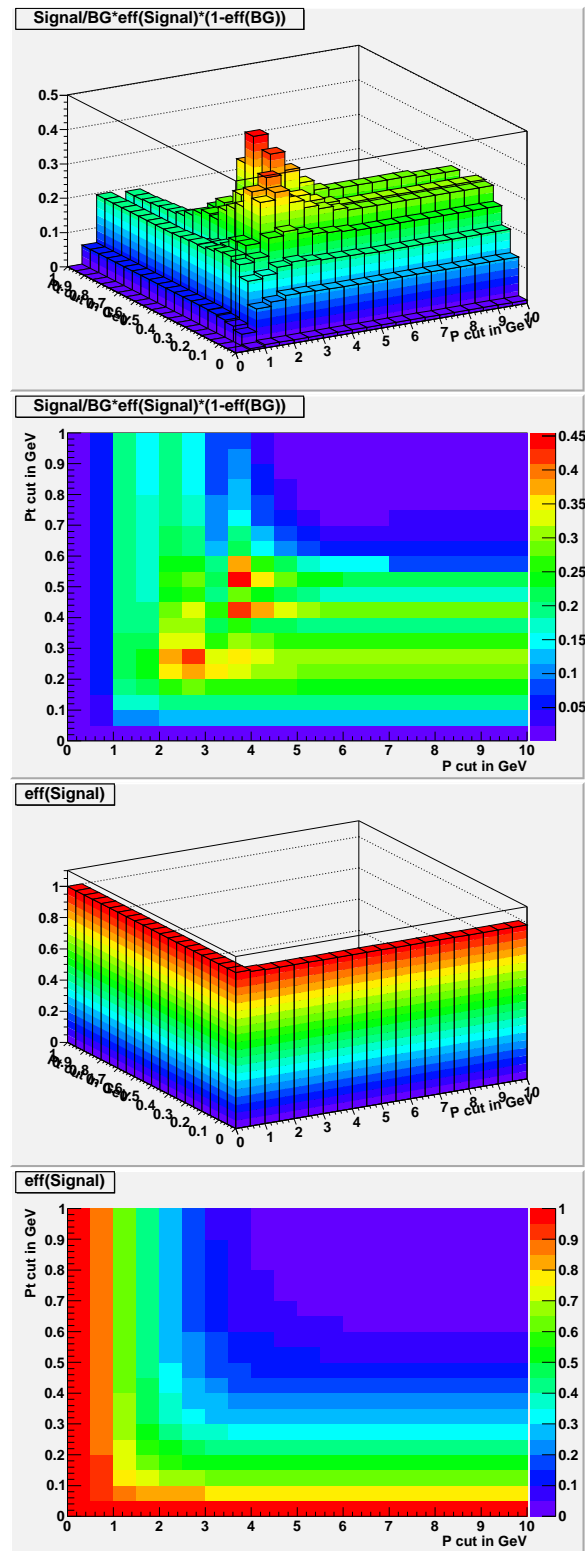
Figure 5.23:   "$P||P_t$" cut for the class short_pt_st: (top) 3-d view of the "figure-of-merit" calculation for the cut, 2-d view below. (bottom) 3-d view of the charm efficiency for the cut, 2-d view below.

class name	momentum P	transverse momentum P_t	cut-shape
short_pt_st	2.0	0.25	$P||P_t$
short_pt_sv	1.5	0.00	$P\&\&P_t$
short_pv_st	2.0	0.05	$P||P_t$
short_pv_sv	2.0	0.15	$P\&\&P_t$
longn_pt_st	1.5	0.20	$P\&\&P_t$
longn_pt_sv	1.0	0.20	$P\&\&P_t$
longn_pv_st	3.0	0.05	$P\&\&P_t$
longn_pv_sv	1.5	0.00	$P\&\&P_t$
longc_pv_st	3.5	0.60	$P||P_t$
longc_pv_sv	5.5	0.15	$P||P_t$

Table 5.11: Summary of the momentum and transverse momentum cuts and the selected cut-shape for an initial vertex probability of 0.5 for the FEDRA reconstruction. The background in three or more prong events was small, thus the cuts are only applied on single tracks and 2-prong vertices.

After applying the cuts, most of the remaining decay daughter candidates will be true charm daughters, as shown in Figure 5.24 and in the Appendix E, Figures E.1 - E.9.

For each cut value for the vertex probability, the P and P_t cuts were optimized according to their "figure-of-merit", and the charm efficiency was calculated, the result is shown in Figure 5.25. Contrary to the continuous increase observed before without P and P_t cuts (see Figure 5.17), the higher number of background tracks from undetached primary tracks forces a tighter cut for large probabilities, thus the efficiency decreases. The highest efficiency is reached for a vertex probability cut of 0.5, thus, the restriction to that value
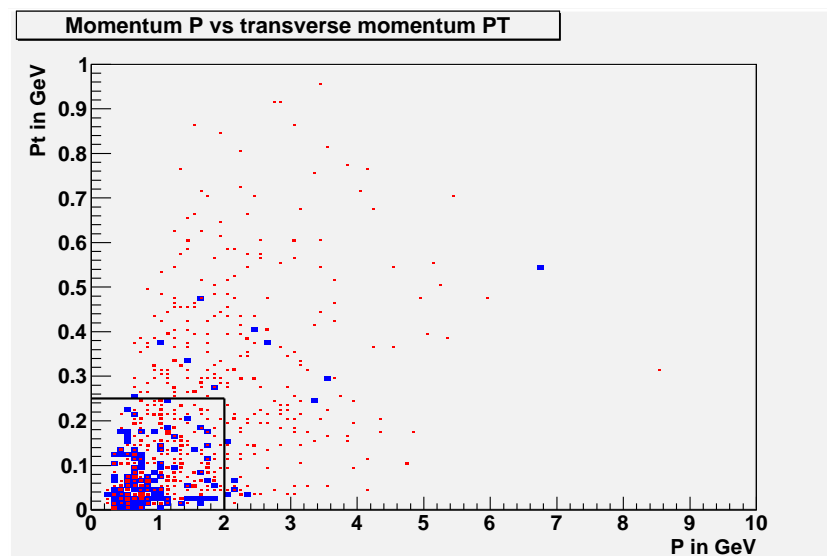
Figure 5.24: *Momentum P versus transverse momentum P_t (relative to parent track) for daughter tracks of the single muon, secondary track short decay topology, the high purity cuts are indicated by the black lines. In red the number of true charm candidates are shown, in blue the background due to non-charm daughters.*
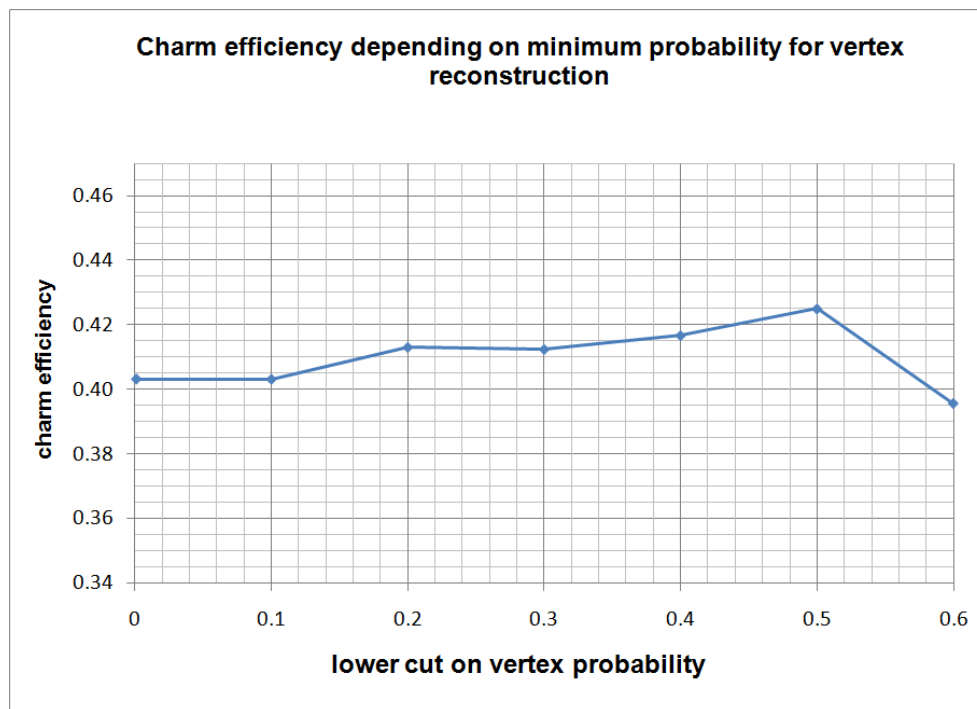
Figure 5.25: *Total charm efficiency depending on the minimum vertex probability cut during the FEDRA vertexing, after applying the high purity cut.*
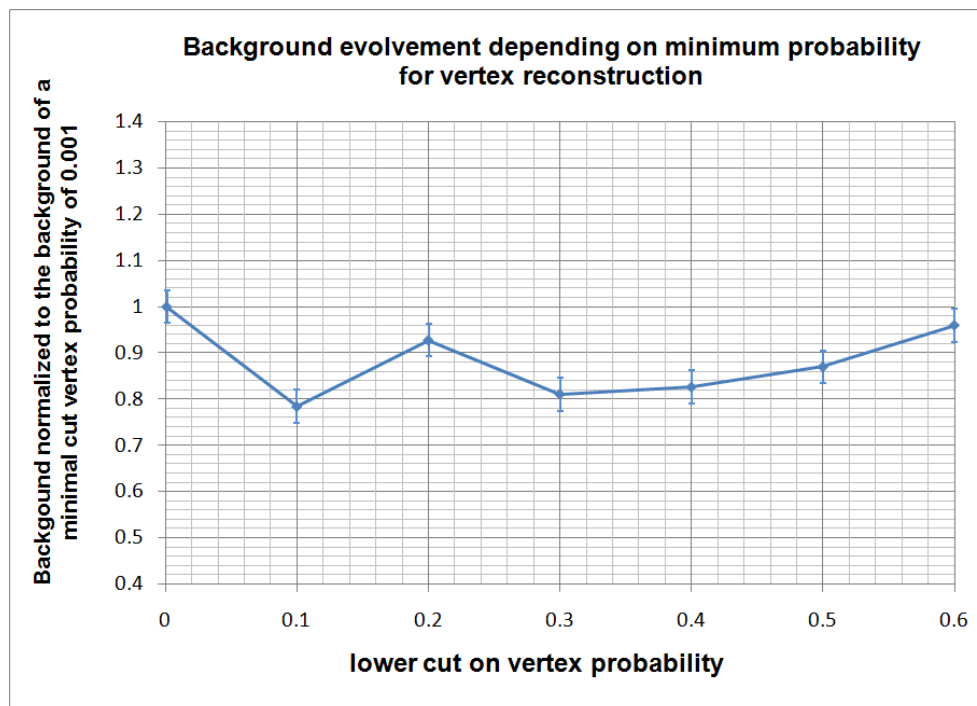
Figure 5.26: *Background evolevement depending on the minimum vertex probability cut during the FEDRA vertexing, after applying the high purity cut.*

for the plots in the previous discussion on background selection.

All surviving background events for each vertex probability cut were inspected by eye at the event display, to confirm the background and evaluate its origin. For the 0.5 vertex probability cut sample 25 background events remain in a total of 7511 ν_μ-CC MC events, nine of them due to the decays of short lived particles as K_s^0 and Λ, the others due to hadronic re-interaction and large angle scattering of protons, π and Kaons. In the charm-CC sample 7361 events were reconstructed, with 15 background events remaining here: four were due to short-lived particles, while the others were due to the hadronic re-interaction and large angle scattering. The topologies to which the background events belong are summarized in Table 5.12. In Figure 5.26 shown is the evolvement of the background versus the cut on the lower vertex probability, as one can see it is flat, with large statistical errors, due to the low number of entries for the final background sample.

ν_μ-CC MC	1 prong	2 prong	3 prong	4 prong
SHORT	1	0	1	0
LONGN	1	7	1	0
LONGC	8	5	1	0

charm-CC MC	1 prong	2 prong	3 prong	4 prong
SHORT	0	0	1	0
LONGN	3	3	1	2
LONGC	2	2	1	0

Table 5.12: Surviving located background events for the various topologies after applying the momentum P and transverse momentum P_t cut on the 7511 ν_μ-CC and 7362 charm-CC MC events.

The previously mentioned background estimation still suffers from both, hadronic background and non-charmed short lived particles decays as K_s^0 and Λ. While using the cuts defined with the "figure-of-merit", only a momentum cut was applied in the multiple prong short and long neutral category, now an additional cut on the minimum transverse momentum was applied to reduce the background of short lived particles further, based on the work by the NOMAD collaboration [266]. The cut on P_t of $0.2\,\text{GeV}$ was required to reduce the Λ and K_s^0 topology, as indicated in Figure 5.27. Summarized in Table 5.13 are the cuts for this "high purity" selection, in *italic* the changes w.r.t. to the previous analysis.

Using the modified cuts, the background was reduced and the final surviving number of background events in the different topologies of the charm-CC and ν_μ-CC Monte Carlo is summarized in Table 5.14.

The final background for the charm analysis was estimated combining the background from the ν_μ-CC and charm-CC sample according to the weighted mean and scaling it to the number of located ν_μ-CC events:

$$BG_{expected} = \left[\frac{BG_{charm-CC}}{N_{charm-CC}} * 0.0438 + \frac{BG_{\nu_\mu-CC}}{N_{\nu_\mu-CC}} * (1 - 0.0438) \right] * N_{located\,CC-Events}$$

$$(5.8)$$
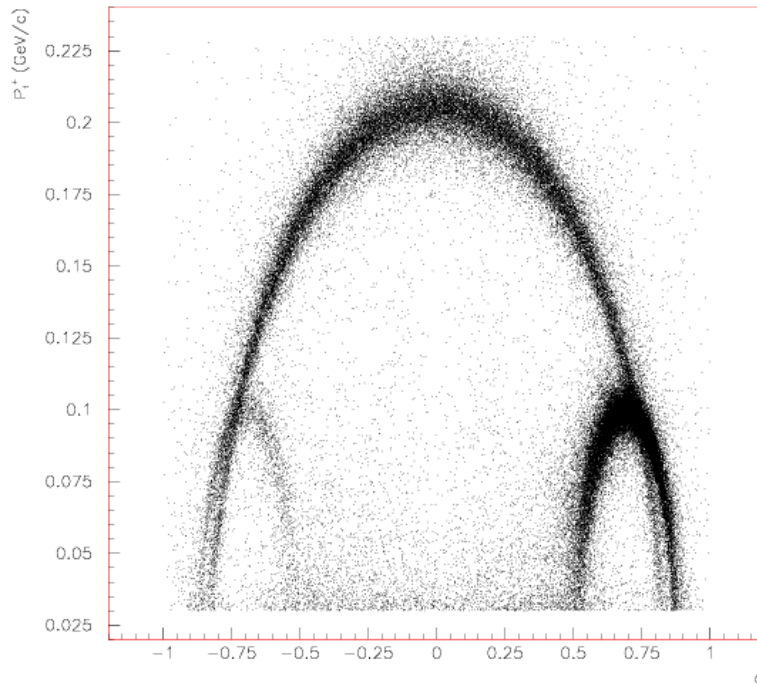
Figure 5.27: *Armenteros' plot for reconstructed V^0's: K^0_s's cluster on the large central ellipse, Λ's on the small right ellipse and the smaller sample of $\overline{\Lambda}$'s on the left one. x-axis $\alpha = \frac{P_l^+ - P_l^-}{P_l^+ + P_l^-}$, y-axis P_t^+. Picture from [266].*

Here $BG_{charm-CC}$ and $BG_{\nu_\mu-CC}$ is the background expected from the MC simulation. The error is calculated using the $\sqrt{BG_{charm-CC}}$ or $\sqrt{BG_{\nu_\mu-CC}}$ respectively, if no surviving background event was confirmed in the Monte Carlo sample, the upper limit was calculated on a 90% confidence level (CL). From the run 2008+09 1088 events had been analyzed at the time of this thesis, of which 187 were NC and 901 were classified as CC

class name	momentum P	transverse momentum P_t	cut-shape
short_pt_st	2.0	0.25	P||P_t
short_pt_sv	1.5	*0.20*	P&&P_t
short_pv_st	2.0	0.05	P||P_t
short_pv_sv	2.0	*0.20*	P&&P_t
longn_pt_st	1.5	0.20	P&&P_t
longn_pt_sv	1.0	0.20	P&&P_t
longn_pv_st	3.0	0.05	P&&P_t
longn_pv_sv	1.5	*0.20*	P&&P_t
longc_pv_st	3.5	0.60	P||P_t
longc_pv_sv	5.5	0.15	P||P_t

Table 5.13: Summary of the momentum and transverse momentum cuts and the selected cut-shape for an initial vertex probability of 0.5 for the FEDRA reconstruction, after applying the high purity cut, indicated in *italic* to suppress short-lived non-charm neutral decays background. The background in three or more prong events was small, thus the cuts are only applied on single tracks and 2-prong vertices.

ν_μ-CC MC	1 prong	2 prong	3 prong	4 prong
SHORT	1	0	0	0
LONGN	0	1	0	0
LONGC	6	2	1	0

charm-CC MC	1 prong	2 prong	3 prong	4 prong
SHORT	0	0	0	0
LONGN	0	2	0	0
LONGC	1	0	1	0

Table 5.14: Surviving located background events for the various topologies after applying the momentum P and transverse momentum P_t cut on the 7511 ν_μ-CC and 7362 charm-CC MC events after applying the high purity cut.

interaction.

topology	1 prong	2 prong	3 prong	4 prong
SHORT	0.11±0.11 (stat.)	<0.28	<0.28	<0.28
LONGN	<0.28	0.13±0.12 (stat.)	<0.28	<0.28
LONGC	0.69±0.29 (stat.)	0.23±0.16 (stat.)	0.12±0.12 (stat.)	<0.28

SUM	1.28±0.39 (stat.)

Table 5.15: Total background expectation for the various topologies with the high purity cuts for 901 located ν_μ-CC events. If no background was observed, the 90% CL upper limit is given.

Thus, the background estimation was normalized to 901 CC events, and is summarized in Table 5.15. An independent Fluka MC estimation by D. Autiero and S. Dusini of the hadronic background in the kink channel, i.e. for the longc single prong topology, with the proposed cuts, gave a result of $5.3 \times 10^{-4}\, BG/CC$ [267]. Normalized on 901 events this gives 0.46 expected background events, and is comparable to the expected 0.69±0.29 (stat.) background events from my MC estimation. The main remaining background is expected to be originating from hadronic re-interactions, and further studies are needed to clarify possible improvements in the charm channel.

5.5.3 Charm efficiencies and expected background for the high purity sample

The influence of the tighter transverse momentum cut on the efficiency was studied too. As in the previous section for the efficiency calculation, the number of located evennts was combined and the efficienicy was obtained with equations 5.2 - 5.5. The located events per charm type and category for the events with a primary vertex/track located in plate 1-47 or 48-57 are summarized in Table 5.16. The combined located events for event categories with a reconstructed vertex/track are summarized in Table 5.17. The combined located events for short and long charm decay topologies is summarized in Table 5.18.

charm-type	primary vertex/track	1 prong		3 prong	
		entries	found	entries	found
D$^+$	prim. vertex (plate 48-57)	16	4	49	25
	prim. vertex (plate 1-47)	165	63	204	118
SHORT	prim. track (plate 48-57)	17	6	35	26
	prim. track (plate 1-47)	154	39	152	104
D$^+$	prim. vertex (plate 48-57)	65	8	92	52
	prim. vertex (plate 1-47)	306	84	417	296
LONG	prim. track (plate 48-57)	5	0	0	–
	prim. track (plate 1-47)	18	0	3	1

charm-type	primary vertex/track	2 prong		4 prong	
		entries	found	entries	found
D^0	prim. vertex (plate 48-57)	202	105	58	34
	prim. vertex (plate 1-47)	1076	573	249	135
SHORT	prim. track (plate 48-57)	45	26	12	9
	prim. track (plate 1-47)	290	163	36	26
D^0	prim. vertex (plate 48-57)	180	104	43	34
	prim. vertex (plate 1-47)	912	605	183	137
LONG	prim. track (plate 48-57)	26	22	4	4
	prim. track (plate 1-47)	173	132	32	28

charm-type	primary vertex/track	1 prong		3 prong	
		entries	found	entries	found
D$_s^+$	prim. vertex (plate 48-57)	5	2	10	3
	prim. vertex (plate 1-47)	45	20	79	39
SHORT	prim. track (plate 48-57)	12	6	9	7
	prim. track (plate 1-47)	49	25	51	40
D$_s^+$	prim. vertex (plate 48-57)	6	3	12	5
	prim. vertex (plate 1-47)	44	23	64	51
LONG	prim. track (plate 48-57)	0	–	0	–
	prim. track (plate 1-47)	0	–	0	–

charm-type	primary vertex/track	1 prong		3 prong	
		entries	found	entries	found
Λ$_c^+$	prim. vertex (plate 48-57)	30	5	78	21
	prim. vertex (plate 1-47)	178	17	367	81
SHORT	prim. track (plate 48-57)	60	12	47	26
	prim. track (plate 1-47)	346	78	294	139
Λ$_c^+$	prim. vertex (plate 48-57)	1	1	3	2
	prim. vertex (plate 1-47)	12	3	20	15
LONG	prim. track (plate 48-57)	0	–	0	–
	prim. track (plate 1-47)	0	–	0	–

Table 5.16: Located charm event tables for D$^+$, D^0, D$_s^+$ and Λ$_c^+$ decays for the two brick zones containing the primary vertex after applying the high purity cuts. The entries are the number of generated (analyzed) MC events.

charm-type	primary vertex/track	1 prong		3 prong	
		entries	found	entries	found
D$^+$	prim. vertex	181	67	253	143
SHORT	prim. track	171	45	187	130
D$^+$	prim. vertex	371	92	509	348
LONG	prim. track	23	0	3	1

charm-type	primary vertex/track	2 prong		4 prong	
		entries	found	entries	found
D^0	prim. vertex	1278	678	307	169
SHORT	prim. track	335	189	48	35
D^0	prim. vertex	1092	709	226	171
LONG	prim. track	199	154	36	32

charm-type	primary vertex/track	1 prong		3 prong	
		entries	found	entries	found
D$_s^+$	prim. vertex	50	22	89	42
SHORT	prim. track	61	31	60	47
D$_s^+$	prim. vertex	50	26	76	56
LONG	prim. track	0	–	0	–

charm-type	primary vertex/track	1 prong		3 prong	
		entries	found	entries	found
Λ_c^+	prim. vertex	208	22	445	102
SHORT	prim. track	406	90	341	165
Λ_c^+	prim. vertex	13	4	23	17
LONG	prim. track	0	–	0	–

Table 5.17: Located charm event table for D$^+$, D^0, D$_s^+$ and Λ_c^+ decays for events with a reconstructed primary vertex or only a primary track after applying the high purity cuts. The entries are the number of generated (analyzed) MC events.

charm-type	1 prong		2 prong		3 prong		4 prong	
	entries	found	entries	found	entries	found	entries	found
D$^+$ SHORT	352	112			440	273		
D$^+$ LONG	394	92			512	349		
D^0 SHORT			1613	867			355	204
D^0 LONG			1291	863			262	203
D$_s^+$ SHORT	111	53			149	89		
D$_s^+$ LONG	50	26			76	56		
Λ_c^+ SHORT	614	112			786	267		
Λ_c^+ LONG	13	4			23	17		

Table 5.18: Located charm event table for all short and long decays after applying the high purity cuts.

The decay topology efficiency for the four charm particles is given in the Table 5.19. The overall charm efficiency per charm type and the overall efficiency are summarized in Table 5.20.

charm-type BF charged (PDG) BF neutral (PDG)	ϵ_{0prong}	ϵ_{1prong}	ϵ_{2prong}	ϵ_{3prong}	ϵ_{4prong}
charm-type	ϵ_{0prong}	ϵ_{1prong}	ϵ_{2prong}	ϵ_{3prong}	ϵ_{4prong}
BF charged (PDG)	–	0.65±0.09	–	0.35±0.06	–
BF neutral (PDG)	0.15±0.06	–	0.70±0.06	–	0.145±0.005
D^+	–	0.273±0.016	–	0.653±0.015	–
D^0	0.	–	0.596±0.009	–	0.660±0.019
D_s^+	–	0.491±0.039	–	0.644±0.032	–
Λ_c^+	–	0.185±0.016	–	0.351±0.017	–

Table 5.19: Efficiency table for all branching topologies, for all charm types after applying the high purity cuts. The errors for the efficiency are statistical, and computed using Equation 5.6. The BF for the decay topologies are taken from Table 5.2.

charm-type	BR	efficiency
D^+	$21.7 \pm 3.4\%$	0.406±0.012 (stat.)±0.046 (syst.)
D^0	$43.8 \pm 3.0\%$	0.513±0.007 (stat.)±0.036 (syst.)
D_s^+	$9.2 \pm 3.8\%$	0.544±0.028 (stat.)±0.059 (syst.)
Λ_c^+	$25.3 \pm 4.9\%$	0.243±0.012 (stat.)±0.027 (syst.)
TOTAL	$\frac{\sigma_{charm}}{\sigma_{CC}} = 4.38 \pm 0.26\%$	**0.424±0.006 (stat.)±0.038 (syst.)**

Table 5.20: Efficiency table for all charm type and total efficiency after applying the high purity cuts.

In the high purity sample the total charm efficiency is 0.424±0.006 (stat.)±0.038 (syst.).

The systematic errors quoted are due to the uncertainty in the decay fraction topology and the production branching fraction; the fractions are obtained from the previous CHORUS experiment and extrapolated to the OPERA energies, hence the large uncertainties [201]. The statistical error on the other hand is defined by the size of individual categories inside the Monte Carlo sample and calculated as mentioned in equation 5.6.

To summarize the efficiency of the decay search procedure, we have one calculation where no cuts were requested to select the events and the high-purity sample based on a "figure-of-merit", taking into account background rejection based on the experience of previous experiments. The results are summarized in the Table 5.21.

No cuts selection	**0.609±0.005 (stat.)±0.054 (syst.)**
High purity selection	**0.424±0.006 (stat.)±0.038 (syst.)**

Table 5.21: Total charm efficiencies.

The statistical error of the efficiency is very small compared to the systematical one, thus, in further plots only the total error will be given.

	exp. charm events on 901 CC	exp. charm events on 100 CC
No cuts selection	24.04±2.58	2.67±0.29
High purity selection	16.75±1.8	1.86±0.20

Table 5.22: Expected charm events for 901 located ν_μ-CC events, and for each 100 located CC events.

5.5.4 Summary of the expected event and background rates

The efficiency calculated in section 5.5.1 and 5.5.3 are now used to calculate the number of expected charm events in the OPERA experiment for 901 ν_μ-CC events analyzed in the data from the years 2008+09. As already mentioned, 1088 neutrino interactions had been observed, and 901 were classified as ν_μ-CC, thus, all numbers represented in Table 5.22 refer to these 901 CC interactions (as on 100 located CC-events, given for completeness).

The Table 5.23 shows a more detailed view on the number of expected events per class for the high purity cut, i.e. for a total charm efficiency of 0.424±0.006 (stat.)±0.038 (syst.). The expected event rate is given per topology as defined in Table 5.3, and taking into account missing tracks at the reconstructed vertex, i.e. charged tracks missing due to large angle or low momentum (for more details, contact the author).

SHORT	1 prong		2 prong		3 prong		4 prong	
	exp.	error	exp.	error	exp.	error	exp.	error
Signal	5.29	0.52	3.59	0.18	1.03	0.16	0.38	0.03
BG	0.11	0.11	*	–	*	–	*	–
LONGN	**1 prong**		**2 prong**		**3 prong**		**4 prong**	
	exp.	error	exp.	error	exp.	error	exp.	error
Signal	0.95	0.03	2.41	0.07	0.16	0.01	0.39	0.03
BG	*	–	0.13	0.12	*	–	*	–
LONGC	**1 prong**		**2 prong**		**3 prong**		**4 prong**	
	exp.	error	exp.	error	exp.	error	exp.	error
Signal	1.66	0.32	0.30	0.10	0.57	0.23	0.01	0.00
BG	0.69	0.29	0.23	0.16	0.12	0.12	*	–

Table 5.23: Signal and Background expectation for the various topologies with the improved cuts. (* means that the expected rate is <0.28 events (90% CL)).

Chapter 6

Comparison of the Monte Carlo simulations with data

To confirm the results obtained with the Monte Carlo simulation, a comparison between real data and Monte Carlo events was made. In a first step, the ν_μ-CC and charm-CC MC sample was compared with the charged current muon data sample, presented in section 6.1. In section 6.2 the reconstruction of the primary vertex of the Monte Carlo simulation and the data will be given, while in section 6.3 the expected number of charm events is compared in detail with the observed data in the detector. Some examples of observed charm candidates will be given in section 6.4.

6.1 Muon momentum and angles (direction) in the MC sample

The most important variables to be compared between real data and MC events is the muon momentum and the slopes TX and TY, here on the data sub-sample of 112 measured muon tracks from the Bern scanning laboratory, which held all information required. As shown in the plots of Figures 6.1 and 6.2 the agreement in the slopes, which can be measured very precisely, is very good. The comparison was tested with a Kolmogorov-Smirnov comparison [268, 269], where a minimum distance estimation is used as a nonparametric test to compare different probability functions. The "goodness" of the agreement is expressed by the probability that both curves are identical. Between the shape of the slope TX w.r.t. the data a 93.9% chance of matching was reached, for the slope TY a 79.6% chance. The Monte Carlo curves were scaled to the number of muon tracks measured in real data.

The momentum comparison of data and MC simulation in the Figure 6.3 suffers from the resolution and the ability to measure the momentum in the bricks. As the momentum in the brick can be measured up to 6 GeV only (with the MCS method) with an error of 25%, only few bins can be compared between data and Monte Carlo simulation, even though statistics of the Monte Carlo simulation for larger momentum values is available. Nevertheless, the agreement between real data and Monte Carlo is good, the Kolmogorov-Smirnov test gave an agreement of 99.9%. The Monte Carlo curve was scaled to the number of real data events with a momentum smaller than 6 GeV, this is the reason
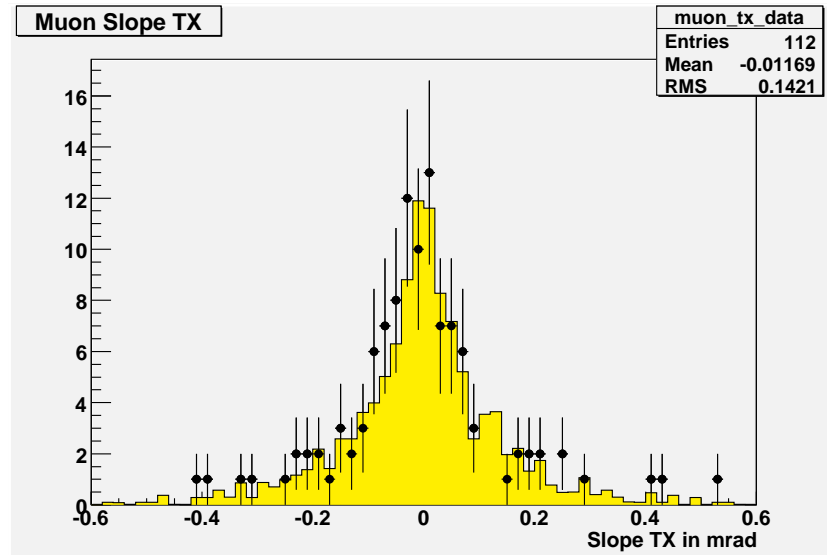
Figure 6.1: *Comparison between data and MC simulation of ν_μ and charm-CC events for the muon slope TX.*
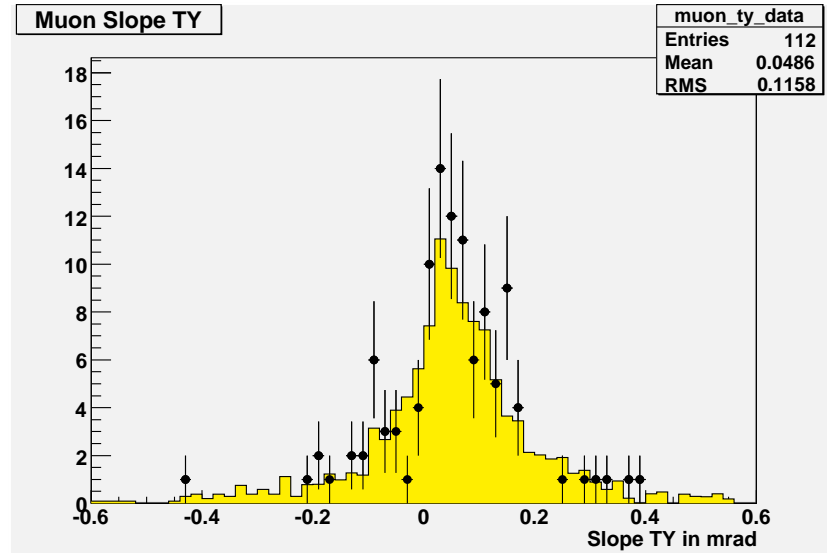
Figure 6.2: *Comparison between data and MC simulation of ν_μ and charm-CC events for the muon slope TY.*
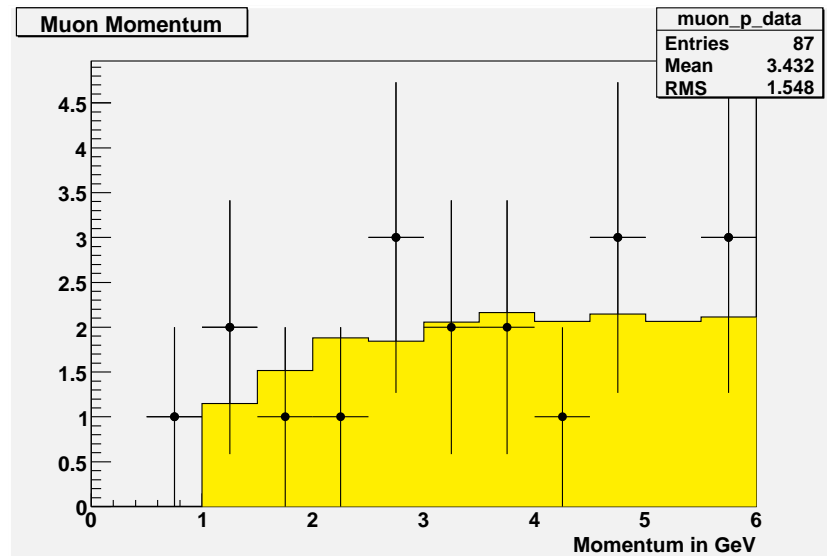
Figure 6.3: *Comparison between muon momentum in real data and MC simulation for ν_μ and charm-CC events in the ECC MC simulation. The error in Y is giving only the bin error, not the error on the momentum.*
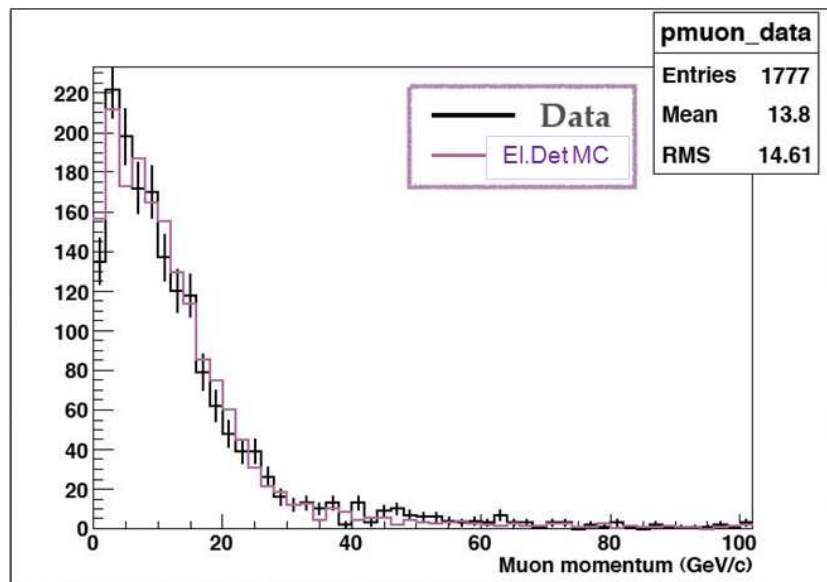
Figure 6.4: *Comparison between muon momentum in real data and MC simulation for ν_μ-CC events of the electronic detector MC simulation.*

why there are less muons in this plot than in the previous TX and TY slope plots. The comparison between larger momenta of the real data with MC was done by A. Meregaglia, using the same beamfile and the electronic detector Monte Carlo OpRelease (see section 4.3.2) and is shown in Figure 6.4. Here the agreement between real data and Monte Carlo is very good.

6.2 Primary vertex reconstruction in the MC sample

The second important verification of the Monte Carlo production is the comparison between the primary vertex reconstruction of the Monte Carlo simulation and the real data. After the decay search was applied, the primary vertex multiplicity and the impact parameter distribution were compared between the weighted ν_μ and charm-CC sample and the real data.

Shown in Figure 6.5 is the distribution of the impact parameter. The Monte Carlo reconstruction and real data agree well, even though the Kolmogorov-Smirnov comparison between the shape of the distribution gave a 18% chance. The Monte Carlo curves were scaled to the number of real data, i.e. all tracks at the primary vertex.

The comparison of the multiplicity between the Monte Carlo reconstruction and the real data is shown in Figure 6.6. As in the beamfile one has either charm or ν_μ charged current events, and the number of pure quasi-elastic events was not present in the beamfiles, the first bins are underestimated in the Monte Carlo. A complete comparison would be possible by adding the quasielastic interactions. Thus, a Kolmogorov-Smirnov comparison between the real data and Monte Carlo gave an agreement of 6.2%. The Monte Carlo curves were scaled to the number of real data events observed in Bern.
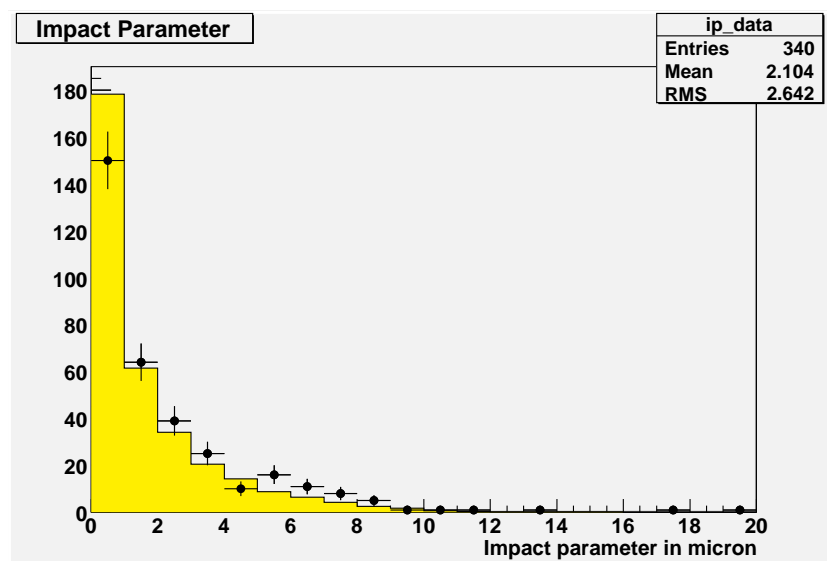
Figure 6.5: *Comparison of the primary vertex impact parameter in real data vs. MC simulation.*
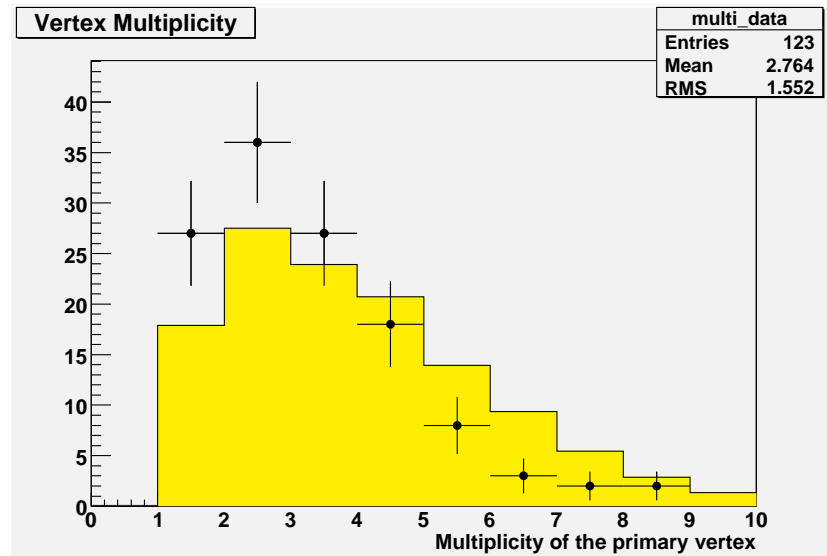
Figure 6.6: *Comparison of primary vertex multiplicity in real data vs. MC simulation.*

6.3 Observed and expected charm events

The number of charm events expected from the Monte Carlo simulation, normalized to 901 observed ν_μ-CC interactions, is compared to the number of charm events observed. To be classified as a charm event, a secondary vertex has to fulfill the following criteria, as decided in the collaboration:

- Decay observed within 5 plates of the primary vertex.

- Daughter tracks found with the decay search procedure.

- Daughter tracks within acceptance of the kinematical cuts, presented in section 5.5.2.

- Minimal kinkangle of 20 mrad between charm parent and daughter for charged charm.

- When no momentum measurement is possible, the Φ angle between charm and muon has to be large ($> 150°$) or the topology has to be background free (i.e. 4 prong events).

The total number of charm candidates found in the various scanning laboratories was 26 events. Applying the same kinematical cuts as to the Monte Carlo data, 8 events were rejected due to low momentum and/or transverse momentum, of which four were kink events, two single daughter neutral tracks and two Vee topologies.

Of the remaining 18 events, 12 could be confirmed by the measurement of the momentum of the charm daughters with the MCS method. For the six other candidates, three were recovered: one of the three was a kink, one a Vee, and they were accepted since their Φ-angle was in very good agreement with the MC expectation for charm, the third event was a 4-Vee decay topology, i.e. from a channel where no background was expected.

The events needed to be recovered, since their momentum could not be measured due to a very downstream interaction in the brick and the missing downstream bricks, as they were produced at the end of the target section. For the other three events the momentum measurement was not finished yet, thus, they were kept in the sample for the time being. In Table 6.1 the expected signal and background and the observed data events are summarized, in Table 6.2 is the summary of all charm candidates observed in the sample of 901 located CC events.

The decay length and Φ angle is compared between the observed events and the MC simulation in Figures 6.7 and 6.8, also here the agreement between data and Monte Carlo, expressed by the Kolmogorov-Smirnov test was very good with an agreement of 97.4% for the decay length and 62.8% for the Φ angle.

SHORT	1 prong events	2 prong events	3 prong events	4 prong events
Signal +BG	5.40±0.53	3.59±0.18	1.03±0.16	0.38±0.03
Data	1+1	0+1	1	1
LONGN	1 prong events	2 prong events	3 prong events	4 prong events
Signal +BG	0.95±0.03	2.54±0.14	0.16±0.01	0.39±0.03
Data	1	4+1	0	1
LONGC	1 prong events	2 prong events	3 prong events	4 prong events
Signal +BG	2.35±0.43	0.53±0.19	0.69±0.26	0.01±0.
Data	3	1	2	–

SUM	1 prong events	2 prong events	3 prong events	4 prong events
Signal +BG	8.71±0.92	6.66±0.41	1.88±0.42	0.78±0.07
Data	5+1	5+2	3	2

Total	MC exp. Signal	**16.75±1.80**
	MC exp. BG	**1.28±0.39**
	Data	**15+3**

Table 6.1: Signal and Background expectation vs. data. The total errors given are using the total efficiency, while for the different topologies they are estimated using the error for each specific topology (thus their sum is different to the total error given in the "Total" row). The data is given as X+Y, where X means the number of events with measured momentum or recovered events (see text) and Y means that the daughter momentum was not measurable.

Event-ID	Brick-ID	Laboratory	Year	Topology
222274169	127653	Padova	2008	Trident
222007691	65097	Bari	2008	Vee
180718369	34730	Napoli	2007	Kink
234654975	85405	Napoli	2008	4Vee
9214106181	66404	Napoli	2009	Kink
231012915	72853	Bern	2008	Vee
228563573	79117	Bern	2008	Vee
228197639	14653	Bern	2008	Vee
236177101	14714	Bern	2008	N1
234341013	27222	Bern	2008	C2
9231046733	35135	Bern	2009	C3
233478285	140875	Bologna	2008	Vee
234539244	51248	Nagoya	2008	Kink
233235784	88427	Nagoya	2008	Vee
23311658	81191	Nagoya	2008	N1
233609422	83484	Nagoya	2008	C3
9163097136	70300	Nagoya	2009	Vee
237491736	139294	Nagoya	2008	Vee
237403844	15459	Nagoya	2008	Vee
230694744	88951	Toho	2008	4Vee

Table 6.2: *Summary table of all charm events observed in the run sample of 901 located CC interactions.*
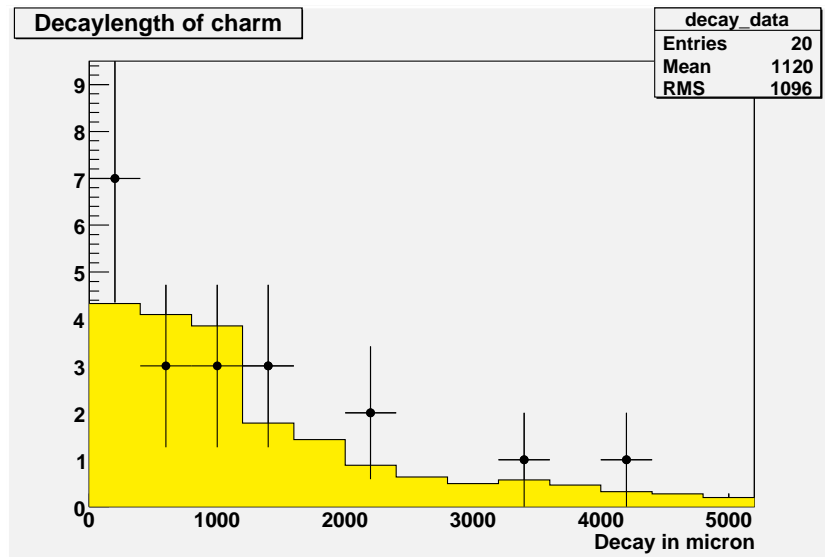
Figure 6.7: *Comparison of the decay length between real data and Monte Carlo.*
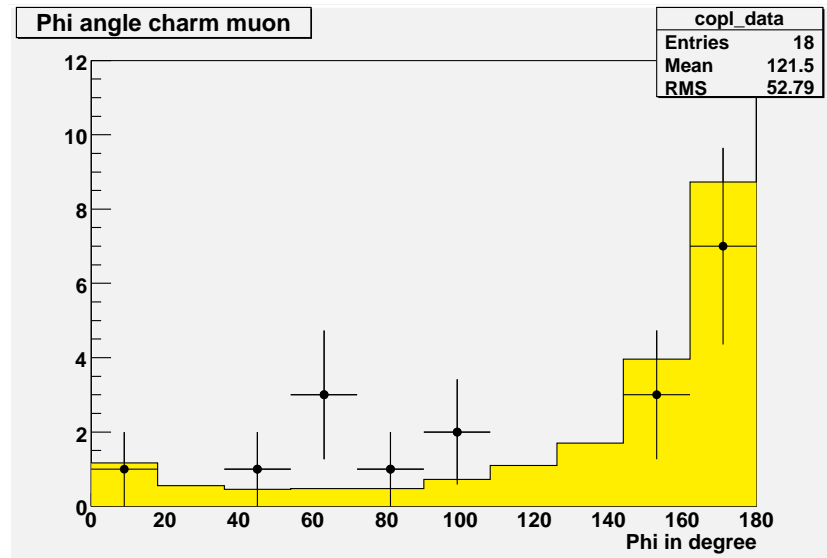
Figure 6.8: *Comparison of the* Φ *angle between real data and Monte Carlo.*

To test whether the observed (small) numbers of charm events in the different categories are statistically compatible with the MC expectations, a χ^2 test was performed (by L. Scotto): The calculated MC event and background rates are taken as "average expected data", and smeared by their error according to a Poisson distribution to simulate the expected data. In doing this, one can simulate several thousand OPERA experiments and calculate for each simulated experiment the χ^2 relative to the "average expected data", a distribution which should have a mean value of one, as shown in Figure 6.9. Afterwards, the χ^2 of the observed data is calculated and compared with the previously obtained χ^2-curve, thus one can test if the experimental observation is statistically in agreement with the expectation, of the observed events. With the high purity cut sample
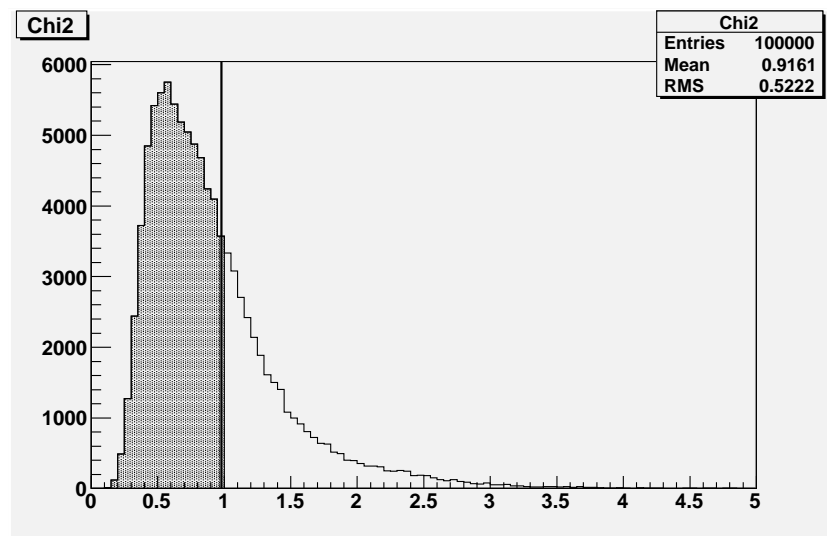
Figure 6.9: χ^2-*comparison of many simulated OPERA experiments with the observed charm events (see text for details).*

a χ^2 of 0.979 was calculated and is indicated by the black line in the Figure 6.9. Integrating the χ^2 from 0 to the observed value should give a number close to 0.5, here about 0.668 was calculated (grey area in the figure), i.e. the statistical agreement is good.

To summarize, 18 charm events were observed in the 901 ν_μ-CC interactions analyzed from the run years 2008+09 in the OPERA experiment, while 16.75$\pm$1.8 (tot.) charm and 1.28$\pm$0.39 (stat.) background events were expected from MC simulation.

The results of this study were used in [267] to demonstrate the feasibility to find and reconstruct short-lived particles in the detector and thus to support the observation of the first τ-decay in OPERA.

6.4 Examples of analyzed charm events

Due to the nice imaging capabilities of an emulsion detector, in the following section two reconstructed charm candidates are shown: the first OPERA charm candidate found in Naples (a kink topology), and a D^0 event found by myself in Bern.

6.4.1 First charm candidate (kink) from Naples
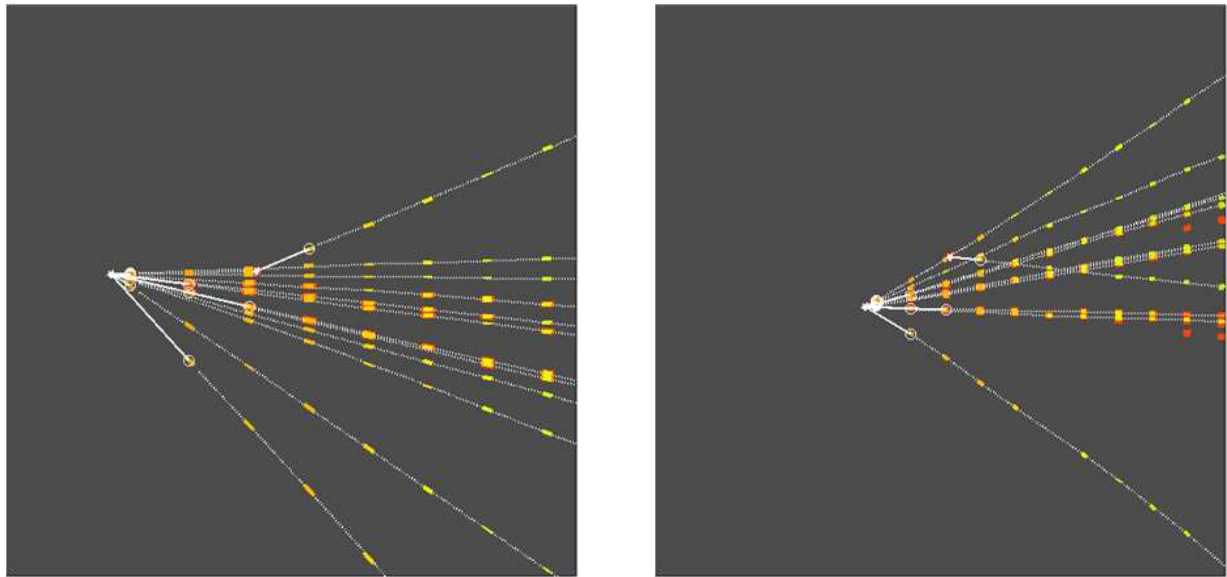
Figure 6.10: *(lfeft) X-view and (right) Y-view of one reconstructed charm kink, event ID 180718369, brick 34730 (run 2007).*

In the run of 2007 only few events were recorded, before it had to be stopped due to technical problems with the CNGS beam. Nevertheless, with more than 30 interactions recorded in the target, the expectation of one charm event was given, and one candidate was found in the Naples scanning lab and is shown in Figures 6.10 and 6.11. The topology was that of a charged kink, with a kink angle of about 200 mrad and a daughter momentum of $3.9^{+1.7}_{-0.9}$ GeV. Thus, the transverse momentum was $0.78^{+0.33}_{-0.19}$ GeV, i.e. within the acceptance of the cuts proposed. The phi angle between charm and muon was calculated to be 164°, the decay length is 3280 μm.
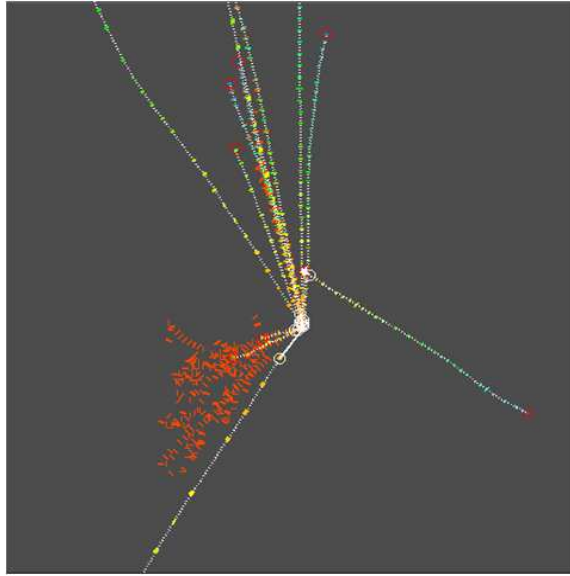
Figure 6.11: *ν-beam direction-view of one reconstructed charm kink, event ID 180718369, brick 34730 (run 2007).*

6.4.2 Charm candidate (Vee) from Bern

In November 2008 one candidate was scanned in Bern, and after following the Scanback predictions, a short decay into a Vee charm candidate with a single muon was found, shown in Figure 6.12. The topology is corresponding exactly to the possible muonic channel for τ-decays, where the μ would not belong to the primary, but the secondary decay vertex, as indicated in the top plot of Figure 6.14.
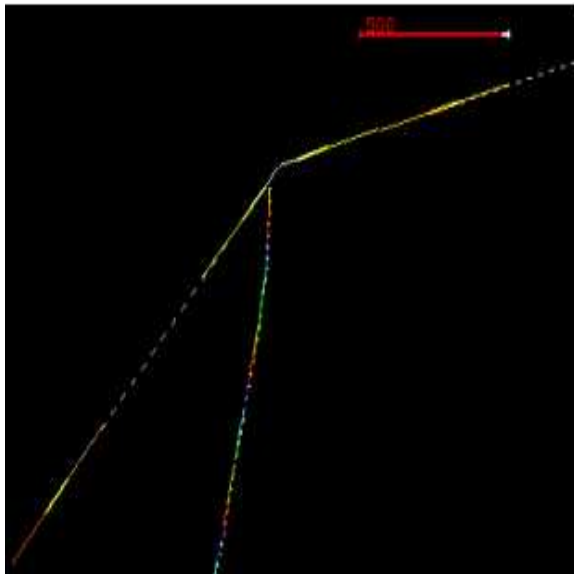
Figure 6.12: *ν-beam-view of event ID 231012915, brick 72853 (run 2008).*
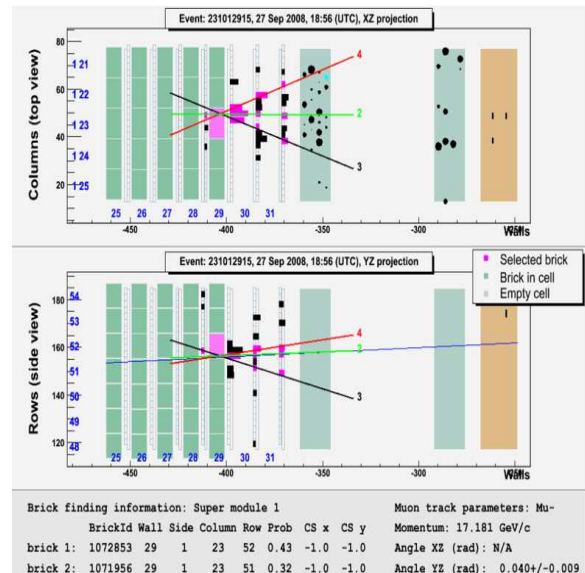
Figure 6.13: *Electronic detector view with overlayed CS candidates.*

The starting point of the tracks was confirmed bye eye in plate 22 of the selected brick, no microtrack could be found in the upstream plate. The Vee vertex was found
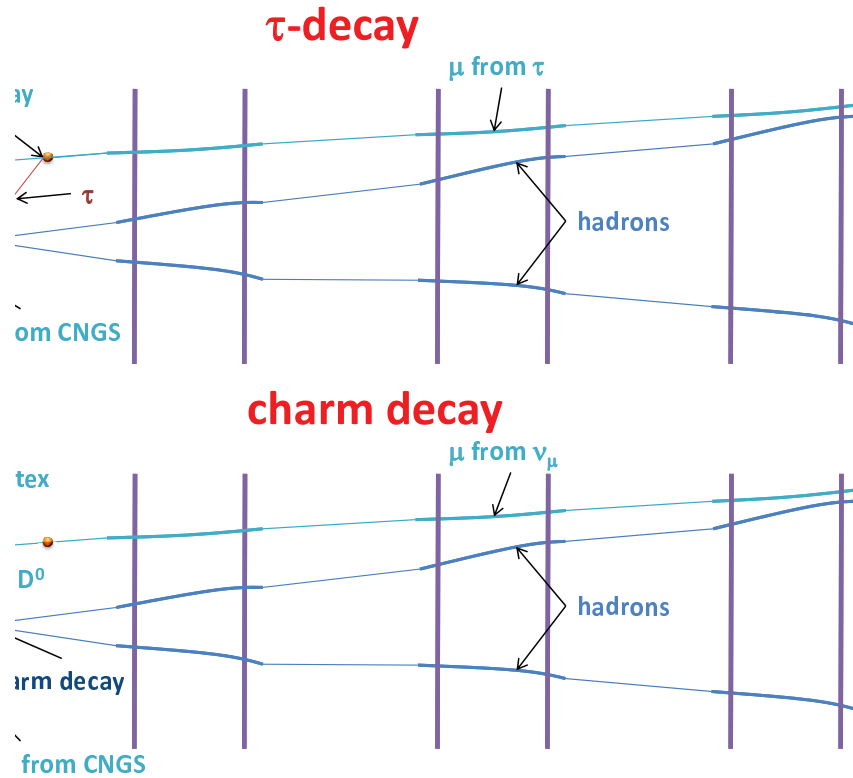
Figure 6.14: *The short decay into a Vee plus one single muon topology can be interpreted in two ways, either as τ-signal or charm, i.e. τ background, depending on the assumed position of the muon (single track) vertex relative to the reconstructed Vee vertex.*
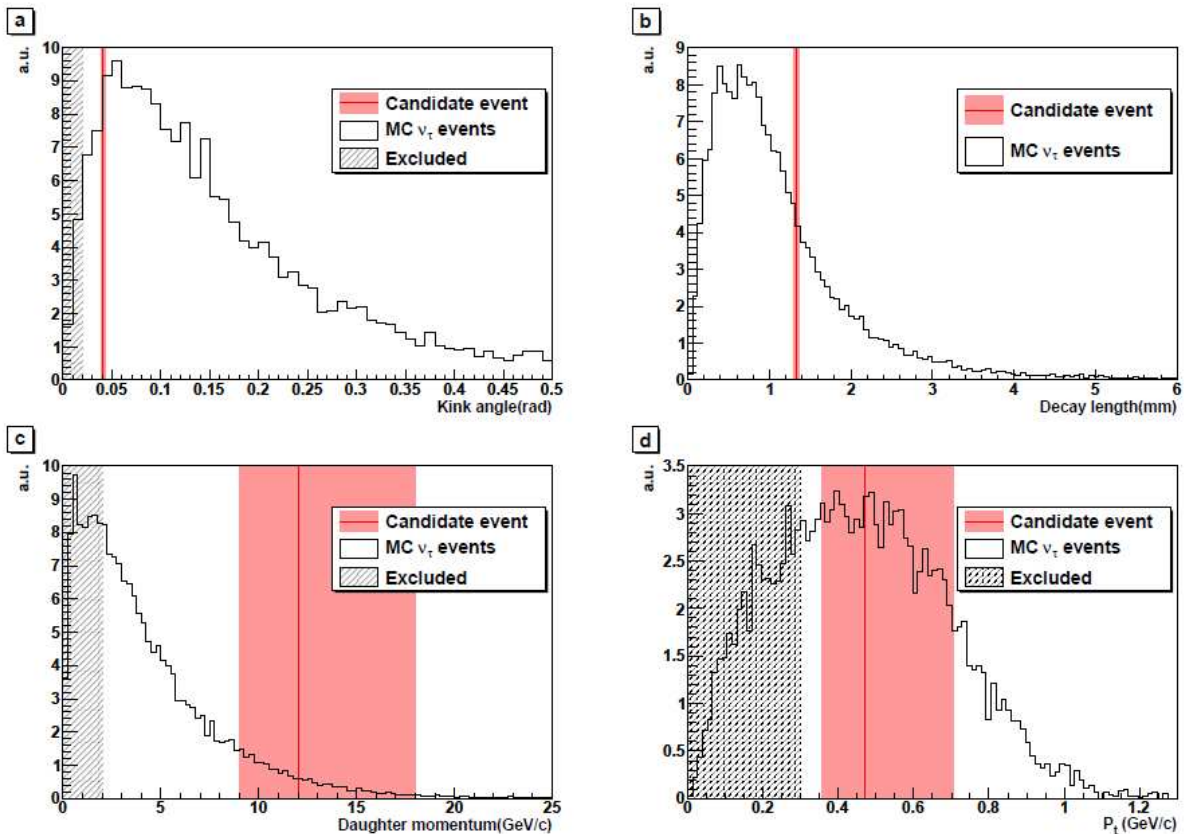
Figure 6.15: *The kinematical and topological τ-decay distributions. Picture from [267]*

$202\,\mu$m upstream plate 22, one of the daughter tracks had a slope of TX: 0.356, TY: 0.156, the other one TX: -0.282, TY: -0.242, their impact parameter to the vertex was $0.5\,\mu$m and $0.4\,\mu$m. The single track with a slope of TX: 0.000, TY: -0.030 had an impact parameter of $63\,\mu$m w.r.t. to that vertex, i.e. was clearly separated and tagged as muon by the electronic detector, as shown in Figure 6.13. No electron showers were found in the scanning volume.

The two possible hypotheses were tested: first is a $\tau \rightarrow \mu$ decay with two charged hadrons from the primary vertex (top of Figure 6.14), and the second hypothesis is a ν_μ-CC event with primary muon and a neutral charm Vee decay $D^0 \rightarrow h^+h^-$ with possible neutral hadrons h^0 (bottom of Figure 6.14). Assuming that a τ was produced, the Vee vertex would be the primary interaction, thus, the flight length of the τ had a maximum of $220\,\mu$m, thus the minimal kink-angle would be 0.312 rad. The momentum of the muon, measured with the electronic detector was about 17 GeV, corresponding to a transverse momentum larger than 5.3 GeV. Shown in Figure 6.15 are the kinematical and topological τ-decay distributions [267]. While the decay length is in agreement with a τ-decay, the minimum kinkangle and the momentum of the muon are in the tail of the expected τ-events (black curve). The transverse momentum in addition is out of the maximum range for τ-decays of about 1 GeV. For this reasons the first hypothesis of a τ-decay was discarded.

The second hypothesis, a single muon at the primary and a charm decay with a 2 prong vertex was favored, as the two vertex tracks had a minimal distance of $37\,\mu$m, respectively $13.5\,\mu$m to the muon, and their momentum was $1.3^{+0.8}_{-0.4}$ GeV, respectively $2.0^{+1.5}_{-0.6}$ GeV. To calculate the neutral charm (D^0) mass, three possible combinations for the hadron type of the daughter tracks were tested:

- Kaon-Pion: D^0 mass 1.26 GeV (+0.52 -0.23)

- Pion-Kaon: D^0 mass 1.30 GeV (+0.52 -0.22)
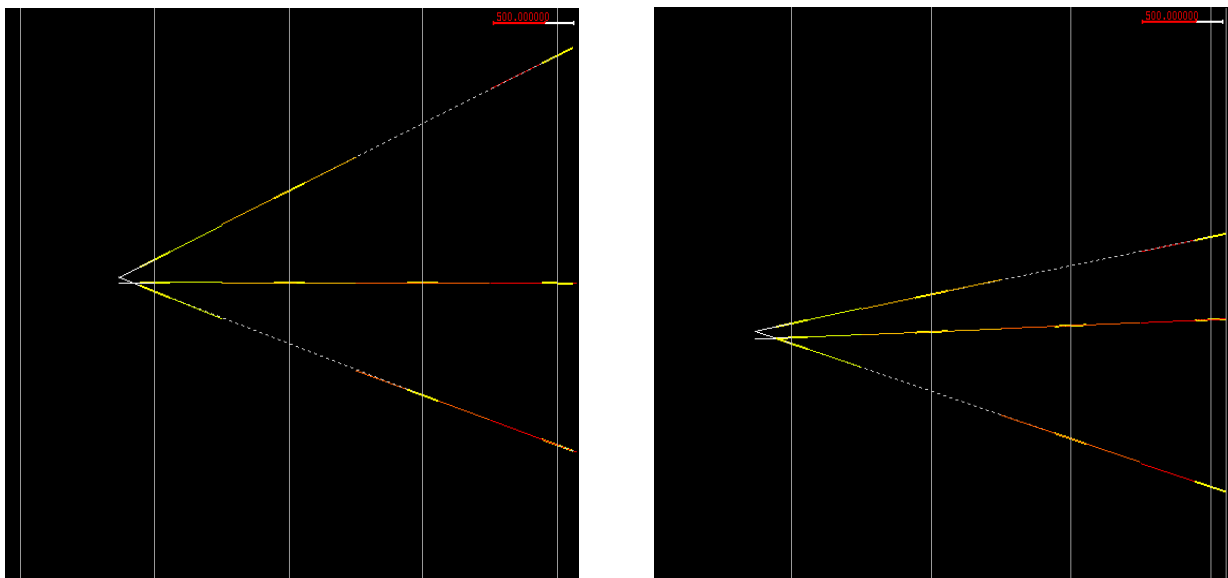
Figure 6.16: *(left) X-view and (right) Y-view of event ID 231012915, brick 72853 (run 2008).*

- Pion-Pion: D^0 mass 1.09 GeV (+0.58 -0.27)

The reconstructed D^0 mass is below the known value of 1.864 GeV. The assumption that one or more neutral tracks are missing at the vertex can account for the mass difference, which would additionally explain the topology of the event in more detail, as the two observed daughter tracks are not perfectly opposite aligned w.r.t to the muon in the transverse plane, as one would expect from a two-body decay at rest. The neutral daughter hypothesis is also favored by the branching topologies for neutral charm, the decay fraction into two charged hadrons plus several neutral hadrons is much higher than the one in two charged hadrons alone. Also from the electronic detector display additional neutral tracks are favored. As the brick was in the last filled downstream row of the target, no further brick could be extracted to search for γ showers from neutral decays. Nevertheless, the event was classified as charm since the minimal transverse momentum of the higher momentum daughter was found to be $0.59^{+0.44}_{-0.18}$ GeV, the minimal kink angle was 0.296 rad, the decay length had a maximum of $662\,\mu$m and the phi angle between charm and muon was at least $145°$, which is well in agreement with a D^0 decay.

Chapter 7

Conclusions

7.1 Summary of the charm efficiency in the OPERA experiment

In this thesis the charm production and detection efficiency in the OPERA experiment was investigated. The results show that a charm efficiency of about 0.425 can be reached in a low background sample, as shown in Table 7.1.

No cuts selection	**0.609±0.005 (stat.)±0.054 (syst.)**
High purity selection	**0.424±0.006 (stat.)±0.038 (syst.)**

Table 7.1: Total charm efficiencies.

With the estimated efficiency, the number of expected charm and background events was calculated, see Table 7.2 and 7.3

	exp. charm events on 901 CC	exp. charm events on 100 CC
No cuts selection	24.04±2.58	2.67±0.29
High purity selection	16.75±1.8	1.86±0.20

Table 7.2: Expected charm events for 901 located ν_μ-CC events, and for each 100 located CC events.

With the data of 901 ν_μ-CC interactions of the run 2008 and part of 2009 a comparison between data and Monte Carlo was made, and the agreement between charm events observed in the detector and the prediction was found to be excellent. In total, 18 charm events were observed in the run 2008+09 in a data sample of 901 CC interactions, when 16.75±1.80 (tot.) charm events and 1.28±0.39 (stat.) background events were expected (see Table 7.3). The observed fractions of the different decay topologies are statistically compatible with the MC expectation. The good agreement between MC simulation and data is shown in Figure 7.1.

The results of this thesis were used to confirm the first observation of a τ decay coming from $\nu_\mu \to \nu_\tau$ oscillation as proof of principle of the OPERA detector's capability to

SUM	1 prong events	2 prong events	3 prong events	4 prong events
Signal +BG	8.71±0.92	6.66±0.41	1.88±0.42	0.78±0.07
Data	5+1	5+2	3	2

Total	MC exp.	**16.75±1.80**
	BG.	**1.28±0.39**
	Data	**15+3**

Table 7.3: Signal and Background expectation vs data. Excerpt from Table 6.1.
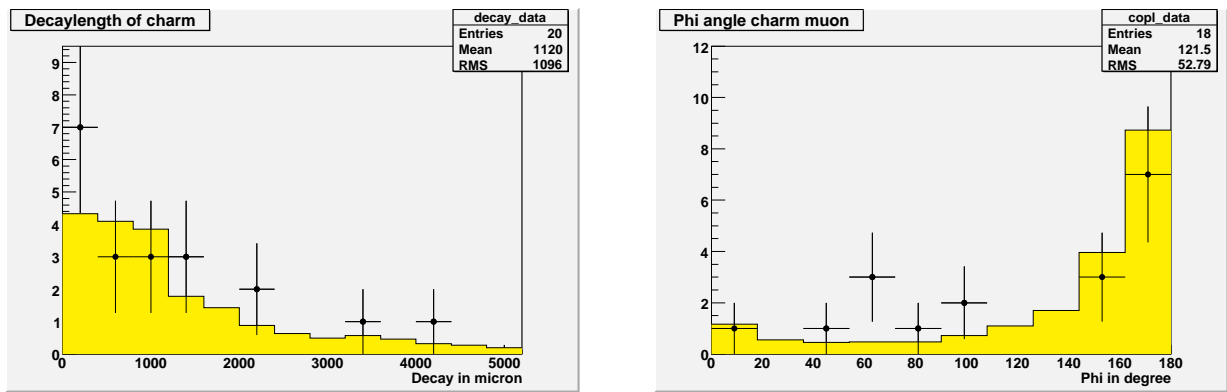
Figure 7.1: *Comparison of (left) the decay length between real data and Monte Carlo simulation and (right) the Φ angle between real data and Monte Carlo simulation.*

detect short-lived particle decays [267]. The efficiency study of this thesis (before cuts) was crosschecked by an independent analysis and the agreement between the two works was found to be excellent.

As a byproduct of the Monte Carlo studies, that were performed by F. Juget (LHEP Bern) and myself, the scanning strategy of the OPERA experiment was modified to an increased scanning volume of ten plates, w.r.t. the previous five, thus, the efficiency for beam ν_e (and also charm decay) detection was increased and already six ν_e events could be observed in the data of 2008 and 2009, compatible with the expectations. Additionally, a common strategy in all scanning laboratories was motivated and a decay search procedure was implemented, which helped recovering previously unnoticed charm events.

7.2   Summary of the HTS results for a LAr TPC

A second part of my work was the test of superconducting cables, see Appendix G. Several cables were tested at liquid argon and liquid nitrogen temperatures. The BSCCO cable was a copper stabilized ribbon of 4 mm width and a thickness of 0.4 mm. Figure 7.2 shows the critical current I_c measured in LN_2 and LAr as a function of the applied parallel and perpendicular magnetic field. The results obtained with second generation YBCO based cables are shown in Figure 7.3 for the 4 mm wide and 0.25 mm thick AMSC cable, and in Figure 7.4 for the 4 mm wide and 0.1 mm thick SuperPower cable. The measured
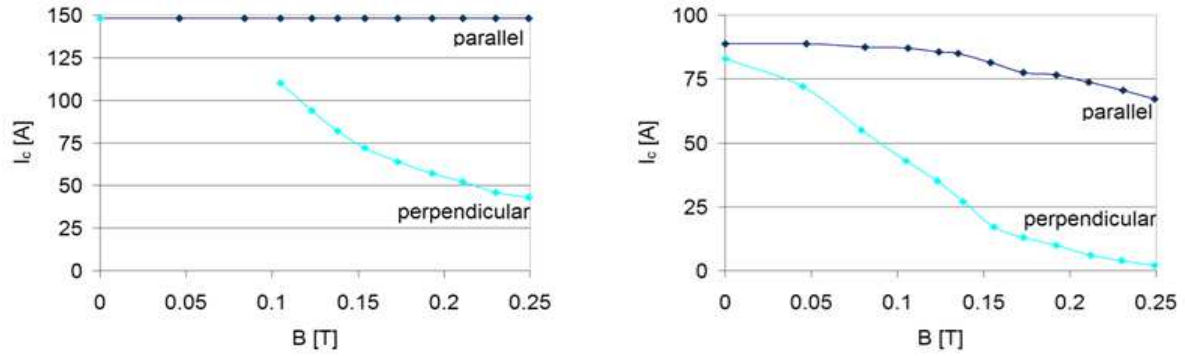
Figure 7.2: *Critical current I_c of the ASMC BSCCO cable measured in (left) LN_2 and (right) LAr as a function of the applied parallel and perpendicular magnetic field.*
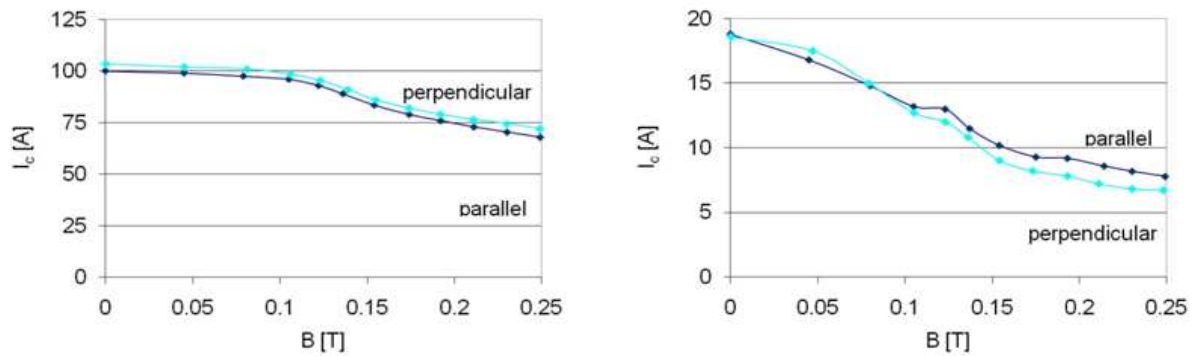
Figure 7.3: *Critical current I_c of the AMSC YBCO cable measured in (left) LN_2 and (right) LAr as a function of the applied parallel and perpendicular magnetic field.*
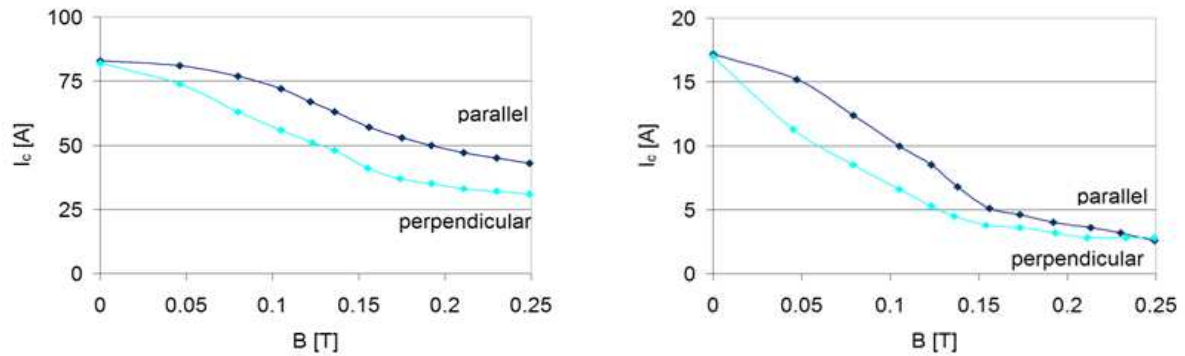
Figure 7.4: *Critical current I_c of the SP YBCO cable measured in (left) LN_2 and (right) LAr as a function of the applied parallel and perpendicular magnetic field.*

critical current at LAr temperature for YBCO is significantly lower than for the BSCCO cable, as the YBCO transition temperature is $90\,\mathrm{K}$ compared to $110\,\mathrm{K}$ for the BSCCO. Hence, we proposed to build a solenoid with the BSCCO cable directly immersed in LAr. If an additional nitrogen shielding of the LAr TPC is foreseen, the possibility of YBCO can be reconsidered [270].

A solenoid was designed, but not built. Nevertheless, we proved the possibility to operate a HTS magnet in a liquid argon bath with of field of about $0.2\,\mathrm{T}$, i.e. that a liquid argon TPC can be magnetized by superconductive wires without the need of an additional nitrogen bath for the HTS coil, which can become a major advantage of the

liquid argon TPC for a future neutrino factory.

Chapter 8

Acknowledgements

First of all I have to thank Prof. André Rubbia for the possibility to get my Ph.D. at the particle physics institute of ETH Zürich. I especially thank Andreas "Res" Badertscher for carefully reading the draft of this thesis and his comments, as well as answering all the daily small problems with physics, without you it would not have worked out.

Secondly I thank Rosa Bächli for the time she spent working on my travel plans, expenses and extra wishes, thank you.

Of course another big thanks goes to my family, thanks for your support!

Another thanks goes to my Zürich office colleagues Adamo Gendotti, Leo Knecht and Gustav "Gusti" Natterer, for making the stay in Zürich such a wonderful time.

Big big thanks goes to the Bern group of the Albert Einstein Institute, foremost Frederic Juget, Igor Kreslo, Ciro Pistillo and Luca Scotto for their encouraging help in understanding the OPERA software, and of course Tomoko and Aki Ariga for their support in the tricky business of scanning and analysis, as Jonas Knüsel and Frank Meisel for the discussions about physics and everything else.

I'd like to thank all the OPERA collaboration people who helped me getting this result, especially Dario Autiero and Stefano Dusini.

Additionally, I like to thank all other young people and friends I met on the way in the various universities around Europe, thanks to you I did not only learn about physics, but also about life!

8.1   Curriculum Vitae

Thomas Strauss

15.3.1981

Oleanderstrasse 12, CH-8050 Zürich
+41 76 424 6093
thomas.strauss@cern.ch

Sprachkenntnisse: Deutsch, Englisch fliessend, Verständnis Französisch, Italienisch

Doktor Sc. ETH (cand.), Dipl. Phys.,

Spezialgebiet:

Datenanalyse, CAD-Design und Simulation, Cryogene-System, Vakuumtechnik,
Hochtemperatursupraleiter und Magnete

AUSBILDUNG

POS Franz Mehring/Sonnenuhrgrundschule, Berlin, BRD
1986 - 1992

Heinrich Hertz Gymnasium, Berlin, BRD
1992 - 2000, Abitur/Matura

Militär Grundwehrdienst, BRD
01. 09.2000 – 31.06.2001

Studium an der Humboldt Universität, Berlin, BRD

01.10.2001 – 22.08.2006
Diplomstudium Physik, Abschlussnote 1.1 „Sehr gut"
- Erasmusaufenthalt an der ETH Zürich
  - 15.10.2004 - 31.07.2005
- Diplomarbeit an der ETH Zürich am Institut für Teilchenphysik
  - 01.08.2005 – 31.03.2006
- Mitglied im Fakultätsrat und Prüfungsausschuss
  - 2002-2004/2002-2006

Dissertation, ETH Zürich, CH

01.10.2006 – 30.06.2010 „Charm production in the OPERA experiment
and the study of a high temperature superconducting solenoid for a
liquid argon time projection chamber"

ERFAHRUNG

Hilfsassistent Studentenbetreuung ETH Zürich, CH
30.03.2005 – 31.07.2005 Übungsgruppen in Physik und Mathematik
15.10.2005 – 31.02.2006 Übungsgruppen in Physik und Mathematik

Appendix A

Full neutrino oscillation parameter space
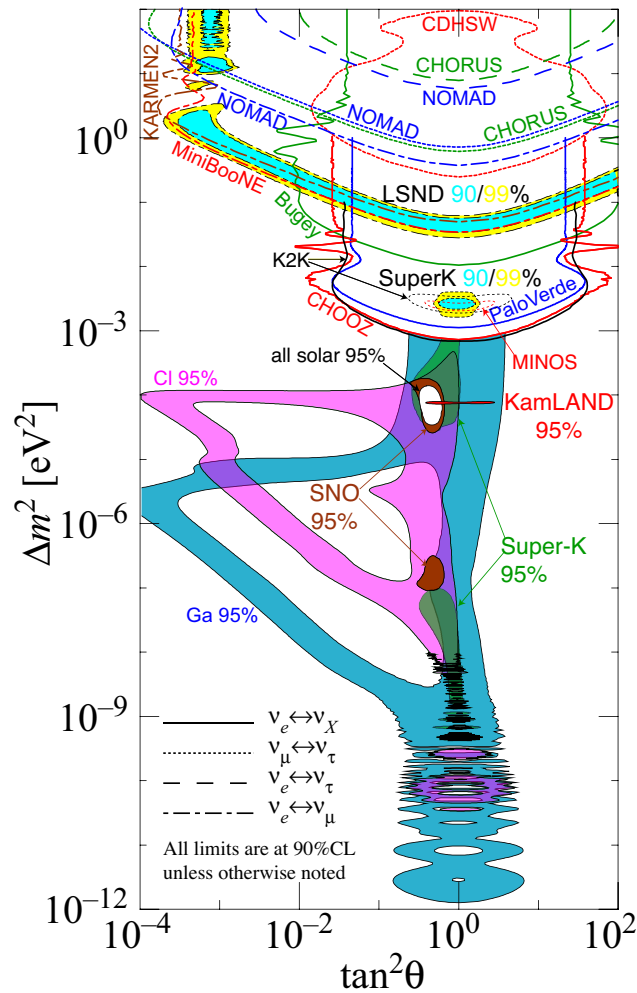
Figure A.1: *The regions of squared-mass splitting and mixing angle favored or excluded by various experiments. Picture from H. Murayama. References to the author and data used in the figure can be found at http:// hitoshi.berkeley.edu/ neutrino/.*

Appendix B

Latent images in emulsion & refreshing
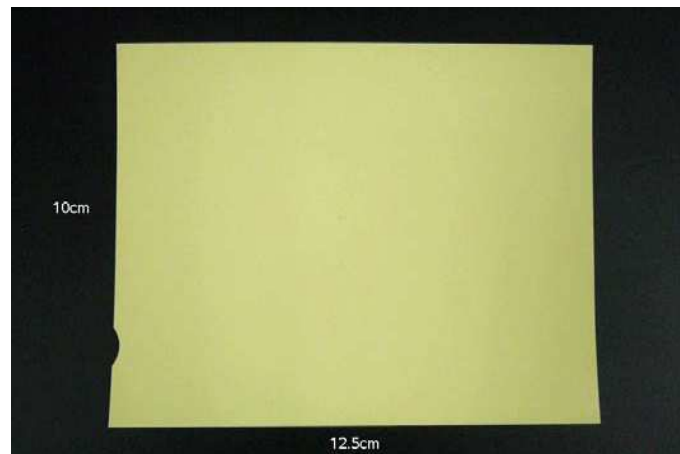
Figure B.1: *Photograph of an OPERA film. Before development it is yellow. Picture from [207].*

This appendix gives more detail on the creation of tracks in the emulsion films and the refreshing procedure. When a charged particle crosses the emulsion layer, the absorption of energy creates a latent image as follows [233]: The charged particle ionizes the bromine ion which transforms into an atom. The ejected electron leads to a region of positive charge in the lattice (a positive hole) but cannot move freely, as it is associated with the silver lattice and is moving inside it, neutralizing one of the silver ions subsequently. Ionization thus transforms two ions of the lattice into atoms. As the electrons and holes can diffuse in the crystal, the holes are accumulated at lattice imperfections on the outside, while the electrons accumulate on impurities inside. To form a latent image enough holes and electrons have to be collected separately as otherwise the atoms could recombine to ions. Free (interstitial) silver ions inside the silver halide lattice can move through the lattice, encountering a trapped electron the charges are neutralized and an atom of metallic silver is formed. Thus the deposition of energy in silver halide creates a concentration of a few silver atoms which can act as a development center, this is the latent image. In Figure B.1 shown is a photograph of the emulsion film before development. Due to the ambient light the emulsion will fade into a purple tone, as the number of silver atoms increases.

In Figure B.2 shown is how the refreshing decreases the number of development centers for minimum ionizing particles.

Figure B.2: *Idea of the refreshing procedure. Picture from [207].*

Appendix C

The Japanese Scanning System S-UTS

Based on the experience gained in the CHORUS and DONUT experiments [271], the Nagoya university developed an upgraded version of the CHORUS scanning system for the OPERA experiment, called Super-UTS (or S-UTS) [240, 241, 207]. The main design goal of the S-UTS was to overcome the time limit of the tomographic image acquisition due to vibrations after the movement of the microscope stage in the previous microscopes, where about 10 ms of waiting time were needed for the relaxation of the vibrations before the image could be taken. Thus, a continuously moving X-stage was used in combination with a lightweight objective lens, following the stage along the X axis to acquire the images in the optical axis (Z coordinate) while the area of the field of view is fixed, as indicated in Figure C.1.
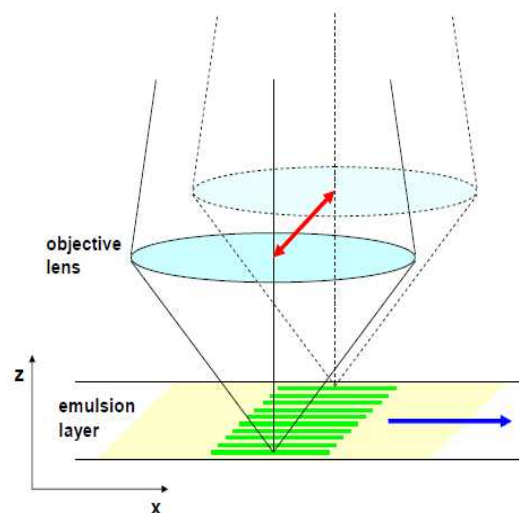
Figure C.1: *Scheme of continuous tomographic image acquisition. Picture from [241].*

In Figure C.2 the layout of the S-UTS is shown, the emulsion is fixed to the glass plate of the stage by a vacuum system, and scanned by moving the stage in both X- and Y-axes. The optical components of the systems are:

- An oil objective lens TIYODA with a magnification of $35\times$, optimized for a wavelength of $550\,nm$ (green) and an aperture of 0.85.

- An ultra fast CMOS camera MEMCAMfx RX-6 (custom) with 512×508 pixel with a readout range of 3000 frames per second.

- A condenser with a Hg-Xe discharge lamp, the light is transferred with a light guide (IR-cut, green filter, Aperture 0.85).

The field of view is $230 \times 228\,\mu m^2$, i.e. $0.45\,\mu m^2$ per pixel. 16 tomographic images along the Z-axis in each field of view are acquired for track reconstruction, thus, the measured scan rate is 60 views/s. Shown in Figure C.3 is the set up of the stage and the objective lens. Fine-step pulse motors are used to drive the X- and Y-axes, the stage's working area is $150\,mm \times 150\,mm$, with a positioning error of $0.1\,\mu$m. The Z-stage is moved with pulse motor of $20\,mm$ working range for coarse and larger movements, i.e. to switch the emulsion layer from one surface to the other. To move the objective lens in the X-position, allowing a synchronization between the stage-movement and for the fine Z-axis movements Piezo actuators and flexure hinges are used, allowing a movement of $110\,\mu m$ along the X-axes, respectively $100\,\mu m$ along to Z-axes. The whole microscope is moved in a $200\,kg$ fixed frame to reduce vibrations on the optical system.
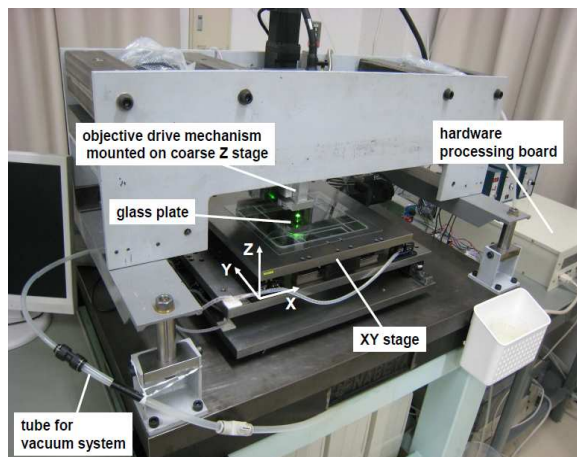
Figure C.2: *S-UTS microscope setup. Picture from [241].*
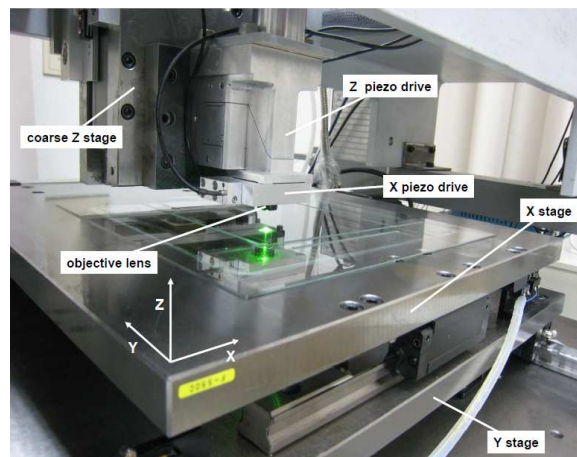
Figure C.3: *Detail view of the S-UTS stage. Picture from [241].*

C.1 S-UTS image processing

The Japanese S-UTS acquires the emulsion images with a high speed CMOS camera at a rate of $1.3\,GB/s$. Two image processing steps are used two process the tomographic images of the emulsion film into a reconstructed track, as shown in Figure C.4. First the data rate is reduced by using Field Programmable Gate Array (FPGA) processes the two-dimensional image, by using the grain information of the emulsion image. This is achieved by application of a one-dimensional high pass filter on the image, to reject background due to fluctuations of the brightness, indicated as FPGA 1. Afterwards, only pixels above a given threshold are further processed (FPGA 2). The third FPGA 3, collects the grain information, and compresses the information into a list of the XY grain

position. The pixel size is then expanded, to recognize tracks. The effect of expanding is shown in Figure C.5, the more pixels are added, the larger the size of the grain and the chance to recognize the track. The cost of adding more pixel is a loss in the angular resolution. Three expansion sizes are possible, 1×1, i.e. no expansion as in Figure C.5 a), 2×2 and 3×3.
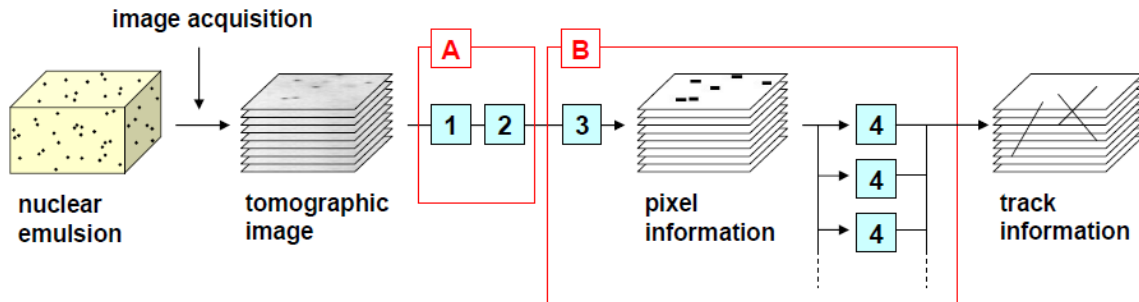
Figure C.4: *A block diagram of hardware processing for track recognition. 'A' is for image processing and 'B' is for track recognition. No.1 to 4 represents one FPGA chip each. No.1 is for high pass filtering, No.2 is to digitize pixels, No.3 is for expand pixels and No.4 is to recognize tracks in a given angle range. Picture from [241].*
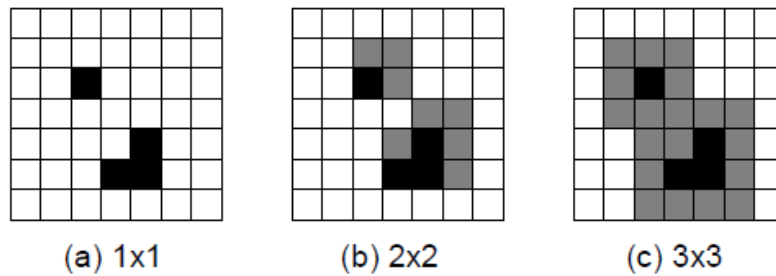
Figure C.5: *Hit pixels are in black. In (b) and (c), gray pixels are added as hit pixels by expansion. Both black and gray pixels are used to recognize tracks. Picture from [241].*

The three-dimensional reconstruction of tracks is achieved by using a large FPGA-array to process the microtrack recognition algorithm. A track crossing the whole emulsion (in a straight perpendicular line), will have grains in nearly all layers at the same XY positions. Thus, the sum of all hit layers, called pulse height (ph), will have a clear signal at the track's position, as shown in Figure C.6. Tracks with an inclination with respect to the emulsion surface can be found in the same way, by applying offset in X and Y, under a specific angle the ph will have a peak, on the cost of summing over the whole angle parameter space. In the S-UTS about 1200 calculations are done to identify all tracks with a $|\tan\theta| < 0.6$ (see Figure C.6 for the definition of θ). The algorithm is an implemented and parallelized process in the FPGA-array, wherein each FPGA calculates a certain angular space and returns the X, Y, Z, $\tan\theta_x$, $\tan\theta_y$ and ph of a microtrack at a rate of about 10 MB/s data rate. With ten FPGA per S-UTS about $72\,\text{cm}^2/\text{h}$ can be analyzed.
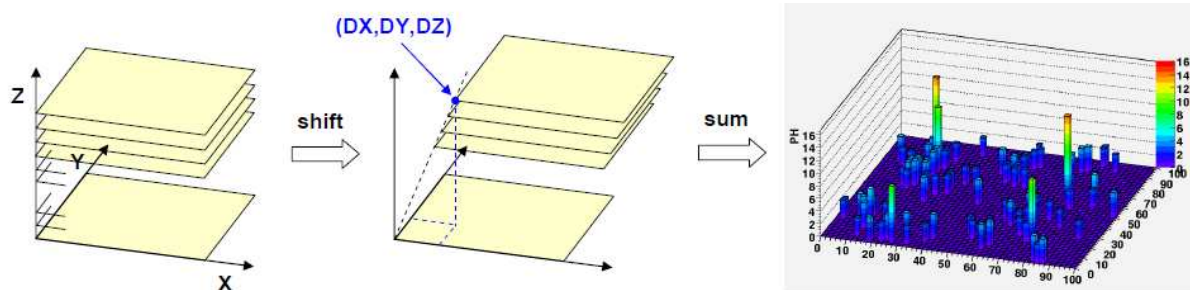
Figure C.6: *Track recognition by summing up tomographic images. Tracks of a certain angle ($TX = \tan\theta_x = DX/DZ$, $TY = \tan\theta_y = DY/DZ$) shown in the left can be recognized by (1) shift relative position among tomographic images in XY axes so that a track of the angle looks perpendicular, (2) then sum up pixels, along Z axis in the figure, as shown in the middle. An example of real data, summed up 16 layers of tomographic images in a microscope view of $100 \times 100\,\mu m^2$ is shown in the right. Picture from [241].*

Appendix D

OPERA Decay Search Procedure

D.1 Vertex reconstruction

[1] In order to locate the position in the brick where the neutrino interaction occurred, tracks found in the Changeable Sheets are followed upstream, film-by-film, until they disappear[2] (Scanback). A surface of $1\,cm^2$ around the most upstream Scanback track point of disappearance is measured in 15 consecutive films (volume scan), 5 upstream and 10 downstream of the lead plate where the vertex is supposed to be located. Track segments are measured within an angular acceptance of $0.6\,rad$.

Emulsion films are aligned with micrometric precision by using cosmic-ray tracks, then tracking and vertex finding are performed. A relevant point of the procedure is the definition of the primary neutrino interaction vertex. Depending on whether the Scanback track is found to form a multi-prong vertex (*main vertex*) with other tracks or is isolated, a different procedure is applied.

D.2 Decay search for multi-prong vertices

D.2.1 First segment measurement

A crucial step for the identification of very-short decays, occurring in the same lead plate as the neutrino interaction vertex, is the use of track information in the film immediately downstream to it (hereafter referred to as *vertex film*), in order to improve the resolution in the determination of its position.

Track segments in the vertex film could not be available in reconstructed data for two main reasons:

1. the basetrack finding efficiency;

2. gamma-conversion in the lead plates downstream of the vertex.

---

[1]official OPERA version of 24-09-2009 (copy&paste)

[2]A track is considered as stopping if it is not found in four consecutive films.

Whenever the segment of any track attached to the vertex is missing, visual inspection is required to identify tracks originating from gamma-conversion and/or recover possible segment inefficiency. In the case of gamma-conversion, two very-close converging track segments are recognized by eye in the downstream films. In the case of inefficiency, the segment can be recognized by eye, and the track parameters can be measured by connecting the points closest to the plastic base. A measurement of all track segments is performed in such cases. Tracks found to be electron-positron pairs are then removed and the vertex position is re-computed. An automatic procedure has been established to recover reconstructed microtracks in the vertex film. These microtracks are present in volume scan output but normally not used for tracking that only uses basetracks. Such a procedure allows thus minimising the number of cases to be visually inspected. The recovery procedure of missing basetracks in the vertex film is illustrated in Figure D.1.
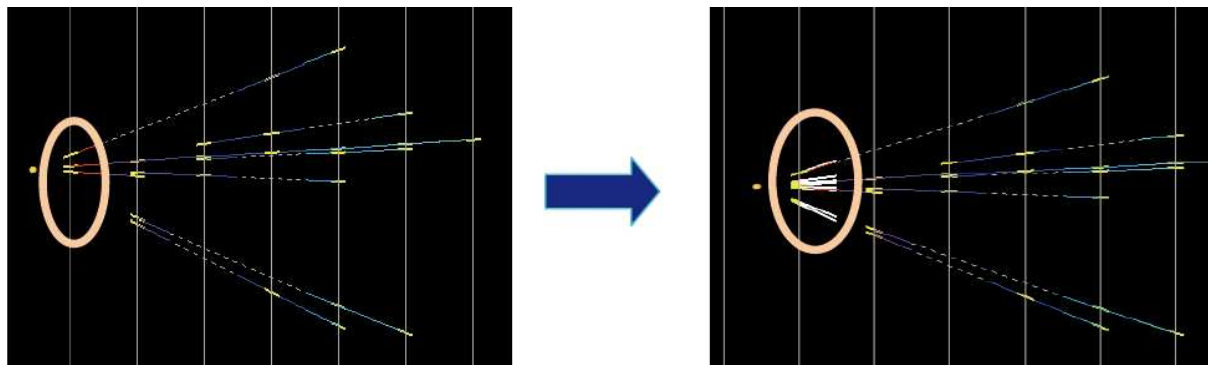
Figure D.1: *Missing basetracks are recovered by visual inspection or automatic microtrack search.*

D.2.2   Vertex analysis

Using the vertex position re-computed as explained in the previous section, if a track is found to have an impact parameter with respect to the vertex larger then 10 microns, it has to be further studied. In order to investigate whether the reason for such anomalous impact parameter is the scattering in the traversed lead thickness, a check of the track slopes has to be performed. By using at least 8 measured basetrack slopes (further measurements are foreseen if data are not available), the RMS of the slope differences is computed in the transverse (T) and in the longitudinal (L) planes according to the following formula:

$$\Delta\theta_{T,L}^{RMS} = \sqrt{\frac{\sum_{i=1}^{N} \Delta\theta_{i,T,L}^2/(\Delta npl)_i}{N}} \tag{D.1}$$

where the $\Delta\theta_{i,T,L}$ are the angular differences in the transverse and longitudinal plane, respectively; Δnpl is the number of lead plates between two segments; N is the total number of angular differences. If both components have $\Delta\theta^{RMS}$ larger than 0.020 rad, the track is classified as a *low momentum* track (the cut roughly corresponds to a momentum lower than 500 MeV/c). For a better determination of the vertex position, the low momentum track is disconnected from the vertex if the multiplicity is larger than 2.

Then, the vertex position and the track impact parameters are re-computed. If the vertex multiplicity equals 2, the track is not removed and the vertex position is determined using both tracks. If any of the two components has a $\Delta\theta^{RMS}$ smaller than 0.020 rad, the track is followed downstream film-by-film up to the end of the brick (Scanforth), in order to perform the momentum estimation by the Multiple Coulomb Scattering method.

D.2.3 Kink search for tracks attached to vertex (in-track decay search)

For each track attached to the vertex, the largest slope difference $\Delta\theta^{MAX}$ in the first 4 films downstream of the vertex are computed as shown in Figure D.2. Then, $\Delta\theta^{RMS}kink$ in the transverse and in the longitudinal planes is calculated by using the following formula:

$$\Delta\theta_{T,L}^{RMS}kink = \sqrt{\frac{\sum_{i!=kink}^{N-1} \Delta_{i,T,L}^2/(\Delta npl)_i}{N-1}} \tag{D.2}$$

If the ratio $R = \theta_{kink}/\Delta\theta_{kink}^{RMS}$ kink is larger than 3, the track needs further investigation. First of all, the anomalous value of $\Delta\theta$ has to be confirmed by visually checking the slopes of the track in the corresponding emulsion films. If the angular deviation is not due to a faulty automatic measurement in either film, the track requires further analysis. In order to determine if the scanforth of the track is needed, the same procedure described in section D.2.2 is applied.
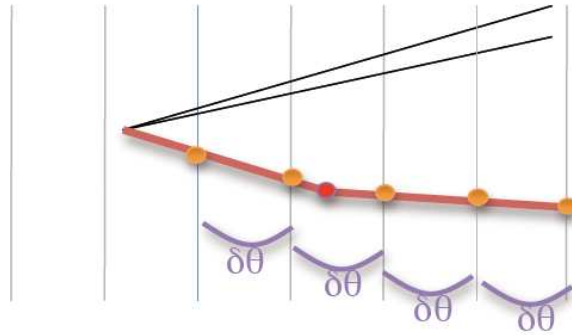
Figure D.2: *In-track decay search: a compatibility check of the angular slope differences along the track is performed.*

D.2.4 Extra-track search

In this step, possible daughter tracks produced in the decay of a short-lived particle are searched for among the other tracks reconstructed in the measured volume and stopping therein. For this purpose, different selection criteria apply for 1-μ events, where the main vertex is clearly identified as the primary neutrino interaction, and 0-μ events, where an ambiguity exists on the main vertex definition (example: a multi-prong vertex with multiplicity 3 could be the secondary vertex generated by a $\tau \to 3$ hadrons decay). In order to better discriminate between penetrating tracks contained in the measured volume

(mainly cosmic rays) and stopping tracks related to the event, a tracking that can use both basetracks and microtracks has been developed, thus improving the purity of the selection. For 1-μ events, a track is selected if the following criteria are satisfied:

1. the most upstream segment of the track is in any of the four emulsion films downstream of the main vertex;

2. the impact parameter with respect to main vertex is smaller than 500 microns if $\Delta z \leq 1\,\mathrm{mm}$, or smaller than 800 microns if $1\,\mathrm{mm} < \Delta z \leq 6\,\mathrm{mm}$. Δz is the longitudinal distance between the vertex and the most upstream segment of the track;

3. the track has at least three segments in the reconstruction and at least two of them are basetracks.

For 0-μ events where the multiplicity of the main vertex is $<= 3$, a track is selected if the following criteria are satisfied:

1. the most upstream segment of the track is in any of the three emulsion films upstream or in any of the four emulsion films downstream of the main vertex;

2. the impact parameter with respect to main vertex is smaller than 800 microns;

3. the track has at least three segments in the reconstruction and at least two of them are basetracks.

Selected tracks are visually inspected in order to reject electron-positron pairs from gamma-conversion and fake tracks, and then classified in two categories:

1. the track stops in the vertex film (*short decay search*);

2. the track stops in any other emulsion film (*long decay search*).

For tracks from category 1. the same procedure described in section D.2.2 applies. For tracks from category 2. a special procedure called *parent search* has been developed: a parent track with an impact parameter smaller than 10 microns with respect to the main vertex, and a minimum distance with respect to the daughter track smaller than 20 microns are searched for in the measured volume as illustrated in Figure D.3. Any candidate parent track is then confirmed by visual inspection. This procedure applies as well when the stopping track is upstream of the main vertex. A search for converging partner tracks is performed for both classes of tracks. If partner tracks are found, the corresponding vertex has to be validated as described in section D.2.1. A careful check for heavily ionizing particles (*black* tracks) is also performed to discriminate between secondary interactions and decay vertices. The Scanforth of all tracks and the kinematical analysis is finally applied to any confirmed decay topology.

If no parent and no partner are detected, the selected track has to be further investigated. A Scanback is performed in order to check whether the track is penetrating or not. If the track is confirmed to stop, the transverse and longitudinal components of $\Delta\theta^{RMS}$ are evaluated by using at least 8 measured basetrack slopes. If $\Delta\theta^{RMS}$ is larger than $0.020\,\mathrm{rad}$, the track is considered as a low momentum track and thus it is rejected. For smaller values of $\Delta\theta^{RMS}$, the scanforth of the track is performed for momentum estimation by the MCS method.
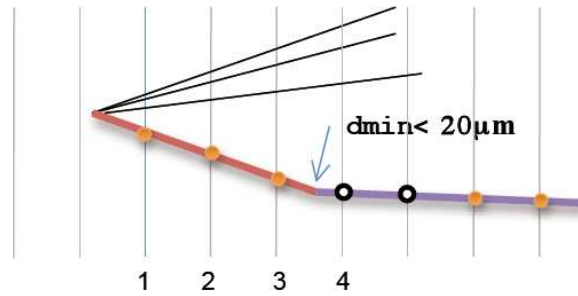
Figure D.3: *Example of an extra-track connected to the main vertex by a parent track.*

D.3 Decay search for isolated muons and single hadrons

If the Scanback track is not associated to any other reconstructed track, the aim of the decay search procedure is to verify whether the stopping track comes from the primary neutrino interaction or from a secondary decay. An extra-track selection is performed with the following criteria:

1. the most upstream segment of the track is in any of the three emulsion films upstream or in any of the four emulsion films downstream of the stopping point of the Scanback track;

2. the impact parameter[3] with respect to the stopping track is smaller than 800 microns;

3. the track has at least three segments in the reconstruction and at least two of them are basetracks.

Depending on the result of the extra-track search, a modified parent search procedure is applied as follows:

- if more than one converging tracks are found, a parent track connecting the vertex and the Scanback track with the same tolerances reported in section D.2.3 is searched for;

- if an isolated track is found, a parent track with a minimum distance smaller than 20 microns with respect to both stopping tracks is searched for;

- if no extra-track is found, a parent track with a minimum distance with respect to the Scanback track smaller than 20 microns is searched for (this is the case of τ decaying in one prong and no other track detected at the primary vertex).

---

[3]The Scanback track is extrapolated to the centre of the upstream lead plate; the impact parameter is calculated with respect to this point.

Appendix E

Remaining P versus P$_t$ plots

In the following pages the momentum P versus transverse momentum P_t are shown for the various decay classes according to Table 5.3, indicated in black is the shape of the cut.
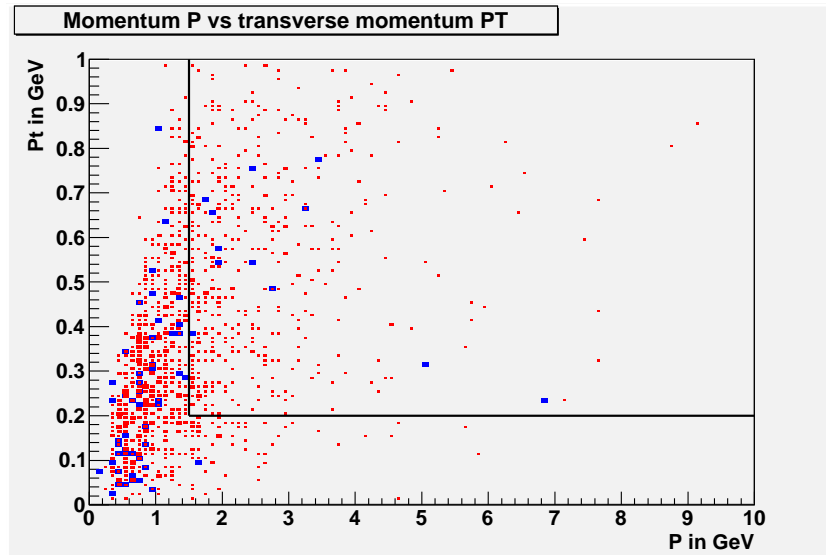
Figure E.1: *Momentum P versus transverse momentum P_t (relative to parent track) for daughter tracks of the single muon, secondary vertex short decay topology, the high purity cuts are indicated by the black lines. In red the number of true charm candidates are shown, in blue the background due to non-charm daughters.*
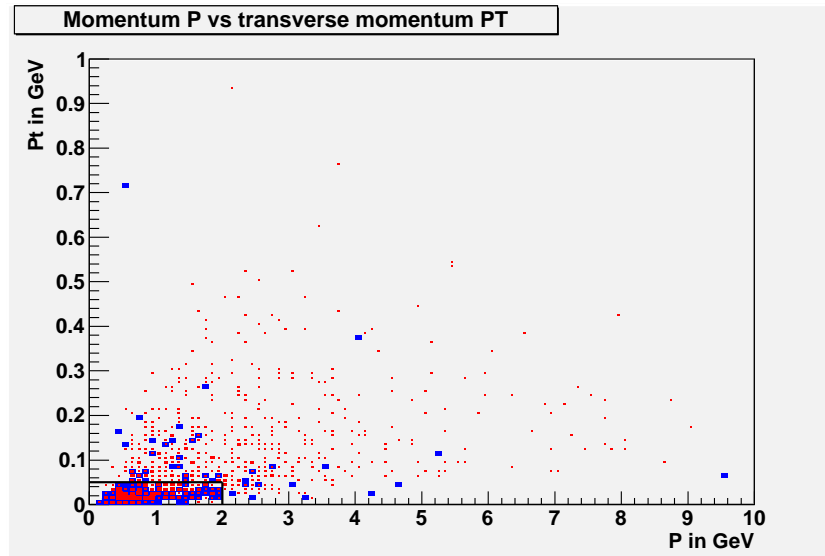
Figure E.2: *Momentum P versus transverse momentum P_t (relative to parent track) for daughter tracks of the primary vertex, secondary vertex short decay topology, the high purity cuts are indicated by the black lines. In red the number of true charm candidates are shown, in blue the background due to non-charm daughters.*
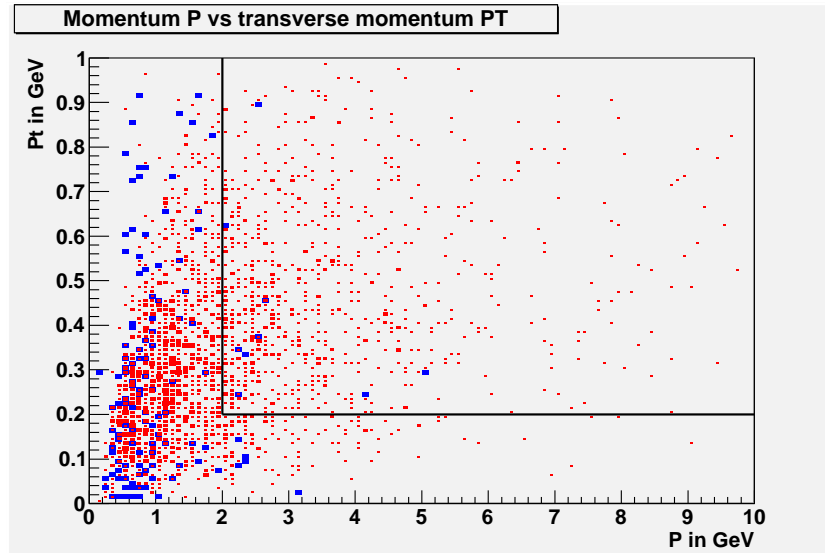
Figure E.3: *Momentum P versus transverse momentum P_t (relative to parent track) for daughter tracks of the primary vertex, secondary vertex short decay topology, the high purity cuts are indicated by the black lines. In red the number of true charm candidates are shown, in blue the background due to non-charm daughters.*
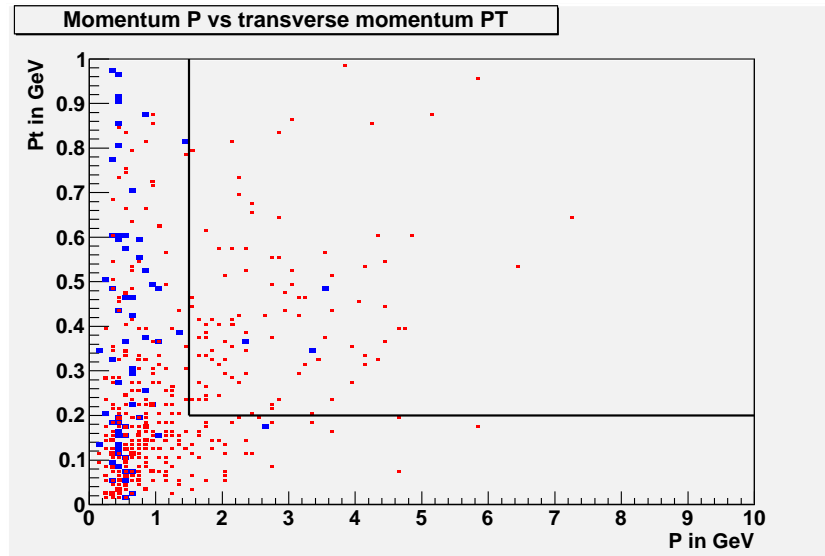
Figure E.4: *Momentum P versus transverse momentum P_t (relative to parent track) for daughter tracks of the single muon, secondary track longn decay topology, the high purity cuts are indicated by the black lines. In red the number of true charm candidates are shown, in blue the background due to non-charm daughters.*
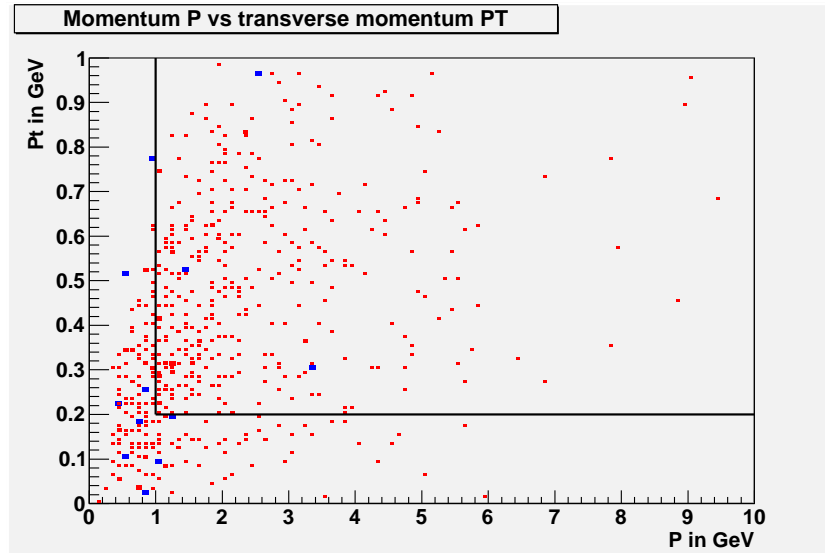
Figure E.5: *Momentum P versus transverse momentum P_t (relative to parent track) for daughter tracks of the single muon, secondary vertex longn decay topology, the high purity cuts are indicated by the black lines. In red the number of true charm candidates are shown, in blue the background due to non-charm daughters.*
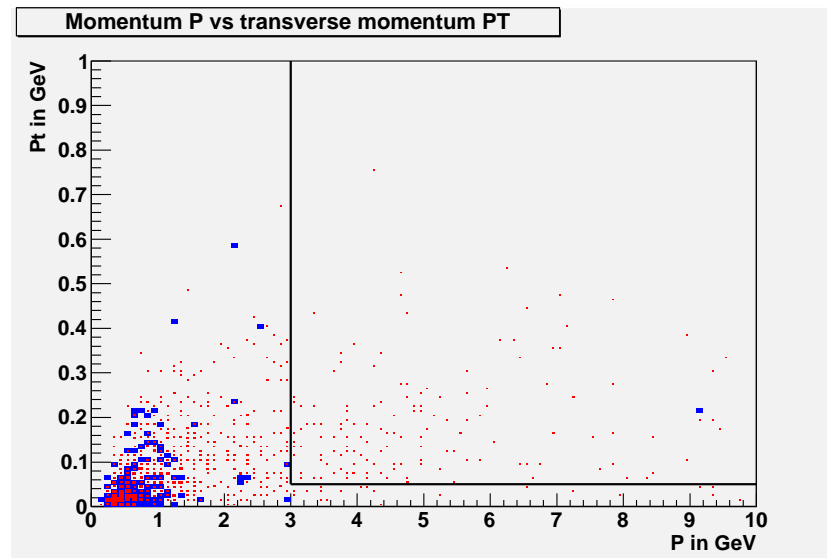
Figure E.6: *Momentum P versus transverse momentum P_t (relative to parent track) for daughter tracks of the primary vertex, secondary track longn decay topology, the high purity cuts are indicated by the black lines. In red the number of true charm candidates are shown, in blue the background due to non-charm daughters.*
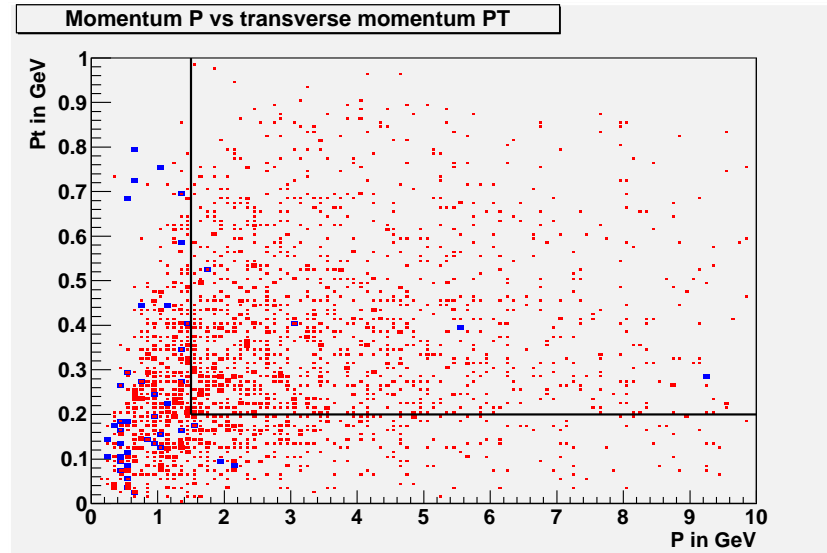
Figure E.7: *Momentum P versus transverse momentum P_t (relative to parent track) for daughter tracks of the primary vertex, secondary vertex longn decay topology, the high purity cuts are indicated by the black lines. In red the number of true charm candidates are shown, in blue the background due to non-charm daughters.*
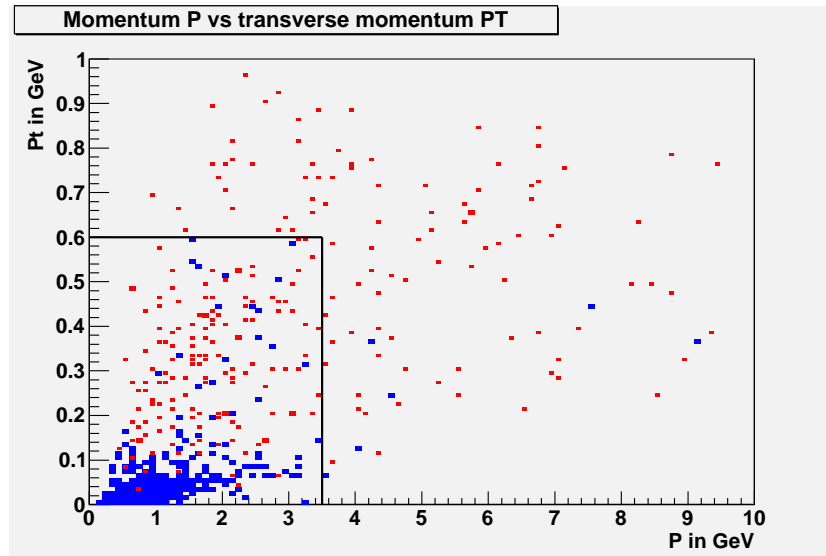
Figure E.8: *Momentum P versus transverse momentum P_t (relative to parent track) for daughter tracks of the primary vertex, secondary track longc decay topology, the high purity cuts are indicated by the black lines. In red the number of true charm candidates are shown, in blue the background due to non-charm daughters.*
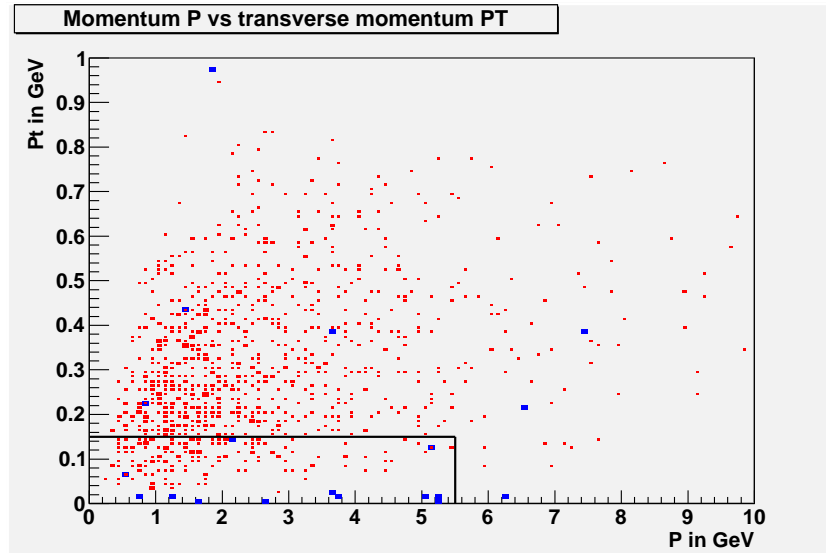
Figure E.9: *Momentum P versus transverse momentum P_t (relative to parent track) for daughter tracks of the primary vertex, secondary vertex longc decay topology, the high purity cuts are indicated by the black lines. In red the number of true charm candidates are shown, in blue the background due to non-charm daughters.*

Appendix F

Remaining plots for the cut selection in a high purity charm sample

In the following pages the plots defining the cut variables, as explained in 5.5.2 are shown for the various decay channels according to Table 5.3.
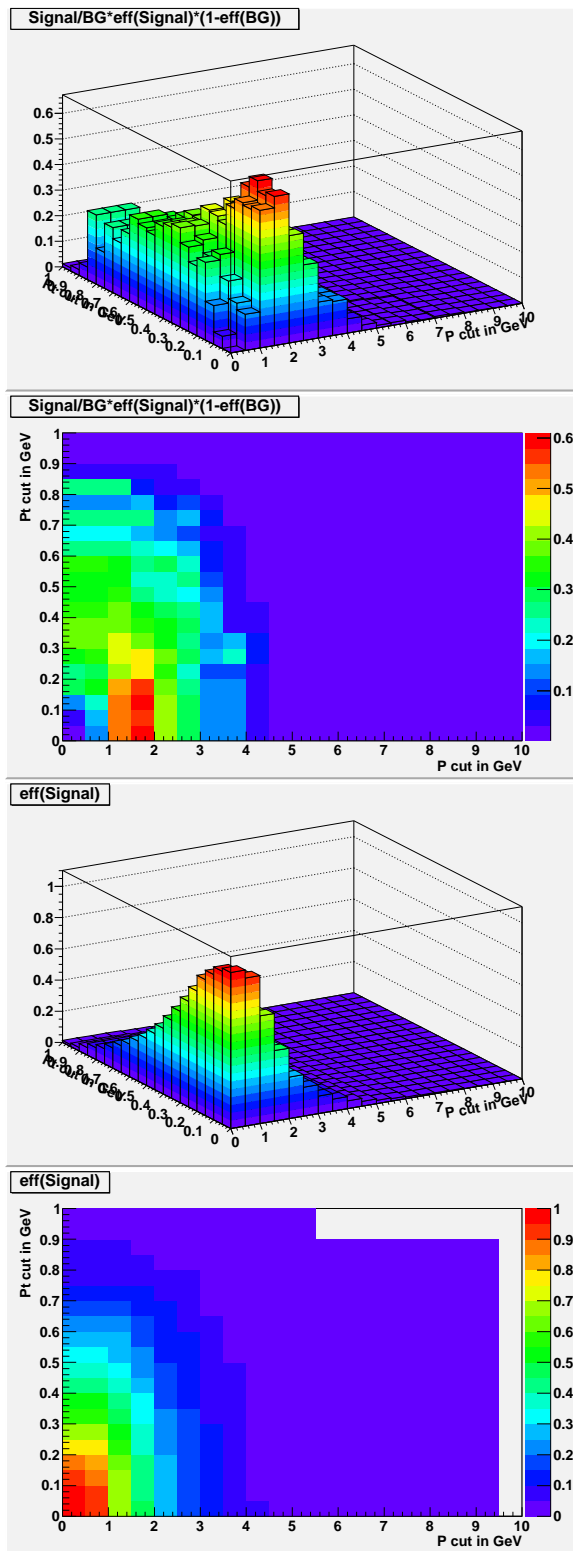
Figure F.1: "P&&P_t" cut for the class short_pt_sv: (top) 3-d view of the "figure-of-merit" calculation for the cut, 2-d view below. (bottom) 3-d view of the charm efficiency for the cut, 2-d view below.
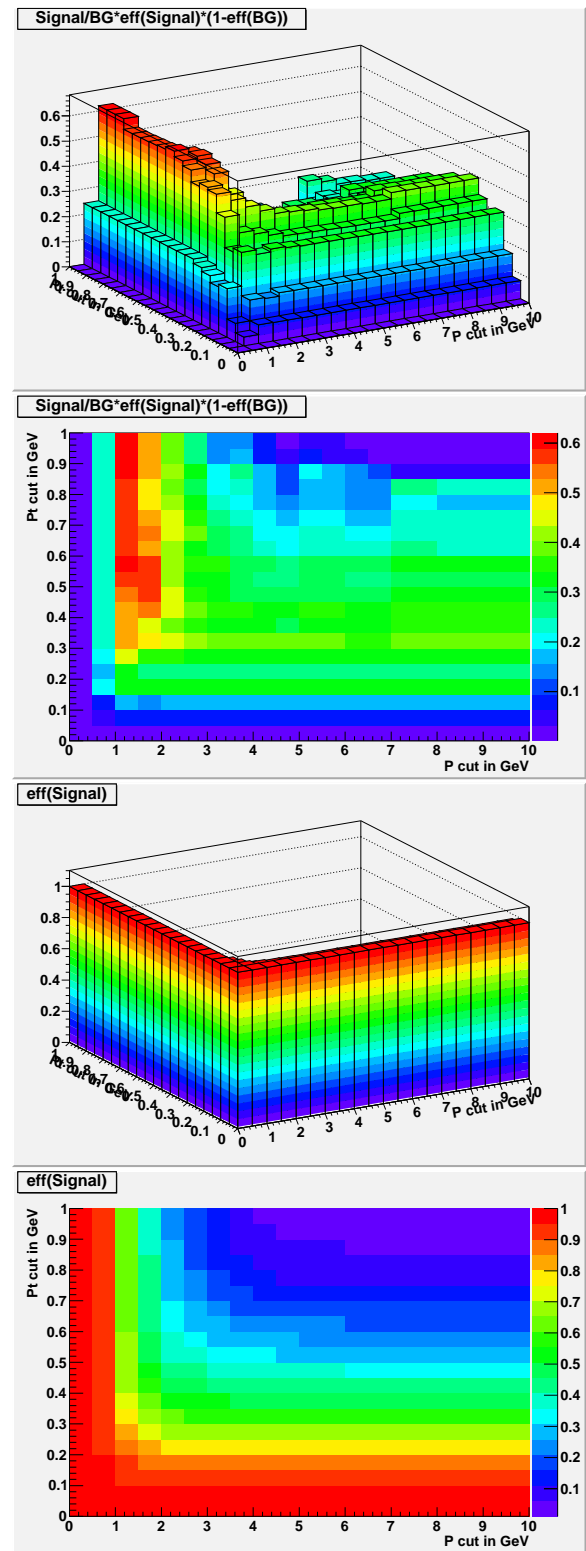
Figure F.2: "P||P_t" cut for the class short_pt_sv: (top) 3-d view of the "figure-of-merit" calculation for the cut, 2-d view below. (bottom) 3-d view of the charm efficiency for the cut, 2-d view below.
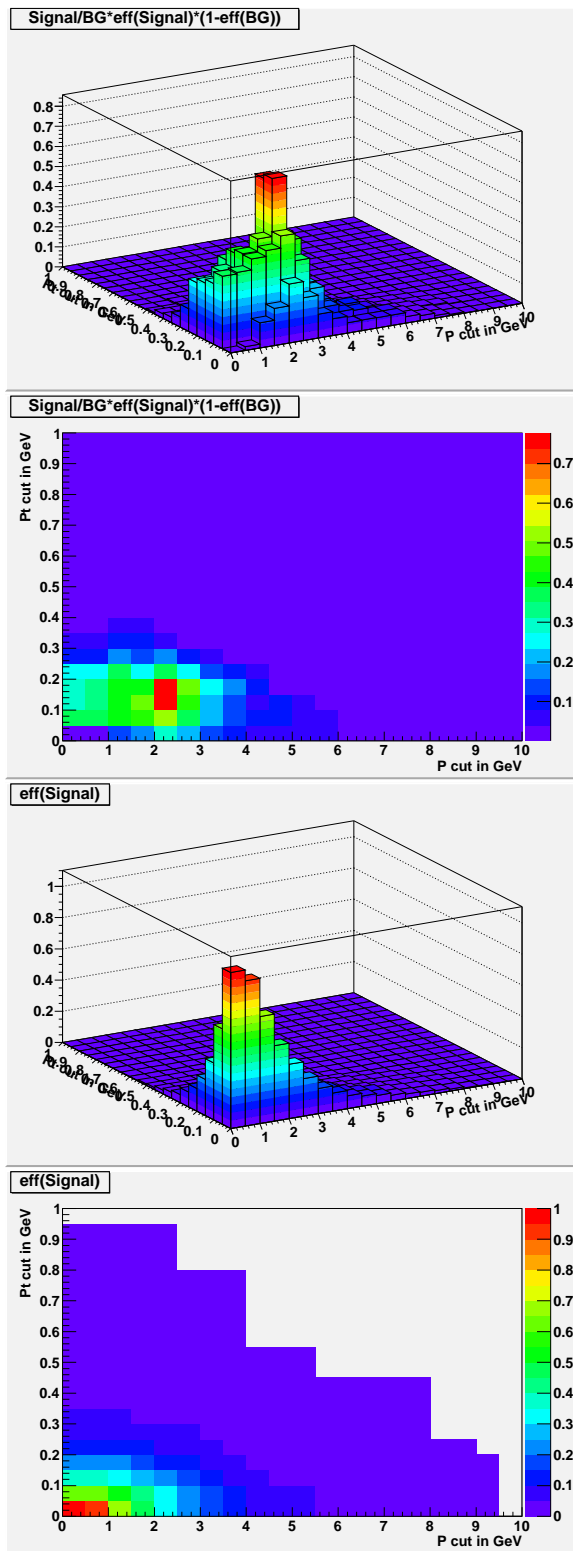
Figure F.3: "P&&P_t" cut for the class short_pv_st: (top) 3-d view of the "figure-of-merit" calculation for the cut, 2-d view below. (bottom) 3-d view of the charm efficiency for the cut, 2-d view below.
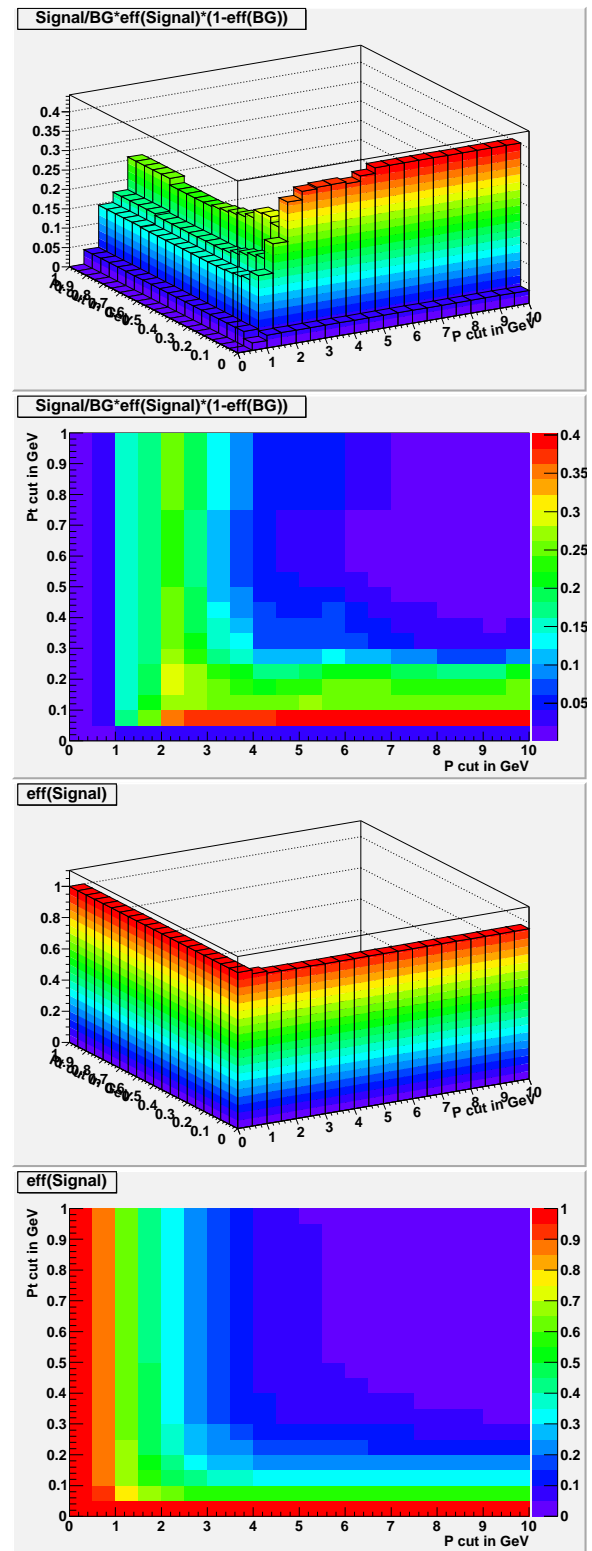
Figure F.4: "P||P_t" cut for the class short_pv_st: (top) 3-d view of the "figure-of-merit" calculation for the cut, 2-d view below. (bottom) 3-d view of the charm efficiency for the cut, 2-d view below.
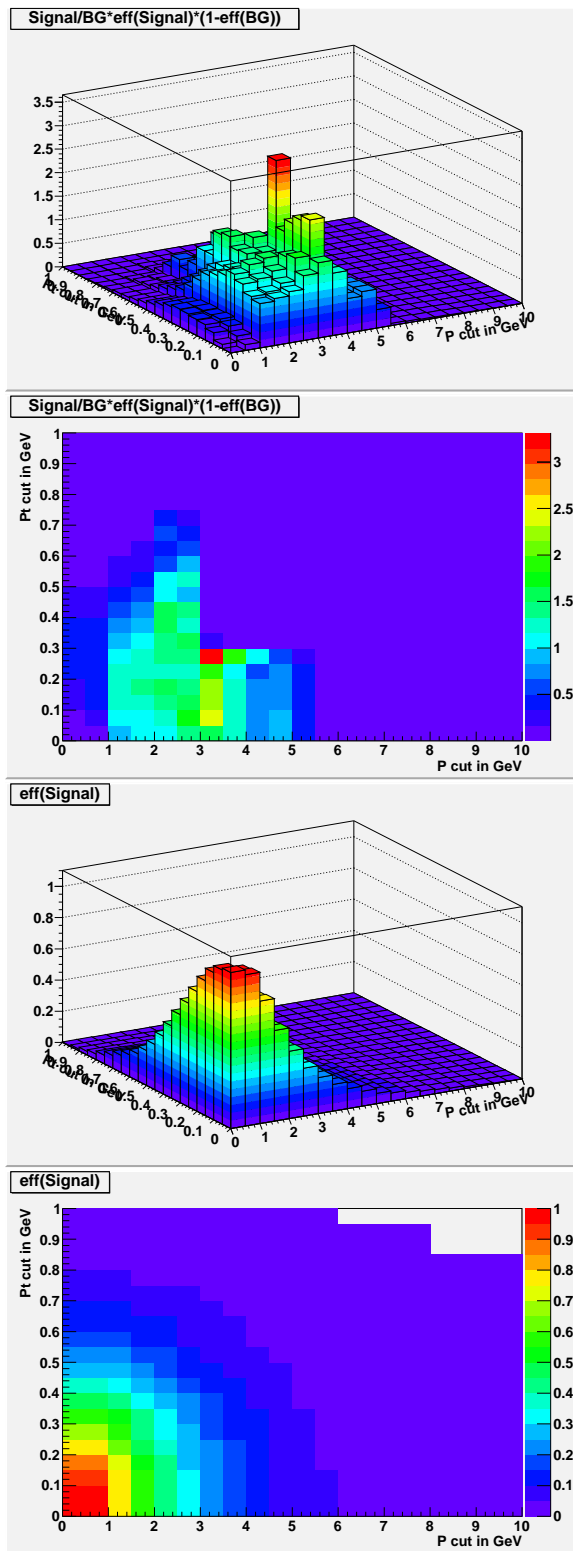
Figure F.5: "$P\&\&P_t$" cut for the class short_pv_sv: (top) 3-d view of the "figure-of-merit" calculation for the cut, 2-d view below. (bottom) 3-d view of the charm efficiency for the cut, 2-d view below.
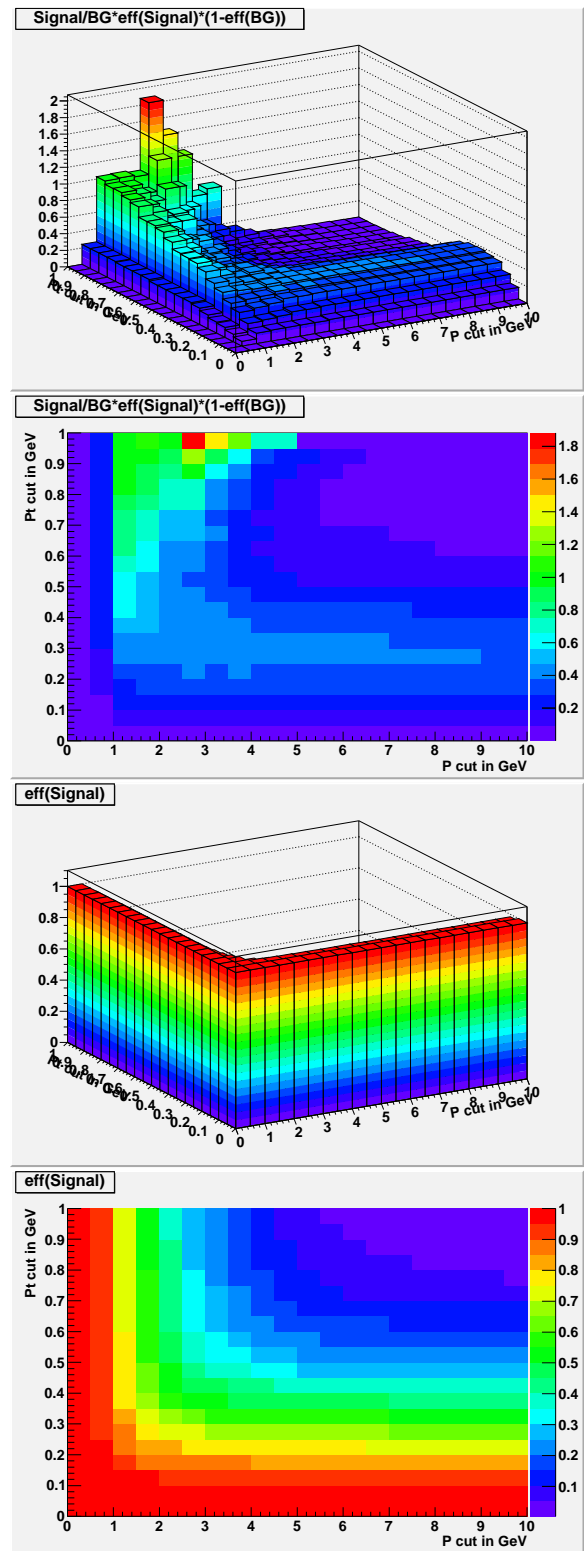
Figure F.6: "$P||P_t$" cut for the class short_pv_sv: (top) 3-d view of the "figure-of-merit" calculation for the cut, 2-d view below. (bottom) 3-d view of the charm efficiency for the cut, 2-d view below.
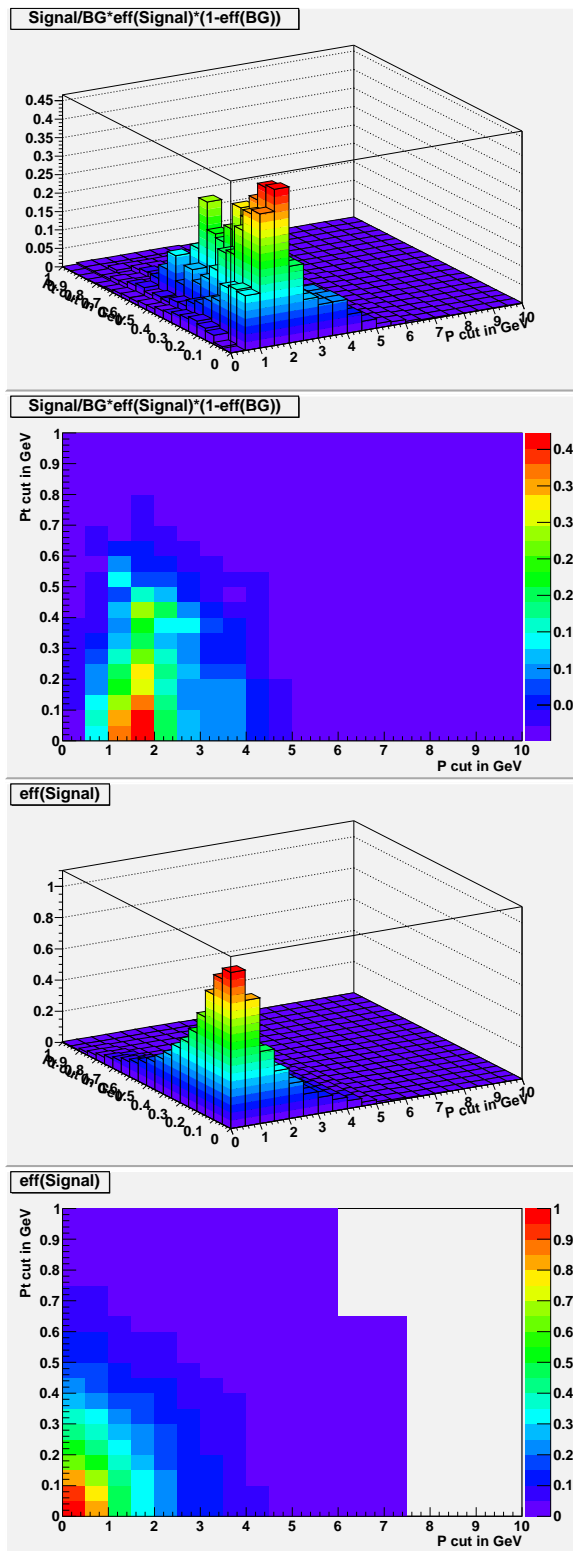
Figure F.7: "P&&P_t" cut for the class longn_pt_st: (top) 3-d view of the "figure-of-merit" calculation for the cut, 2-d view below. (bottom) 3-d view of the charm efficiency for the cut, 2-d view below.
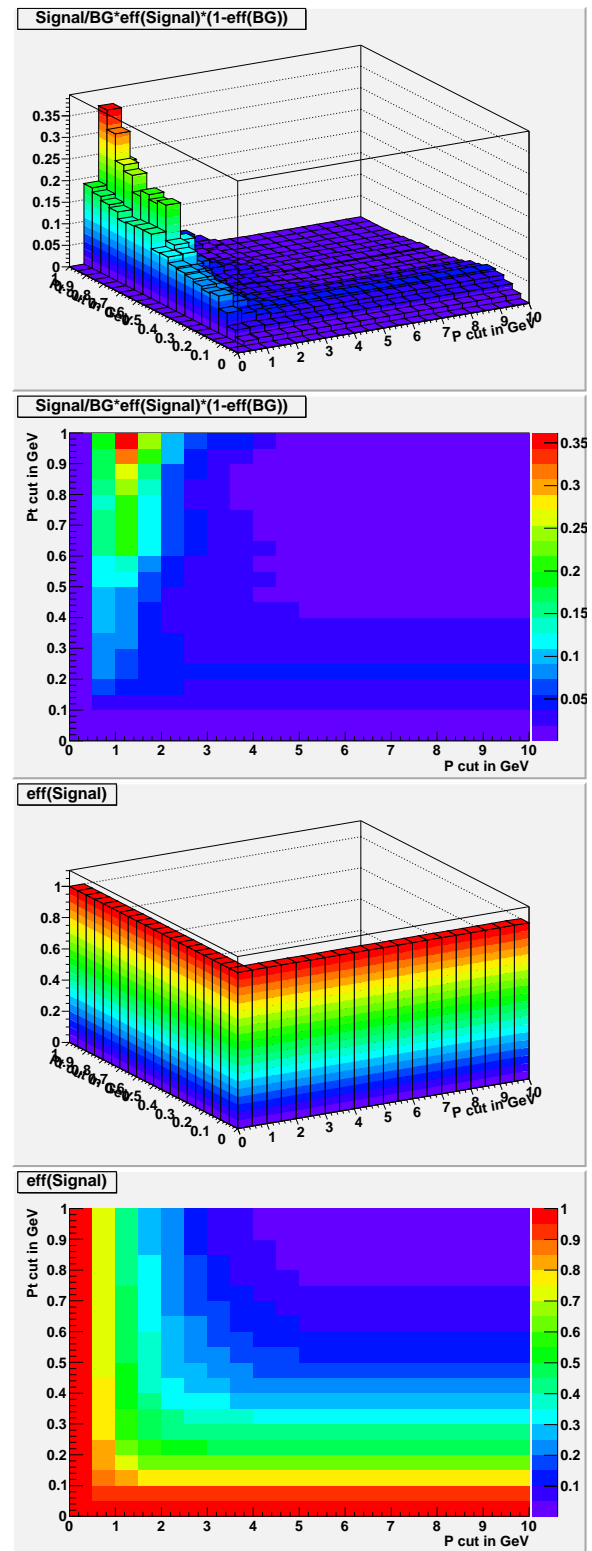
Figure F.8: "P||P_t" cut for the class longn_pt_st: (top) 3-d view of the "figure-of-merit" calculation for the cut, 2-d view below. (bottom) 3-d view of the charm efficiency for the cut, 2-d view below.
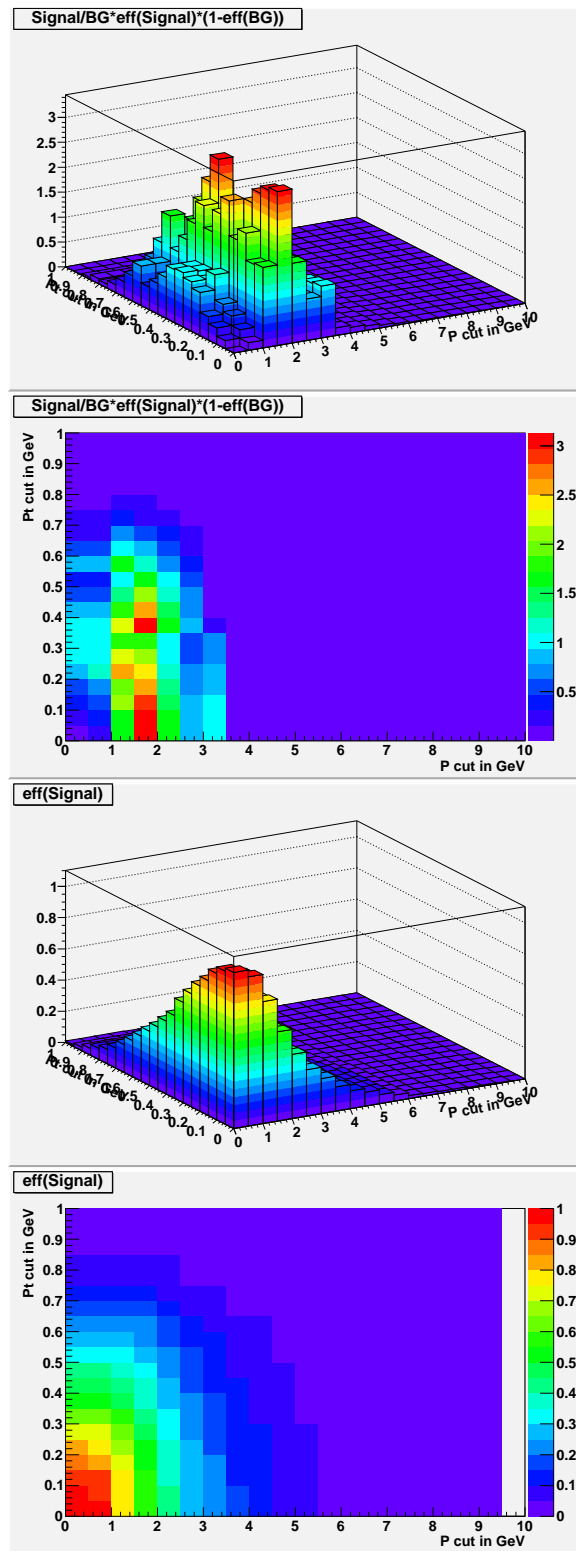
Figure F.9: "$P\&\&P_t$" cut for the class longn_pt_sv: (top) 3-d view of the "figure-of-merit" calculation for the cut, 2-d view below. (bottom) 3-d view of the charm efficiency for the cut, 2-d view below.
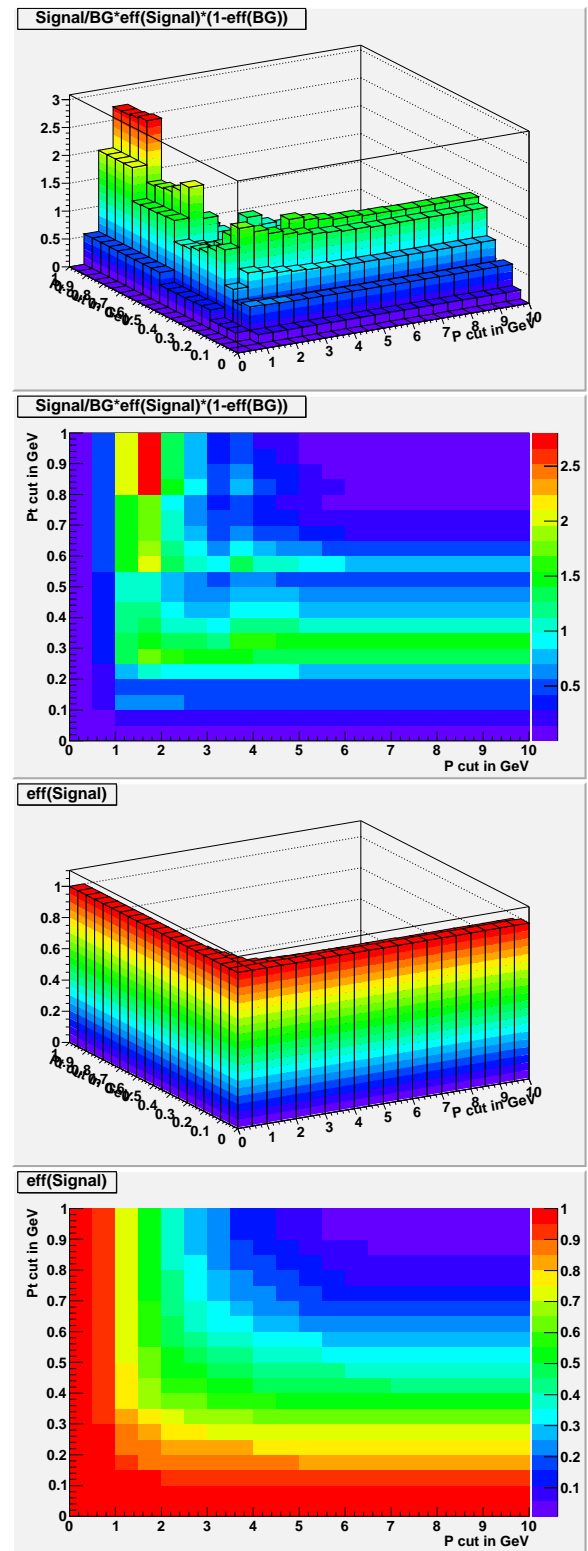
Figure F.10: "$P||P_t$" cut for the class longn_pt_sv: (top) 3-d view of the "figure-of-merit" calculation for the cut, 2-d view below. (bottom) 3-d view of the charm efficiency for the cut, 2-d view below.
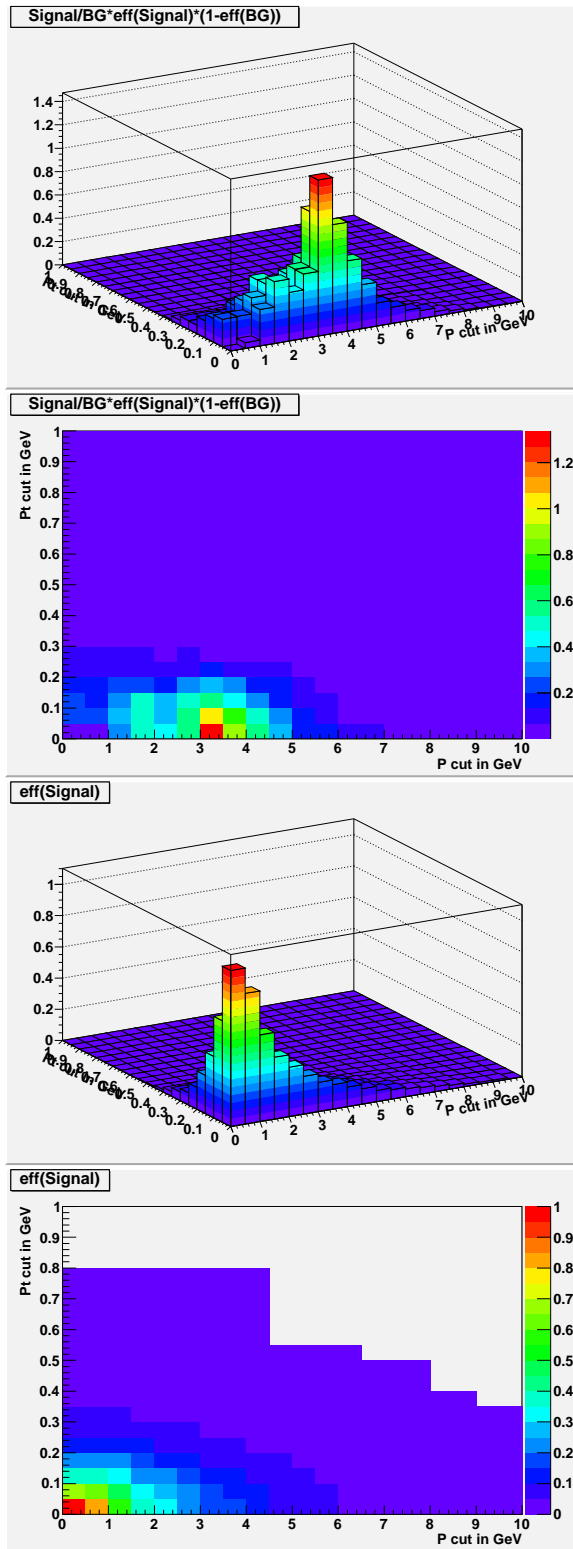
Figure F.11: "$P\&\&P_t$" cut for the class longn_pv_st: (top) 3-d view of the "figure-of-merit" calculation for the cut, 2-d view below. (bottom) 3-d view of the charm efficiency for the cut, 2-d view below.
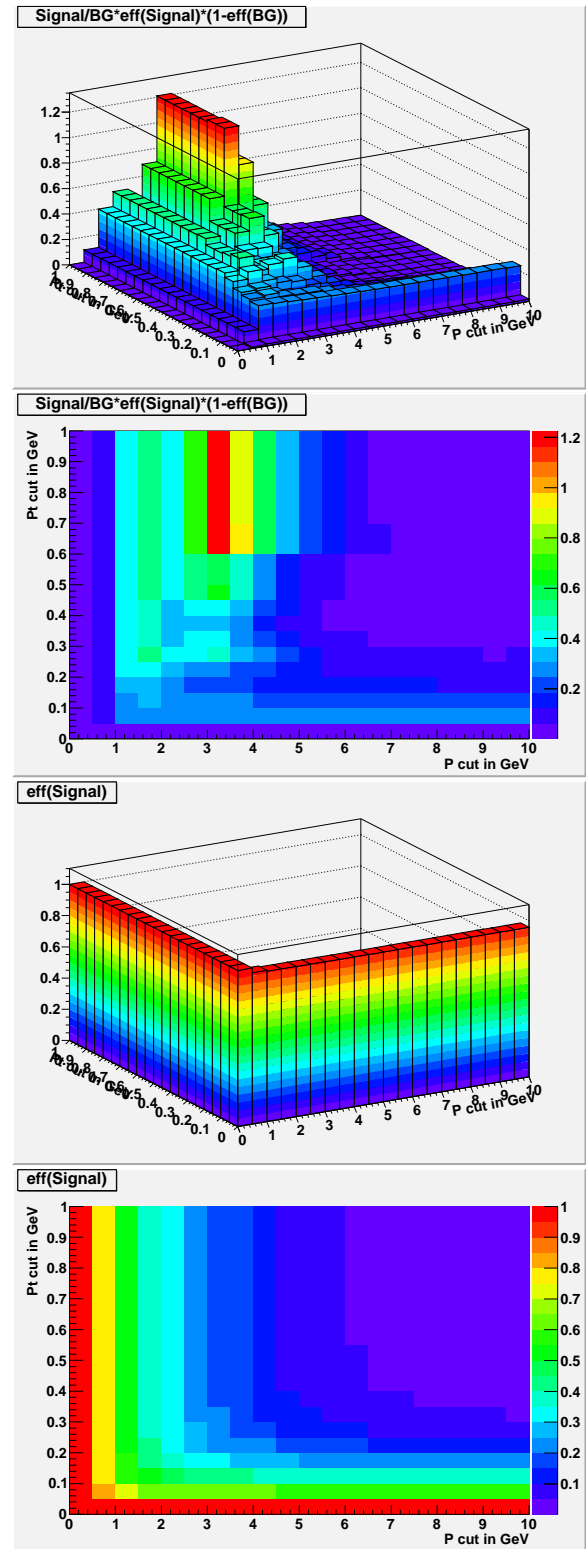
Figure F.12: "$P||P_t$" cut for the class longn_pv_st: (top) 3-d view of the "figure-of-merit" calculation for the cut, 2-d view below. (bottom) 3-d view of the charm efficiency for the cut, 2-d view below.
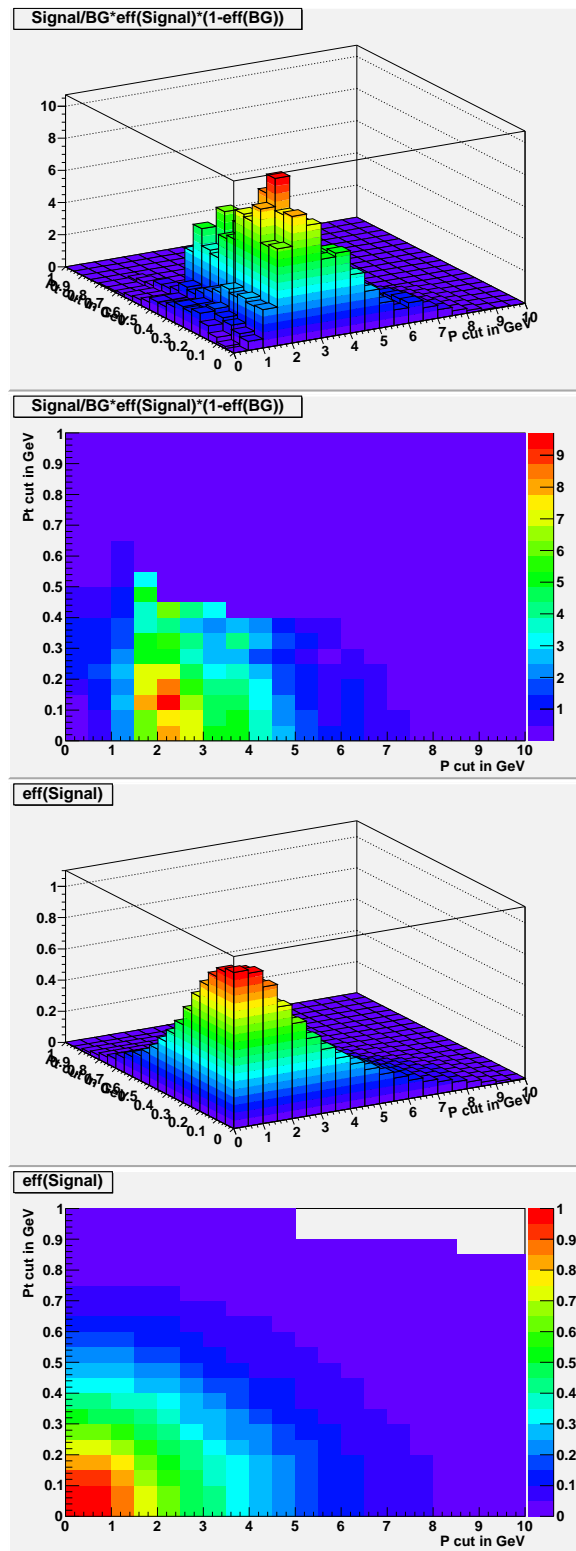
Figure F.13: "$P\&\&P_t$" cut for the class longn_pv_sv: (top) 3-d view of the "figure-of-merit" calculation for the cut, 2-d view below. (bottom) 3-d view of the charm efficiency for the cut, 2-d view below.
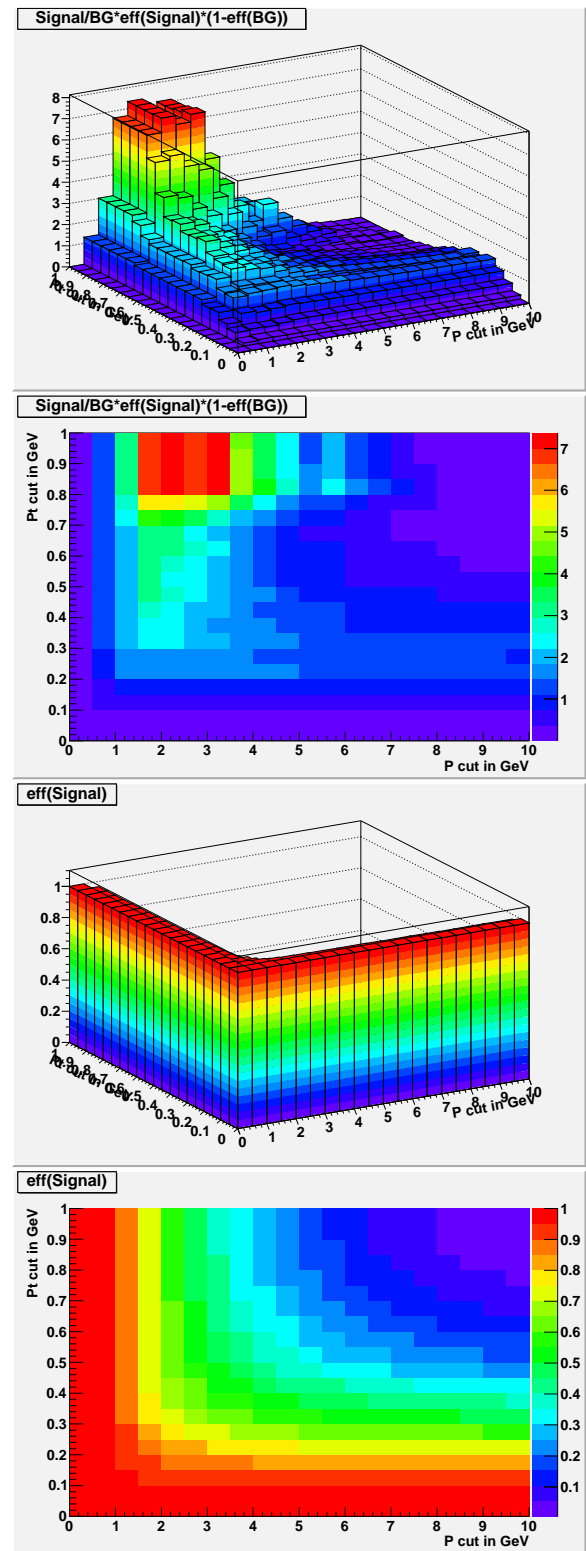
Figure F.14: "$P||P_t$" cut for the class longn_pv_sv: (top) 3-d view of the "figure-of-merit" calculation for the cut, 2-d view below. (bottom) 3-d view of the charm efficiency for the cut, 2-d view below.
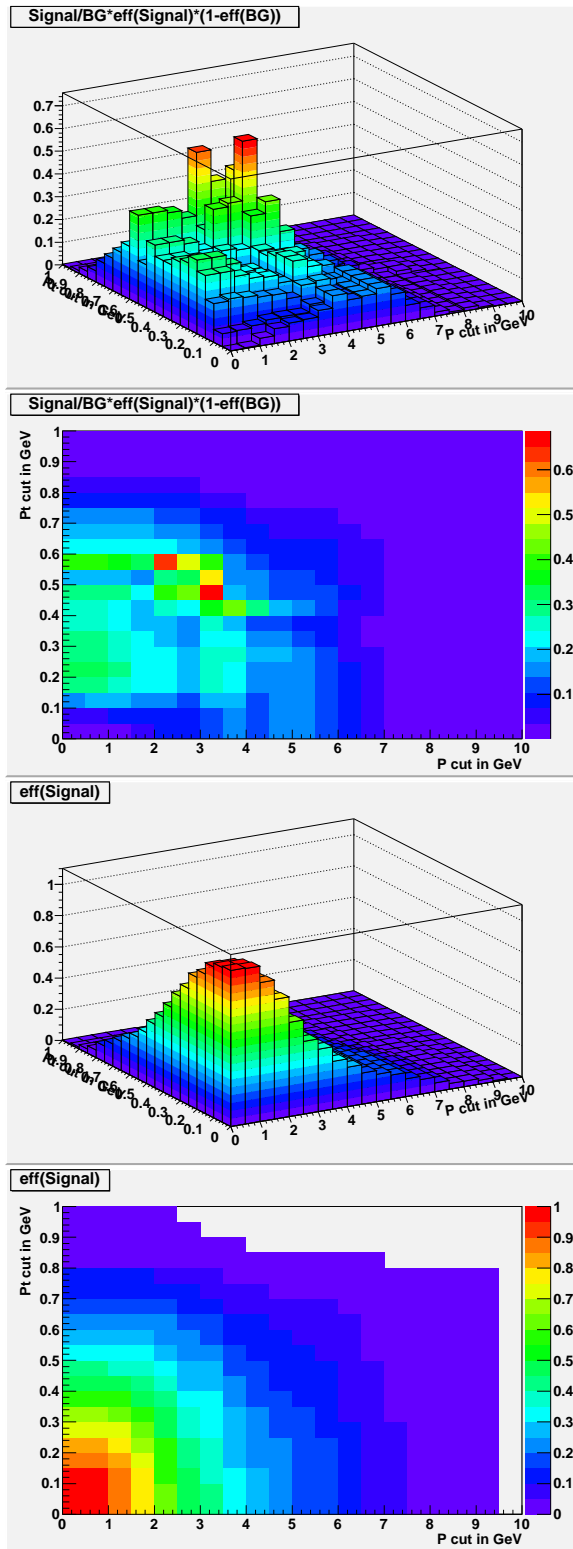
Figure F.15: "P&&P_t" cut for the class longc_pv_st: (top) 3-d view of the "figure-of-merit" calculation for the cut, 2-d view below. (bottom) 3-d view of the charm efficiency for the cut, 2-d view below.
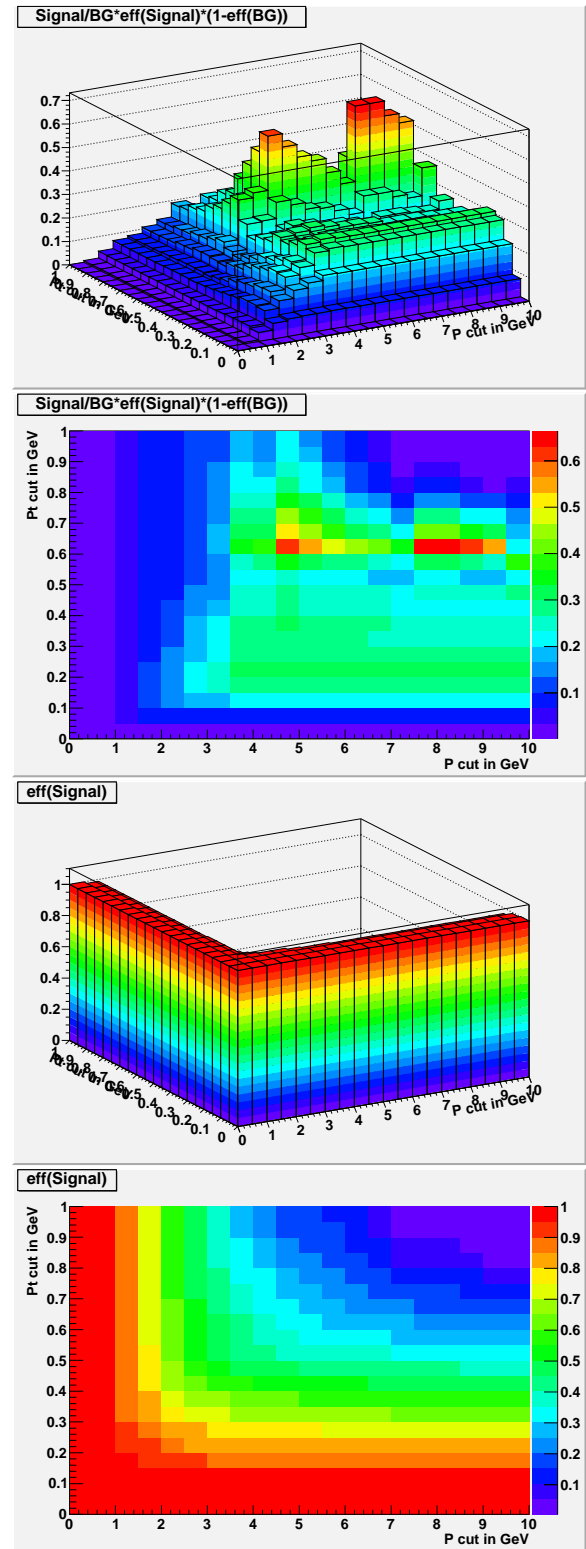
Figure F.16: "P||P_t" cut for the class longc_pv_st: (top) 3-d view of the "figure-of-merit" calculation for the cut, 2-d view below. (bottom) 3-d view of the charm efficiency for the cut, 2-d view below.
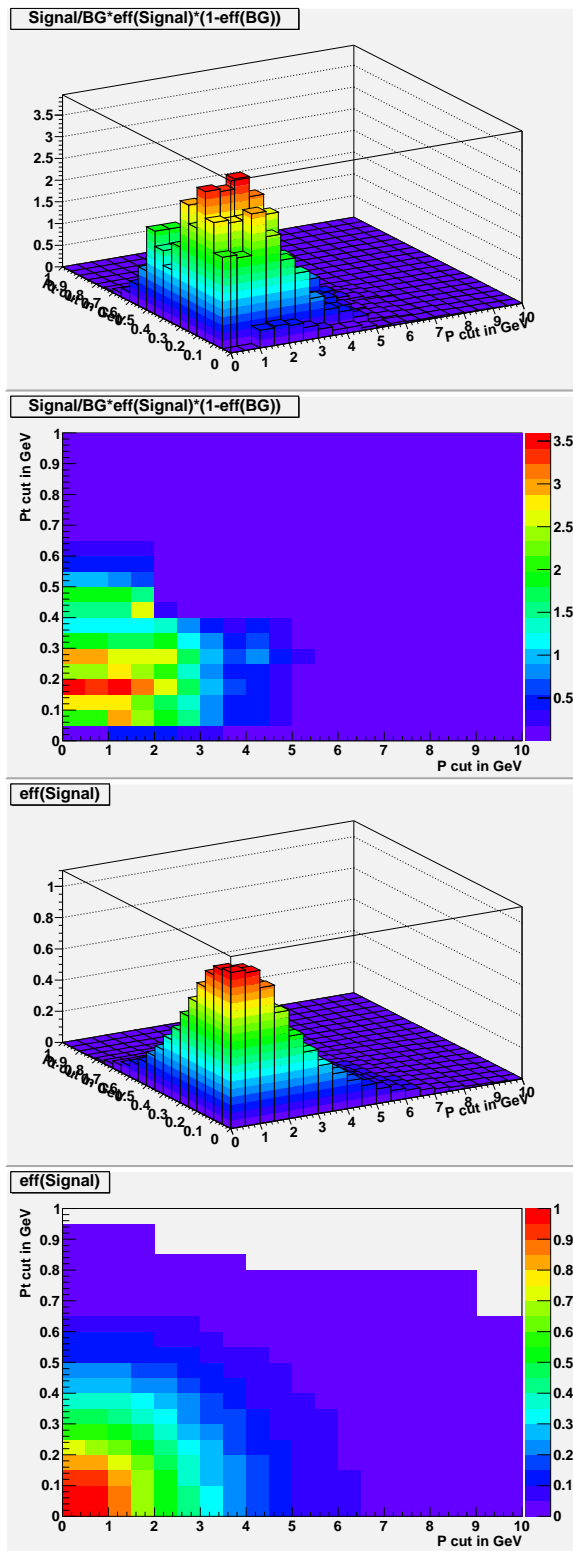
Figure F.17: "$P\&\&P_t$" cut for the class longc_pv_sv: (top) 3-d view of the "figure-of-merit" calculation for the cut, 2-d view below. (bottom) 3-d view of the charm efficiency for the cut, 2-d view below.
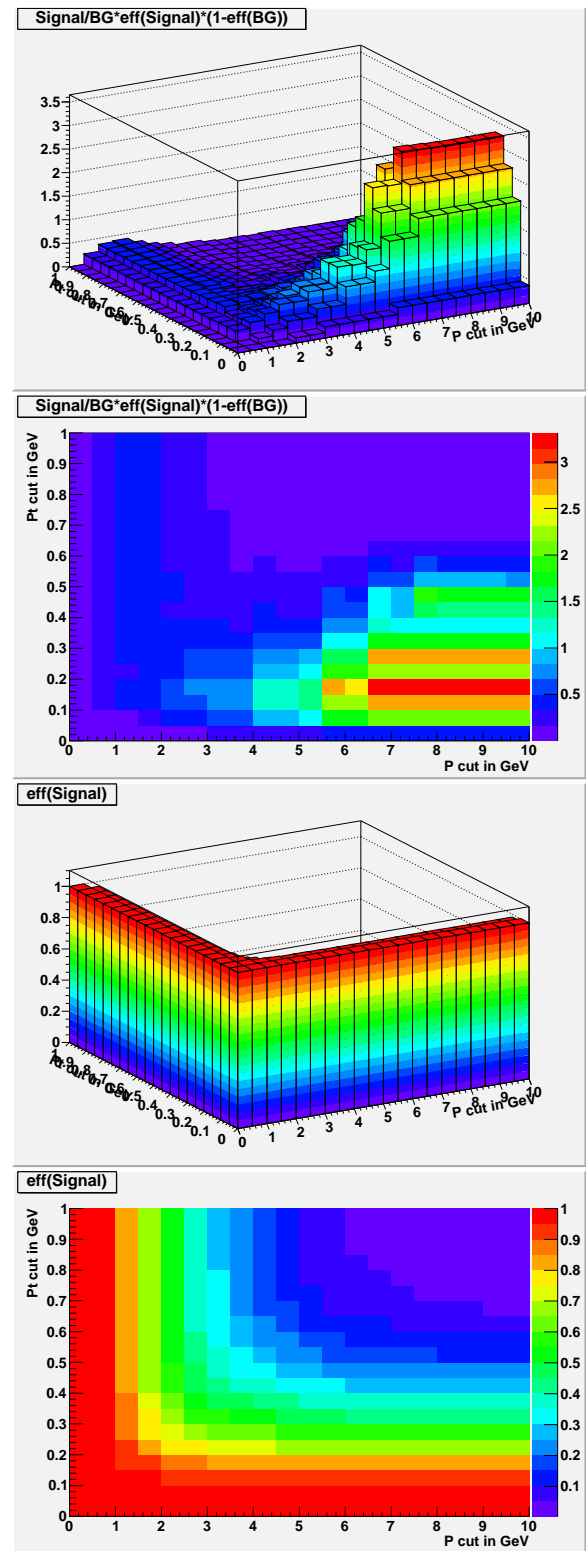
Figure F.18: "$P||P_t$" cut for the class longc_pv_sv: (top) 3-d view of the "figure-of-merit" calculation for the cut, 2-d view below. (bottom) 3-d view of the charm efficiency for the cut, 2-d view below.

Appendix G

A HTS Solenoid for a LAr TPC

The work summarized here was done as a continuation of my diploma work on R&D activities in the ETHZ neutrino group [272]. I will skip any introduction to superconductors or the LAr TPC technology [273, 274], as these topics were already included in my diploma thesis. Usage of high temperature superconductors in liquid argon profits from the advantage of an already existing cryogenic environment needed for the liquid argon time projection chamber (LAr TPC) itself. Argon has a boiling temperature of 87.15 K (at 1 bar), which is below the critical temperature of some HTS wires like BSCCO (110 K, 1st generation) or YBCO (90 K, 2nd generation). Additionally, the size of superconductive coils is usually smaller than the size of a conventional coil, and due to the superconductivity the losses due to resistance are vanishing, thus the magnetized "dead" volume is diminished. Even though the final prototype chamber wasn't realized, this work will be useful for future experiments, where the charge identification of the tracks in the LAr TPC will be needed to understand and obtain the physics results, as e.g. in CP-violation studies at a future neutrino factory, like the proposed GLACIER experiment, which aims at the construction of a 100 kton LAr TPC where a conventional magnet would dissipate about 17 MW of heating power at a field of 0.2 T (or 88 MW for 1 T) [176, 178, 179, 183, 180, 185, 275, 276].

A magnetized LAr TPC allows the determination of the electric charge and a measurement of the momentum of particles escaping the detector, resulting in a precise measurement of the kinematics also for partially contained events. A first successful test of a small LAr TPC in a magnetic field perpendicular to the drift direction has shown that the imaging properties are not significantly deteriorated by the magnetic field [275, 277]. The magnetic field was 0.55 T and was produced with the normal conducting SINDRUM I solenoid obtained from PSI[1], the setup is shown in Figure G.1.

As described in [278], a giant liquid argon TPC (e.g. GLACIER) would be an excellent detector for a future neutrino factory, as explained in section 1.3.4. To search for CP-violating effects in the lepton sector at a ν-factory, a magnetized detector is absolutely necessary in order to determine the electric charge of muons and/or electrons occurring in the CC interactions [183]; for the muons a field of the order of 0.1 T is needed and for the electrons approximately 1 T would be required. Thus, the most attractive design would be a superconducting solenoid built into the cylindrical liquid argon tank, i.e. directly immersed in the LAr of the detector. This would require high performance HTS cables

---

[1]Paul Scherrer Institut, CH-5232 Villigen PSI, Switzerland
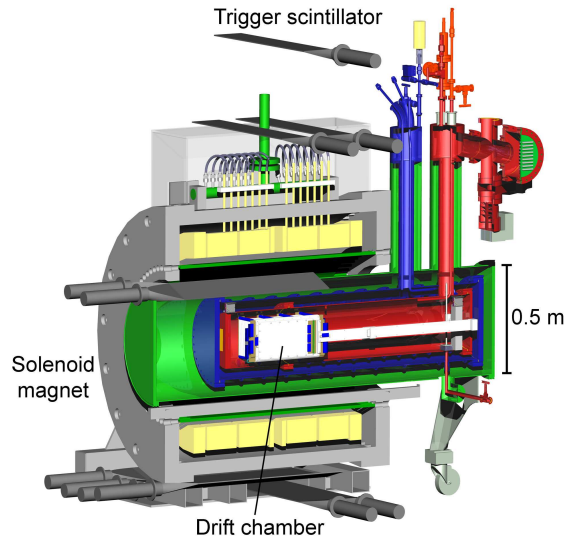
Figure G.1: *Setup of the small LAr TPC embedded in a magnetic field.*

with a high enough critical current at LAr temperature (87 K). As usually HTS cables are used at liquid nitrogen or lower temperatures, we first had to measure the critical current of BSCCO and YBCO based cables as a function of a parallel and perpendicular external magnetic field at LN_2 and LAr temperatures. A very small prototype HTS solenoid was built from about 100 m of BSCCO cable and was successfully tested [272].

Data from the manufacturer on the critical current of their HTS wires are only available up to the LN_2 temperature of about 77 K. For high temperature superconductors the transition from the normal to the superconducting state is not as sharp as for low temperature superconductors. Hence, the critical current for HTS is usually defined as the current for which the voltage drop in the superconductor reaches the value of $1\,\mu V/cm$; it is very sensitive to the temperature and the applied magnetic field.

To study these effects, we got a small sample of HTS cables from the American Superconductor Corporation[2] (AMSC:BSCCO+YBCO) and SuperPower[3] (SP:YBCO).

---

[2]http://www.amsuper.com
[3]http://www.superpower-inc.com
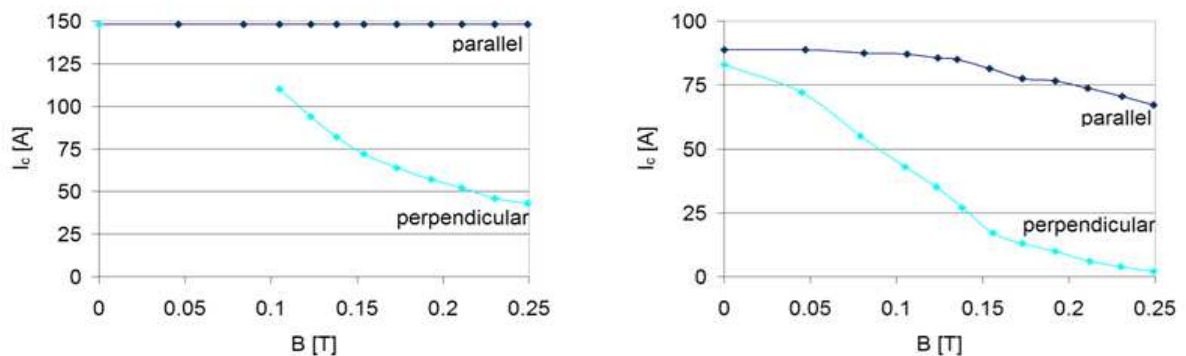
Figure G.2: *Critical current I_c of the ASMC BSCCO cable measured in (left) LN_2 and (right) LAr as a function of the applied parallel and perpendicular magnetic field.*
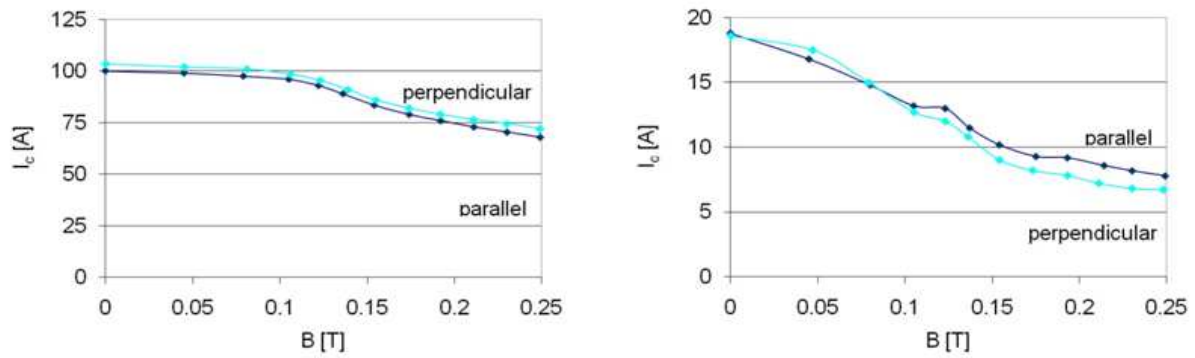
Figure G.3: *Critical current I_c of the AMSC YBCO cable measured in (left) LN_2 and (right) LAr as a function of the applied parallel and perpendicular magnetic field.*
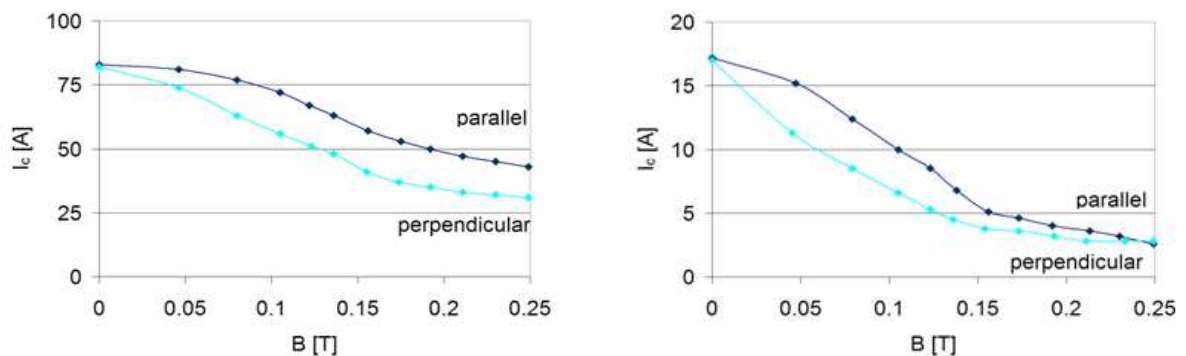
Figure G.4: *Critical current I_c of the SP YBCO cable measured in (left) LN_2 and (right) LAr as a function of the applied parallel and perpendicular magnetic field.*

The BSCCO cable was a copper stabilized ribbon of 4 mm width and a thickness of 0.4 mm. Figure G.2 shows the critical current I_c measured in LN_2 and LAr as a function of the applied parallel and perpendicular magnetic field. The results obtained with second generation YBCO based cables are shown in Figure G.3 for the 4 mm wide and 0.25 mm thick AMSC cable, and in Figure G.4 for the 4 mm wide and 0.1 mm thick SuperPower cable.
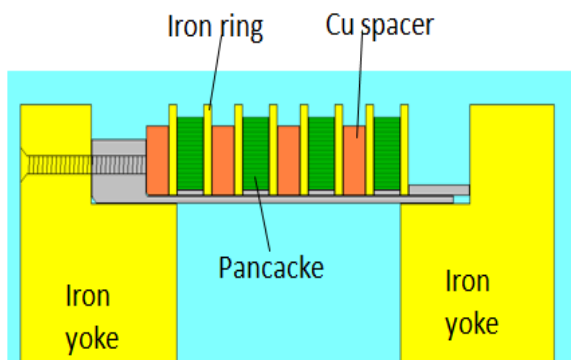
Figure G.5: *Drawing of the test solenoid. The lower edge corresponds to the solenoid axis. Picture from [272].*
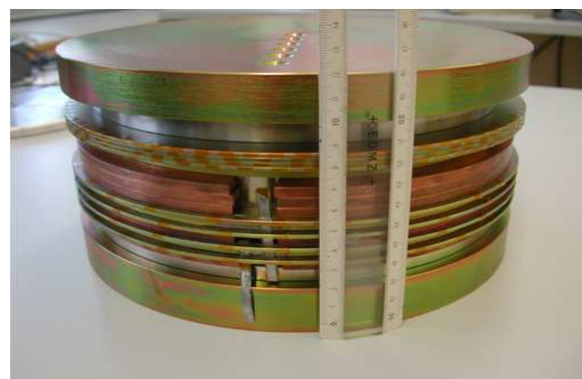
Figure G.6: *Picture of the test solenoid. The height of the solenoid is about 14 cm. Picture from [272].*
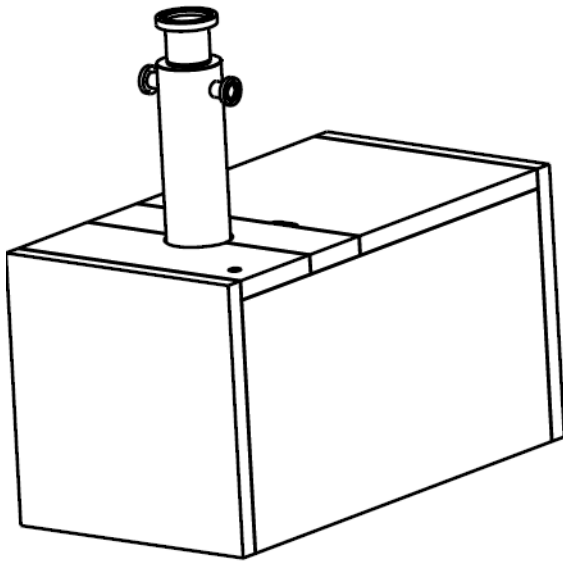
Figure G.7: *CAD- drawing of the test setup in its cooling box.*
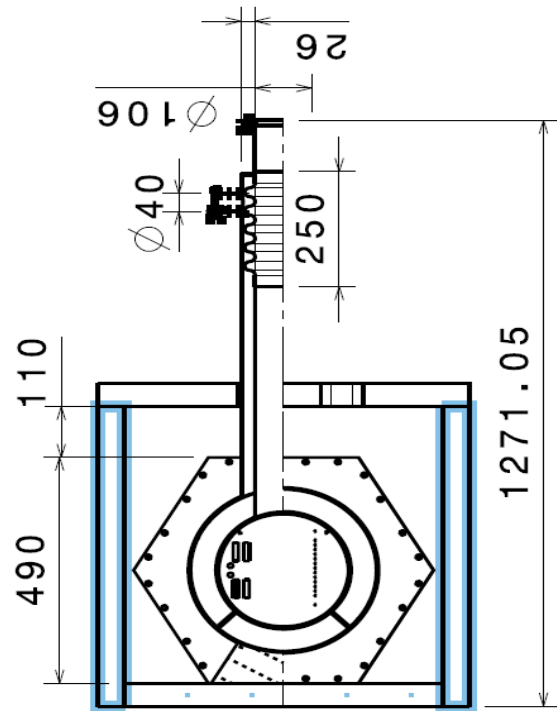
Figure G.8: *CAD-cut through the prototype setup.*

The measured critical current at LAr temperature for YBCO is significantly lower than for the BSCCO cable, as the YBCO transition temperature is $90\,\mathrm{K}$ compared to $110\,\mathrm{K}$ for the BSCCO. Hence, we propose to build a directly immersed solenoid with the BSCCO cable. If an additional nitrogen shielding of the LAr TPC is foreseen, the possibility of YBCO can be reconsidered [270].

As already mentioned in the introduction, a very small prototype solenoid was built with the BSCCO cable. Figures G.5 and G.6 show a drawing and a picture of this magnet. It consists of four so called pancake coils with 30 windings each and connected in series. Between the pancakes there was a copper spacer and iron shielding rings to shape the magnetic field in order to reduce the component perpendicular to the cable. The solenoid was closed with iron end plates at both ends, no barrel yoke was used because of space limitations. The total HTS cable length used was less than $100\,\mathrm{m}$. The maximal magnetic field measured at the center was $0.2\,\mathrm{T}$ in $\mathrm{LN_2}$ and $0.11\,\mathrm{T}$ in LAr.

Based on the obtained result, a design for a test setup was made to re-use the previously mentioned TPC, as shown in Figure G.7 and G.8. As improvement, the high voltage of the drift chamber was to be applied by a Greinacher (Cockroft/Walton) circuit, tested successfully up to $70\,\mathrm{kV}$ and the feasibility of a Geiger-mode avalanche photo diode (GAPD) light read-out to be used as trigger on LAr scintillation was considered. For the time being this project was not pursued.

List of Figures

Bibliography

[1] N. Schmitz. *Neutrinophysik.* Teubner Verlag, 1997

[2] D. Verkindt. NEUTRINO HISTORY
URL `http://wwwlapp.in2p3.fr/neutrinos/aneut.html`

[3] C. Giunti and M. Laveder. Neutrino Unbound
URL `http://www.nu.to.infn.it/`

[4] A. G. van Melsen. *From Atomos to Atom.* Mineola, N.Y.: Dover Publications, 1952

[5] E. W. Weisstein. Lavoisier, Antoine (1743-1794)
URL `http://scienceworld.wolfram.com/biography/Lavoisier.html`

[6] J. L. Proust. Researches on Copper. *Ann. chim.*, 32:26–54, 1799

[7] J. Dalton. On the Absorption of Gases by Water and Other Liquids. *Memoirs of the Literary and Philosophical Society of Manchester*, 1803

[8] A. Avogadro. Essay on a Manner of Determining the Relative Masses of the Elementary Molecules of Bodies, and the Proportions in Which They Enter into These Compounds. *Journal de Physique*, 73:58–76, 1811

[9] A. Einstein. On the Movement of Small Particles Suspended in Stationary Liquids Required by the Molecular-Kinetic Theory of Heat. *Annalen der Physik*, 17, 1905

[10] G. Patterson. Jean Perrin and the triumph of the atomic doctrine. *Endeavour*, 31(2):50 – 53, 2007

[11] J. Thomson. Cathode Rays, facsimile from Stephen Wright, Classical Scientific Papers, Physics (Mills and Boon, 1964). *Philosophical Magazine*, 44, 1897

[12] J. Thomson. On the Structure of the Atom: an Investigation of the Stability and Periods of Oscillation of a number of Corpuscles arranged at equal intervals around the Circumference of a Circle; with Application of the Results to the Theory of Atomic Structure. *Philosophical Magazine*, 7, 1904

[13] H. Becquerel. Sur quelques proprietés nouvelles des radiations invisibles émises par divers corps phosphorescents. *Comptes Rendus*, 122:559–564, 1896

[14] E. Rutherford. Uranium Radiation and the Electrical Conduction produced by It. *Philosophical Magazine*, Ser. 5, xlvii:109–163, 1899

[15] G. H. and M. E. On a Diffuse Reflection of the α-Particles. *Proceedings of the Royal Society*, A 82:495–500, 1909

[16] E. Rutherford. The Scattering of α and β Particles by Matter and the Structure of the Atom. *Philosophical Magazine*, 21, 1911

[17] N. Bohr. On the constitution of atoms and molecules. *Philosophical Magazine*, 26, 1913

[18] F. Soddy. Intra-atomic Charge. *Nature*, 92:399–400, 1913

[19] J. Thomson. Rays of positive electricity. *Proceedings of the Royal Society*, A 89:1–20, 1913

[20] M. Curie. Rayons émis par les composés de l'uranium et du thorium. *Comptes Rendus*, 126:1101–1103, 1898

[21] P. Curie and M. Curie. Sur une substance nouvelle radio-active, contenue dans la pechblende. *Comptes Rendus*, 127:175–178, 1898

[22] P. Curie, M. Curie, and G. Bmont. Sur une nouvelle substance fortement radioactive, contenue dans la pechblende. *Comptes Rendus*, 127:1215–1217, 1898

[23] O. Hahn and L. Meitner. Über die Absorption der β-Strahlen einiger Radioelemente. *Physikalische Zeitschrift*, 9:321–333, 1908

[24] O. Hahn and L. Meitner. Über die Strahlen des Aktiniums. *Physikalische Zeitschrift*, 9:697–704, 1908

[25] O. Hahn and L. Meitner. Über eine typische β-Strahlung des eigentlichen Radiums. *Physikalische Zeitschrift*, 10:641–745, 1909

[26] O. Hahn and L. Meitner. Eine neue β-Strahlung bein Thorium X; Analogien in der Uran- und Thoriumreihe. *Physikalische Zeitschrift*, 11:493–497, 1910

[27] O. von Baeyer and O. Hahn. Magnetic Line Spectra of Beta Rays. *Physikalische Zeitschrift*, 11:448–493, 1910

[28] O. H. Otto von Baeyer and L. Meitner. Nachweis von β-Strahlen bei Radium D. *Physikalische Zeitschrift*, 12:378–379, 1911

[29] O. Hahn and L. Meitner. Über die β-Strahlen des aktiven Niederschlags des Thoriums. *Physikalische Zeitschrift*, 12:273–279, 1911

[30] W. Wilson. On the Absorption of Homogeneous β-Rays by Matter, and on the Variation of the Absorption of the Rays with Velocity. *Proceedings of the Royal Society London*, A82:612–628, 1909

[31] J. Chadwick. Intensitätsverteilung im magnetischen Spektrum der β-Strahlen von Radium B+C. *Verhandlungen der Deutschen Physikalischen Gesellschaft*, 16:383–391, 1914

[32] J. Chadwick. Possible Existence of a Neutron. *Nature*, page 312, 1932

[33] J. Chadwick. The existence of a neutron. *Proceedings of the Royal Society London*, A136:692–708, 1932

[34] C. D. Anderson. The Apparent Existence of Easily Deflectable Positives. *Science*, 76:238–239, 1932

[35] C. D. Anderson. The Positive Electron. *Phys. Rev.*, 43(6):491–494, 1933

[36] P. Dirac. The Quantum Theory of the Electron. *Proceedings of the Royal Society A*, 117:610–624, 1928

[37] W. Pauli. The structure and properties of atomic nuclei. *Rapports du Septième Conseil de Physique Solvay*, 1933

[38] F. Perrin. Possibilité d'émission de particules neutres de masse intrinsequement nulle dans les radioactivités β. *Comptes rendus de l'Académie des Sciences*, 197:1625, 1933

[39] F. Joliot and I. Curie. Èmission de protons de grande vitesse par les substances hydrogénées sous l'influence des rayons g trés pénétrants. *Comptes rendus hebdomadaires des séances de l'Académie des Sciences*, 194:273–275, 1932

[40] E. Fermi. Versuch einer Theorie der β-Strahlen. *Zeitschrift für Physik*, 88:161, 1934

[41] H. A. Bethe and R. Peierls. The neutrino. *Nature*, 133:532, 1934

[42] L. W. Alvarez and R. Cornog. Helium and Hydrogen of Mass 3. *Phys. Rev.*, 56(6):613, 1939

[43] KATRIN. KATRIN: A next generation tritium beta decay experiment with sub-eV sensitivity for the electron neutrino mass, 2001

[44] L. Meitner and O. R. Frisch. Disintegration of Uranium by Neutrons: a New Type of Nuclear Reaction. *Nature*, 143,3615:239–240, 1939

[45] H. A. Bethe. Energy Production in Stars. *Phys. Rev.*, 55(1):103, 1939

[46] K.-C. Wang. A Suggestion on the Detection of the Neutrino. *Phys. Rev.*, 61:97, 1942

[47] E. P. Hincks and B. Pontecorvo. Inverse β process. *National Research Council of Canada, Division of Atomic Energy. Chalk River, Report PD-205)*, 1946

[48] F. Reines and C. L. Cowan. A Proposed Experiment to Detect the Free Neutrino. *Phys. Rev.*, 90:492, 1953

[49] F. Reines and C. L. Cowan. Detection of the Free Neutrino. *Phys. Rev.*, 92:830, 1953

[50] C. L. Cowan, F. Reines, F. B. Harrison, H. W. Kruse, and A. D. McGuire. Detection of the Free Neutrino: A Confirmation. *Science*, 124:103, 1956

[51] F. Reines, C. L. Cowan, F. B. Harrison, A. D. McGuire, and H. W. Kruse. Detection of the Free Antineutrino. *Phys. Rev.*, 117(1):159–173, 1960

[52] R. Davis. Attempt to Detect the Antineutrinos from a Nuclear Reactor by the $Cl^{37}(\overline{\nu}, e^-)Ar^{37}$ Reaction. *Phys. Rev.*, 97(3):766–769, 1955

[53] R. Davis. A review of the homestake solar neutrino experiment. *Progress in Particle and Nuclear Physics*, 32:13–32, 1994

[54] B. Pontecorvo. Electron and muon neutrinos. *Sov. Phys. JETP*, 10:1236–1240, 1960

[55] M. Schwartz. Feasibility of Using High-Energy Neutrinos to Study the Weak Interactions. *Phys. Rev. Lett.*, 4(6):306–307, 1960

[56] J. Cronin and G. Renninger. Studies of a Neon filled spark chamber. Technical Report No. 25. *Instrumentation for High-Energy Physics, Proceedings (CA. Interscience Publications)*, page (271), 1960 (1961)

[57] G. Danby, J.-M. Gaillard, K. Goulianos, L. M. Lederman, N. Mistry, M. Schwartz, and J. Steinberger. Observation of High-Energy Neutrino Reactions and the Existence of Two Kinds of Neutrinos. *Phys. Rev. Lett.*, 9(1):36–44, 1962

[58] T. D. Lee and C. N. Yang. Theoretical Discussions on Possible High-Energy Neutrino Experiments. *Phys. Rev. Lett.*, 4:307–311, 1960

[59] T. D. Lee and C. N. Yang. Question of Parity Conservation in Weak Interactions. *Phys. Rev.*, 104(1):254–258, 1956

[60] R. H. Dalitz. The tau-theta puzzle. *Discovery of weak neutral currents: the weak interaction before and after*, 300(1):141–158, 1994

[61] C. S. Wu, E. Ambler, R. W. Hayward, D. D. Hoppes, and R. P. Hudson. Experimental Test of Parity Conservation in Beta Decay. *Phys. Rev.*, 105(4):1413–1415, 1957

[62] R. L. Garwin, L. M. Lederman, and M. Weinrich. Observations of the Failure of Conservation of Parity and Charge Conjugation in Meson Decays: the Magnetic Moment of the Free Muon. *Phys. Rev.*, 105(4):1415–1417, 1957

[63] M. Goldhaber, L. Grodzins, and A. W. Sunyar. Helicity of Neutrinos. *Phys. Rev.*, 109(3):1015–1017, 1958

[64] T. Nakano and K. Nishijima. Charge Independence for V-particles. *Progress of Theoretical Physics*, 10(5):581–582, 1953

[65] K. Nishijima. Charge Independence Theory of V Particles. *Progress of Theoretical Physics*, 13(3):285–304, 1955

[66] M. Gell-Mann. The interpretation of the new particles as displaced charge multiplets. *Il Nuovo Cimento (1955-1965)*, 4(0):848–866, 1956

[67] CERN. CHARM and CHARM 2 Collection
URL http://library.web.cern.ch/library/Archives/isad/isacharm.html

[68] C. Giunti and M. Laveder. CHARM publications collection (CERN-Hamburg-Amsterdam-Rome-Moscow Collaboration)
URL http://www.nu.to.infn.it/exp/all/charm/

[69] C. Giunti and M. Laveder. CDHS publications collection (CERN, Dortmund, Heidelberg and Saclay)
URL http://www.nu.to.infn.it/exp/all/cdhsw/

[70] C. Giunti and M. Laveder. BEBC publications collection (Big European Bubble Chamber Collaboration)
URL http://www.nu.to.infn.it/exp/all/bebc/

[71] M. Gell-Mann. A schematic model of baryons and mesons. *Phys. Let.*, 8(3):214–215, 1964

[72] G. Zweig. An SU(3) Model for Strong Interaction Symmetry and its Breaking. *CERN Report No.8181/Th 8419*, 1964

[73] G. Zweig. An SU(3) Model for Strong Interaction Symmetry and its Breaking: II. *CERN Report No.8419/Th 8412*, 1964

[74] M. Gell-Mann. The Eightfold Way: A theory of strong interaction symmetry. *Synchroton Laboratory Report CTSL-20*, 1961

[75] J. H. Christenson, J. W. Cronin, V. L. Fitch, and R. Turlay. Evidence for the 2π Decay of the K_2^0 Meson. *Phys. Rev. Lett.*, 13(4):138–140, 1964

[76] S. G. B.J. Bjorken. Elementary Particles and SU(4). *Phys. Let.*, 11(3):255–257, 1964

[77] A. Salam and J. Ward. Electromagnetic and weak interactions. *Phys. Let.*, 13(2):168–171, 1964

[78] S. L. Glashow. Partial Symmetries of Weak Interactions. *Nucl. Phys.*, 22:579–588, 1961

[79] S. Weinberg. A Model of Leptons. *Phys. Rev. Lett.*, 19(21):1264–1266, 1967

[80] P. W. Higgs. Broken Symmetries and the Masses of Gauge Bosons. *Phys. Rev. Lett.*, 13:508–509, 1964

[81] G. S. Guralnik, C. R. Hagen, and T. W. B. Kibble. Global Conservation Laws and Massless Particles. *Phys. Rev. Lett.*, 13:585–587, 1964

[82] F. Englert and R. Brout. Broken Symmetry and the Mass of Gauge Vector Mesons. *Phys. Rev. Lett.*, 13:321–323, 1964

[83] E. Bloom. High-Energy Inelastic e-p Scattering at 6° and 10°. *Phys. Rev. Lett.*, 23(16):930–934, 1969

[84] M. Breidenbach. Observed Behavior of Highly Inelastic Electron-Proton Scattering. *Phys. Rev. Lett.*, 23(16):935–939, 1969

[85] R. Feynman. Very High-Energy Collisions of Hadrons. *Phys. Rev. Lett.*, 23(24):1415–1417, 1969

[86] S. L. Glashow, J. Iliopoulos, and L. Maiani. Weak Interactions with Lepton-Hadron Symmetry. *Phys. Rev. D*, 2(7):1285–1292, 1970

[87] M. Kobayashi and T. Maskawa. *CP*-Violation in the Renormalizable Theory of Weak Interaction. *Progress of Theoretical Physics*, 49(2):652–657, 1973

[88] F. Hasert *et al.* Search for elastic muon-neutrino electron scattering. *Phys. Let. B*, 46(1):121 – 124, 1973

[89] F. J. Hasert *et al.* Observation of neutrino-like interactions without muon or electron in the Gargamelle neutrino experiment. *Phys. Lett.*, B46:138–140, 1973

[90] F. J. Hasert *et al.* Observation of neutrino like interactions without muon or electron in the GARGAMELLE neutrino experiment. *Nucl. Phys.*, B73:1, 1974

[91] J. E. Augustin *et al.* Discovery of a Narrow Resonance in $e^+ - e^-$ Annihilation. *Phys. Rev. Lett.*, 33:1406–1408, 1974

[92] D. H. Perkins. *Introduction to high-energy physics; 4th ed.* Cambridge Univ. Press, Cambridge, 2000

[93] J. J. Aubert *et al.* Experimental Observation of a Heavy Particle *J*. *Phys. Rev. Lett.*, 33(23):1404–1406, 1974

[94] S. W. Herb *et al.* Observation of a Dimuon Resonance at 9.5 GeV in 400-GeV Proton-Nucleus Collisions. *Phys. Rev. Lett.*, 39(5):252–255, 1977

[95] M. L. Perl *et al.* Evidence for Anomalous Lepton Production in $e^+ - e^-$ Annihilation. *Phys. Rev. Lett.*, 35(22):1489–1492, 1975

[96] T. A. Collaboration, T. D. Collaboration, the L3 Collaboration, T. O. collaboration, T. S. Collaboration, the LEP Electroweak Working Group, the SLD Electroweak, and H. F. Groups. Precision electroweak measurements on the Z resonance. *Physics Reports*, 427(5-6):257 – 454, 2006

[97] S. van der Meer. Optimum gain and phase for stochastic cooling systems. *CERN/PS-AA/83*, 1983

[98] D. Möhl, G. Petrucci, L. Thorndahl, and S. van der Meer. Physics and technique of stochastic cooling. *Physics Reports*, 58(2):73–102, 1980

[99] G. Arnison *et al.* Experimental observation of isolated large transverse energy electrons with associated missing energy at $\sqrt{s} = 540\,GeV$. *Phys. Let. B*, 122(1):103 – 116, 1983

[100] G. Arnison *et al.* Experimental observation of lepton pairs of invariant mass around 95 GeV/c^2 at the CERN SPS collider. *Phys. Let. B*, 126(5):398 – 410, 1983

[101] G. Arnison *et al.* Observation of the muonic decay of the charged intermediate vector boson. *Phys. Let. B*, 134(6):469 – 476, 1984

[102] G. Arnison *et al.* Observation of muonic Z^0-decay at the $p\bar{p}$ collider. *Phys. Let. B*, 147(1-3):241 – 248, 1984

[103] CERN. The UA2 Collaboration collection, Underground Area 2
URL `http://library.web.cern.ch/library/Archives/isad/isaua2.html`

[104] M. Banner *et al.* Observation of single isolated electrons of high transverse momentum in events with missing transverse energy at the CERN $p\overline{p}$ collider. *Phys. Let. B*, 122(5-6):476 – 485, 1983

[105] P. Bagnaia *et al.* Evidence for $Z^0 \rightarrow e^+e^-$ at the CERN $p\overline{p}$ collider. *Phys. Let. B*, 129(1-2):130 – 140, 1983

[106] D. Buskulic and others (Aleph Collaboration). Update of electroweak parameters from Z decays. *Z.Phys.*, C(60):71–82, 1993

[107] F. Abe *et al.* Evidence for top quark production in $p\bar{p}$ collisions at $\sqrt{s}$ =1.8 TeV. *Phys. Rev. Lett.*, 73(2):225–231, 1994

[108] S. Abachi and others (DØ Collaboration). Search for High Mass Top Quark Production in p$\overline{p}$ Collisions at $\sqrt{s}$= 1.8 TeV. *Phys. Rev. Lett.*, 74:2422–2426, 1995

[109] DONUT Collaboration *et al.* Observation of tau neutrino interactions. *Phys. Let. B*, 504:218–224, 2001

[110] K. Kodama *et al.* Detection and analysis of tau-neutrino interactions in DONUT emulsion target. *Nucl. Instr. and Meth. A*, 493, Issues 1-2:45–66, 2002

[111] N. Cabibbo. Unitary Symmetry and Leptonic Decays. *Phys. Rev. Lett.*, 10(12):531–533, 1963

[112] C. Amsler and others (Particle Data Group). Review of Particle Physics (partial update 2009). *Phys. Let. B*, 667(1):1–1340, 2008

[113] L. Chau and W.-Y. Keung. Comments on the Parametrization of the Kobayashi-Maskawa Matrix. *Phys. Rev. Lett.*, 53:1802, 1984

[114] L. Wolfenstein. Parametrization of the Kobayashi-Maskawa Matrix. *Phys. Rev. Lett.*, 51:1945, 1983

[115] CERN. European Organization for Nuclear Research
URL `http://www.cern.ch`

[116] A. Rubbia. List of Dark Matter experiments available at
URL `http://neutrino.ethz.ch/ArDM/otherexp.html`

[117] M. Guler. D^0 production rate measurement in neutrino interactions. Ph.D. thesis, Middle East Technical University, 2001
URL `http://choruswww.cern.ch/Reference/Theses/guler.pdf`

[118] B. T. Cleveland *et al.* Measurement of the solar electron neutrino flux with the Homestake chlorine detector. *Astrophys. J.*, 496:505–526, 1998

[119] C. F. von Weizsäcker. Über Elementumwandlungen im Innern der Sterne. II. *Physikalische Zeitschrift*, 39:633, 1938

[120] B. Pontecorvo. Neutrino Experiments and the Problem of Conservation of Leptonic Charge. *Zh. Eksp. Teor. Fiz.*, 53:1717, 1967. Reproduced and translated in Sov. Phys. JETP 26, pp. 984. (1968)

[121] B. Pontecorvo. Mesonium and anti-mesonium. *Zh. Eksp. Teor. Fiz.*, 33:549, 1957. Reproduced and translated in Sov. Phys. JETP 6, pp. 429 (1958)

[122] B. Pontecorvo. Inverse beta processes and nonconservation of lepton charge. *Zh. Eksp. Teor. Fiz.*, 34:247, 1958. Reproduced and translated in Sov. Phys. JETP 7, pp. 172 (1958)

[123] Z. Maki, M. Nakagawa, and S. Sakata. Remarks on the Unified Model of Elementary Particles. *Progress of Theoretical Physics*, 28:870, 1962

[124] L. Wolfenstein. Neutrino oscillations in matter. *Phys. Rev. D*, 17(9):2369–2374, 1978

[125] S. P. Mikheev and A. Y. Smirnov. Resonance enhancement of oscillations in matter and solar neutrino spectroscopy. *Sov. J. Nucl. Phys. (Yadernaya Fizika) (Nuovo Cimento)*, 42 (42) (9 C:913–917 (1441) (17), 1985 (1985) (1986)

[126] Y. Fukuda *et al.* Evidence for Oscillation of Atmospheric Neutrinos. *Phys. Rev. Lett.*, 81(8):1562–1567, 1998

[127] K. S. Hirata *et al.* Observation of B-8 Solar Neutrinos in the Kamiokande-II Detector. *Phys. Rev. Lett.*, 63:16, 1989

[128] S. Hatakeyama *et al.* Measurement of the Flux and Zenith-Angle Distribution of Upward Through-Going Muons in Kamiokande $II+III$. *Phys. Rev. Lett.*, 81(10):2016–2019, 1998

[129] K. S. Hirata *et al.* Observation in the Kamiokande-II Detector of the Neutrino Burst from Supernova SN 1987a. *Phys. Rev.*, D38:448–458, 1988

[130] K. Hirata *et al.* Observation of a Neutrino Burst from the Supernova SN 1987a. *Phys. Rev. Lett.*, 58:1490–1493, 1987

[131] K. S. Hirata *et al.* Experimental limits on nucleon lifetime for lepton + meson decay modes. *Phys. Lett.*, B220:308, 1989

[132] K. S. Hirata *et al.* Observation of a small atmospheric ν_μ/ν_e ratio in Kamiokande. *Phys. Lett.*, B280:146–152, 1992

[133] G. Zacek *et al.* Neutrino-oscillation experiments at the Gösgen nuclear power reactor. *Phys. Rev. D*, 34(9):2621–2636, 1986

[134] J. F. Cavaignac *et al.* Indication for neutrino oscillation from a high statistics experiment at the Bugey reactor. *Phys. Lett.*, B148:387–394, 1984

[135] Y. Ashie *et al.* Evidence for an Oscillatory Signature in Atmospheric Neutrino Oscillations. *Phys. Rev. Lett.*, 93(10):101801, 2004

[136] M. H. Ahn *et al.* Indications of Neutrino Oscillation in a 250 km Long-Baseline Experiment. *Phys. Rev. Lett.*, 90(4):041801, 2003

[137] M. H. Ahn *et al.* Measurement of neutrino oscillation by the K2K experiment. *Phys. Rev. D*, 74(7):072003, 2006

[138] K. Abe *et al.* Measurement of Atmospheric Neutrino Flux Consistent with Tau Neutrino Appearance. *Phys. Rev. Lett.*, 97(17):171801, 2006

[139] GALLEX-collaboration
URL `http://www.mpi-hd.mpg.de/nuastro/gallex.html`

[140] SAGE-collaboration. http://www.nu.to.infn.it/exp/all/sage/

[141] J. N. Abdurashitov *et al.* Measurement of the solar neutrino capture rate by the Russian-American gallium solar neutrino experiment during one half of the 22-year cycle of solar activity. *J. Exp. Theor. Phys.*, 95:181–193, 2002

[142] J. N. Abdurashitov *et al.* Measurement of the solar neutrino capture rate with gallium metal. III. Results for the 2002–2007 data-taking period. *Phys. Rev. C*, 80(1):015807, 2009

[143] F. Kaether, W. Hampel, G. Heusser, J. Kiko, and T. Kirsten. Reanalysis of the Gallex solar neutrino flux and source experiments. *Phys. Let. B*, 685(1):47 – 54, 2010

[144] J. N. Bahcall, F. Calaprice, A. B. McDonald, and Y. Totsuka. Solar Neutrino Experiments: The Next Generation. *Physics Today*, 49(7):30–36, 1996

[145] Q. R. Ahmad *et al.* Measurement of Day and Night Neutrino Energy Spectra at SNO and Constraints on Neutrino Mixing Parameters. *Phys. Rev. Lett.*, 89(1):011302, 2002

[146] Q. R. Ahmad *et al.* Direct Evidence for Neutrino Flavor Transformation from Neutral-Current Interactions in the Sudbury Neutrino Observatory. *Phys. Rev. Lett.*, 89(1):011301, 2002

[147] T. S. Collaboration. Low Energy Threshold Analysis of the Phase I and Phase II Data Sets of the Sudbury Neutrino Observatory. *Phys. Rev. C*, 2009

[148] Q. R. Ahmad *et al.* Measurement of the Rate of $\nu_e + d \rightarrow p + p + e^-$ Interactions Produced by $B8$ Solar Neutrinos at the Sudbury Neutrino Observatory. *Phys. Rev. Lett.*, 87(7):071301, 2001

[149] B. Aharmim *et al.* Independent Measurement of the Total Active $B8$ Solar Neutrino Flux Using an Array of $He3$ Proportional Counters at the Sudbury Neutrino Observatory. *Phys. Rev. Lett.*, 101(11):111301, 2008

[150] T. Araki *et al.* Measurement of neutrino oscillation with KamLAND: Evidence of spectral distortion. *Phys. Rev. Lett.*, 94:081801, 2005

[151] K. Eguchi *et al.* First Results from KamLAND: Evidence for Reactor Antineutrino Disappearance. *Phys. Rev. Lett.*, 90(2):021802, 2003

[152] S. Abe *et al.* Precision Measurement of Neutrino Oscillation Parameters with KamLAND. *Phys. Rev. Lett.*, 100(22):221803, 2008

[153] K. Eguchi *et al.* A high sensitivity search for $\overline{\nu_e}$'s from the sun and other sources at KamLAND. *Phys. Rev. Lett.*, 92:071301, 2004

[154] T. Araki *et al.* Experimental investigation of geologically produced antineutrinos with KamLAND. *Nature*, 436:499–503, 2005

[155] M. Mezzetto and T. Schwetz. θ_{13}: phenomenology, present status and prospect. *EURONU-WP6-10-15*, 2010

[156] P. Adamson *et al.* Study of muon neutrino disappearance using the Fermilab Main Injector neutrino beam. *Phys. Rev. D*, 77(7):072002, 2008

[157] D. G. Michael *et al.* Observation of Muon Neutrino Disappearance with the MINOS Detectors in the NuMI Neutrino Beam. *Phys. Rev. Lett.*, 97(19):191801, 2006

[158] P. Adamson *et al.* Measurement of Neutrino Oscillations with the MINOS Detectors in the NuMI Beam. *Phys. Rev. Lett.*, 101(13):131802, 2008

[159] The Soudan 2 Collaboration, W. W. M. Allison, *et al.* The Atmospheric Neutrino Flavor Ratio from a 3.9 Fiducial Kiloton-Year Exposure of Soudan 2. *Phys. Let. B*, 449:137, 1999

[160] Marco Collaboration, A. Surdo, *et al.* Atmospheric neutrino oscillations in the MACRO experiment. *Nucl. Phys. B Proceedings Supplements*, 110:342–345, 2002

[161] F. Boehm *et al.* Final results from the Palo Verde neutrino oscillation experiment. *Phys. Rev. D*, 64(11):112001, 2001

[162] C. Athanassopoulos *et al.* Evidence for neutrino oscillations from muon decay at rest. *Phys. Rev. C*, 54(5):2685–2708, 1996

[163] A. A. Aguilar-Arevalo *et al.* A Search for Electron Antineutrino Appearance at the $\Delta m^2 \sim 1\text{eV}^2$ Scale. *Phys. Rev. Lett.*, 103:111801, 2009

[164] P. Astier *et al.* Search for $\nu_\mu \to \nu_e$ oscillations in the NOMAD experiment. *Phys. Let. B*, 570(1-2):19 – 31, 2003

[165] E. Eskut *et al.* Final results on $\nu_\mu \to \nu_\tau$ oscillation from the CHORUS experiment. *Nucl. Phys. B*, 793(1-2):326 – 343, 2008

[166] A. M. Bakalyarov, A. Y. Balysh, S. T. Belyaev, V. I. Lebedev, and S. V. Zhukov. Results of the experiment on investigation of Germanium-76 double beta decay. *Phys. Part. Nucl. Lett.*, 2:77–81, 2005

[167] M. Apollonio *et al.* Search for neutrino oscillations on a long base-line at the CHOOZ nuclear power station. *European Physical Journal C*, 27:331, 2003

[168] Das Mainzer Neutrinomassen-Experiment
URL http://www.physik.uni-mainz.de/exakt/neutrino/

[169] K. Jakobs. Vorlesung Elementarteilchen II, WS 09 Universität Freiburg, WS 2009

[170] P. Adamson *et al.* Measurement of neutrino velocity with the MINOS detectors and NuMI neutrino beam. *Phys. Rev. D*, 76(7):072005, 2007

[171] A. B. Balantekin and D. Yilmaz. Contrasting solar and reactor neutrinos with a non-zero value of θ_{13}. *Journal of Physics G: Nuclear and Particle Physics*, 35(7):075007, 2008

[172] G. L. Fogli, E. Lisi, A. Marrone, A. Palazzo, and A. M. Rotunno. Neutrino oscillations, global analysis and θ_{13}, 2009

[173] A. de Gouvea, J. Jenkins, and B. Kayser. Neutrino Mass Hierarchy, Vacuum Oscillations, and Vanishing $|U_{e3}|$. *Phys. Rev. D*, 71:113009, 2005

[174] A. de Gouvea and J. Jenkins. Non-Oscillation Probes of the Neutrino Mass Hierarchy and Vanishing $|U_{e3}|$, 2005

[175] C. Guinti and M. Laveder. Collection of links related to neutrino factory
URL http://www.nu.to.infn.it/Neutrino_Factory/

[176] GLACIER-Project
URL http://neutrino.ethz.ch/GLACIER/

[177] A. Rubbia *et al.* LAGUNA: Design of a pan-European Infrastructure for Large Apparatus studying Grand Unification and Neutrino Astrophysics. Design Study of FP7, Project Reference 212343 of the European Commission Research Infrastructures
URL http://laguna.ethz.ch/

[178] A. Bueno, M. Campanelli, S. Navas-Concha, and A. Rubbia. On the energy and baseline optimization to study effects related to the delta-phase (CP-/T-violation) in neutrino oscillations at a neutrino factory. *Nucl. Phys.*, B631:239–284, 2002

[179] A. Ereditato and A. Rubbia. The liquid argon TPC: A powerful detector for future neutrino experiments and proton decay searches. *Nucl. Phys. Proc. Suppl.*, 154:163–178, 2006

[180] A. Ereditato and A. Rubbia. Conceptual design of a scalable multi-kton superconducting magnetized liquid argon TPC. *Nucl. Phys. Proc. Suppl.*, 155:233–236, 2006

[181] A. Ereditato and A. Rubbia. Ideas for future liquid argon detectors. *Nucl. Phys. Proc. Suppl.*, 139:301–310, 2005

[182] I. Gil-Botella and A. Rubbia. Decoupling supernova and neutrino oscillation physics with LAr TPC detectors. *JCAP*, 0408:001, 2004

[183] A. Rubbia. Experiments for CP-violation: A giant liquid argon scintillation, Cerenkov and charge imaging experiment? *Venice 2003, Neutrino oscillations*, pages 321–350, 2004

[184] A. Rubbia. Review of massive underground detectors. *Perugia 2004, Calorimetry in particle physics*, pages 485–506, 2004

[185] A. Rubbia. Neutrino factories: Detector concepts for studies of CP and T violation effects in neutrino oscillations. *Venice 2001, Neutrino telescopes*, 2:435–462, 2001

[186] A. de Gouvea and W. Winter. What would it take to determine the neutrino mass hierarchy if θ_{13} were too small? *Phys. Rev. D*, 73:033003, 2006

[187] P. Huber, M. Lindner, T. Schwetz, and W. Winter. First hint for CP violation in neutrino oscillations from upcoming superbeam and reactor experiments. *JHEP*, 0911:044, 2009

[188] M. Gell-Mann, P. Ramond, and R. Slansky. Complex Spinors and Unified Theories. *Supergravity: Proceedings of the Supergravity Workshop at Stony Brook*, pages 315–321, 1979

[189] T. Yanagida. Horizontal Symmetry and Masses of Neutrinos. *Progress of Theoretical Physics*, 64(3):1103–1105, 1980

[190] R. N. Mohapatra and G. Senjanović. Neutrino Mass and Spontaneous Parity Non-conservation. *Phys. Rev. Lett.*, 44(14):912–915, 1980

[191] W. Verkerke. Measurement of charm production in deep inelastic scattering. Ph.D. thesis, University of Amsterdam, 1998

[192] A. Kayis-Topaksu *et al.* Associated Charm Production in Neutrino-Nucleus Interactions. *Eur. Phys. J.*, C52:543–552, 2007

[193] A. Kayis-Topaksu *et al.* Charged Particle Multiplicities in Neutrino Interactions. *Eur. Phys. J.*, C51:775–785, 2007

[194] A. Kayis-Topaksu *et al.* Measurement of topological muonic branching ratios of charmed hadrons produced in neutrino induced charged- current interactions. *Phys. Lett.*, B626:24–34, 2005

[195] A. Kayis-Topaksu *et al.* Cross-section measurement for quasi-elastic production of charmed baryons in νN interactions. *Phys. Lett.*, B575:198–207, 2003

[196] A. Kayis-Topaksu *et al.* Measurement of Λ_c^+ production in neutrino charged-current interactions. *Phys. Lett.*, B555:156–166, 2003

[197] K. van der Poel. Neutrino induced charm production in the CHORUS calorimeter. Ph.D. thesis, Nationaal instituut voor subatomaire fysica (NIKHEF) Amsterdam, 1999
URL `http://choruswww.cern.ch/Reference/Theses/vanderpoel.pdf`

[198] F. Spada. Neutrino production of charmed particles in the CHORUS experiment. Ph.D. thesis, Università degli Studi di Roma "La Sapienza", 2002

[199] R. M. Barnett. Evidence For New Quarks and New Currents. *Phys. Rev. Lett*, 36:1163–1166, 1976

[200] R. M. Barnett. Neutral currents in elastic and inelastic neutrino scattering. *Phys. Rev. D*, 14(11):2990–2997, 1976

[201] F. di Capua. Charm hunting in OPERA. *OPERA Sorrento Workshop*, 2008

[202] CERN. General description of the CERN project for a neutrino beam to Gran Sasso (CNGS). *CERN AC Note (2000-03)*, 2002
URL `http://proj-cngs.web.cern.ch/proj-cngs/`

[203] D. Autiero. CNGS status report. *OPERA Collaboration Meeting, September at LNGS*, 2009

[204] E. Gschwendtner. The CNGS Facility: Performance and operational Experience. *11th ICATPP Conference on Astroparticle, Particle, Space Physics, Detectors and Medical Applications, Villa Olmo, Como, Italy*, 2009

[205] M. Giovannozzi, R. Cappi, S. S. Gilardoni, M. Martini, E. Métral, A. S. Müller, P. Scaramuzzi, and R. Steerenberg. Multiturn extraction based on trapping in stable islands. *AIP Conf. Proc.*, 773(CERN-AB-2004-095):296–300. 4 p, 2004

[206] R. Cappi, S. Gilardoni, M. Giovannozzi, M. Martini, E. Métral, and R. Steerenberg. Final results from the novel multi-turn extraction studies at the CERN proton synchroton. *Proceedings of 2005 Particle Accelerator Conference, Knoxville, Tennessee*, 2005

[207] A. Ariga. Development and realization of a super-low-background interface detector using emulsions for the OPERA experiment. Ph.D. thesis, Nagoya University, 2008

[208] A. Eriditato *et al.* Status of OPERA, Presentation to LNGSC. *XXXII LNGSC*, 2009

[209] P. Sala. CNGS Neutrino Flux Calculations
URL `http://www.mi.infn.it/ psala/Icarus/cngs2005.html`

[210] R. Acquafredda *et al.* The OPERA experiment in the CERN to Gran Sasso neutrino beam. *JINST*, 4(04):P04018, 2009

[211] S. Kretzer and M. H. Reno. Tau neutrino deep inelastic charged current interactions. *Phys. Rev. D*, 66(11):113007, 2002

[212] M. Dracos. Neutrinos from CERN to Gran Sasso: The CNGS project. *Journal of Physics: Conference Series*, 203(1):012013, 2010

[213] LVD-collaboration
URL `http://www.bo.infn.it/lvd/`

[214] BOREXIONO-collaboration
URL `http://borex.lngs.infn.it/`

[215] ICARUS-collaboration
URL `http://www.aquila.infn.it/icarus/`

[216] M. Guler *et al.* OPERA: An appearance experiment to search for $\nu_\mu \longleftrightarrow \nu_\tau$ oscillations in the CNGS beam. Experimental proposal. *CERN-SPSC-2000-028, CERN-SPSC-P-318, LNGS-P25-00*, page 265, July 2000. CERN-SPSC-2000-028

[217] DONUT-collaboration
URL `http://www-donut.fnal.gov/`

[218] CHORUS-collaboration
URL `http://choruswww.cern.ch/`

[219] J. Knüsel. Development of advanced measurement techniques for emulsion films of the OPERA neutrino experiment. Master's thesis, University Bern, LHEP, 2007

[220] T. Adam *et al.* The OPERA experiment Target Tracker. *Nucl. Instr. and Meth. A*, 577(3):523 – 539, 2007

[221] M. Dracos *et al.* Desription of the OPERA Target Tracker (TT) production in Strasbourg. *Institut de Recherches Subatomiques, Strabourg*

[222] A. Cazes, A. Cecchetti, B. Dulach, F. Iungo, M. Incurvati, *et al.* Electromagnetic characterization of the 990 ton gapless magnets for the OPERA experiment. *JINST*, 2(03):T03001, 2007

[223] M. Incurvati and F. Terranova. Modeling skin effect in large magnetized iron detectors. *Nucl. Instr. and Meth. A*, 500(1-3):441 – 445, 2003. NIMA Vol 500

[224] M. Dracos *et al.* The OPERA Experiment. *Physics of Atomic Nuclei*, 67, N0. 6:1092–1124, 2004

[225] A. Bertolin *et al.* The RPC system of the OPERA experiment. *Nucl. Instr. and Meth. A*, 602(3):631 – 634, 2009. Proceedings of the 9th International Workshop on Resistive Plate Chambers and Related Detectors - RPC08

[226] S. Dusini *et al.* Design and prototype tests of the RPC system for the OPERA spectrometers. *Nucl. Instr. and Meth. A*, 508(1-2):175 – 180, 2003. Proceedings of the Sixth International Workshop on Resistive Plate Chambers and Related Detectors

[227] M. Bazzi *et al.* The I-meter, a distributor unit for the OPERA RPC HV system. *Nucl. Instr. and Meth. A*, 580(3):1441 – 1445, 2007

[228] A. Bergnoli *et al.* Performances of the OPERA RPCs. *Nucl. Instr. and Meth. A*, 602(3):635 – 638, 2009. Proceedings of the 9th International Workshop on Resistive Plate Chambers and Related Detectors - RPC08

[229] A. Bergnoli *et al.* Tests of OPERA RPC detectors. *Nuclear Science, IEEE Transactions on*, 52(6):2963 –2970, 2005

[230] A. Mengucci, A. Paoloni, M. Spinetti, and L. Votano. Gas mixture studies for streamer operation of Resistive Plate Chambers at low rate. *Nucl. Instr. and Meth. A*, 583(2-3):264 – 269, 2007

[231] R. Zimmermann, J. Ebert, C. Hagner, B. Koppitz, V. Saveliev, W. Schmidt-Parzefall, J. Sewing, and Y. Zaitsev. Erratum to: "The precision tracker of the OPERA detector": Nucl. Instr. and Meth. A 555 (2005) 435-450. *Nucl. Instr. and Meth. A*, 557(2):690 – 690, 2006

[232] R. Zimmermann, J. Ebert, C. Hagner, B. Koppitz, V. Saveliev, and Y. Z. W. Schmidt-Parzefall, J. Sewing. The precision tracker of the OPERA detector. *Nucl. Instr. and Meth. A*, 555(1-2):435–450, 2005

[233] C. Pistillo. An automatic scanning system for nuclear emulsion analysis in the OPERA experiment. Ph.D. thesis, Universitá degli Studi di Napoli Federico II

[234] A. Marotta. Performances of the OPERA experiment to search for $\nu_\mu \to \nu_\tau$ oscillations in the CNGS neutrino beam. Ph.D. thesis, Universitá degli Studi di Napoli Federico II, 2005

[235] D. Frekers and V. Pilipenko. Status of lead production october till november 2006. *OPERA Board Meeting November 2006*, 2006

[236] A. Anokhina *et al.* Study of the effects induced by lead on the emulsion films of the OPERA experiment. *JINST*, 3(07):P07002, 2008

[237] A. Anokhina *et al.* Emulsion sheet doublets as interface trackers for the OPERA experiment. *JINST*, 3(07):P07005, 2008

[238] A. Ariga and for the OPERA collaboration. Emulsion sheet doublets as interface trackers for the OPERA experiment, 2008

[239] G. Rosa, G. Romano, and C. Sirignano. Automatic development of OPERA emulsion films - Overview of the project. *Internal OPERA Note*, 2004

[240] T. Fukuda, K. Kodama, M. Komatsu, S. Miyamoto, K. Morishima, *et al.* The analysis of interface emulsion detector for the OPERA experiment in JAPAN Scanning facility. *JINST*, 5(04):P04009, 2010

[241] K. Morishima and T. Nakano. Development of a new automatic nuclear emulsion scanning system, S-UTS, with continuous 3D tomographic image read-out. *JINST*, 5(04):P04011, 2010

[242] N. Armenise *et al.* High-speed particle tracking in nuclear emulsion by last-generation automatic microscopes. *Nucl. Inst. and Meth.*, A551:261–270, 2005

[243] L. Arrabito *et al.* Hardware performance of a scanning system for high speed analysis of nuclear emulsions. *Nucl. Inst. and Meth.*, A568:578–587, 2006

[244] L. Arrabito *et al.* Track reconstruction in the emulsion-lead target of the OPERA experiment using the ESS microscope. *JINST*, 2:P05004, 2007

[245] I. Kreslo, M. Cozzi, A. Ereditato, M. Hess, J. Knuesel, *et al.* High-speed analysis of nuclear emulsion films with the use of dry objective lenses. *JINST*, 3(04):P04006, 2008

[246] C.Girerd, S.Gardien, J.Burch, S.Katsanevas, and J.Marteau. Ethernet network-based DAQ and smart sensors for the OPERA long-baseline neutrino experiment. *OPERA note 21 23-11-2000*, 2008

[247] J. Marteau. The OPERA global readout and GPS distribution system, 2009 URL `http://arxiv.org/abs/0906.1494`

[248] N. Strasbourg, Bern and Dubna. A global Data Acquisition System for the OPERA Experiment (baseline). *OPERA note 29 17-4-2002*, 2002

[249] B. Steinke, C. Göllnitz, B. Janutta, R. Zimmermann, A. Paoloni, *et al.* The OPERA PT trigger system: implementation and performance results. *OPERA note 90 3-06-2008*, 2008

[250] C. Jollet and A. Meregaglia. Comparison of the kinematical variables between Monte-Carlo and data on 2008 and 2009 runs. *OPERA note 114 05/3/2010*, 2010

[251] J. Marteau. OPERA first events from the CNGS neutrino beam, 2007
URL http://arxiv.org/abs/0706.1699

[252] A. Garfagnini and C. Pistillo. Observation of neutrino interactions in the OPERA detector, 2008
URL http://arxiv.org/abs/0805.3243

[253] N. Agafonova. The detection of neutrino interactions in the emulsion/lead target of the OPERA experiment. *JINST*, 4:06020, 2009

[254] G. Lutter. The OPERA experiment: Preliminary results from the 2008 run, 2009
URL http://arxiv.org/abs/0905.4521

[255] M. Sioli *et al.* Measurement of the atmospheric muon charge ratio with the OPERA detector. *Eur. Phys. J. C*, 67(1):25, 2010

[256] D. Di Ferdinando *et al.* Nuclear emulsions in the OPERA experiment, 2009
URL http://arxiv.org/abs/0812.0451

[257] L. Patrizii and for the OPERA collaboration. Study of the effects induced by lead on the emulsion films of the OPERA experiment. *JINST*, 3:07002, 2008

[258] A. Bertolino. A preliminary analysis of the 2009 OPERA data. *OPERA note 108 12/1/2010*, 2010

[259] E. Barbuto, C. Bozza, and C. Sirignano. Vertex Reconstruction in SySal.NET: the "global vertexing" algorithm. *OPERA note 78 4-06-2006*, 2006

[260] V. Tioukov, I. Kreslo, Y. Petukhov, and G. Sirri. The FEDRA–Framework for emulsion data reconstruction and analysis in the OPERA experiment. *Nucl. Instr. and Meth. A*, 559(1):103 – 105, 2006. Proceedings of the X International Workshop on Advanced Computing and Analysis Techniques in Physics Research - ACAT 05

[261] M. Besnier and D. Duchesneau. Reconstruction et analyse d'interactions de neutrinos dans les blocs cibles mulsions d'OPERA et discrimination du fond charm dans le canal $\tau \rightarrow 3h$. Ph.D. thesis, Savoie U., Annecy, 2008

[262] D. Autiero. The OPERA event generator and the data tuning of nuclear re-interactions. *Nucl. Phys. B - Proceedings Supplements*, 139:253 – 259, 2005

[263] L.Chaussard. OpGeom: software model of the OPERA detector. *OPERA note 69 07/1/2005*, 2005

[264] A. V.Chukanov, D. V.Naumov, E. A.Naumova, A. S.Sheshukov, and S. G.Zemskova. Fedra Virtual Monte Carlo. Applications. *OPERA note 95 25-10-2008*, 2008

[265] T. Glebe. Vt++ Version 1.0. *HERA-B Note 00-175, Software 00-013*, 2000
URL http://www-hera-b.desy.de/notes/00/00-175.ps

[266] M. Anfreville *et al.* The drift chambers of the NOMAD experiment. *Nucl. Instr. and Meth. A*, 481(1-3):339 – 364, 2002

[267] N. Agafonova *et al.* Observation of a first ν_τ candidate in the OPERA experiment in the CNGS beam. *Phys. Let. B*, 691:138–145, 2010

[268] A. Kolmogorov. Confidence limits for an unknown distribution function. *Annals of Mathematical Statistics*, 12:461–483, 1941

[269] N. Smirnov. Table for estimating the goodness of fit of empirical distribution. *Annals of Mathematical Statistics*, 19:279–281, 1948

[270] A. Badertscher, L. Knecht, M. Laffranchi, G. Natterer, A. Rubbia, and T. Strauss. Test of a LAr TPC in a magnetic field and investigation of high temperature superconductors in liquid argon and nitrogen. *To appear in Proc. 1st International Workshop towards the Giant Liquid Argon Charge Imaging Experiment (GLA2010)*, 2010

[271] S. Aoki, K. Hoshino, M. Nakamura, K. Niu, K. Niwa, and N. Torii. Fully automated emulsion analysis system. *Nuclear Instruments and Methods in Physics Research Section B: Beam Interactions with Materials and Atoms*, 51(4):466 – 472, 1990

[272] T. Strauss. Test of a high temperature superconductor coil in liquid nitrogen and liquid argon. Master's thesis, Humboldt-Universität Berlin, ETH Zürich, 2006

[273] C. Rubbia. The Liquid-argon time projection chamber: a new concept for Neutrino Detector. *CERN-EP*, 77:08, 1977

[274] S. Amerio *et al.* Design, construction and tests of the ICARUS T600 detector. *Nucl. Instr. and Meth. A*, 527, Issue 3:329–410, 2004

[275] A. Badertscher, M. Laffranchi, A. Meregaglia, and A. Rubbia. First operation of a liquid argon TPC embedded in a magnetic field. *New J. Phys.*, 7:63, 2005

[276] D. B. Cline, J. G. Learned, K. McDonald, and F. Sergiampietri. LANNDD–a massive liquid argon detector for proton decay, supernova and solar neutrino studies and a neutrino factory detector. *Nucl. Instr. and Meth. A*, 503, Issues 1-2:136–140, 2003

[277] A. Badertscher, M. Laffranchi, A. Meregaglia, A. Muller, and A. Rubbia. First results from a liquid argon time projection chamber in a magnetic field. *Nucl. Inst. and Meth.*, A555:294–309, 2005

[278] T. I. D. W. Group, T. Abe, *et al.* International Scoping Study (ISS) for a future neutrino factory and Super-Beam facility. Detectors and flux instrumentation for future neutrino facilities. *JINST*, 4(05):T05001, 2009